UNIVERSITY OF OKLAHOMA

GRADUATE COLLEGE

NUCLEAR MAGNETIC RESONANCE (NMR) STUDY OF FREEZING AND THAWING OF SATURATED POROUS MEDIA AND APPLICATION TO SHALE AND PORE VOLUME COMPRESSIBILITY ESTIMATION

A DISSERTATION

SUBMITTED TO THE GRADUATE FACULTY

in partial fulfillment of the requirements for the

degree of

DOCTOR OF PHILOSOPHY

By

RAHUL DASTIDAR
Norman, Oklahoma
2007

UMI Number: 3283875

ProQuest Information and Learning Company
300 North Zeeb Road
P.O. Box 1346
Ann Arbor, MI 48106-1346

NUCLEAR MAGNETIC RESONANCE (NMR) STUDY OF FREEZING AND THAWING OF SATURATED POROUS MEDIA AND APPLICATION TO SHALE AND PORE VOLUME COMPRESSIBILITY ESTIMATION

A DISSERTATION APPROVED FOR THE
MEWBOURNE SCHOOL OF PETROLEUM AND GEOLOGICAL ENGINEERING

BY

Dr. Carl H. Sondergeld, Chair

Dr. Chandra S. Rai

Dr. Richard F. Sigal

Dr. Faruk Civan

Dr. Roger M. Slatt

ACKNOWLEDGEMENTS

Translation of gratitude into mere words doesn't seem to be an adequate expression to people who helped in many ways to achieve my goal. But, the least I can do is to thank them with all my heart.

Firstly, I would like to thank my major advisor, **Dr. Carl H. Sondergeld**. I could not have imagined having a better advisor and mentor for my Ph.D. His attitude, the constant strive to be perfect and heartfelt passion for work is what I will always look upto and will try to have a similar outlook on life and work. I am highly indebted for all his time and effort. **Dr. Chandra S. Rai** is a man of constant source of inspiration. His guidance, constructive criticism and scholastic advice kept me in focus throughout my Ph.D. study. On another note, I would also like to thank **Mrs. Rosemary Sondergeld** and **Mrs. Usha Rai** for all the mouth watering food they cooked for all the students. I would like to thank my committee members **Dr. Richard F. Sigal**, **Dr. Faruk Civan** and **Dr. Roger M. Slatt** for providing me with technical assistance and valuable inputs while reviewing my work.

I would like to thank **Gary Stowe** and **Bruce Spears** at the Integrated Core Characterization Center of the University of Oklahoma for all the help and support. I would like to thank all members of the **Experimental Rock Physics Consortium** for granting access to the cores and providing me the financial assistance towards my graduate study. I would like to thank my friends **Rehan Shahreyar, Aristotelis Pagoulatos, Anup T. Hunnur, Rehan Javed, Rishi Singh, Dung Tran, Juan Gomez Pablo, Argyrios Karastathis, Mriganko Sarkar, Venkataraman Jambunathan** and my other colleagues who shared office or lab space with me and if not, constantly

dropped into my office for coffee and delightful chats. I would like to thank **Erricos Durham** at Anadarko Petroleum for being a wonderful mentor during my internship and becoming a life time friend. I also thank **Dr. William J. Carey** at Los Alamos National Laboratory for providing me valuable work experience. I extend my thanks to all current and previous staff of MPGE who helped me directly or indirectly and made my stay at University of Oklahoma a memorable one.

Last but not the least, I would like to thank my family who are of utmost importance to me, I would like to say "Thank you" to my **Mom and Dad** for all sacrifices they have made for me. Their constant inspiration, boundless love and affection have molded me in a manner that I can stride gracefully in this world with head held high. I would like to thank my brother **Dr. Arindam Dastidar**, sister-in-laws **Dr. Supriya Dastidar**, **Mrs. Minu Basu** and my **parents–in–law** for their constant support throughout my Ph.D. study. Finally, I would like to thank my dearest wife **Vishakha** for standing beside me while I was going through roller coaster of euphoria and frustration as a graduate student. I can't thank her enough for all the support she gave me over the last few years. Lastly, I would like to thank **God** for his blessings without which nothing can be accomplished.

Rahul Dastidar

Norman, Oklahoma

October, 2007

TABLE OF CONTENTS

LIST OF TABLES

LIST OF FIGURES

ABSTRACT

This study has three parts each focusing on applying NMR to classical problem; first, I studied the process of freezing and thawing in reservoir sandstones; second, I study the application of NMR to the determination of porosity (ϕ) and water saturation (S_w) of shales, and to evaluate if meaningful ϕ, S_w values could be measured on drilling cuttings using NMR; and third, I measured pore volume compressibility using NMR.

NMR is used routinely in the oil and gas industry to determine in-situ water saturation and bound or non movable water saturation. It is used for rock typing and to provide estimates of permeabilities. Extending these uses to zones of permafrost and hydrate requires understanding NMR measurements in the presence of cold temperature and ice. The porous media in permafrost region generally contain ice in addition to brine. The presence of ice complicates the fluid dominated NMR response. The main objective of this study is to understand the freeze-thaw behavior of NMR in saturated reservoir rocks using a 2 MHz (oilfield operating frequency) NMR spectrometer and a Carr, Purcell, Meiboom and Gill (CPMG) pulse sequence technique. In this experimental based study, brine saturated reservoir and synthetic core plugs were temperature cycled from 22 ^{0}C to -12 ^{0}C. Core porosities ranged from 18% to 37% while Klinkenberg permeabilities ranged from 10 md to 5000 md. Quartz is the dominant mineral present in all the core plugs. Effective surface relaxivities were determined using high pressure mercury injection test on parallel samples. The surface relaxivity ranged from 21.5 μm/sec to 59.7 μm/sec. Attempts to estimate the surface relaxivity of the ice produced mixed results. Temperature effects are shown to be important in estimating porosity at low temperature; failure to correct for temperature lead to overestimation of porosity. Temperature

dependent frequency shifts in T_2 distribution are attributed to the temperature dependency of surface relaxivity. Liquid water is present at temperature as low as -12 ^{0}C. Hysteresis in the NMR response exists between freezing and thawing. Melting is a gradual process, and one model suggests that ice in small pores thaws before the ice in big pores thaws. Indirect evidence suggests that the surface relaxivity of ice (ρ_i) is similar to that of the rock matrix.

Conventional logging tool response is complicated by the presence of shale making it difficult to interpret the log response. Water saturation in shales assumes the shales are filled with brines found in nearby sands. In gas shales where brines cannot be sampled it is impossible to measure shale water saturation. The ϕ and S_w of six unpreserved shale samples and their pulverized equivalents were measured with NMR. The estimated NMR porosity from the cuttings is always lower than plug porosity but within +/- 1.0 p.u. The estimated water saturation from cuttings is about 60% lower than that of plugs and may be a function of cutting size. Ninety percent of the water present in the all the six shale plugs/cuttings is bound to the surface of the core either as hydration water or by capillary forces. An obvious drawback of the study is the use of unpreserved core plugs. Immersion of cuttings in water and oil indicate the estimation of ϕ and S_w by NMR was possible in oil based mud.

Many pore volume compressibility estimation measurement are performed with non-polar fluids such as kerosene, mineral oil, air and nitrogen (N_2). Applying NMR to brine saturated core plugs subjected to hydrostatic stress, allowed us to measure compressibility in the presence of natural polar fluid. NMR measured compressibilities to 5000 psi were compared to those measured using helium. For 5/6 samples, measurements

from brine saturated yielded higher compressibility then when filled with helium. The role of water in softening clays and hydrating bonds cannot be overlooked when measuring compressibility.

OUTLINE

This study is divided into six chapters.

Chapter 1 develops the motivation to understand freeze-thaw process in a saturated porous media.

Chapter 2 presents sufficient theoretical background to understand and interpret NMR result for the freeze-thaw experiments. Fundamental petrophysical concepts such as NMR porosity, bound water estimation, and surface relaxivity are also discussed. A brief review of previous studies made on ice in porous media (soil, porous glass, and sand) are presented. These include interpretations of indirect measurements (NMR, x-ray diffraction, acoustics and electrical measurements), direct measurements (microscope) or theoretical.

Chapter 3 describes the experimental techniques which include sample preparation, equipment and measurement procedures.

Chapter 4 contains the results and conclusion of detailed freeze-thaw studies on reservoir rocks.

Chapter 5 presents the motivation behind measurement of porosity and water saturation for shale using NMR. Chapter 5 also describes the experimental procedure and summarizes results of the study.

Chapter 6 introduces the motivation to estimate pore volume compressibility using NMR. Chapter 6 describes the experimental procedure and contains and conclusions of the pressure study.

CHAPTER 1

1.1 Motivation

Most recently, the potential for huge oil and gas resources in the form of hydrates (e.g. North Slope) and existing oil fields located in permafrost regions (e.g. Kuparuk field, Sakhalin) have drawn considerable interest in permafrost process by the oil and gas industry. A few of the major issues associated with reservoirs in these conditions are: 1) estimation of hydrate resources, 2) drilling and recovery stability, and 3) building infrastructure such as platform, pipelines etc. In-situ conversion process (ICP) is a technique to convert the kerogen in oil shale into liquid hydrocarbon in the subsurface by heating, which involves the use of a "freeze wall". To prevent mixing of the hydrocarbon in the ground water "ice wall" technology is being used (www.shell.com). Ice wall technology is an artificially created no flow boundary in the subsurface created by freezing the pore water. The stability of rock during and after freezing becomes a major concern.

In nature, the freezing and thawing is observed mainly in cold artic regions which are covered by permafrost such as parts of Russia, northern Canada and Alaska, which are completely frozen during the winter and partly thawed in summer. Permafrost is defined as consolidated or unconsolidated water saturated porous media at or below 0 ^{0}C for more than two years consecutively (Andersland and Ladanyi, 2004). Permafrost can be continuous or discontinuous laterally with varying thickness. Permafrost has been studied for many years in civil engineering (road construction, bridges, facilities etc.) due to seasonal changes in the mechanical strength of the frozen ground as a result of the

freeze-thaw cycle. In civil engineering, strength of the foundation plays a very important role in determining the stability of the infrastructure. During winter, the pore water is frozen completely or partially depending on various factors such as temperature, salinity of the pore water, strongly or weakly bonded to the mineral surface, etc. Ice adds mechanical support to porous media. However when ice melts, or thaws, the unfrozen ground has to bear the overburden stress associated with the existing infrastructure. This plays an important role in the design of roads, building foundations, etc. The creation of ice in small pores and cracks leads to volume expansion which progressively leads to fracturing and degradation of the material. The climatic and hydrogeological conditions above the permafrost present extremely difficult conditions to the drilling and production operation over extended time.

Nuclear Magnetic Resonance (NMR) has many applications in the conventional oil and gas industry. A fundamental question to be answered is: which fraction of the pore space freezes if the entire pore space is not frozen? Historical freeze-thaw studies on naturally occurring porous media used seismic and electrical measurements. Recent NMR related studies are based on water saturated artificial porous material such as silica gel, vycor glass, powdered silica, and activated charcoal at resonating frequencies different from oilfield spectrometer frequency (e.g. Allen et al., 1997, 1998, Hansen et al., 1996, 2002, Overloop and Gerven, 1992, Strange and Webber, 1997, Stapf and Kimmich, 1995 and Valiullin and Furo, 2002). A 2MHz NMR poorly constrained study of thawing a unconsolidated sandstone from North Slope of Alaska was performed by Kleinberg and Griffin, 2005.

In my thermal cycling study, all of the porous media are brine saturated naturally

occurring reservoir rocks except one which is a glass bonded silica (Filtros). I used a 2MHz (oilfield operating frequency) NMR spectrometer and a Carr, Purcell, Meiboom and Gill (CPMG) pulse sequence technique.

CHAPTER 2 – NMR BACKGROUND

2.1 Introduction

Interactions of subatomic particles such as protons in the presence of known magnetic field is known as nuclear magnetic resonance phenomenon. It is similar to other electromagnetic wave interactions with the matter such as microwave, X-rays, etc. NMR (Bloch et al., 1946) uses the intrinsic magnetic properties of spinning protons by resonating the ^{1}H atom at its Larmor frequency. Elements with odd number of protons such as ^{1}H, ^{13}C or ^{23}Na are suitable for NMR measurement due to non zero spin quantum number. The frequency range for NMR measurement usually lies in the range of 10^{6}-10^{9} Hz (Cowan, 1997).

2.2 Nuclear Magnetic Resonance (NMR) Phenomenon

2.2.1 NMR Physics

An atomic nucleus is composed of protons and neutrons. A proton is a small particle with a positive charge, while a neutron has no electric charge but has a mass similar to that of a proton. Both proton and neutron have magnetic moments, μ. The presence of a proton in the ^{1}H atom and the prevalence of ^{1}H atom in most fluids causes the fluid to have a net magnetic moment when placed in a magnetic field. In the absence of any other external magnetic field the individual magnetic moments are aligned with earth's magnetic field. However, if externally a magnetic field (denoted as B_o) is applied there is a tendency for the individual magnetic moments of ^{1}H atoms to align with the applied magnetic field (B_o) i.e., along the direction of the field (longitudinal plane). The individual protons

precess at a frequency called the **Larmor frequency.** The Larmor frequency (*f*) is related to the applied magnetic field (B_o) by a simple relationship:

$$f = \frac{\gamma B_o}{2\pi} \quad \{2.1\}$$

where, γ is the gyromagnetic ratio, which is a measure of the strength of the nuclear magnetism and is constant for each nucleus. The different nuclei have different gyromagnetic ratios, the species can be differentiated on the basis of their Larmor frequencies. This is a fundamental equation for all NMR techniques.

When a secondary oscillating magnetic field (B_1) is applied perpendicular (90^0 – transverse plane) to the static magnetic field (B_o), it causes the net magnetization of ^1H atom to tip from longitudinal plane to the transverse plane. When the secondary magnetic field (B_1) is turned off, the proton population begins to lose coherency, and as a result the induced signal in the receiver coil decays. This decay of the signal is called the **Free Induction Decay (FID)** and is usually exponential in time. It is denoted as T_2^* and is on the order of a few tenths of a microsecond. The decay is due to the nonuniformity in the B_o magnetic field resulting in protons at different locations precessing at different Larmor frequencies. This nonuniformity in the static magnetic field can be suppressed by employing **Spin-Echo** techniques. Dephasing due to inhomogeneity in the static magnetic field, B_o, can be reversed by applying a 180^0 pulse (Keller, 1991). The 180^0 pulse is applied at a time τ after the 90^0 pulse. Refocusing occurs at 2τ (Inter Echo spacing, TE) after the 90^0 pulse. Due to this application of the refocusing pulse the phase angle of the transverse magnetization of ^1H atom will be reversed. At each inter echo time TE a signal will be generated in the receiver coil. This signal is called a spin echo. Once the 180^0 pulse is removed, the vectors (magnetic moment) start to diphase due to

molecular interaction and diffusion. These effects result in loss of coherency which produces the spin echo decay. The magnitude of this spin echo decays exponentially with a time constant known as **Transverse Relaxation Time, T_2**. For simple systems the spin echo can be fitted to an exponential form as described by:

$$M(t) = M_o e^{\frac{-t}{T_2}} \quad \text{.....} \{2.2\}$$

where M(t) is the magnitude of the transverse magnetization at a time t; t is the time after protons are exposed to the 180^0 pulse and M_o is the magnitude of the transverse magnetization at t = 0. Because a single spin echo decays very rapidly, a series of 180^0 pulses is applied at an interval of TE to generate a train of spin echoes.

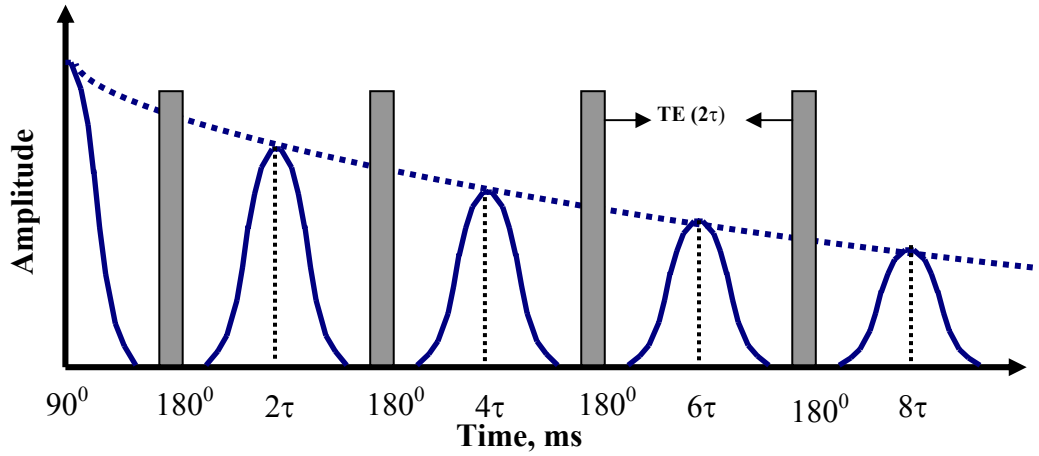

Figure 2.2.1: Idealized Spin-Echo Train, Coates et al. (1999). A series of spin echoes with decreasing amplitude. The CPMG pulse sequence consists of one 90^0 pulse followed by a series of 180^0 pulses. 2τ is the inter echo spacing (TE) or time between 180^0 pulses.

The entire pulse sequence i.e., – a 90^0 followed by a series of 180^0 pulses, is known as a **CPMG** sequence (**Fig. 2.2.1**) named after the inventors Carr, Purcell, Meiboom, and Gill (Brownstein and Tarr, 1979). The above spin echo is for a single pore body. For a multiple pore body system such as a porous network, the exponential decay is a summation of the individual decays. Using an inversion processing technique the raw

decay curve can be fitted to a T_2 spectrum or distribution. All of the NMR interpretation and the estimated petrophysical parameters such as porosity, bound volume/ free fluid index, etc. are based on this T_2 distribution. The process is inherently non-linear and requires a smoothing function to be well behaved. The exact details of the spectrum depend on the smoothing function and the number of the basis elements. However as shown in **Appendix B**, characteristics appear insensitive to the actual number of exponentials used in the fit.

2.2.2 Temperature Effect on NMR Response

The magnetization $M_x(t)$ or net magnetic moment at any time, t and temperature T is mathematically defined by Curie's law (Cowan, 1997):

$$M_0 = N\frac{\gamma^2 h^2 I(I+1)}{3(4\pi^2)kT}B_0 \quad \text{.....} \{2.3\}$$

where N is number of nuclei per unit volume, γ is gyromagnetic ratio, h is Planck's constant (6.626×10^{-34} J/s), I is the spin quantum number of the nucleus (1/2), B_0 is the static magnetic field, k is Boltzman's constant (1.3807×10^{-23} J/K) and T is the temperature in Kelvin. Gyromagnetic ratio (γ for ^1H is 4257.7 Hz/G). Thus, M_0 is directly proportional B_0 and inversely related to absolute temperature T provided the porous medium is with in the "sweet spot" of the instrument. Sweet spot is the position in the instrument over which the magnetic field, B_0, is constant. For a constant magnetic field B_0, the net magnetization is only affected by the temperature of the precessing protons (^1H). Thus **Eqn. 2.3** can be modified for a constant magnetic field B_0:

$$M(t,T) = \frac{C}{T} \quad \text{.....} \{2.4\}$$

where $C = N\frac{\gamma^2 h^2 I(I+1)}{3(4\pi^2)k}B_0$

At t = 0, M (0, T) is equal to M_0. All of the remaining parameters are constant. The total area under the T_2 distribution is same as magnetization M (t, T) at t = 0 i.e., M (0, T). The effect of temperature on precession is especially important because the tools that are used in the oil and gas field are calibrated at ambient conditions. The temperature of the subsurface can vary approximately from 300 ^{0}C to -20 ^{0}C, i.e., high temperature reservoir to cold permafrost region. It is conceivable that under field conditions downhole NMR measurements systems, i.e. logging tools, could experience the entire temperature range. However, even under generic logging conditions, it becomes important to correct the tool response for elevated temperatures found in reservoirs. Numerous authors have investigated the effect of temperature on the NMR response (Cowan, 1997, Godefroy et al., 2001, Gultekin and Gore, 2005, Latour et al., 1992). Most data is reported temperature corrected. However this assumes the temperature is measured correctly. Temperature in logging should be reported separately and uncorrected data should be made available.

Although the nuclear magnetism is inversely related to temperature (Cowan, 1997), it is observed that magnitude of NMR signals can decrease, increase, or remain unchanged with increasing temperature for common pulse sequences (Gultekin and Gore, 2005). Surface dominated relaxation processes have been reported to show temperature dependence in natural rock (Godefroy et al., 2001). **Fig. 2.2.2** shows the theoretical variation (Curie's law) in NMR estimated porosity for a rock whose porosity is 19%

(estimated at 28 ^{0}C – room condition) over the temperature range from 200 ^{0}C to -20 ^{0}C. Thus an NMR tool calibrated at ambient conditions, will over estimate porosity in the permafrost region and underestimate porosity in regular to high temperature reservoirs. This will have a direct impact on the estimation of hydrocarbons in place and will affect the economics of the reservoir. Thus, it becomes essential to correct the net magnetization (**Eqn. 2.3**) for the temperature.

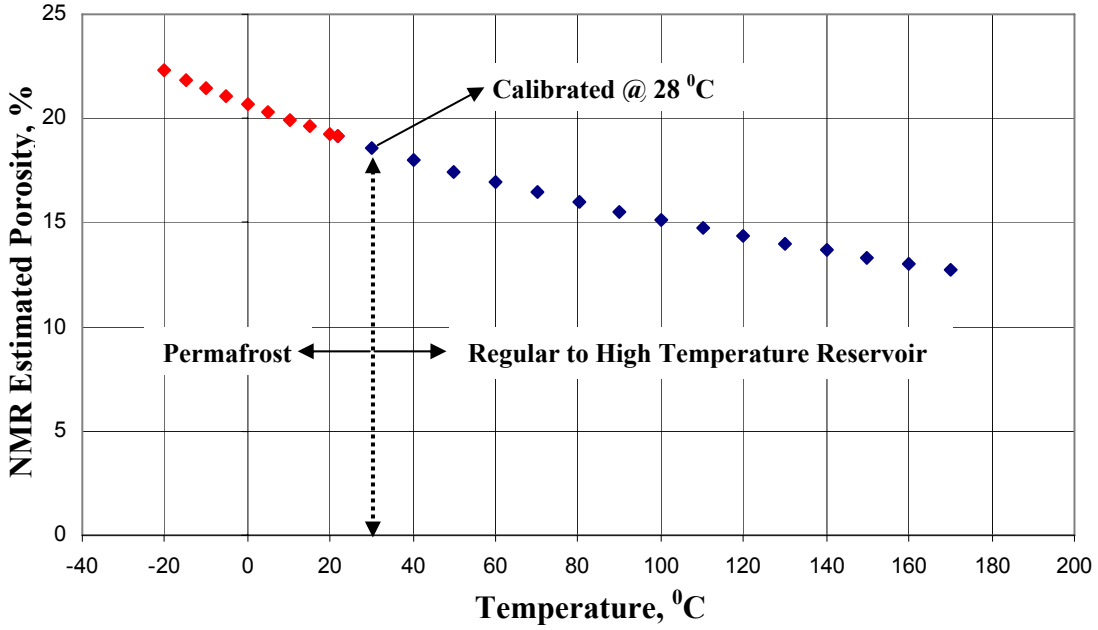

Figure 2.2.2: NMR estimated porosity at different temperature for a rock whose porosity is 19% at room conditions (28 ^{0}C). The variation in porosity is due to the effect of temperature on magnetization.

A porous media can be thought of as a random arrangement of pore bodies of same or different dimensions connected by pore throats. Pore bodies can be associated with a single exponential decay, assuming they are in the fast diffusion limit (Dunn et al., 2002). The net CPMG pulse sequence response is a summation of the individual exponential decays described by:

$$M(t) = \sum_{i=1}^{n} M_{oi} e^{\frac{-t}{T_{2i}}} \quad \text{.....\{2.5\}}$$

where M_{oi} is the magnitude of the i^{th} pore at t = 0 relaxing with a decay constant T_{2i}. T_2 is the characteristic time constant known as transverse relaxation time. There are three mechanisms responsible for transverse relaxation of hydrogen atoms:

1. **Bulk Relaxation** (T_{2Bulk}): Relaxation in the bulk fluid primarily arises as a result random motion of hydrogen atoms which is an intrinsic property of the fluid (Coates et al, 1999). It is related to fluid viscosity by:

$$\frac{1}{T_{2Bulk}} = \frac{1}{3}\left(\frac{298\eta}{T_K}\right) \quad \{2.6\}$$

where η is the viscosity in cp and T_K is the temperature in ^{0}K.

2. **Surface Relaxation** ($T_{2Surface}$): Relaxation occurs at the fluid-solid interface and is described by the following equation (Kenyon, 1992):

$$\frac{1}{T_2} = \rho_2\left(\frac{S}{V}\right)_{pore} \quad \{2.7\}$$

where ρ_2 is the surface relaxivity, a property of the matrix, and $\left(\frac{S}{V}\right)_{pore}$ is the ratio of the pore surface to the pore volume.

3. **Diffusion Relaxation** ($T_{2Diffusion}$): The presence of a gradient in the static magnetic field causes diffusional relaxations (Bendel, 1990). Mathematically this is:

$$\frac{1}{T_{2diffusion}} = \frac{D(\gamma * G * TE)}{12} \quad \{2.8\}$$

where D is the molecular diffusion coefficient and γ is the gyromagnetic ratio of a

proton, G is the field-strength gradient (Gauss/cm) and TE is the inter-echo spacing used in the CPMG sequence. If the field is uniform, then G is zero and there is no diffusion.

In the presence of a uniform magnetic field, the diffusion relaxation is zero as there is no gradient. The transverse relaxation time (T_2) is dominated by surface relaxation and the bulk fluid relaxation. Transverse relaxation in the water filled pores is dominated by surface relaxation. However surface relaxation can fall into three categories (Brownstein and Tarr, 1979) based on pore dimension (r):

$$\text{Fast Diffusion: } \frac{\rho r}{D} << 1$$

$$\text{Intermediate Diffusion: } 1 << \frac{\rho r}{D} << 10$$

$$\text{Slow Diffusion: } 10 << \frac{\rho r}{D}$$

Fast and slow diffusion influence the shape of the T_2 distribution. In case of the fast diffusion, the unrelaxed proton (^1H) bounces back and forth around the entire pore space before being relaxed. This may result in loss of finer details of the pore structure and the entire porous network can be viewed as a single pore body, i.e., a single exponential fit to the decay curve. In slow diffusion, the unrelaxed proton does not wander around the entire pore body; instead the relaxed proton is concentrated near the pore surface. A much finer resolution of the pore surface can be generated, and a single pore body can be viewed as a multiexponential decay.

There are two schools of thought about the dependence of surface relaxation on temperature. One group (Latour et al., 1992) concluded that temperature has little or no effect on T_2 or T_1 time for water saturated sandstone and the other Godefroy et al., 2001 observed shifts in the peak T_2 relaxation time with temperature.

Latour et al., (1992) performed a series of NMR experiments on water and oil saturated sandstone and water saturated carbonates over the temperature range from 25 ^{0}C to 175 ^{0}C. It was observed that magnetization decreases with increase in temperature (Curie's law) and there is a very slight shift in T_2 and T_1 times for all the water saturated sandstones and carbonates with increase in temperature (**Fig. 2.2.3**).

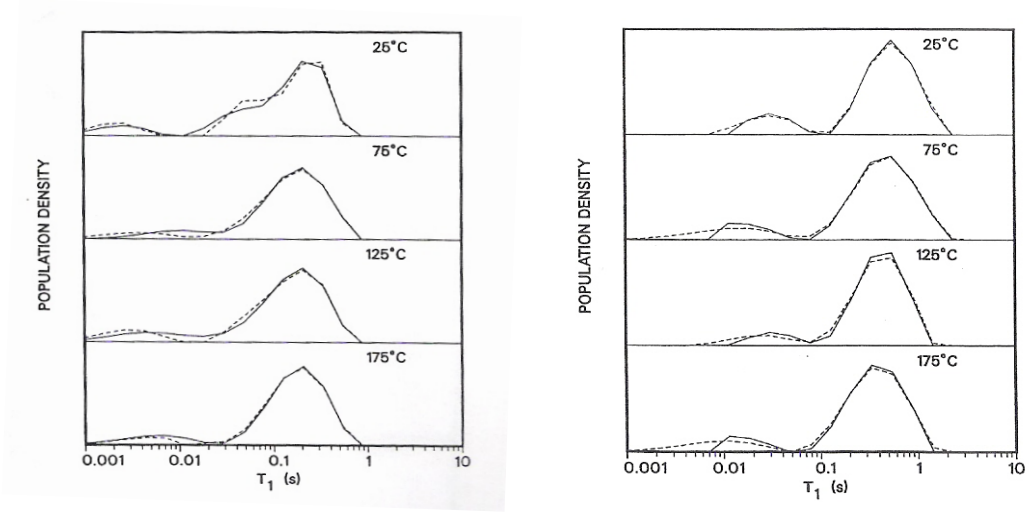

Figure 2.2.3: T_1 distribution for two different water saturated sandstones at 25, 75, 125 and 175 ^{0}C. The absence of shift in T_1 distributions suggests that surface relaxation is independent of temperature (Latour et al., 1992).

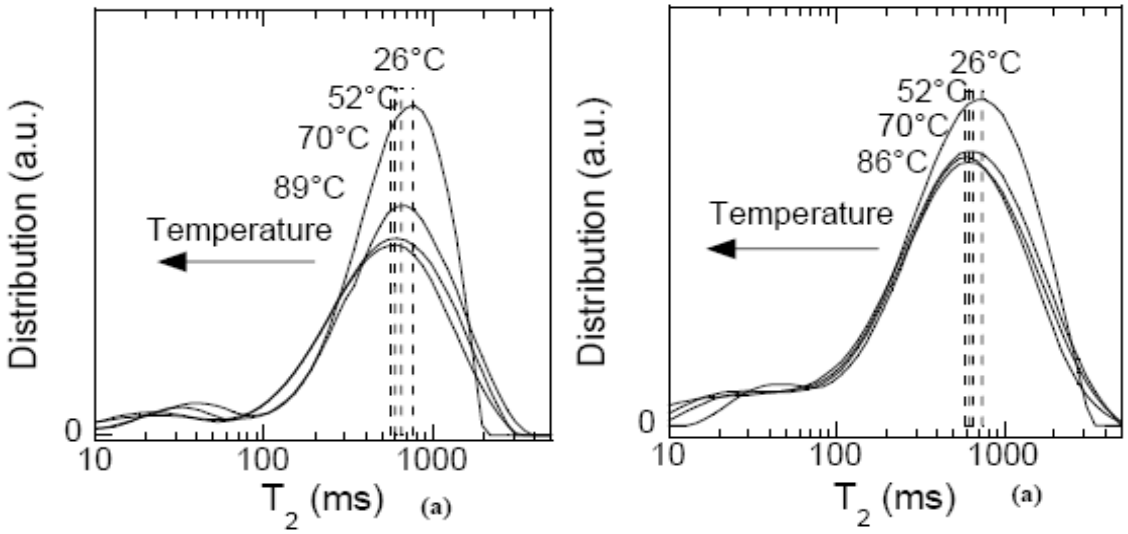

Figure 2.2.4: Variation in the T_2 distribution for two different water saturated sandstones with increase in temperature from 26 ^{0}C to 89 ^{0}C. The T_2 distributions tend to shift towards smaller time with increase in temperature (Godefroy et al., 2001).

The lack of shift in the T_2 distribution suggests that surface relaxation is independent of temperature. On the other hand, Godefroy et al., 2001 observed shifts in the peak T_2 relaxation time (**Fig. 2.2.4**) with temperature. The relaxation time decreases with increase in temperature for sandstone and increases for carbonates. This variation was not only observed at 2.2 MHz (laboratory spectrometer and downhole NMR logging tool operate at this frequency) but at different Larmor frequencies. Godefroy et al., (2001) introduced two concepts; one, translation correlation time (τ_m), and two, surface residence time (τ_s). Each water molecule is constantly exchanged at the pore surface between the different mineral sites such as between SiO_2 and paramagnetic impurities (Fe^{2+} or Fe^{3+}). The contact duration with this mineral is known as translation correlation time (τ_m). The surface residence time (τ_s) is the exchange time between the surface associated water and the bulk water. The translation correlation time (τ_m) depends on temperature and is mathematically related to activation energy (ΔE) (Godefroy et al., 2001):

$$\tau_m = \tau_{m0} \exp\left(\frac{\Delta E}{RT}\right) \quad \{2.9\}$$

where τ_m is the translation correlation time, ΔE is the effective activation energy, R is the universal gas constant and T is the temperature. The surface relaxivity is proportional to correlation time as follows (Godefroy et al., 2001):

$$\rho_2(T) \propto \alpha * \tau_m(T) \quad \{2.10\}$$

where $\rho_2(T)$ is the surface relaxivity, α is a parameter dependent upon pore fluid and pore surface, and τ_m is the translation correlation time. Surface relaxivity is directly proportional to the difference in the activation energy (ΔE) describing surface translation (E_m) and energy associated with the surface chemical bonding (E_s) which depends on the temperature of the system. Thus surface relaxation is an energy activated process which

in turn influences the frequency dependence of the transverse relaxation of the precessing protons. In the current study of freezing and thawing of saturated porous media, a shift in the peak T_2 time with temperature is also observed for all the core plugs.

2.2.3 NMR Porosity Estimation

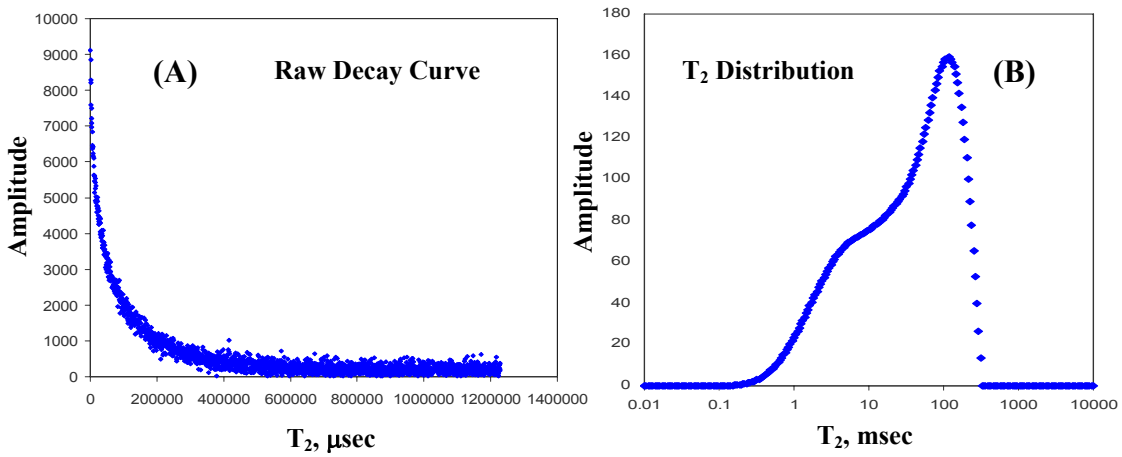

Figure 2.2.5 The raw decay curve (A) is inverted to produce a T_2 distribution (B) using multi exponent (256) function (see Appendix B for effect of fit parameters). These data were obtained on Berea sandstone at room temperature. The total area under the distribution (B) is equal to the amplitude at $T_2 = 0$, which is proportional to the porosity of the sample.

Porosity is defined as the ratio of the pore volume to bulk total volume of the sample. In a water-saturated rock, the total porosity is proportional to the number of the hydrogen atoms in fluid. The number of protons is proportional to the proton density, which is the amplitude of the raw decay curve of a spin echo train at t = 0 time. This initial amplitude of the raw decay curve is equal to the total area under the T_2 distribution curve as shown in **Fig. 2.2.5**. Using a calibrated scaling factor the total area is transformed into porosity of the rock sample:

$$\text{Porosity} = \frac{\text{Total Area}}{\text{Scaling factor} * \text{No. of Scans} * \text{Bulk Vol.(cc)}} \quad \ldots\ldots\ldots\ldots\ldots\ldots \{2.11\}$$

Scaling factor is instrument dependent and is estimated by calibrating the NMR responses

with known volumes of brine at room temperature. A step by step procedure to calibrate the instrument is described in **Appendix A**[1]. The estimated scaling factor for the NMR instrument is 24 (refer to Section 3.7 Nuclear Magnetic Resonance, NMR).

2.2.4 Bound Volume Estimation

The NMR response (**Fig. 2.2.6**) of the fluid inside a porous network can be broadly classified as free fluid index (FFI) and bulk volume irreducible (BVI).

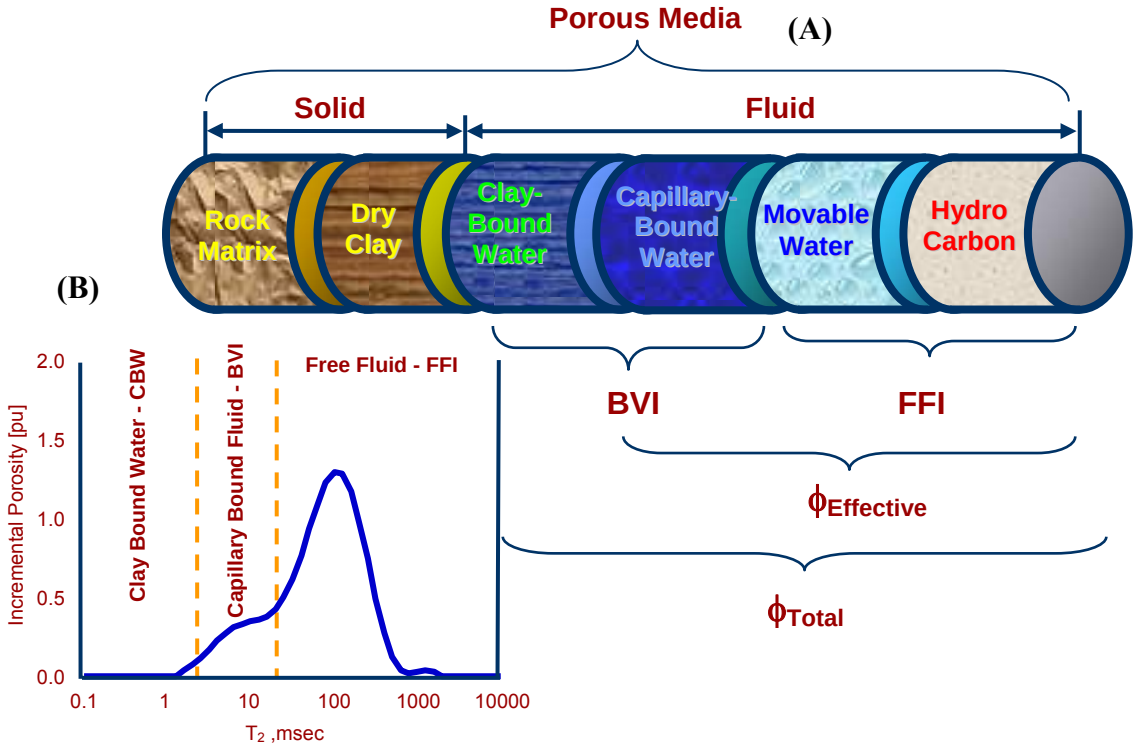

Figure 2.2.6: (A) NMR porosity model. (B)The T_2 distribution is divided into three fluid regions: 1) free 2) capillary bound and 3) clay bound fluid. For sandstone the boundaries are defined by T_2 values of 33 msec and 3 msec respectively (Coates et al., 1999). These T_2 times are referred to as cutoffs.

Coates et al., 1999, defined bound water volume (BVI) as the volume of water that will not flow during the production or the volume of water that cannot be displaced by hydrocarbon during the filling of the reservoir. The BVI depends on capillary properties

[1] Class notes (PE 3213) taught by Dr. Carl H. Sondergeld, University of Oklahoma, Norman (2006).

of the rock and FFI (the free fluid index i.e., the movable water volume) depends on both capillary properties and position relative to the free water elevation. The free fluid is comprised of movable water and hydrocarbon while the bound fluid is comprised of capillary bound and clay bound water in water wet rocks. The boundary between FFI and BVI is a relative permeability concept. In NMR it is usually determine by a centrifuge capillary pressure measurements. It is just a correlation that relates the centrifuge measurement to movable water. It is very difficult to estimate the percentage of movable fluid in the pore space using conventional logging tools such as resistivity, SP, etc., because they analyze the invaded zone. For typical sandstones the bulk volume irreducible is determined either by Cutoff BVI (CBVI) or by Spectral BVI (SBVI) technique (Coates et al., 1997). It is observed that T_2 relaxation times < 3 msec are associated with clay bound water; those between 3 and 33 msec are associated with capillary bound water while times greater than 33 msec are related to movable or free fluid regime (Martinez and Davis, 2000 and Matteson et al., 2000).

2.3 Freezing Process – Ice Formation

The process of removing heat (ΔH) from a fluid such as liquid water resulting in its solid form known as ice; the process is termed freezing (**Fig. 2.3.1**). Latent Heat of Fusion (ΔH) is defined as the amount of thermal energy which must be absorbed or evolved for a substance to change states from a liquid to a solid or vice versa (Mullin, 2001). It is also called the latent heat of fusion or the enthalpy of fusion, and the temperature at which it occurs is called the freezing or melting point. The latent heat of fusion of ice at 0 ^{0}C is 80 calorie/gm at 1 atm. This means that to convert 1 gm of water at 0 ºC to 1 gm of ice at 0 ºC, 80 calories of heat have to be extracted.

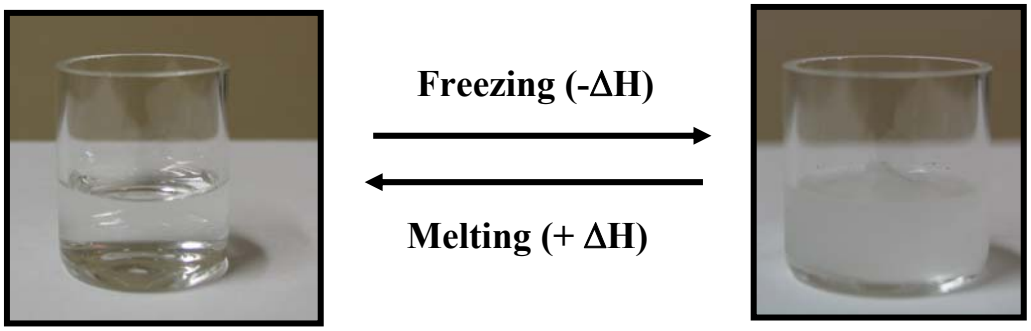

Figure 2.3.1: Liquid water is turned into solid ice by the process of freezing or crystallization.

Freezing and crystallization are interchangeable terms for this process. The removal of heat will reduce the temperature but not necessarily lead to freezing at 0 ^{0}C. This phenomenon is known as super cooling. Monitoring the freezing process has some very important practical implications in exploration and production from permafrost, in civil engineering, in freezing/thawing of food and in containing in-situ retorting of oil shale.

2.3.1 Nucleation

Freezing is defined as the crystallization of liquid water into solid form of water known as ice. The process is initiated by nucleation. According to the classical theory of nucleation (Mullin, 2001), the formation of stable nuclei is a sequence of processes in which atoms or molecules of a liquid phase join to form a stable nucleus. There are two different ways by which nucleation can take place:

1. **Homogeneous Nucleation**: This type of nucleation occurs only in the pure systems due to the random fluctuation of density. Clusters of molecules arise spontaneously due to difference in the density of the system. This is an ideal case and difficult to achieve.

2. **Heterogeneous Nucleation**: Heterogeneous nucleation occurs in the presence of a nucleating agent such as the wall of a container, foreign bodies, impurities etc. These bodies act as a site for nucleation processes. Freezing in porous media is dominated by heterogeneous nucleation.

The presence of a nucleating agent lowers the minimum Gibbs Free energy (ΔG) which accelerates the crystallization process as compared to that of homogeneous nucleation. Heterogeneous and homogeneous nucleation are related by:

$$\Delta G_{Het.} = f\Delta G_{Hom.} \quad \{2.12\}$$

where $\Delta G_{Het.}$ is the Gibbs Free energy associated with heterogeneous nucleation, $\Delta G_{Hom.}$ is the Gibbs Free energy associated with homogeneous nucleation and f is correlating factor which is related to the contact angle, θ by the following relation:

$$f = \frac{(2+\cos\theta)(1-\cos\theta)^2}{4} \quad \{2.13\}$$

where θ is determined by Young's relation.

$$\theta = \frac{\gamma_{sl} - \gamma_{cs}}{\gamma_{cl}} \quad \{2.14\}$$

where γ_{sl}, γ_{cs} and γ_{cl} are the interfacial tensions between solid-liquid interface, crystal-solid interface and crystal-liquid interface, respectively (**Fig 2.3.2**).

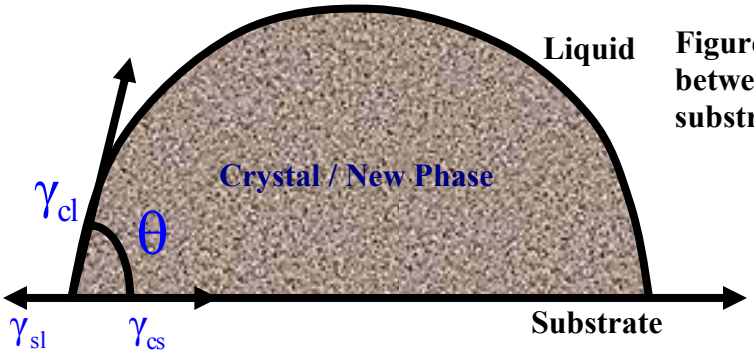

Figure 2.3.2: Contact angle, θ, between crystal-liquid and crystal-substrate interface.

If $\theta < 90^0$ the crystal will wet the substrate while if $\theta > 90^0$ there will always be a layer of

liquid water between the substrate and crystal. This is very important because this will govern where the nucleation starts and how it advances. Where ice forms, will influence the NMR response. Conversion of liquid water into ice, i.e., freezing is a phase transformation process. Whenever there is phase change, energy has to be added (boiling) or removed (freezing) to increase or decrease the randomness of the system. The presence of impurities or solute in solvent increase the randomness (entropy) of the system. The increase in randomness requires an extra energy to initiate the freezing of the solution. This extra energy results in cooling the solution to a temperature below the freezing point of pure solvent i.e., depression in freezing point. **Fig. 2.3.3** shows the phase diagram of pure solvent and of solution (solvent and solute).

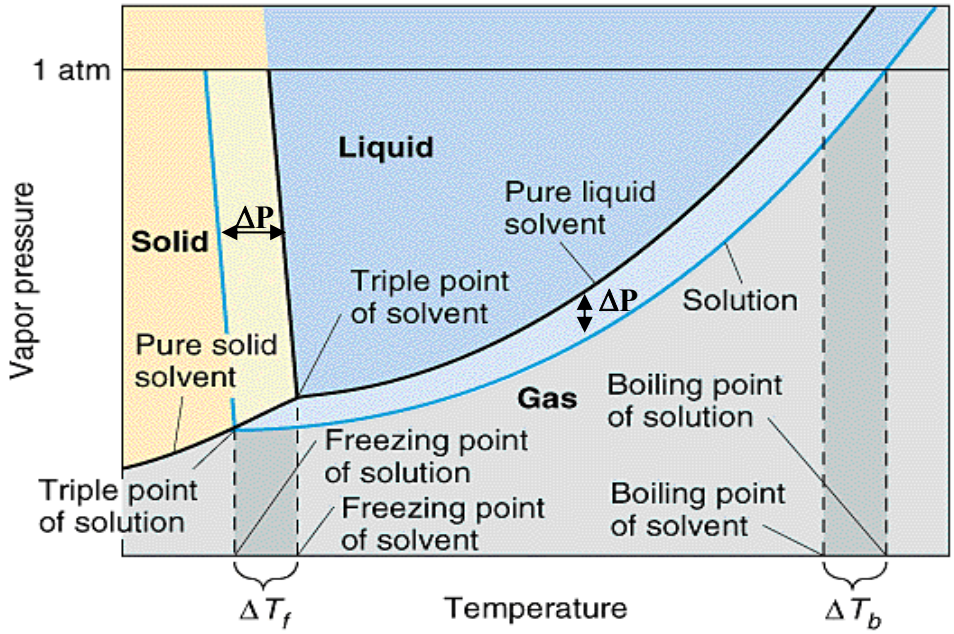

Figure 2.3.3: Phase diagrams of solvent and solution. The phase diagram of pure solvent (black line) and that of solution (blue line) show that, a dissolved solute depresses the freezing point by ΔT_f). Solution is defined as pure solvent with known concentration of solute (www.chem.ufl.edu/~itl/4411/colligative/lec_i.html**, 09/12/07).**

Adding of solute results in depression of freezing point and the depression of freezing point depends on the concentration of the solute present in the system. The freezing point

of t_f for a saline solution is given as (Hofonoff and Millard, 1984):

$$t_f = a_0 S + a_1 S^{3/2} + a_2 S^2 + bp \quad \{2.15\}$$

where t_f is the freezing point of the saline solution, S is the salinity of the brine in ppm, p is the pressure in bar and a_0 = -0.0575, a_1 = 1.710523 * 10^{-3}, a_2 = -2.154996 * 10^{-4} and b = -7.53 * 10^{-4}. The freezing point of a 25,000 ppm NaCl brine at 1 atm is -1.36 ^{0}C.

2.3.2 Freezing in Porous Media

Pressure, temperature, pore dimension, concentration, mineralogy and pore surface properties are some of the factors which influence the freezing point of the fluid inside a porous media. Capillary pressure depresses the freezing point of the pure water. From the thermodynamics point, the freezing point in a capillary tube is given by the Gibbs-Thompson equation (Clennell et al., 1999):

$$\frac{\Delta T_f}{T_{fb}} = \frac{T_f - T_{fb}}{T_{fb}} = -\frac{2\gamma_{lc}\cos\theta}{\rho_i r_p L_{fb}} \quad \{2.16\}$$

where T_f (^{0}K), T_{fb} (^{0}K) are the pore and bulk freezing temperature, γ_{lc} (J/m^2) is the liquid-solid interfacial tension, θ is the contact angle, ρ_i (kg/m^3) is the density of ice, L_{fb} (KJ/kg) is the latent heat of melting in the bulk and r_p (μm) is the pore radius. For a typical ice-water system, T_{f_b} is 273.15 ^{0}K, γ_{lc} is 0.0267 J/m^2, θ is 0^0 or 180^0 depending on whether ice wets the surface or not , ρ_c is 0.916 gm/cc and L_{fb} is 334 KJ/kg. The above equation implies that a small degree of super cooling is required before freezing initiates inside the pores.

This super cooled water is in metastable state which finally stabilizes into ice by heterogeneous nucleation. In a porous media such as soil, silica gel, or activated charcoal

part of the water always remains unfrozen which is known as non-freezing water (Churaev et al., 1993, Hansen et al., 1996, and Overloop and Gerven, 1992, etc.). Most of the studies on ice in porous media (soil, porous glass, and sand) are either interpretations of indirect measurement (Hansen et al., 1995, Morishige and Kawano, 1999, Overloop and Gerven, 1992, Stapf and Kimmich, 1995, etc.) or direct measurement (Colbeck, 1981) or theoretical (Everett, 1961). In this study it is observed that supercooling is required before nucleation occurs inside the porous media and part of pore fluid remains unfrozen. This lead to an important question; where in the pore structure is that unfrozen fluid residing?

Hansen et al., (1996), Overloop and Gerven (1992) and Stapf and Kimmich (1995) based on their NMR measurement suggested that part of the water freezes based on the Gibbs-Thompson relation and rest of the water remains unfrozen between the solid ice and pore surface. This layer of water is termed as "non-freezing" in the sense that it has not formed ice (Stapf and Kimmich, 1995). This "non-freezing" water is adsorbed on the surface of the porous media and is one to two monolayers in thickness.

Overloop and Gerven (1992) observed that the water adsorbed on activated charcoal never froze, which lead them to conclude that the unfrozen water is always surface adsorbed and its thermodynamics are different than bulk water. Hansen et al., (1996) believes that the nonfreezing water of the pore is between the pore wall and solid ice. The thickness of the interfacial water decreases with temperature. Due to the interfacial water, the Gibbs-Thompson equation is modified as:

$$\Delta T_f = \frac{K}{(R - t)} \quad \{2.17\}$$

where ΔT_f (^{0}K) is the depression in freezing point, K is a constant (494 ± 19.6 K Å^{-1}) and

t is the thickness of the non freezing water layer. Stapf and Kimmich (1995) draw their conclusion based on presence of hydration water layer on the protein surfaces (hydrophilic in nature) even below freezing. A similar argument is being applied to the adsorb water layer on the silica surface in porous media. Colbeck (1981) observed the porous media in presence of ice under microscope. His observation reveals interesting facts such as air-ice interface is convex, all of the pores are not completely frozen, various crystalline shapes of the ice and most importantly smaller pores seem to freeze first. But he argued that this is probably due to rapid cooling. One interesting observation was that a thin liquid layer (~100 μm) remains unfrozen after refreezing the melt water. Colbeck (1981) could not test this step during the freezing process, as it was instantaneous. Once nucleation take place the shape of the ice is governed by the shape of the pore structure.

Churaev et al. (1993), using capillary dilatometery, estimated the thickness of the non-freezing water layer as a function of temperature, which decreases exponentially. On average the thickness of the water layer becomes less than 1nm for temperature below -1.5 ^{0}C. Most minerals are water wet i.e., the contact angle is 0^{0}, however using digital imaging Liu et al., (2003) observed that ice-water interface inside a capillary tube is close to hemispherical with a contact angle close to 180^{0}. This suggests that ice is non wetting in nature.

Morishige and Kawano (1999) performed x-ray diffraction measurements on freezing and melting of water in a single cylindrical pore of different siliceous materials and a vycor. The authors suggest that a supercooling of the fluid takes place before the pore water freezes. These researchers also observed that the hysteresis between the onset

of freezing and thawing depends on the radius of the cylindrical pore. The smaller pore shows negligible hysteresis as compared to the bigger pore.

All of the researchers cited above believe or assume that the non-freezing water is between the ice and the pore wall and ice is non wetting (**Fig. 2.3.4**). The exact thickness of the water layer is not known, but is assumed to be one to two monolayers along the porous matrix.

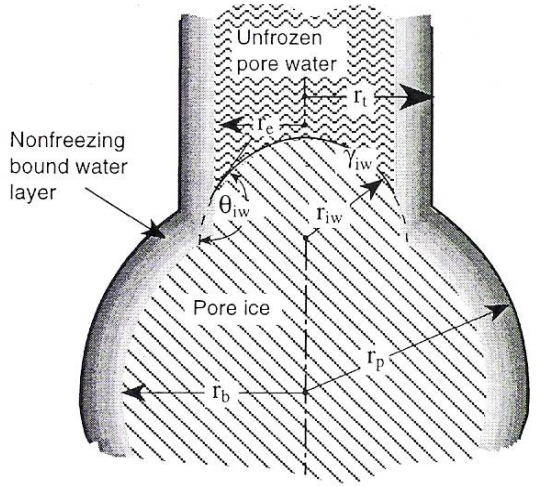

Figure 2.3.4: A sketch of a commonly accepted freezing model in a capillary tube. Unfrozen water exists along the wall of the pore body and its thickness depends on the temperature. Gibbs-Thompson equation is modified to take into consideration the effective pore radius. Ice is non wetting in nature i.e., contact angle is between 90^0 and 180^0(Clennell et al., 1999).

2.3.3 Surface Relaxivity and Relevance

Interpretation of NMR requires the knowledge of surface relaxivity (ϱ, μm/sec) (**Eqn. 2.7**). The T_2 value of a single water wet pore (100 % saturated) is a measure of the size of the pore. The T_2 distribution of all the pores in the rock represents the spectrum of pore sizes within the rock. Surface relaxivity critically affects the response and is sensitive to the mineralogy but is not often measured directly. Thus surface relaxivity is an independent variable in many measurements, especially those which are log based. One of the established methods of estimating ρ is by scaling the normalized incremental mercury injection curve (MICP) with the normalized T_2 distribution (Straley et al., 1997).

For a water filled pore body T_2 is directly proportional to the size of a pore body (**Eqn. 2.7**). Capillary pressure is described by the Washburn equation (Washburn, 1921) where the dependence is on the pore neck or pore throat. Thus both NMR and capillary pressure measurements represent a distribution of volume which correspond to a certain pore size (α R_{body}) or a certain pore neck size (α $\frac{1}{r_{throat}}$). Comparison of T_2 distributions and pore throat size distributions will provide the equivalent information if there is no distinction between the pore throat and body or if there is some fixed relation between the two. It is reasonable to expect the T_2 distribution mapping pore sizes to be related to the incremental Hg injection curve mapping pore throats. At present it is not known which pore body captured in an NMR response is reflected in the corresponding pore throat recorded by mercury injection capillary pressure (MICP). Consequently the working assumption is that with increase in pore body size there is a corresponding increase in pore throat. This may not be true in all cases. Thus by using a single scaling factor the two distributions can be matched. Scaling is such that the large pore throat appears on the right in NMR T_2 spectra, which corresponds to the large pore bodies. The scaling factor is used to calculate the surface relaxivity of the rock. It is well known that surface relaxivity depends on the surface chemistry, i.e., the mineralogical composition of the matrix (Coates et al., 1999) and is constant for fixed mineralogical composition. Surface relaxivity of different porous materials e.g., sandstone and carbonates is already established (Dunn et al., 2002) by different techniques such as gas adsorption, mercury injection, etc.

Where permafrost exists, there exists the additional surface of ice within the pore space. The relaxivity of pore-water system remains the same and its value is already

established for different mineralogies (Dunn et al., 2002). The relaxivity of ice-water system is unknown but attempts have been made to model the end members (Kleinberg et al., 2003a, 2003b). The knowledge of surface relaxivity of ice/water is important in interpreting the NMR response in a permafrost region. When a porous material is saturated with water, the total area under the T_2 distribution is proportional to the porosity of the sample and the T_2 spectrum indicates that pores having different dimensions are present in the porous network. When the pore fluid starts to freeze there is a decrease in the total NMR amplitude, equivalent to a decrease in the porosity of the core sample. At 2 MHz resonance frequency, MARAN Ultra® spectrometer is unable to detect the hydrogen atom present in the ice (T_{2ice} ~ 17μsec, Okada et al., 2002). Thus the relaxation associated with ice goes undetected.

At present there are two conceptual models (Kleinberg and Griffin, 2005) regarding ice formation in porous media; first ice forms at the pore wall and second ice forms at the center of the pore (**Fig. 2.3.5**)

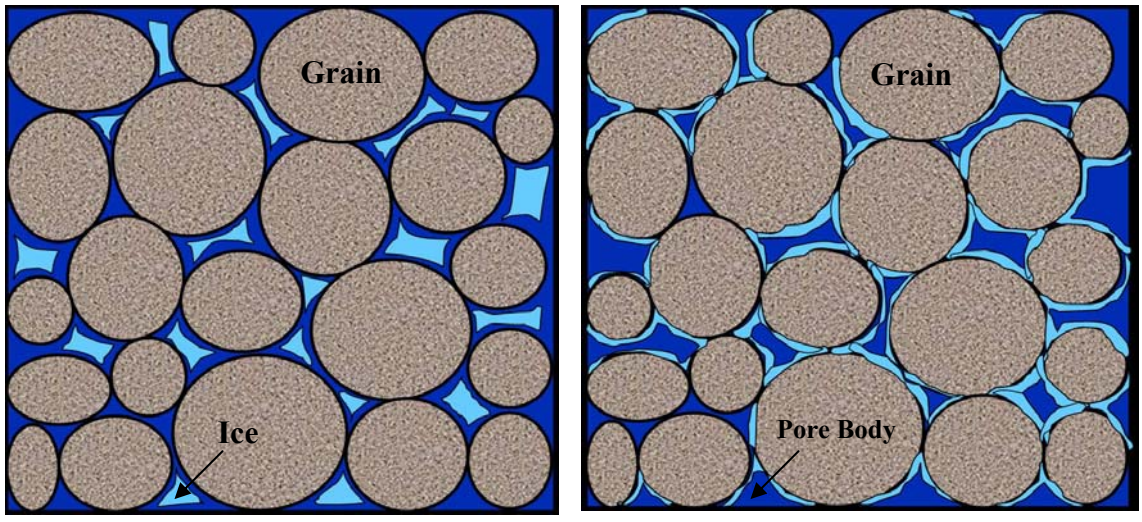

Figure 2.3.5: Conceptual models representing ice formation. (A) Pore filling (B) Pore Lining. The dark blue area is the pore body while the light blue area in the pore space is ice.

In the presence of a partially frozen porous media, **Eqn. 2.7** can be modified as[2]:

$$\frac{1}{T_2} = \rho_p \left(\frac{S_p}{V}\right) + \rho_i \left(\frac{S_i}{V}\right) \quad \{2.18\}$$

where ρ_p is the surface relaxivity of pore, $\left(\frac{S_p}{V}\right)$ is the ratio of the pore surface to the remaining pore fluid volume, ρ_i is the surface relaxivity of ice and $\left(\frac{S_i}{V}\right)$ is the ratio of the ice surface to the remaining pore fluid volume. Only ρ_p is known, $\left(\frac{S_p}{V}\right)$ and $\left(\frac{S_i}{V}\right)$ can be calculated for simple models. The real unknown is ρ_i, the surface relaxivity of ice. The above equation can be applied directly to the pore filling case but in case of pore lining it reduces to the form of **Eqn. 2.7** by replacing ρ_p with ρ_i. In either case, the ρ_i value is required for interpretation of the T_2 distribution. The above models are based on the assumption that the ice is a continuous phase within the pore body particularly for the pore lining case.

2.4 Literature Review

The similarity between the physical properties of ice and gas hydrates makes them indistinguishable to most geophysical technologies. The **Table 1** shows a comparison of some of the properties of both ice and clathrates. The mechanical properties of ice are consistently greater than those of the hydrates. The higher thermal conductivity of ice

[2] Personal Communication with Dr. Richard F. Sigal, University of Oklahoma, Norman (2006).

indicates the ice is a better thermal conductor than hydrate which indicates higher probability of having ice around the hydrate than vice versa.

Thermal Properties	Ice	Gas Hydrates
Density (gm/cc)	0.917	0.914
Possion's Ratio	0.33	0.33
Young's Modulus (GPa)	9.5	8.4
Bulk Modulus (GPa)	8.8	5.6
Shear Modulus (GPa)	3.9	2.4
Thermal conductivity (W/m-K)	2.23	0.49

Table 1: Summary of some physical properties of ice and gas hydrate (Sloan, 1990).

Zones with hydrate are likely to compact more due to the lower elastic moduli. Though the differences in the properties are subtle, researchers (Dvorkin et al., 2000 and Kleinberg et al., 2003a, 2003b) have argued that the growth of the hydrate in a sediment produces similar mechanical effects to that of ice. This has not been yet confirmed. One of the fundamental questions in hydrate resource evaluation is how to quantify hydrate concentrations. A step in answering this question is to understand how ice affects NMR signals, because ice is commonly found in association with hydrate bearing formation. The physical properties of such a rock are governed by matrix characteristic, fluid present in the system (gas or oil), frozen/unfrozen fraction of the brine and the location of the frozen part within the pore body. Previous studies were performed at different resonance frequency i.e., 5, 20, 90 and 300 MHz none of which are the same as the operating frequency of the oilfield logging instruments. Different researcher used different pulse

sequences; for example Free Induction Decay (Overloop and Gerven, 1992), spin-lattice (Hansen et al., 1996, 2002), spin-echo (Allen et al., 1997, 1998) and Goldman-Shen technique (Valiullin and Furo, 2002) to understand the freezing and melting process in a porous media. This freeze-thaw study is based on brine saturated natural porous media using a 2 MHz NMR spectrometer and a CPMG pulse sequence technique.

All previous work (see Section 2.3.2) indicates that liquid inside the porous media freezes below the bulk freezing point of water as described by Gibbs-Thompson equation. It is assumed that there is always a non-freezing water layer present along the matrix and is thought to be one to two monolayer in thickness. Fluid present in a pore is divided into two parts; free and bound fluid. Free fluid resides in the center of the pore while bound fluid is present along the boundary of the pore wall. It was assumed that the free fluid freezes first as compared to the bound fluid. Also, the presence of hysteresis in the thermal cycling is due to the freeze-thaw of the free fluid and not related to the bound fluid (Overloop and Gerven, 1992). Overloop and Gerven (1992) observed that there is no decrease in magnetization when the temperature of the adsorbed activated charcoal is lowered from 275 ^{0}K to 255 ^{0}K. The pores of the activated charcoal are so small that the adsorbed water never freezes. It is non freezing in the sense that it never attains the hexagonal ice structure. The non-freezing layer has a long transverse relaxation time as compared to the ice present in the middle of the pore (Valiullin and Furo, 2002).

The freezing process is initiated by formation of a stable nucleus of ice followed by the growth of ice. Fluid present in a confined system such as a capillary tube behaves differently than that in the bulk state. The variation is due to influence of the different factors on the freezing point, such as pore dimension, salt concentration, mineralogy and

pore surface properties. On a broad scale it is well established that confinement and presence of salt lowers the freezing point (Clennell et al., 1999 and Mullin, 2001). Freezing of a salt solution releases the salt to the residual brine resulting in increased salinity; hence even further lower the freezing point. Most of the freezing and thawing investigation in naturally occurring porous media used seismic and electrical measurements (e.g. Pandit and King, 1979, King, 1977, King et al., 1988, Timur, 1968, Sondergeld and Rai, 2007).

Pandit and King, 1979, King, 1977, King et al., 1988 and Timur, 1968 observed that there is an increase in compressional wave velocity when the core plug is temperature cycled through the freezing process. The velocity and resistivity were measured separately. The increase in resistivity is due to the decrease in the conductive pore fluid i.e., transformation of brine into nonconductive ice. The increase in amount of unfrozen water in clay and silt below freezing condition made the researchers (Pandit and King, 1979, King, 1977, King et al., 1988, and Timur, 1968) believe that big pores freeze first as compared to the smaller one. Sondergeld and Rai, 2007 measured velocity and resistivity simultaneously. They also observed an increase in velocity (compressional and shear wave) and resistivity due to freezing of the pore fluid. The change in shear wave velocity was observed to be more than compressional wave velocity. They reasoned that this could be explained if the small pores or the cracks are preferentially freezing before the big pores. This is opposite to the traditional concept of big pores freezing first.

An NMR study of thawing core from North Slope of Alaska was performed by Kleinberg and Griffin, 2005. The retrieved core plugs were refrozen back to their insitu reservoir condition (-14 ^{0}C). The CMR logging tool was used to acquire the NMR spectra

during the thawing process from -14 ^{0}C to 18 ^{0}C (room condition). Reading were taken every hour. The amplitude of the T_2 distribution is smaller and is centered at the early relaxation times. As time progress, the amplitude increases and the distribution start to shift towards the longer relaxation time as expected. Though the starting liquid filled porosity for mudstone is smaller than sandstone, both reach the same porosity once completely thawed. Based on observed shift of the T_2 distribution with thawing, it was concluded that ice preferentially fills the center of the pores causing a water layer between the ice grain surface. The conclusion was in accordance with the known fact that a thin layer of water surrounds the soil matrix and lies between the ice and the grains (Patrick and Tice, 1989).

The knowledge of the amount of unfrozen brine/water is not only important in predicting mechanical, thermal and hydraulic properties of the soil but also to water saturation estimation which is tied back to the economics of the reservoir. Anderson and Tice, 1973 and Civan, 2000 proposed correlations to predict the unfrozen water content of soil. Anderson and Tice, 1973 suggested a power law model between amount of unfrozen water, W, and the soil temperature:

$$W = \alpha \Delta T^{\beta} \quad \{2.19\}$$

where W is the ratio of the mass of the unfrozen water to the dry mass of the soil, α and β are empirically determined characteristic parameters of the soil and ΔT is the difference in the temperature between the soil and the freezing point of pure water (0 ^{0}C). The implicit assumption in the model is that at infinitely low temperature no water remains unfrozen.

However, Civan (2000) and Nakano and Brown (1971) proposed an exponential

model which takes into consideration the presence of unfrozen water irrespective of temperature. The exponential model is of the following form:

$$W = W_a + (W - W_a)\exp(-k\Delta T) \quad \{2.20\}$$

Where W is the ratio of the mass of the unfrozen water to the dry mass of the soil, W_a is the adsorbed mass of the water to the dry mass of the soil, k is an empirical constant and ΔT is the difference in soil temperature and the temperature at which pure water freezes i.e., 0 ^{0}C. It was observed that both freezing and thawing data points are mapped quite well using the exponential decay function.

2.5 Summary

The near immunity to matrix properties and its fluid dominated sensitivity results in NMR being used to estimate some of the important petrophysical parameters such as porosity, permeability, and bound water estimation. The effect of temperature on NMR response is not negligible and needs to be compensated for. This is especially important when the measurement in the laboratory is compared to a field measurement, both of which are conducted at different temperatures. The transverse relaxation time (T_2) is dominated by surface relaxation. The most commonly used pulse sequence technique in oilfield measurement is CPMG pulse sequence. The dependence of surface relaxation on temperature seems to be debatable (Godefroy et al., 2001 and Latour et al., 1992).

Heterogeneous nucleation dominates the ice nucleation process due to the presence of pore wall and its associated surface roughness. The freezing point of water is altered due to presence of salt (Hofonoff and Millard, 1984) and confinement as described by Gibbs-Thompson equation (Clennell et al., 1999). Supercooling is required

before freezing initiates inside the pores. Fluid present in a pore is divided into two parts free and bound fluid. Free fluid resides in the center of the pore while bound fluid is present along the wall of the pore. Direct and indirect evidence suggest that there is always a non-freezing water layer present along the matrix and is one to two monolayer in thickness (Churaev et al., 1993, Hansen et al., 1996 and Overloop and Gerven, 1992, etc.). It is non-freezing in the sense that it never attains the hexagonal structure of the ice. The presence of ice in the pore complicates the interpretation of NMR, acoustic and electrical tools. Pandit and King (1979), King (1977), King et al., (1988) and Timur (1968) believe that the big pores freeze first. However, Sondergeld and Rai (2007) concluded that small pores or the cracks are preferentially freezing before the big pores. NMR interpretation of permafrost requires the knowledge of surface relaxivity of ice. Indirect evidence suggested the relaxivity of ice to be less than that of the mineral matrix (Kleinberg and Griffin, 2005), and ice preferentially fills the center of the pore with water or brine lying next to the mineral matrix.

Anderson and Tice (1973) developed a power law model while Civan (2000) and Nakano and Brown (1971) developed an exponential to estimate the amount of unfrozen water content in soil.

CHAPTER 3 – EXPERIMENTAL PROCEDURE

3.1 Introduction

This section describes laboratory procedures employed in this study. All core plugs were first cleaned in a Soxhlet extractor (20% methanol and 80% toluene by volume). Once cleaned the samples were then dried in a gravity convection oven at a constant temperature of 100 ^{0}F. The porosities of the dried samples were determined using Helium Boyle's law porosimeter. The dry core plugs were then saturated using 25,000 ppm NaCl brine at 1000 psi for 24 hrs to insure full saturation. Saturation was checked gravimetrically. All saturated core samples were temperature cycled in a fiberglass pressure vessel from 22 ^{0}C to -12 ^{0}C. NMR spectra were acquired for all saturated core plugs over this temperature range. Each procedure is described in more detail below.

3.2 Core Cleaning and Drying

Figure 3.2.1: Soxhlet extractor used to cleaning core samples. Boiling flask filled with 20% methanol and 80% toluene by volume mixture.

In this experiment a distillation technique was used to clean the samples in a Soxhlet extractor. The solution used to clean the samples was a mixture of 20% methanol and 80 % toluene by volume. Methanol removes oils as well as salt. This distillation process continued for 24 hours to insure that the plugs were totally clean. Samples were removed and placed in a convection oven overnight at 100^0 F. Drying is continued until the weight of the sample becomes constant.

3.3 Porosity Estimation

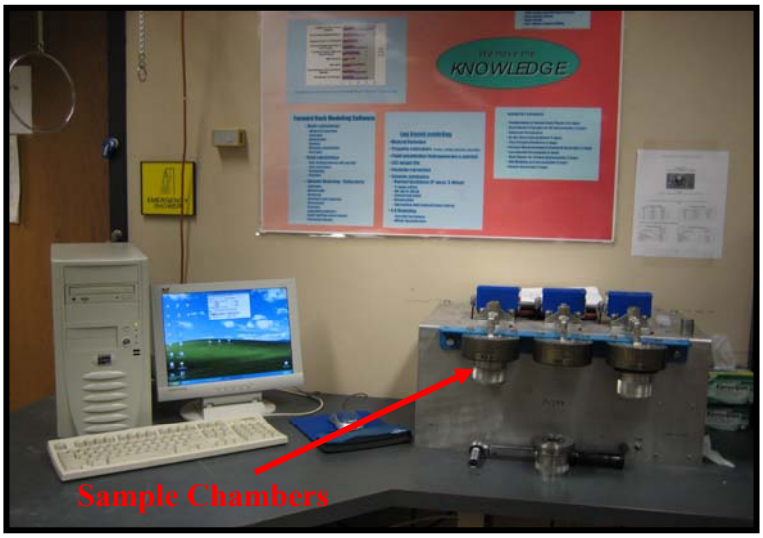

Figure 3.3.1: Boyles' law Porosimeter (HPP).

Porosity is defined as the ratio of the volume of void space to the bulk volume of the material. Porosity is an intrinsic property of the reservoir rocks. Void space volume can be expressed as the difference between bulk volume and grain volume. Porosity can be expressed as:

$$\phi = \frac{V_P}{V_B} = \frac{V_B - V_G}{V_B} \quad \{3.1\}$$

where V_P is the pore volume of the rock, V_B is the bulk volume of the plug, V_G is the

grain volume and ϕ is the porosity of the core sample. The type of porosity measured depends upon the technique used. The precision with which porosity can be calculated depends on the method of measurement. Bulk volume is determined by a mercury immersion technique which is based on Archimedes principle. The 1 inch by 1 inch core plug is forced immersed in mercury. The force is then used to calculate the temperature corrected mercury volume displaced by the core plug. The displaced volume of the mercury is equivalent to the bulk volume of the core plug. This assumes that mercury is non-wetting and does not enter large vugs or holes in the core. The grain volume is measured using a porosimeter which injects helium at a pressure of 100 psi. The porosimeter was calibrated by making two sets of measurements: one made with the sample chamber filled with steel billets of known volume; and the second after removing all the billets. Once the porosimeter is calibrated a standard quartz crystal is used to verify the calibration. We therefore measure helium porosity which is a good surrogate for total porosity.

3.4 Permeability Estimation

Permeability is defined as the measure of ease with which fluids flow through a porous medium. Darcy's law states that the steady state velocity, v, of a homogeneous fluid in a porous medium is directly proportional to the pressure gradient, $\frac{dp}{dl}$, and inversely proportional to the fluid viscosity, μ, (Craft and Hawkins, 1959). The constant of proportionality is the permeability. For a homogeneous, isotropic porous medium the permeability is same in all directions. In general rocks are neither homogeneous nor isotropic, i.e., permeability is directionally dependent. Permeability is the fluid flow

analog of electrical or thermal conductivity. It is another very important petrophysical property of a porous rock which strongly controls the economics of a field.

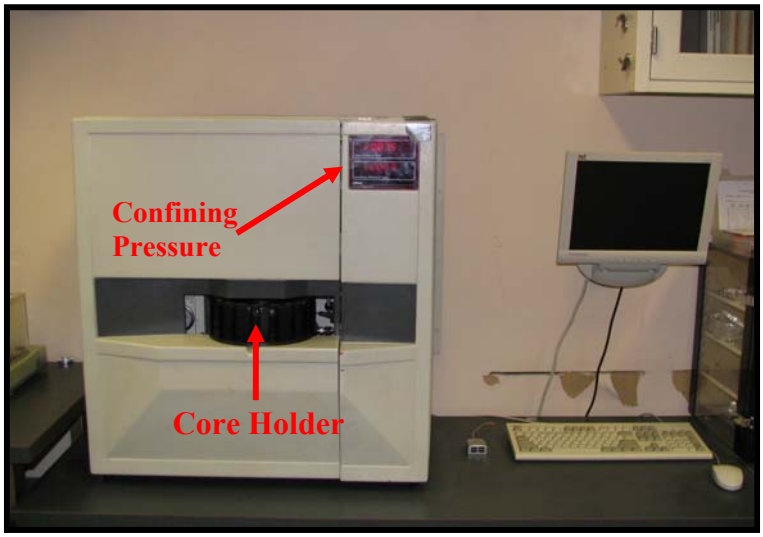

Figure 3.4.1: Core Measurement System 300 (CMS 300[3]). This instrument measures porosity and permeability at prescribed confining pressures.

The CMS 300[3] (**Fig. 3.4.1**) uses an unsteady-state method to determine the air permeability on plug samples (Jones, 1972). Klinkenberg corrected permeabilities are reported after making measurements at a number of mean gas pressures.

3.5 Fourier Transform Infrared Spectroscopy (FTIR)

Transmission Fourier Transform Infrared Spectroscopy (FTIR) is used to identify and quantify mineralogy of the core plugs used in this study. FTIR (**Fig. 3.5.1**) is based on the absorption of the infrared energy as a function of the wavenumber or frequency. Each molecular component has a specific infrared absorption band with the exception of compounds containing only ionic bonds. When infrared energy passes through a sample, energy is absorbed by the molecule at characteristic frequency.

[3] Core Laboratories Instruments, USA

Figure 3.5.1: Fourier Transform Infrared Spectroscopy (FTIR).

These frequencies corresponds to the bond and mode of vibration excited. The absorption spectrum obtained is a characteristic of that particular mineral. FTIR absorbance spectra for some of the pure minerals of interest are shown in **Fig. 3.5.2**. Quartz has a dominant peak at 1150 cm^{-1} wave number while calcite has a main peak at 1500 cm^{-1}.

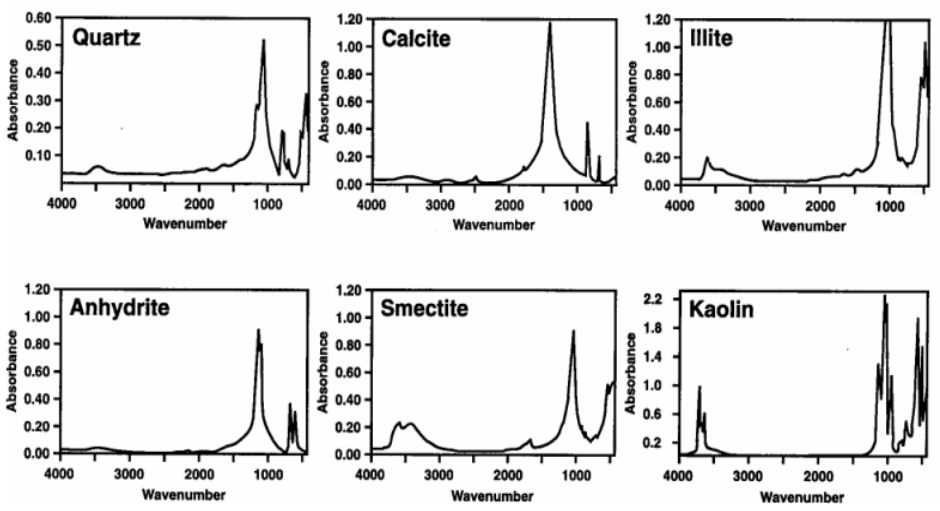

Figure 3.5.2: FTIR spectra for pure minerals (Sondergeld and Rai, 1993). Note the presence of diagnostic peaks for clays.

A Fast Fourier Transform is used to do a spectral decomposition of the observed spectra.

The total amplitude of the FTIR spectra is proportional to the summation of the product of the concentration of each mineral, its absorptivity and the absorption path length, *Beer's Law.* Mathematically it can be written as:

$$A = \sum_{i=1}^{n} \varepsilon_i l c_i \quad \text{.....} \{3.2\}$$

where A is the absorbance of a mineral mixture at a particular frequency, ε_i is the absorptivity of the i^{th} component, l is the absorption path length, c_i is the concentration of the i^{th} component and n is the number of components. Sample preparation is very crucial for any FTIR analysis. An extremely finely ground portion of the sample (0.0005 gm) is mixed with 0.3 gm of potassium bromide (KBr). This ratio of sample to KBr allows the absorption bands to fall in the linear region of Beer's Law and creates a disc of constant path length, l, for all specimens. This powder mixture is pressurized to 10,000 psi in a pellet press to form a solid disc. This disc is placed in the spectrometer for analyzing. KBr is transparent to mid-infrared ($\lambda \approx 10$ μm) and displays a constant absorbance across the frequency range as long as the thickness is constant. The background information is obtained using pellet made of pure KBr and is subtracted from the observed spectra of the sample. The position of amplitude peaks in the spectra determine the minerals present and their concentrations are determined using an inversion software (Sondergeld and Rai, 1993). Using the modified inversion software[4] sixteen different minerals can be identified; these include quartz, calcite, dolomite, siderite, albite, orthoclase, oligoclase, illite, smectite, kaolinite, chlorite, mixed layer clay, anhydrite, pyrite, apatite, and aragonite.

[4] Modified by Mr. Bryce Ballard and presented at the Undergraduate Research Day, University of Oklahoma, Norman (2007).

3.6 High Pressure Mercury Injection (HICP)

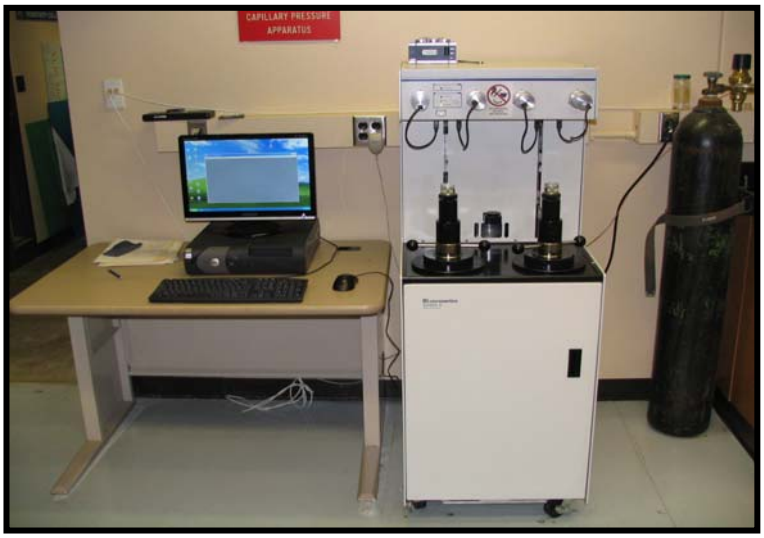

Figure 3.6.1: Micromeritics AUTO PORE–IV. This system has two independent pressurizing systems capable of injection pressures of 60,000 psi.

Mercury porosimetry is based on the Washburn equation (Washburn, 1921)

$$P_c = \frac{-4\gamma\cos\theta}{D} \quad \{3.3\}$$

where, D is diameter of the capillary in microns, γ is the interfacial tension in dyne/cm (485 dynes/cm for Air-Hg), θ is the contact angle (140^0) and P_c is the capillary pressure in psi. Measurements were made on small, clean and dry discs cut from the ends of the core plug samples. Mercury was subsequently injected into the sample and incremental recordings of volume injected at each pressure were made. Intrusion is not a single step process; rather it is a multi stepwise increase of the pressure until a maximum limit of 60,000 psia is attained. During each step, both the pressure and volume of mercury are measured after reaching equilibrium. The volume of mercury intruded is measured with a precise capacitance displacement transducer. All measurement reported here have been blank corrected, i.e., the apparent volume change without a sample in the penetrometer is

subtracted from the actual injection curve. The pore size at each specified step is calculated by applying the Washburn equation **(Eqn. 3.3)**. Thus each pressure step is associated with a particular pore throat size. High pressure corresponds to small pore sizes.

3.7 Nuclear Magnetic Resonance, NMR

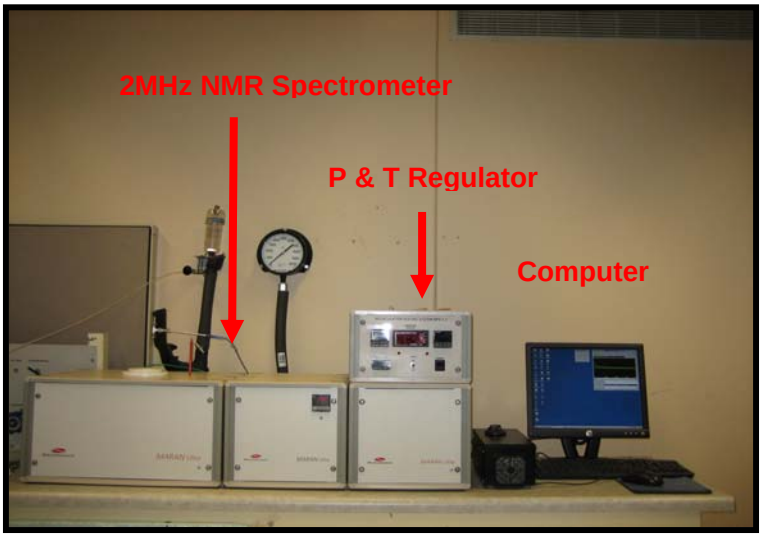

Figure 3.7.1: MARAN Ultra[5] Resonance Instrument

A 2 MHz MARAN Ultra[5] spectrometer (**Fig. 3.7.1)** was used to obtain the NMR data in this freezing and thawing study. RINMR[5], a commercial data acquisition and processing software, provides the software to control the hardware, to perform eleven pulse sequences (CPMG), and numerous other functions. A step by step procedure to calibrate the instrument is described in **Appendix A**[1]. The CPMG pulse sequence was used to measure the transverse relaxation (T_2). The inter echo spacing (TE) and the wait time (TW) were adjusted in such a way that the NMR estimated porosity is within ± 0.5 % of the independently measured saturated porosity. Saturated porosity is defined as the ratio

[5] Oxford Instruments Molecular Biotools Limited, UK

of the saturated pore volume to the bulk volume of the core plug. The acquisition and processing parameters used for this experiment are shown in **Appendix C**. The inter echo spacing (TE = 0.6, 1.0, 1.5 and 3.0 msec) and wait time (TW = 1.0, 6.0 and 8.0 sec.) were adjusted for all the samples before the start of the each temperature cycling experiment. Selection of proper inter echo spacing and wait time is crucial for NMR data acquisition. Detailed description is in **Appendix D**. **Table 2** summarizes the TE and TW used for the six different core plugs samples during the thermal cycle.

Core Sample	Inter echo spacing(TE) msec	Wait time (TW) sec
Filtros, F1	3.0	8.0
Berea, 33H	1.5	8.0
Castlegate, CG1	1.0	8.0
Tuscaloosa Sand, 10744.2 ft	1.0	1.0
Hollin, 6715v	1.5	6.0
William Fork, WF1A	0.6	8.0

Table 2: Summary of inter echo spacings (TE) and wait times (TW)

All decay curves were phase rotated to minimize quadrature component prior to fitting. A fitting program, RI WinDXP[5], was used to obtain the T_2 distribution from the raw NMR decay curve. RI WinDXP[5] is an exponential analysis software program used to perform distributed fitting on the decay curves acquired using RINMR[5]. The T_2 decay curve (**Fig. 2.2.5(A))** is fitted to a series of 256 exponentials. The total area under the T_2 distribution is used to calculate the NMR porosity by the following formula:

$$\text{NMR Porosity} = \frac{\text{Total Area}}{\text{Scaling factor} * \text{No. of Scans} * \text{Bulk Vol.(cc)}} \quad \ldots\ldots\ldots\ldots \{3.4\}$$

The scaling factor determined for our instrument is 24. The scaling factor is instrument dependent and thus calibration is a required step, as it provides the conversion of the total area under the curve to pore volume. We calibrated the instrument response using a series

of known volumes of brine (25,000 ppm NaCl), i.e., 1, 2, 3 and 4 cm^3. Calibration was performed at 28 ^{0}C. Both acquisition and fitting parameters should be the same for all the measurements. Pore volume is calculated using the formula:

$$\text{Pore Volume} = \frac{\text{Total Area}}{\text{Scaling factor} * \text{No. of Scans}} \quad \ldots\ldots\ldots\ldots\ldots\ldots\{3.5\}$$

Figure 3.7.2 shows a plot volume of brine estimated from NMR measurement (using Eqn. 3.5) versus the known volume and the estimate R^2 value along with a 1:1 line.

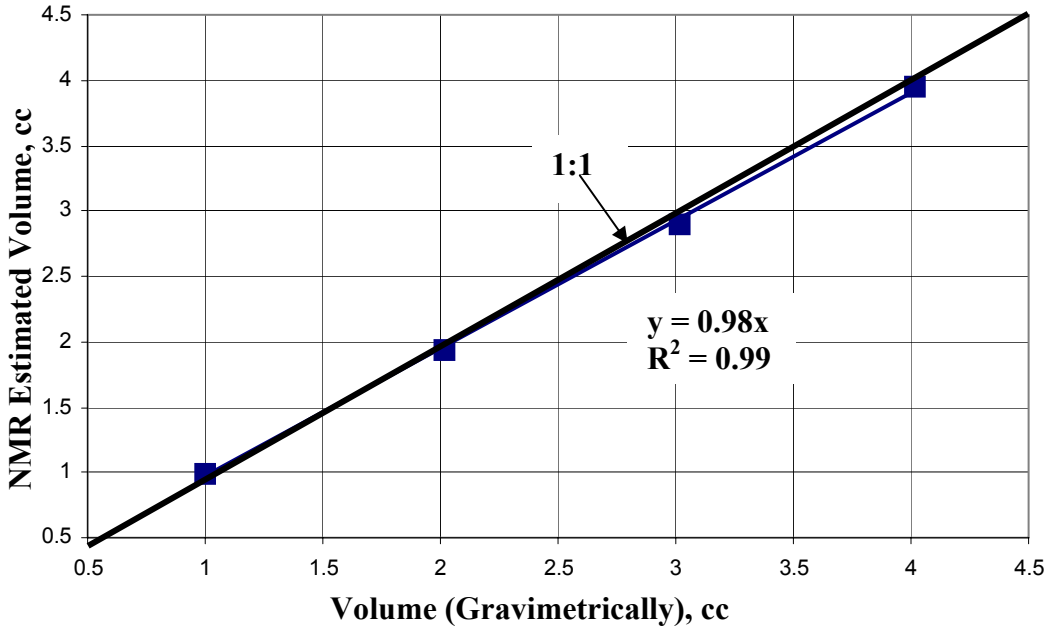

Figure 3.7.2: Crossplot of NMR estimated volume and known volume of brine (25,000 ppm NaCl) estimated gravimetrically. The NMR estimated volume is determined using a scaling factor of 24.

The fit of scaling factor yields a regression coefficient (R^2) close to 1 and is the scaling factor for that particular type of fluid. For estimation of surface relaxivity of ice, a different NMR instrument (inside temperature maintained at 30 ^{0}C) was being used. The scaling factor determined for this instrument is 98.

3.8 Freezing & Thawing Cycle

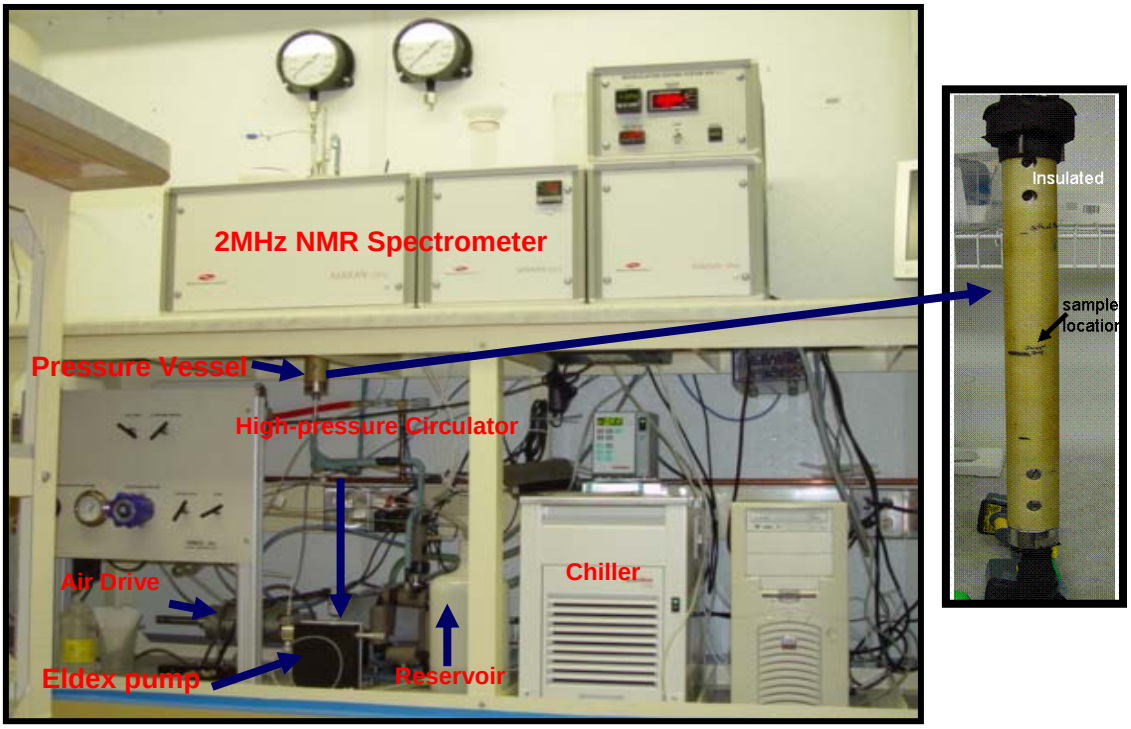

Figure 3.8.1: Experimental setup for acquiring NMR spectra while freezing and thawing of core samples

Fig. 3.8.1 is a picture of a composite measurement system consisting of a standard 2MHz NMR spectrometer, a fiberglass pressure vessel to hold the saturated sample, a programmable chiller and a high pressure circulating pump. A fiberglass pressure vessel was used to hold the saturated and jacketed core plugs and to facilitate the circulation of a cooling fluid (see **Fig. 3.8.2**). The circulating fluid is FLUORINERT[6] (FC-40). The fluid is devoid of any hydrogen atoms thus generates no NMR signal. Samples were saturated with 25,000 ppm NaCl brine. The saturated samples were then placed inside the rubber jacket (Aflas – a fluoroelastomer) with PEEK (Polyetheretherketones) plugs placed at the top and bottom of the core sample.

[6] 3M Specialty Materials, St. Paul, Minneapolis, USA.

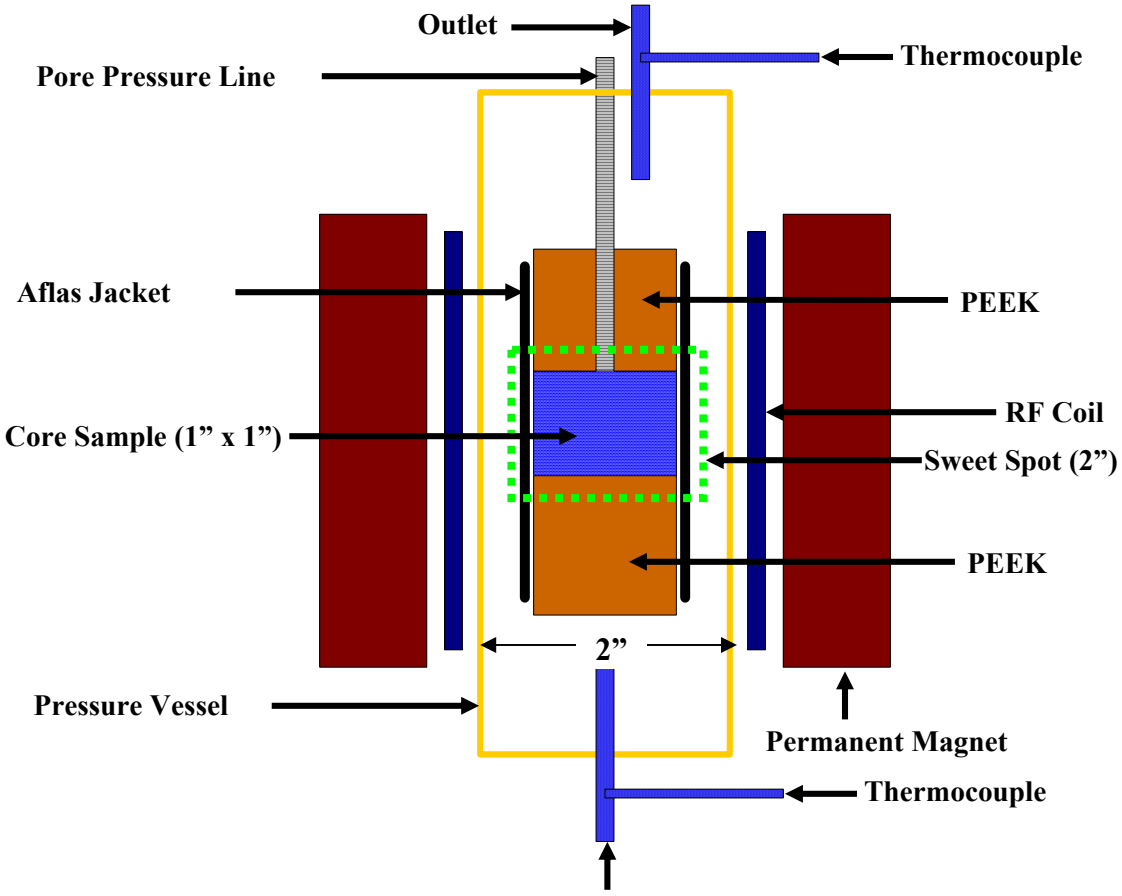

Figure 3.8.2: Block diagram showing the position and configuration of the sample relative to the fiber glass pressure vessel and the pole of the spectrometer.

The complete assembly was then placed in the pressure vessel. The pressure vessel is designed to fit inside the spectrometer. The vessel is assembled and mounted in the spectrometer. Using height adjustment screws, the vessel is placed in such a way that the center of the sample coincides with the center of the magnetic field, i.e., "the sweet spot". The temperature of the circulating fluid is lowered using the programmable chiller (JULABO F-32). An Eldex pump pressurizes the Fluorinert[6] and supplies the high pressure confining fluid to the chilled high pressure circulating system (see **Fig. 3.8.1**).

Once Fluorinert[6] is inside the circulating system, it is chilled externally by passing it through a heat exchanger. The air driven high pressure circulation system is a dual equal diameter, separately chambered, set of pistons and a series of check valves. The chilled Fluorinert[6] is then forced into the pressure vessel around the jacketed saturated core sample. Thermocouples in the inlet and outlet path of the circulating fluid at the pressure vessel monitor temperatures. The thermocouples were calibrated at two known temperature, 0 ^{0}C and 22 ^{0}C. Once the temperature stabilized and reached the desired values (22, 10, 5.5, 3.5, 2.0, 0, -1.5, -3.0, -4.0, -4.6, -6.0, -12.0 ^{0}C) NMR spectra were acquired after an additional 2 hours of equilibration. This procedure is followed during the freezing and thawing process. A series of longer term experiments established this wait time as optimal (refer to Section 4.3).

The inter echo spacing (0.3, 0.5, 0.75 and 1.5 msec) and wait times (1.0, 6.0 and 8.0 sec.) were adjusted for all the samples before the start of the temperature cycling. The effect of inter echo spacing and wait time on T_2 distribution is discussed in detail with an example in **Appendix D**. The raw T_2 decay is fitted to a series of 256 exponentials using the standard software package. In separate calibration experiment saturating fluids were also temperature cycled over the same temperature range and NMR spectra were acquired. This is required to estimate the effect of temperature on the bulk fluid. The pressure assembly without the core plug was temperature cycled from 22 ^{0}C to -12 ^{0}C, to evaluate the background response (refer to Section 4.2). During the thawing process, the partially frozen core plugs were then temperature cycled from -12 ^{0}C to 22 ^{0}C. The NMR spectra were acquired at each temperature point during the thawing cycle after 2 hours of

equilibration. This one cycle (whole procedure) of the freezing and thawing lasted for approximately 4 days.

The freezing and thawing experiment were performed during the winter time when the humidity is quite low. A series of experiments were also performed during summer when the humidity is relatively high. It was observed that a considerable amount of condensation developed along the wall of the pressure vessel during the summer. This condensation results in an increase in an apparent magnetization which results in abnormal increase in NMR estimated porosity. To prevent condensation the 2MHz MARAN Ultra^5 spectrometer was sealed and continuously purged with dry air (free of moisture). The inside temperature of 2MHz MARAN Ultra^5 spectrometer was still maintained at 28 ^{0}C irrespective of the purging. An obvious key learning is that a controlled and very low humidity environment is required when carrying out low temperature NMR experiments.

CHAPTER 4 – DATA ANALYSIS – PERMAFROST PROBLEM

4.1 Introduction

This study examines the freeze–thaw process in a brine saturated porous media using NMR. Six different core plugs were temperature cycled from 22 ^{0}C to -12 ^{0}C. All samples, except Filtros, are naturally occurring sandstones from reservoirs. **Table 3** summarizes the average properties of the core plugs.

S.No.	Sample	Predominant Mineral	Core Image	Porosity %	Permeability md	Effective Surface Relaxivity, µm/sec
1	Filtros	Quartz		35.0	5000	21.5
2	Berea, 33H	Quartz		22.7	889	21.5
3	Castlegate, CG1	Quartz		26.0	1000	21.5
4	Hollin, 6715v	Quartz		18.4	160	10.5
5	Tuscaloosa Sand, 10744.2 ft	Quartz, Clays & Carbonates		31.9	10	59.7
6	William Fork, WF1A	Quartz & Feldspar		24.9	80	29.8

Table 3: Summary of core information used for freeze - thaw study. Note the wide range in permeabilities but narrow range in porosity.

Filtros is a glass bonded silica (SiO_2) manufactured through a sintering process. All six saturated core samples were temperature cycled from 22 ^{0}C to -12 ^{0}C and then back to 22 ^{0}C in a fiberglass pressure vessel. NMR spectra were acquired at each temperature after waiting 2 hours for thermal equilibration.

4.2 NMR Signature of Background

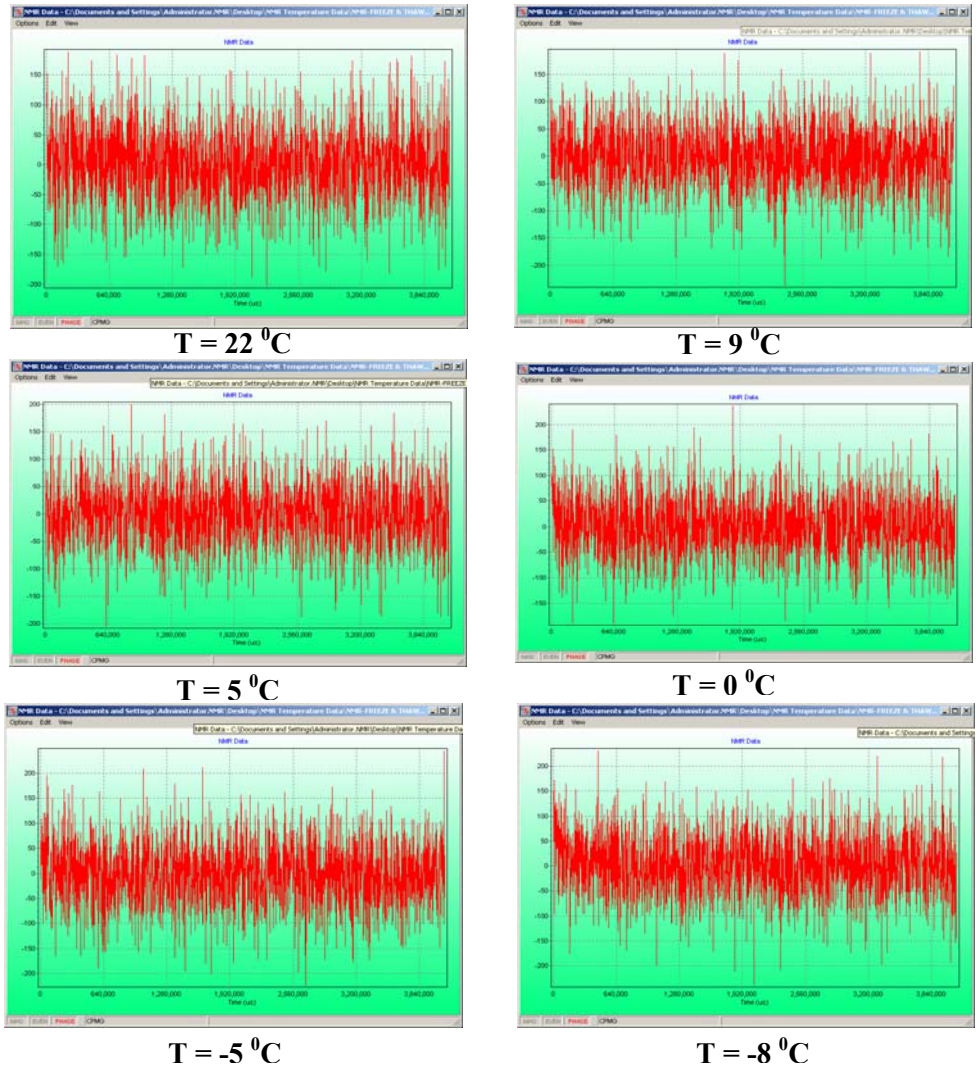

T = 22 ^{0}C **T = 9 ^{0}C**

T = 5 ^{0}C **T = 0 ^{0}C**

T = -5 ^{0}C **T = -8 ^{0}C**

Figure 4.2.1: Raw NMR signal of the complete pressure assembly without core sample at different temperature. Note no measurable background signal.

A fiberglass pressure vessel is used to hold the saturated and jacketed core plug and to facilitate the circulation of Fluorinert[6]. The inside temperature of the MARAN Ultra[5]

spectrometer (**Fig. 3.7.1)** is maintained at 28 ^{0}C. The chilled pressure vessel produces an unwanted condensate when humidity was high. The complete pressure assembly (without any core plug was temperature cycled from 22 ^{0}C to – 12 ^{0}C to examine the background effect. The raw noisy data (**Fig. 4.2.1)** indicate the background is negligible.

4.3 Thermodynamic Equilibrium

To ensure that ^{1}H atom present in the brine is at thermodynamic equilibrium, a set of experiments was performed to acquire the NMR spectra as a function of time with varying temperature. This set of experiments becomes important as the area under the NMR spectra and the transverse relaxation time (T_2) are temperature dependent. A glass vial (**Fig. 4.3.1**) filled with 3 cc 25,000 ppm NaCl brine is placed in the pressure vessel and temperature cycled from 22 ^{0}C to -12 ^{0}C.

Figure 4.3.1: Empty Glass Vial (Internal Diameter = 1.0" and Height = 1.2").

NMR spectra were acquired at each temperature point for several hours before switching to the next temperature set point. The estimated amplitude and the characteristic T_2 time is plotted as a function of wait time at different temperatures in **Fig. 4.3.2**. Bulk relaxation is the sole mechanism in the fluid sample.

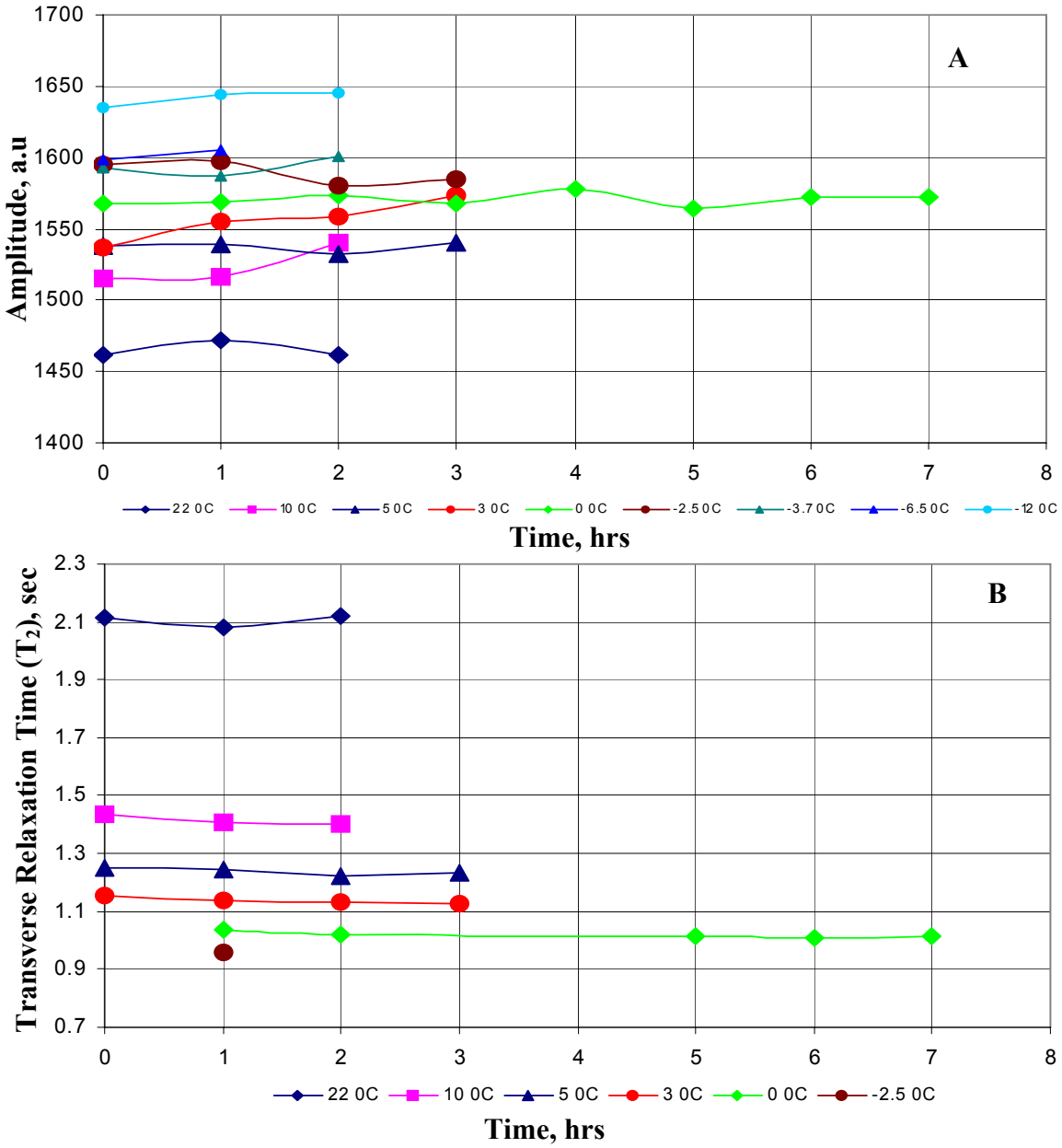

Figure 4.3.2: NMR spectra were acquired for 3 cc of 25,000 ppm NaCl brine in a glass vial as a function of time with varying temperature. (A) Area under the T_2 distribution. (B) Characteristic T_2 time derived after fitting a single exponential function to each of the raw NMR decay. The increase in amplitude with decrease in temperature is consistent with Curie's law. The decrease in T_2 time is due to a decrease in the viscosity of the fluid.

The increase in amplitude with temperature (**Fig. 4.3.2 (A)**) is attributed to the increase in net magnetization predicted by Curie's law (Eqn. 2.3) (Cowan, 1997). At a particular

temperature the maximum fluctuation in the recorded amplitude is less than 3%. This fluctuation results in negligible variation in actual volume of pore fluid present in the system. 0^{th} hour indicates the measurement is taken as soon as the desired temperature is reached. Regardless of the wait time, the position of the T_2 distribution and the observed total amplitude remain constant after the desired temperature is reached (**Fig. 4.3.3**).

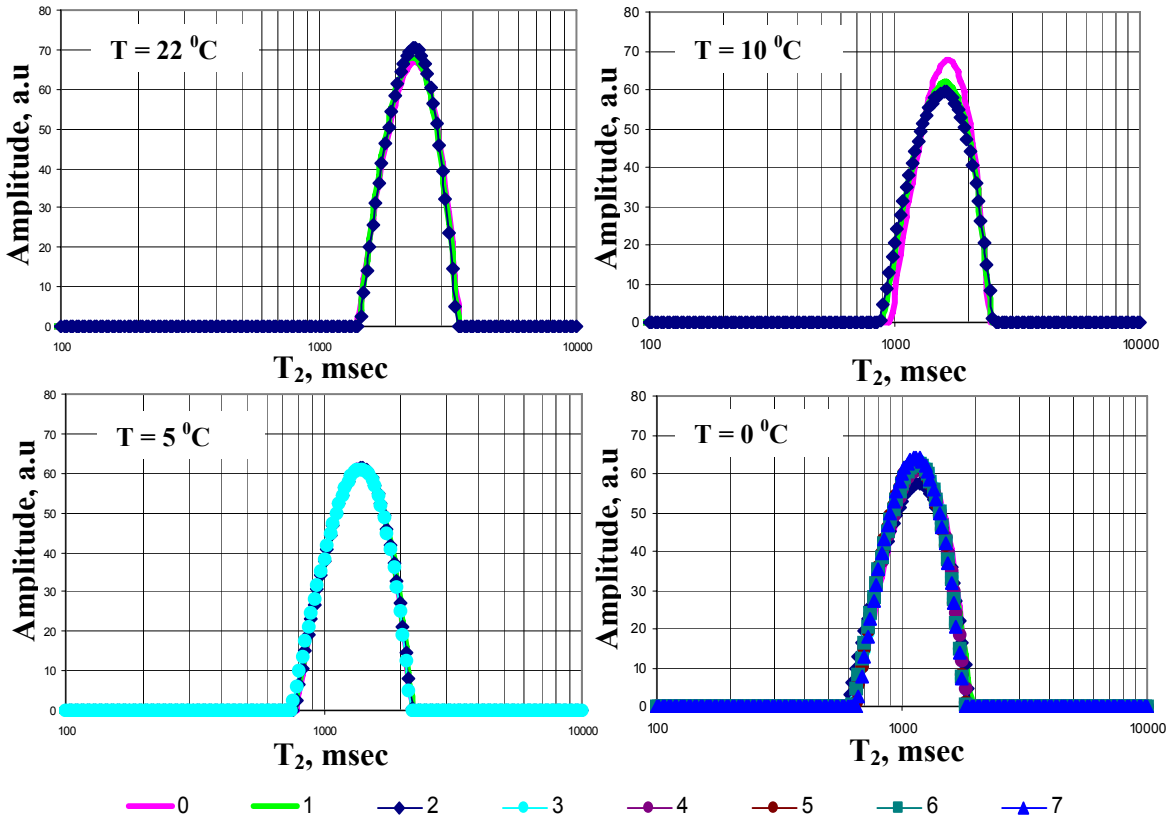

Figure 4.3.3: T_2 distribution for 3 cc of 25,000 ppm NaCl brine in a glass vial as a function of time with varying temperature. The different colors and symbols indicate the time (in hours) at which the NMR spectra have been acquired. The position and amplitude of the T_2 distribution remains constant after the temperature reached the desired point.

This suggests that the ^1H atom reaches thermodynamic equilibrium very quickly. Based on this experiment, the wait period before NMR measurements was set to 2 hours. The relaxation process of the ^1H atom in this experiment is purely bulk relaxation. A single

exponential fit **(Eqn. 2.2)** to the raw decay curve estimates the characteristic T_2 time i.e., the bulk relaxation (T_{2Bulk}) of the brine. The bulk relaxation is a simple function of the fluid viscosity. (see **Eqn. 2.6**). With decrease in temperature the viscosity decreases which results in decrease in T_{2Bulk}. Below -2.5 ^{0}C, the raw decay could no longer be fitted to a single exponent.

4.4 Temperature Correction

Eqn. 2.4 is very useful for comparing the observed magnetization with the calculated and also for temperature calibration. Each observed magnetization was temperature corrected as follows

$$M(0,T)_{Corrected} = M(0,T)_{Uncorrected}\left(\frac{T}{T_{cal}}\right) \quad \{4.1\}$$

where $M(0, T)_{Corrected}$ is the temperature corrected magnetization at temperature T, $M(0, T)_{Uncorrected}$ is the experimentally observed magnetization at temperature T (^{0}K) is the temperature at which NMR spectrum was acquired, T_{cal} is equal to 295.15 ^{0}K. All of the NMR spectra were temperature corrected based on **Eqn. 4.1**. The thermocouples used for determining the temperature were calibrated at 0 ^{0}C and at 22 ^{0}C. The thermocouples were placed in the circulating fluid entry and exit of the pressure vessel (see **Fig. 3.8.2**). The temperature of the core is estimated by taking the arithmetic average of the two thermocouple readings. **Eqn. 2.4** was further used to estimate the temperature of the precessing hydrogen atom and compared with the averaged value.

$$T = \frac{M_{@\,295.15\,^0K} * 295.15\ ^0K}{M_{@\,T\,^0K}} \quad \{4.2\}$$

The magnetization for 1.0 cc and 3.0 cc 25,000 ppm NaCl brine were used to back calculate the temperature of the precessing hydrogen atom. The difference in the estimated temperature derived from the experimentally observed magnetization and the arithmetic average is within ± 2.0 ^{0}C (**Fig. 4.4.1**). The difference in temperature is due to measurement configuration. For 1.0 cc brine the difference in temperature is smaller as compared to that of 3.0 cc brine.

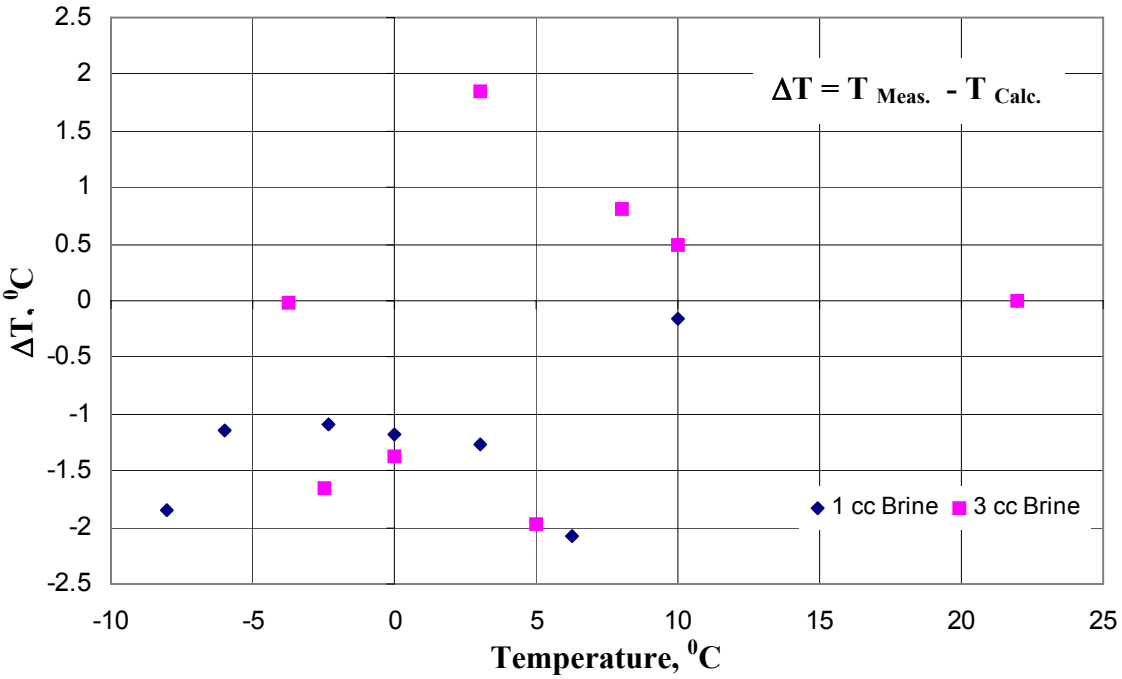

Figure 4.4.1: Difference in the estimated temperature derived from the experimentally observed magnetization and the arithmetic average of the two thermocouple readings. All differences are within ± 2.0 ^{0}C.

Fig. 4.4.2 is a crossplot between the calculated and the experimentally observed magnetization for all the six core plugs for the temperature range from 22 ^{0}C to 0 ^{0}C. The magnetization at 22 ^{0}C is known. Magnetization at a particular temperature is calculated as follows:

$$M(@T)_{cal} = M(@22^0C)\left(\frac{295.15\ ^0K}{T\ ^0K}\right) \quad \{4.3\}$$

The error in the experimentally observed magnetization is within ± 5.0 % of the calculated magnetization. The error in the magnetization is mainly due to the difference in the temperature between the observed and the actual temperature of the precessing ^{1}H atoms. This variation in the calculated and observed magnetization influences the porosity estimation by a maximum of ± 0.6 %. The close accordance between the calculated and the observed magnetization provides information that there is very little drift in the instrument during the measurement cycle.

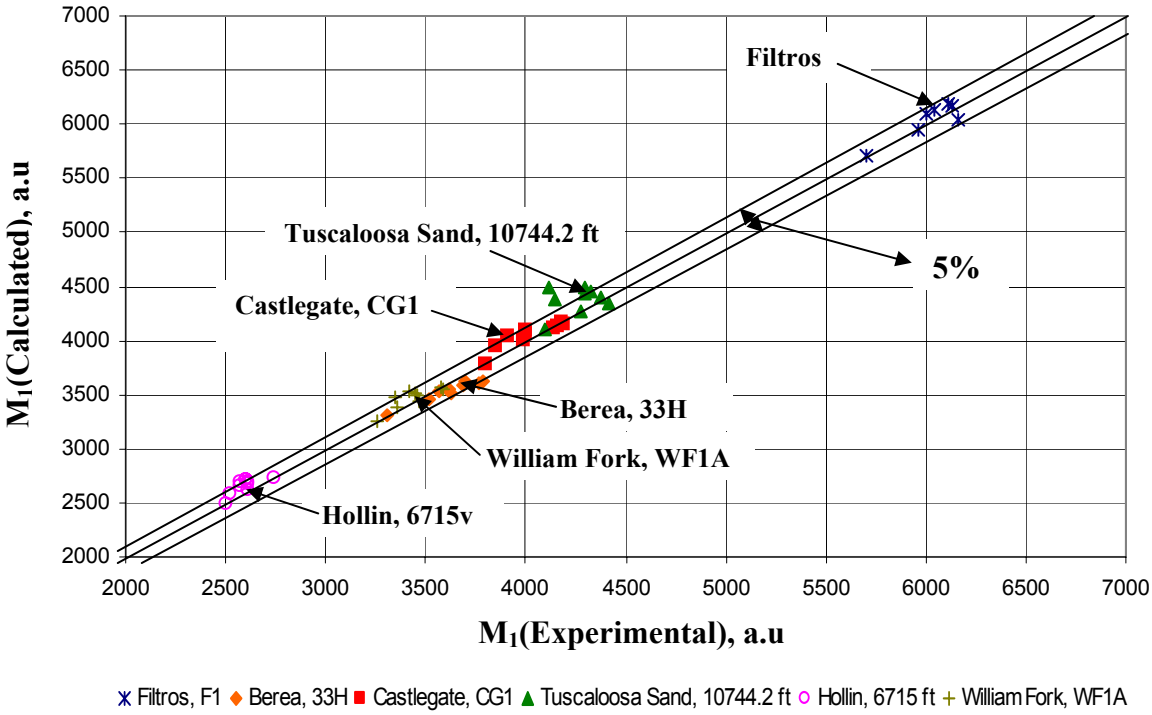

Figure 4.4.2: Crossplot of experimentally determined magnetization versus calculated magnetization for the temperature range from 22 ^{0}C to 0 ^{0}C. The different symbols indicate the different sample groups. The experimentally determined magnetization lies within ± 5.0 % of the calculated magnetization.

4.5 NMR Estimated Porosity and Temperature Effect

Fig. 4.5.1 shows the cross plot of NMR porosity (@ room condition) and saturated porosity obtained using a gravimetric technique.

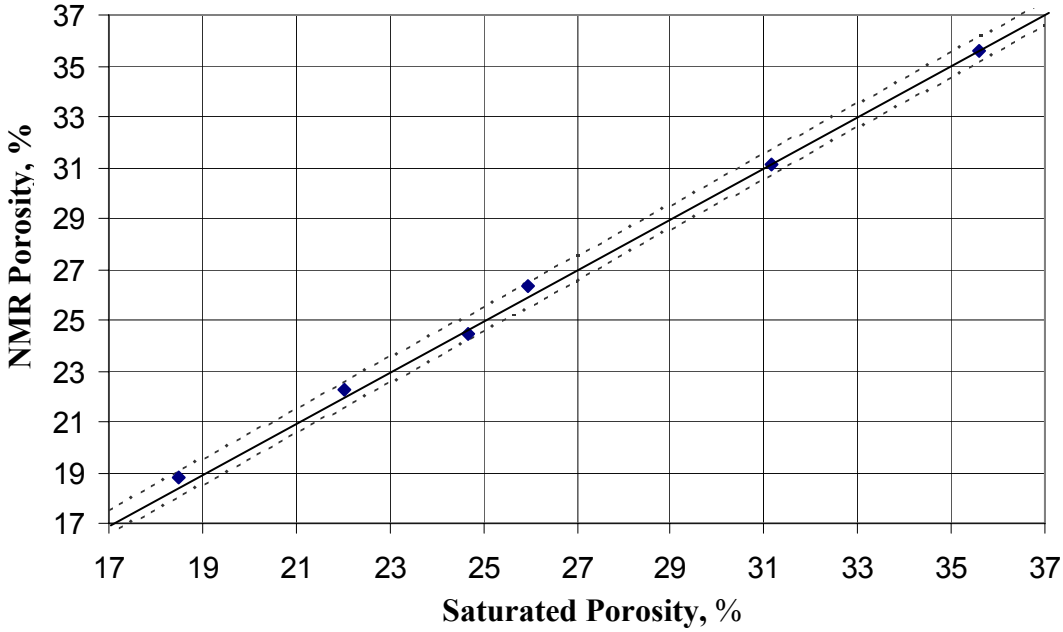

Figure 4.5.1: Crossplot of saturated porosity versus NMR estimated porosity. The saturated porosity was determined gravimetrically. The NMR estimated porosity (@ room condition) lies within ± 0.5 % (dashed line) of the standard measure of porosity. The solid line is a 1:1 line.

The estimated porosity is within ± 0.5% of the gravimetric porosity. This agreement indicates that NMR porosity estimated at the room condition is quite accurate and also that the acquisition and processing parameters are correctly adjusted.

The saturated samples were placed in the pressure vessel and temperature cycling experiments were performed. The T_2 distribution for all the six core plugs during the freezing cycle are shown in **Fig. 4.5.2 - 4.5.7**. With a decrease in temperature the total amplitude or the area under the T_2 distributions increases for all the six core plugs until freezing initiates. As soon as the pore fluid freezes there is a drastic decrease in the amplitude and a shift in the peak T_2 time.

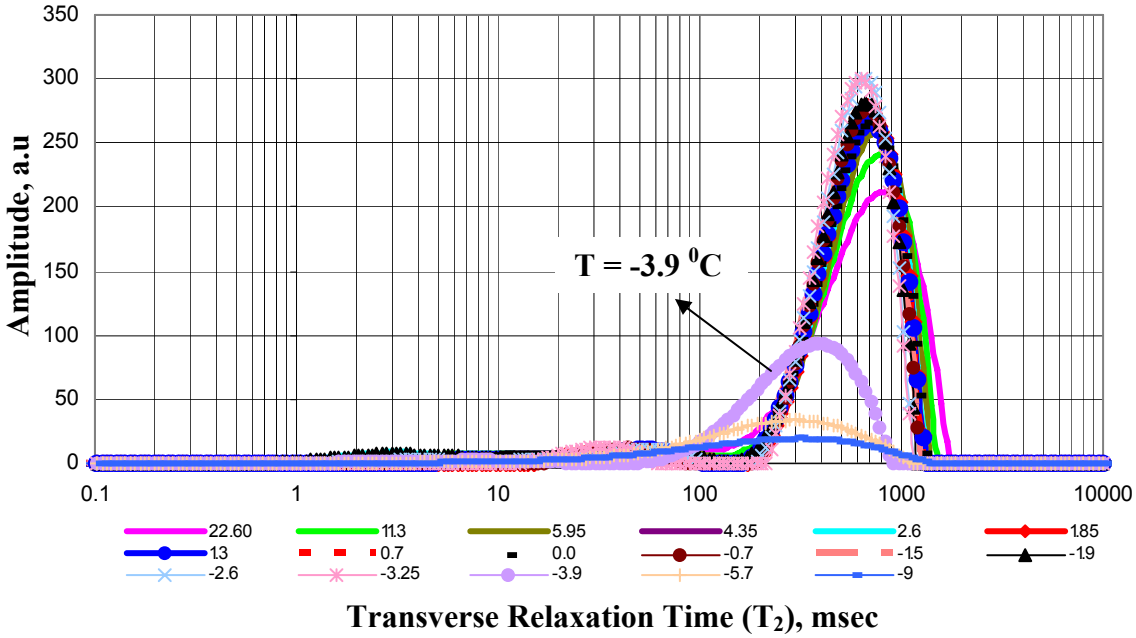

Figure 4.5.2: T_2 distributions of Filtros saturated with 25K ppm NaCl brine as a function of temperature from 22 ^{0}C to -9 ^{0}C. The decrease in amplitude (@ -3.9 ^{0}C) is caused by ice formation. The time shift in T_2 distribution is due to freezing of the big pores and results in an increased dominance of the smaller ones.

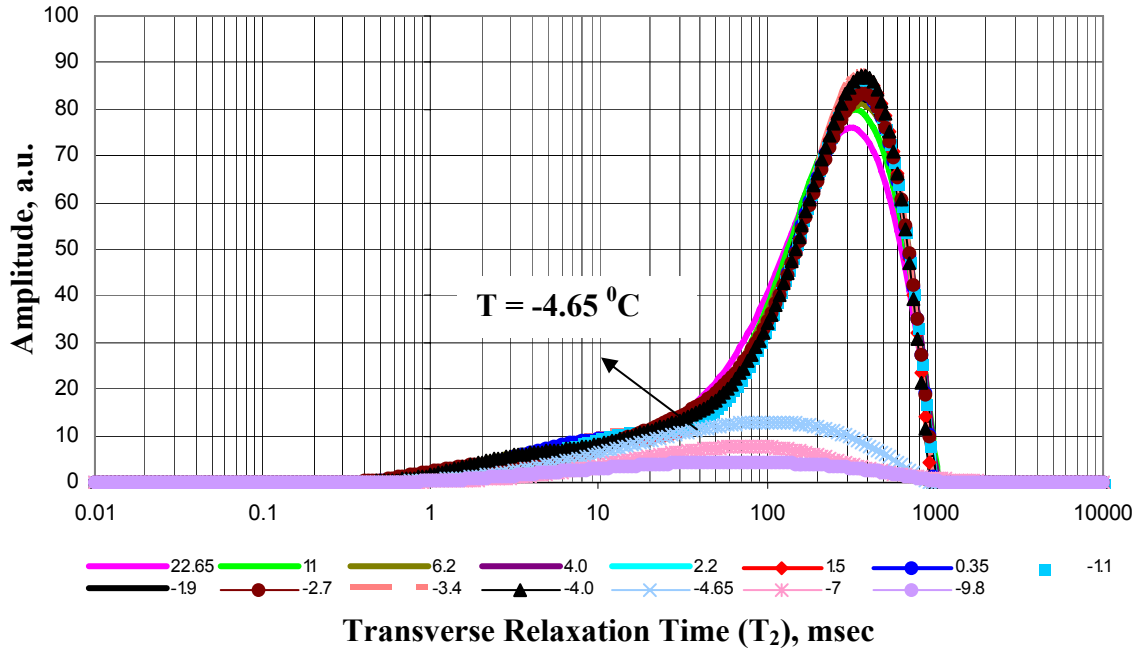

Figure 4.5.3: T_2 distributions of Berea, 33H saturated with 25K ppm NaCl brine as a function of temperature from 22 ^{0}C to -10 ^{0}C. The different colors indicate the different temperatures. The decrease in amplitude (@ -4.65 ^{0}C) is caused by ice formation. Shift in the peak T_2 time is due to freezing of the big pores.

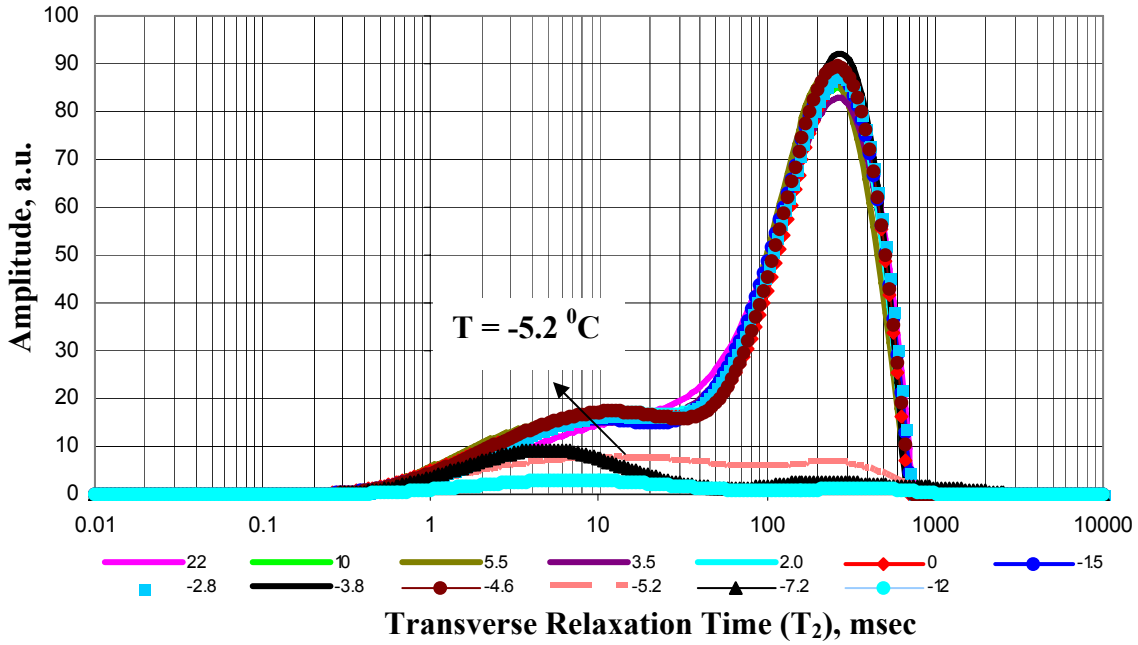

Figure 4.5.4: T_2 distributions of Castlegate, CG1 saturated with 25K ppm NaCl brine as a function of temperature from 22 ^{0}C to -12 ^{0}C. The different colors indicate the different temperatures. The decrease in amplitude (@ -5.2 ^{0}C) is caused by ice formation. The T_2 distribution retains the bimodal behavior till -12 ^{0}C.

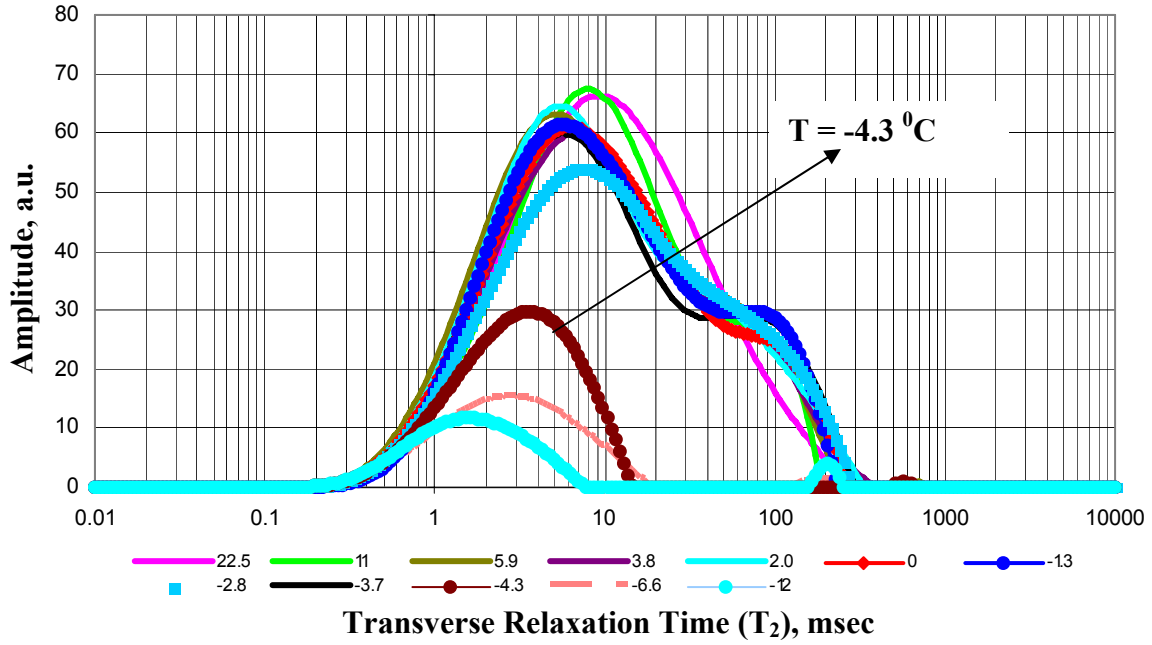

Figure 4.5.5: T_2 distributions of Tuscaloosa Sand, 10744.2 ft saturated with 25K ppm NaCl brine as a function of temperature from 22 ^{0}C to -12 ^{0}C. The different colors indicate the different temperatures. The decrease in amplitude (@ -4.3 ^{0}C) is caused by ice formation. The big pores are frozen completely with a systematic shift towards the smaller T_2 time.

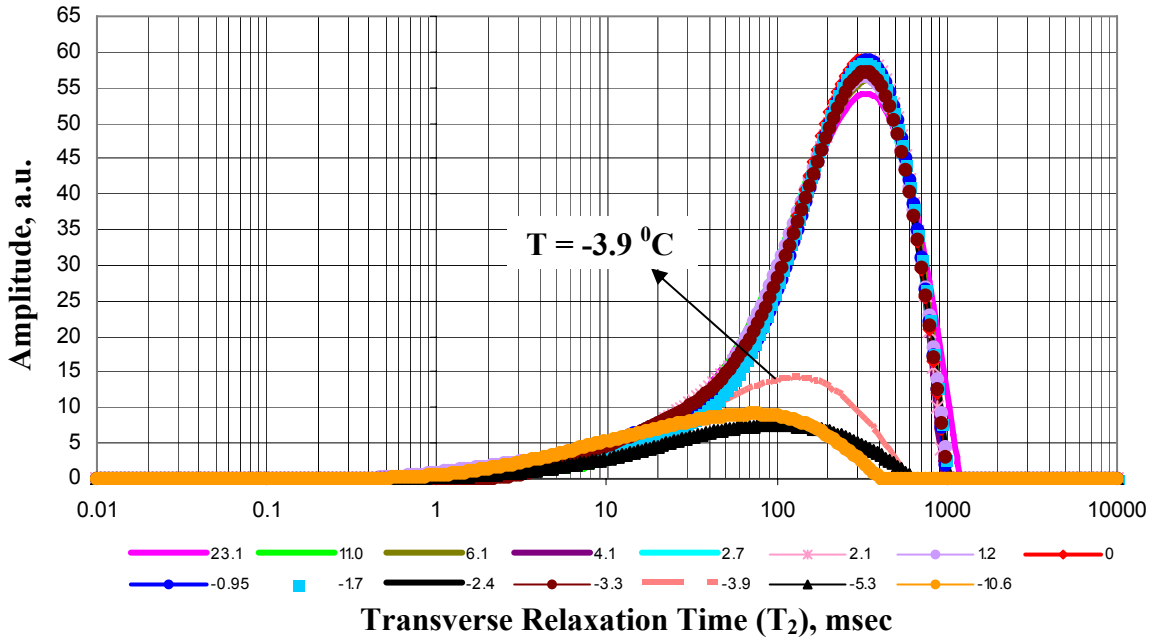

Figure 4.5.6: T_2 distributions of Hollin, 6715v saturated with 25K ppm NaCl brine as a function of temperature from 22 ^{0}C to -10.6 ^{0}C. The different colors indicate the different temperatures. The decrease in amplitude (@ -3.9 ^{0}C) is caused by ice formation. The shift in the T_2 distribution is due to freezing of the big pores and increase dominance of the smaller ones.

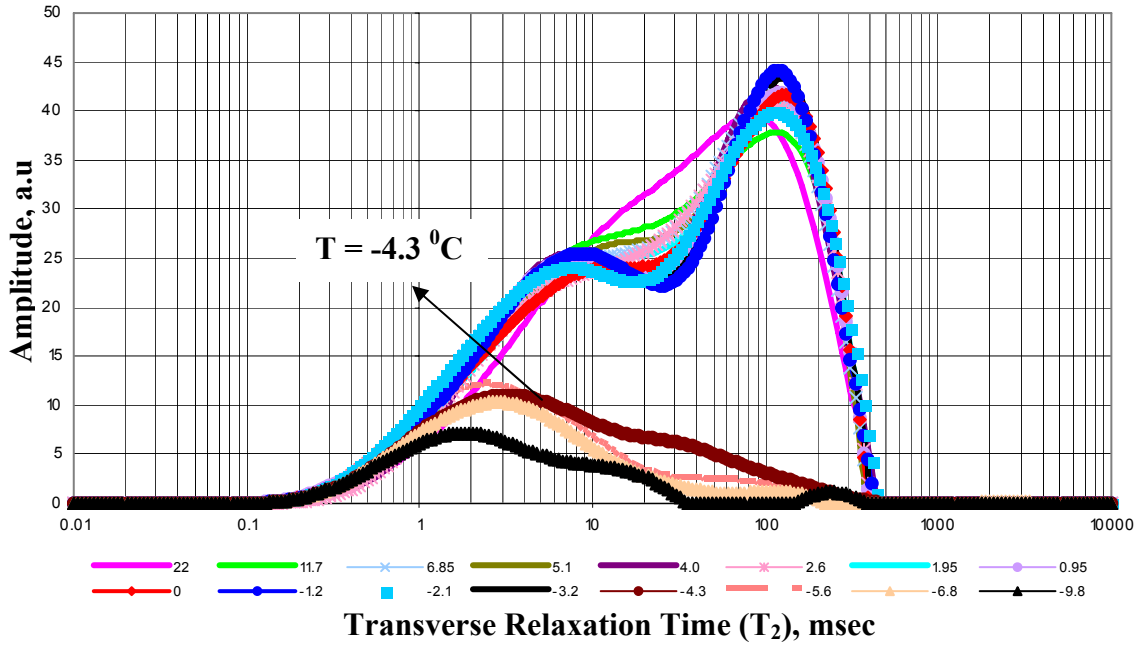

Figure 4.5.7: T_2 distributions of William Fork, WF1A saturated with 25K ppm NaCl brine as a function of temperature from 22 ^{0}C to -10 ^{0}C. The different colors indicate the different temperatures. The decrease in amplitude (@ -4.3 ^{0}C) is caused by ice formation. The bimodal nature of the T_2 distribution is retained till -6.8 ^{0}C with a consistent shift in the peak T_2 time towards shorter time.

The amplitudes are temperature corrected using Curie's law. Except for Tuscaloosa sand (10744.2 ft) (**Fig. 4.5.5**) the majority of the fluid present lies in the larger pores at room condition. Castlegate, CG1, Tuscaloosa sand (10744.2 ft) and William Fork, WF1A show a distinctive bimodal nature of the T_2 distribution. The increase in amplitude due to cooling results in a monotonic increase of the NMR porosity with temperature. The estimated NMR porosity is temperature corrected using **Eqn. 4.1**. **Fig. 4.5.8** shows both uncorrected and corrected porosity as a function of temperature for Filtros. The increase in porosity is between 0.3 % to 3 % for the temperature range of 22 ^{0}C to -10 ^{0}C.

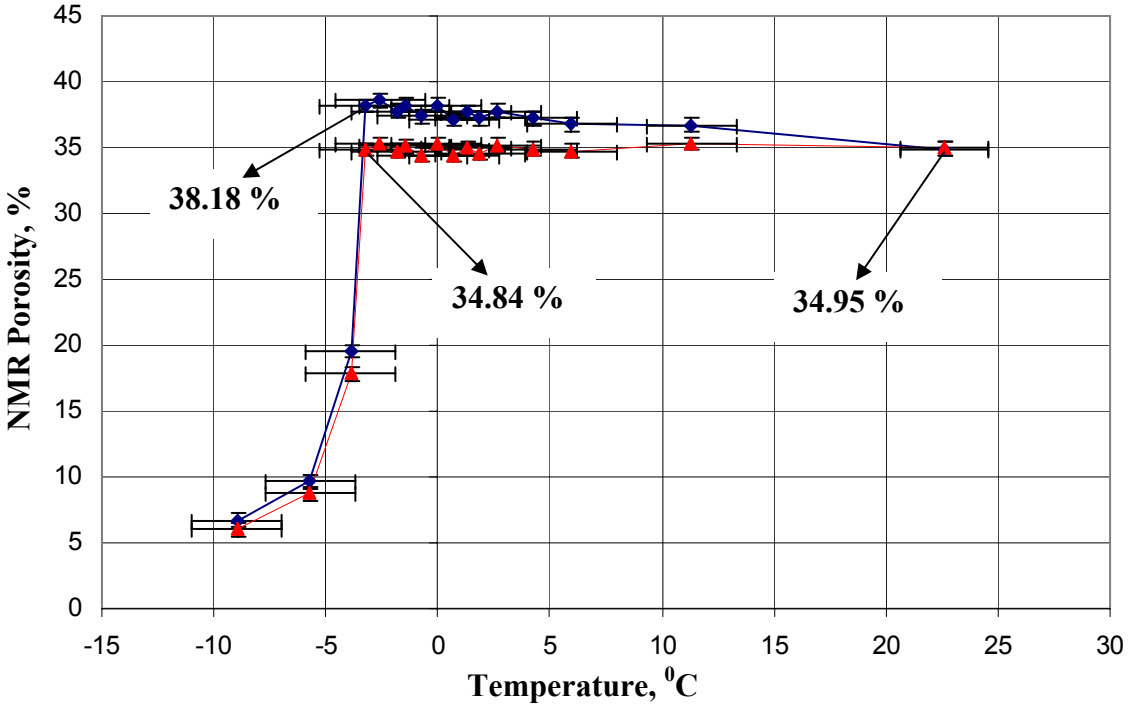

Figure 4.5.8: Uncorrected (diamond) and temperature corrected (triangle) NMR porosity as a function of temperature for Filtros. With decrease in temperature the apparent NMR porosity monotonically increases. After the temperature corrections, the difference in the porosity is ± 0.5 % and it remains unchanged until freezing starts at ~ -4.0 ^{0}C. The error bar in temperature is ± 2.0 ^{0}C.

As soon as freezing initiates, the amplitude drops significantly (**Fig. 4.5.8**) because of the ice formation at -4.0 ^{0}C. At 2 MHz operating resonant frequency of our spectrometer ice

is invisible. Both CMR[7] (Combinable Magnetic Resonance) and MRIL[8] (Magnetic Resonance Imaging Logging) logging tools operate at this frequency too. The freezing process does not initiate precisely at 0 ^{0}C. The presence of salt in the water lowers the freezing point. The freezing point of a 25,000 ppm NaCl brine at 1 atm is -1.36 ^{0}C (Hofonoff and Millard, 1984). Also, the fluid is present inside a capillary which further depresses the freezing point (**Fig. 4.5.12**). For Filtros the freezing initiates between -3.3 ^{0}C and – 4.0 ^{0}C while for the remaining core samples the process initiates between -4.0 ^{0}C and – 4.6 ^{0}C. The freezing of the brine increases the salt concentration of the remaining fluid, resulting in further depression of the freezing point. Refer to Section 4.7 for the effect of salinity on freezing point depression.

Based on the NMR porosity model (**Fig. 2.1.3**) the estimated value of free fluid, capillary bound and clay bound porosity are calculated and plotted as function of temperature (**Fig. 4.5.9**) for all the six core plugs. Except Tuscaloosa sand (10744.2 ft) the amount of free fluid porosity is always greater than the capillary bound and clay bound porosity. Tuscaloosa sand is rich is chlorite (**Fig. 4.6.4**) which results in this anomalous behavior.

[7] Mark of Schlumberger

[8] Mark of Halliburton

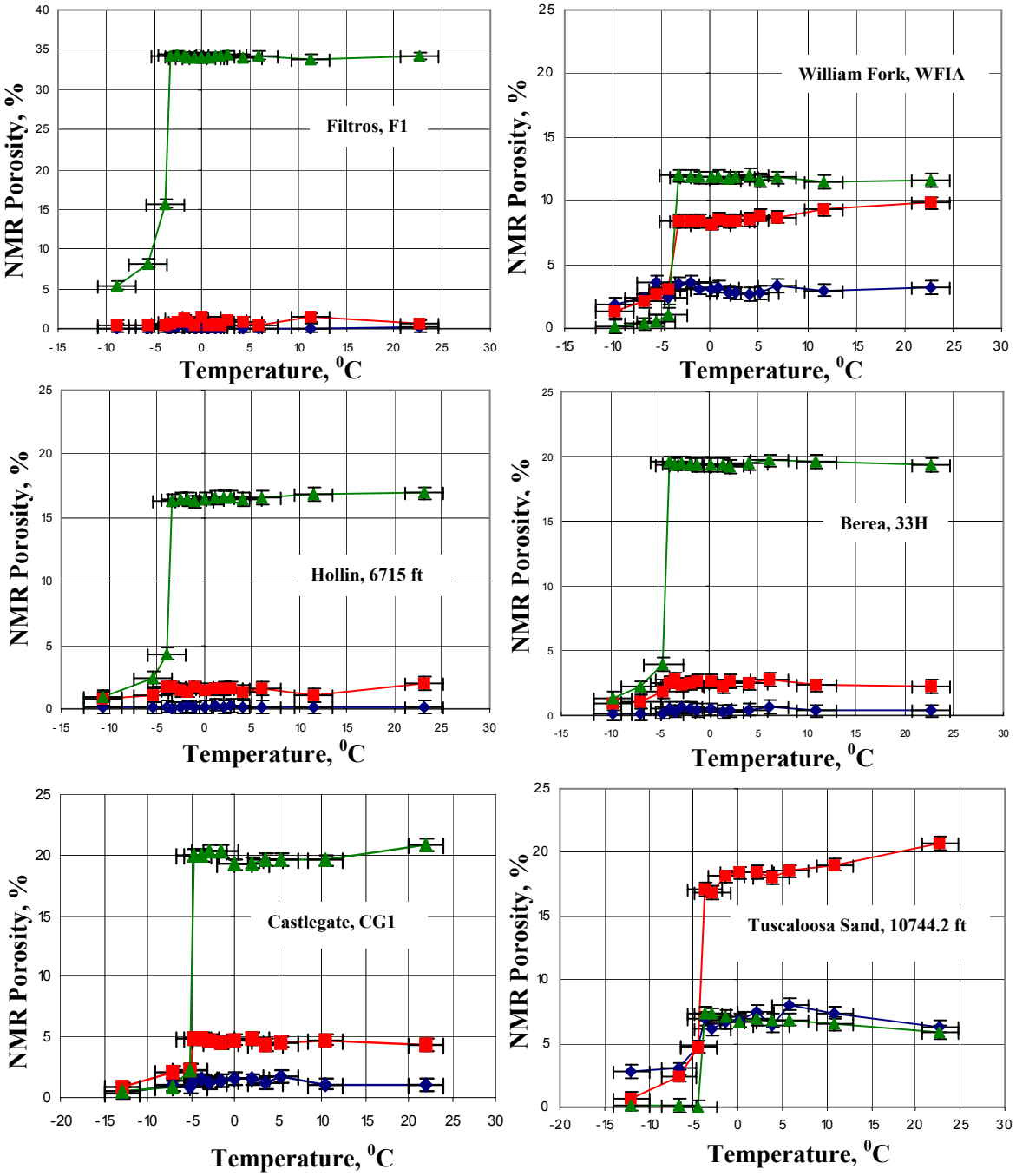

Figure 4.5.9: Plot of free fluid (triangle), capillary bound (square) and clay bound (diamond) NMR porosity as a function of temperature for the six core plugs. The error bar in temperature is ± 2.0 ^{0}C and in NMR porosity is ± 0.5 %. It seems that the freezing initiates at the same temperature for free fluid, capillary bound and clay bound porosity. Except Tuscaloosa sand, the amount of free fluid porosity is always greater than the capillary bound porosity. Porosity is temperature corrected.

The porosity of the core plugs remains constant (within the experimental error) until the

freezing process initiates. Freezing result in a decrease in the liquid filled porosity. As observed in **Fig. 4.5.9** freezing takes place in all pore bodies simultaneously within the time resolution of our experiment. Either the experimental set up is not sensitive enough to capture the very minute details or the dimension of the pore body does not matter during freezing process. Each T_2 relaxation time corresponds to a unique pore body (fast diffusion limit). The area under the T_2 distribution (**Fig. 4.5.10**) for $T_2 < 3$ msec corresponds to the clay bound porosity, between 3 msec and 33 msec (for clastics) it is capillary bound porosity while greater than 33 msec is related to free fluid porosity (Matteson et al., 2000).

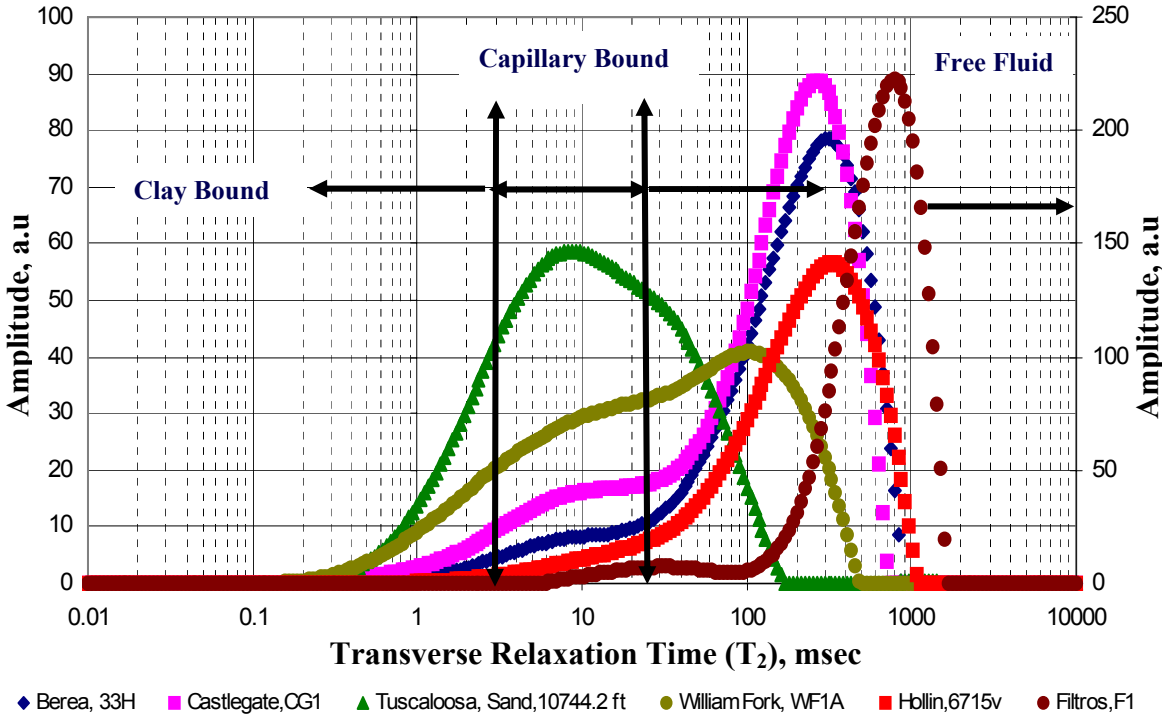

Figure 4.5.10: T_2 distribution of all the six saturated core plugs at room conditions. Majority of the fluid present is free fluid in all core plugs except Tuscaloosa sand and the William Fork where the T_2 distribution is bimodal.

Estimation of the pore radii from NMR T_2 distributions requires knowledge of surface relaxivity. Assuming a cylindrical pore network model the surface relaxivity is estimated

by comparing the normalized incremental mercury injection curve (**Appendix E)** with the normalized T_2 distribution (**Fig. 4.5.11**) (Straley et al., 1997).

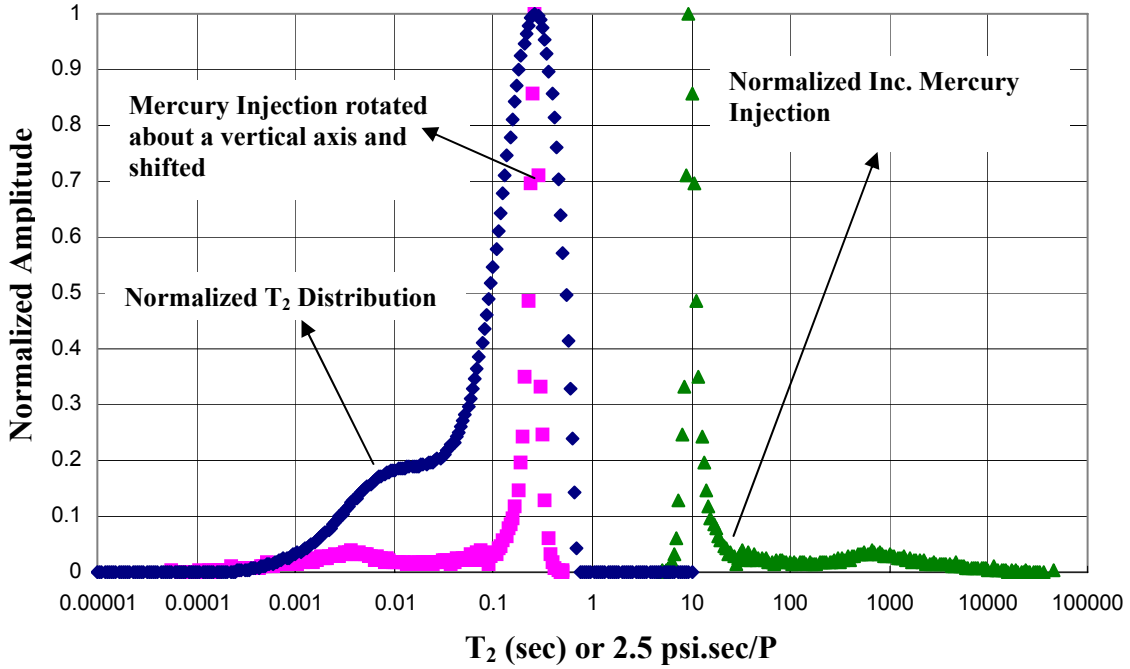

Figure 4.5.11: Comparison of normalized T_2 distribution (diamond) and incremental mercury injection (triangle) for a core plug (Castlegate, CG1). The incremental mercury injection is rotated along the vertical axis (square) and overlaid on the T_2 distribution. The scaling factor of 2.5 psi.sec is used to calculate the surface relaxivity (Dastidar et al., 2006).

A detailed procedure to calculate the surface relaxivity (ρ) is described in **Appendix F.** The estimated surface relaxivity for Castlegate, CG1, is 21.5 μm/sec. A similar approach is used for the other core plugs and their respective surface relaxivity values are presented in **Table 3**. Assuming a cylindrical pore geometry and surface relaxivities (ρ) are 10.5, 21.5, 29.8 and 59.7 μm/sec (**Table 3**), the calculated pore radii corresponding to T_2 = 3 msec are 0.063, 0.13, 0.18 and 0.36 μm. Similarly for T_2 = 33 msec the calculated pore radii are 0.69, 1.42, 1.97 and 3.94 μm, respectively. Supercooling is required to freeze fluid inside a capillary tube (Gibbs-Thomson equation, **Eqn. 2.16**). The numerical values of each of the constants used to calculate the depression in freezing point (**Eqn. 2.16**) are

in **Table 4.**

Thermodynamic Properties	Values
Bulk freezing point, T_{fb}, (^{0}K)	273.15
Ice-Water interfacial tension, γ_{iw}, (J/m^2)	0.0267
Contact angle, θ, degree	0
Density of Ice, ρ_c, kg/m^3	917
Latent heat of melting, L_{fb}, J/kg	334000

Table 4: Thermodynamic properties of water, ice and ice/water interface (Clennell et al., 1999).

Using the thermodynamic properties (**Table 4**), **Eqn. 2.16** can be plotted (**Fig. 4.5.12**) as a function of pore radius

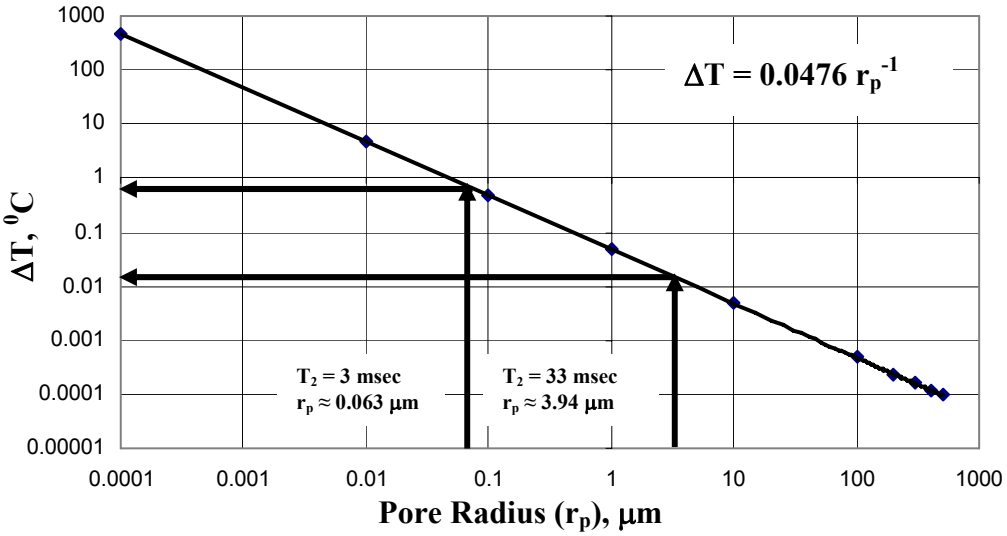

Figure 4.5.12: Depression in freezing point as a function of pore radius.

Thus for a pore radius of 0.063 μm the estimated depression in the freezing point is 0.76 ^{0}C and for 3.94 μm it is 0.069 ^{0}C. The difference in the estimated depression in the freezing point due to capillarity is less than 1 ^{0}C, which is less than our temperature resolution, ± 2.0 ^{0}C. It may be due to this factor that the freezing in clay bound, capillary

bound and free fluid porosity appears simultaneous (**Fig. 4.5.9**). -12 ^{0}C is the maximum subzero temperature achievable in our system.

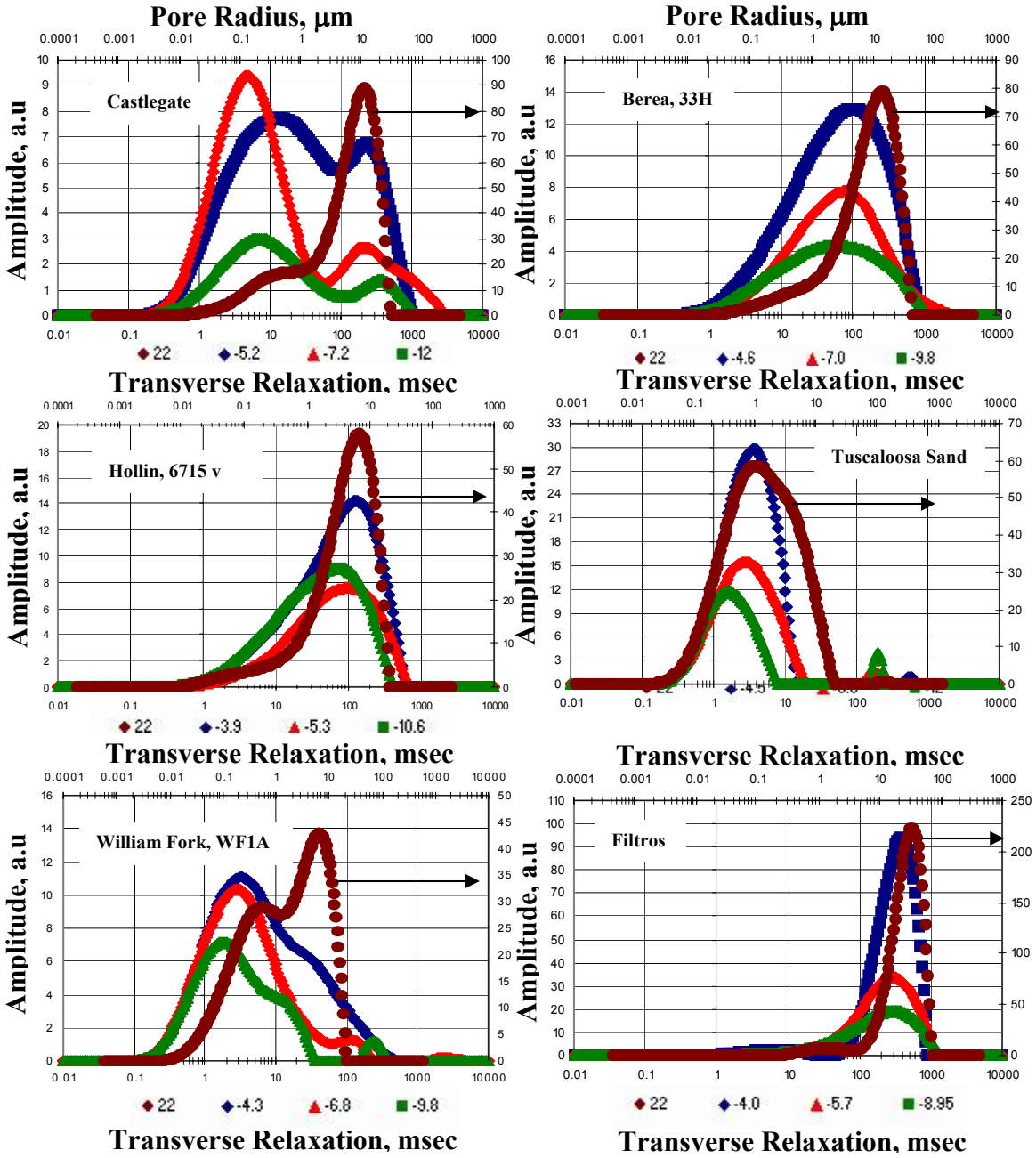

Figure 4.5.13: NMR T_2 distributions for all six core plugs at 22 ^{0}C (brown circle) and at different subzero temperature after freezing is initiated. Unfrozen sample is characterized by higher amplitude with long relaxation time, while partially frozen samples are characterized by mixed behavior. Tuscaloosa sand is exceptional to both unfrozen and frozen characteristics because of high chlorite content. The presence of short and long relaxation time in partially frozen samples, suggest all pores are not completely filled with ice. The freezing of the brine increases the salinity of the remaining solution which depresses the freezing point considerably.

Theoretically, in a water-wet rock any pore body of radius smaller than 0.004 μm will be liquid filled even at -12 ^{0}C. **Fig. 4.5.13** shows the T_2 distribution at 22 ^{0}C and at all temperatures below which freezing initiated for all six core plugs. The pore radius (r) is estimated assuming a cylindrical pore space (S/V = 2/r) using **Eqn. 2.7**. The surface relaxivity of ice is considered to be negligible (refer to Section 4.8). When the samples are unfrozen, higher amplitudes are observed at longer relaxation times. However, in the partially frozen samples there exists mixed behavior; liquid filled pores are present in short and long relaxation time (T_2). This suggest that all the pores are not completely filled with ice. Theoretically (**Fig. 4.5.12)** all pore (r > 0.004 μm) should be completely frozen at around -12 ^{0}C.

The starting fluid is saline in nature which will cause the salinity of the remaining fluid to increase as freezing progresses. This increase in salinity depresses the freezing point of the remaining solution considerably so that pore bodies of radius less than 0.004 μm remain unfrozen even at -12 ^{0}C. Because ice has lower density than water, the same amount of water occupies less volume. The volume expansion due to ice formation results in some of the remaining brine of higher salinity being pushed out of the sample. The expelled brine is observed as free fluid in the NMR T_2 distribution (T_2 > 1sec) **Fig. 4.5.13**. The high salt concentration prevents the expelled water from freezing. One important observation (see **Fig. 4.5.13**) is that there is a continuous distribution of the unfrozen fluid around the whole pore network. However, this is not observed for Tuscaloosa sandstone core plug, where a very small free fluid region is completely separated from the clay bound region. Tuscaloosa sand is rich in chlorite; the majority of the fluid present is capillary bound (**Fig. 4.5.9**). These capillaries correspond to pore

bodies of radii between 0.36 μm and 3.94 μm. The majority of the fluid in the other plugs lies in free fluid region. As soon as freezing starts, the ice displaces the remaining fluid. It is easier to displace the remaining brine out of the capillary bound pore bodies as compared to clay bound region. This results in a systematic decrease in amplitude with shift in smaller T_2 relaxation time.

Recovered sediments (sandstone and mudstone) from the well on North Slope of Alaska were brought to near in-situ conditions by freezing down to -14 ^{0}C (Kleinberg and Griffin, 2005). NMR spectra were acquired every one hour during the thawing process. At zero time the samples were characterized by small amplitude at early time i.e., any pore bodies (0.002 μm < r < 0.05μm) are liquid filled even at -14 ^{0}C (**Fig. 4.5.14**). At -14 ^{0}C, pore bodies of radii less than 0.04 μm are liquid filled in both sandstone and mudstone.

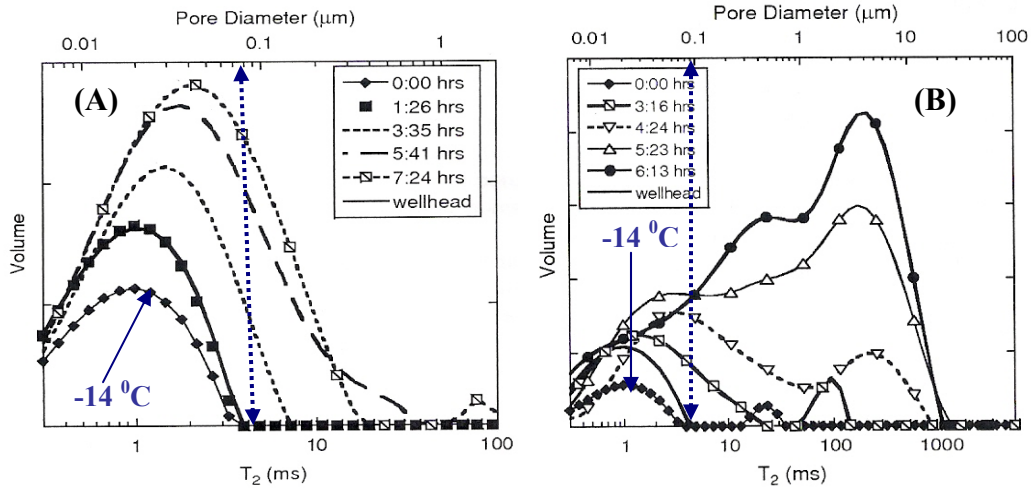

Figure 4.5.14: NMR T_2 distribution during thawing of mudstone (A) and sandstone (B) from -14 ^{0}C to room temperature as a function of time (Kleinberg and Griffin, 2005) .

This is in close agreement to the observation made in this freeze-thaw study (**Fig. 4.5.13**) at -12 ^{0}C except for the presence of unfrozen brine in long relaxation time. One probable cause is the difference in the salinity of the pore water. The salinity of the recovered core

samples was 2-19 ppt (Kleinberg and Griffin, 2005) which is less than 25k ppm used in this study. Lower salinity will result in more freezing as compared to that higher salinity brine. This results in the presence of brine even in the big pores at comparable sub zero temperatures.

4.6 Effect of Temperature on Transverse Relaxation Time

Pure fluids were temperature cycled from 22 ^{0}C to 0 ^{0}C in a pyrex glass vial to estimate the bulk relaxation. The T_{2Bulk} is estimated by a single exponential fit to the raw NMR signal. The T_{2Bulk} of the brine and HPLC (High Performance Liquid Chromatography) pure water used for the study is 2.1 sec at 22 ^{0}C while for the mineral oil it is 0.061 sec at 22 ^{0}C. With a decrease in temperature, the bulk relaxation times decrease (**Fig. 4.6.1**) as it is inversely related to viscosity (see **Eqn. 2.6**).

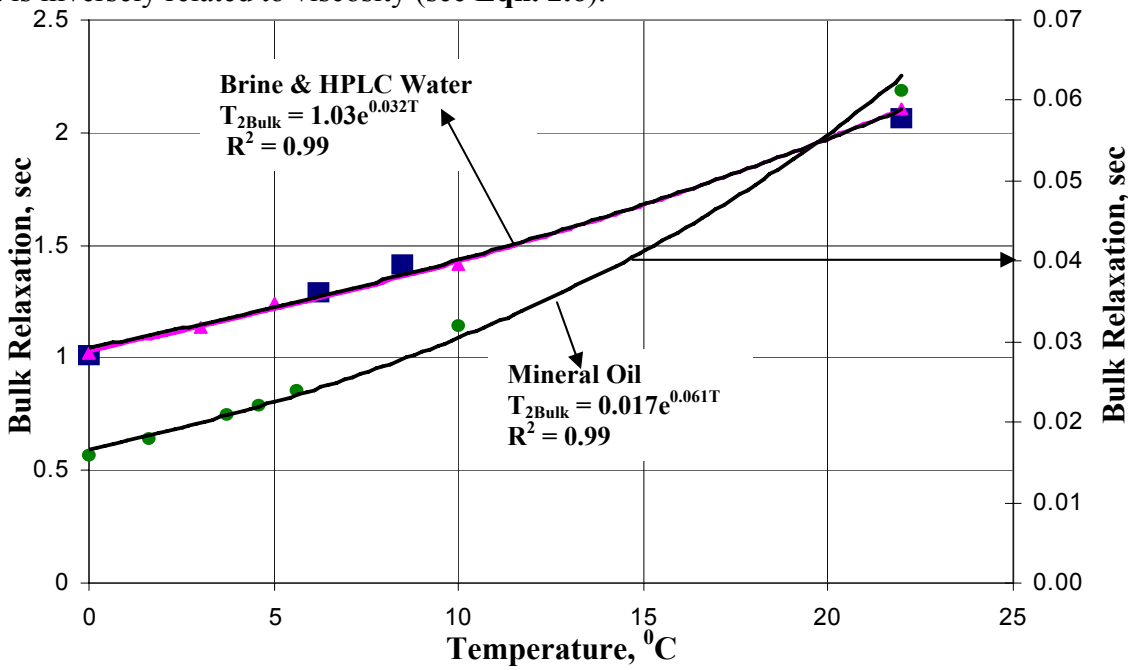

Figure 4.6.1: Estimated bulk relaxation time for HPLC water (square), 25,000 ppm NaCl brine (triangle) and mineral oil (diamond) as a function of temperature. The bulk relaxation time (T_{2Bulk}) of brine and HPLC water are similar and follow the same trend as a function of temperature.

The bulk relaxation of HPLC water and brine overlay each other indicating that the effect

of salt on bulk relaxation is negligible. In all six core plugs the surface relaxation mechanisms dominate. **Fig. 4.6.2** shows the dependence of the main T_2 peak time as a function of temperature for all six core plugs.

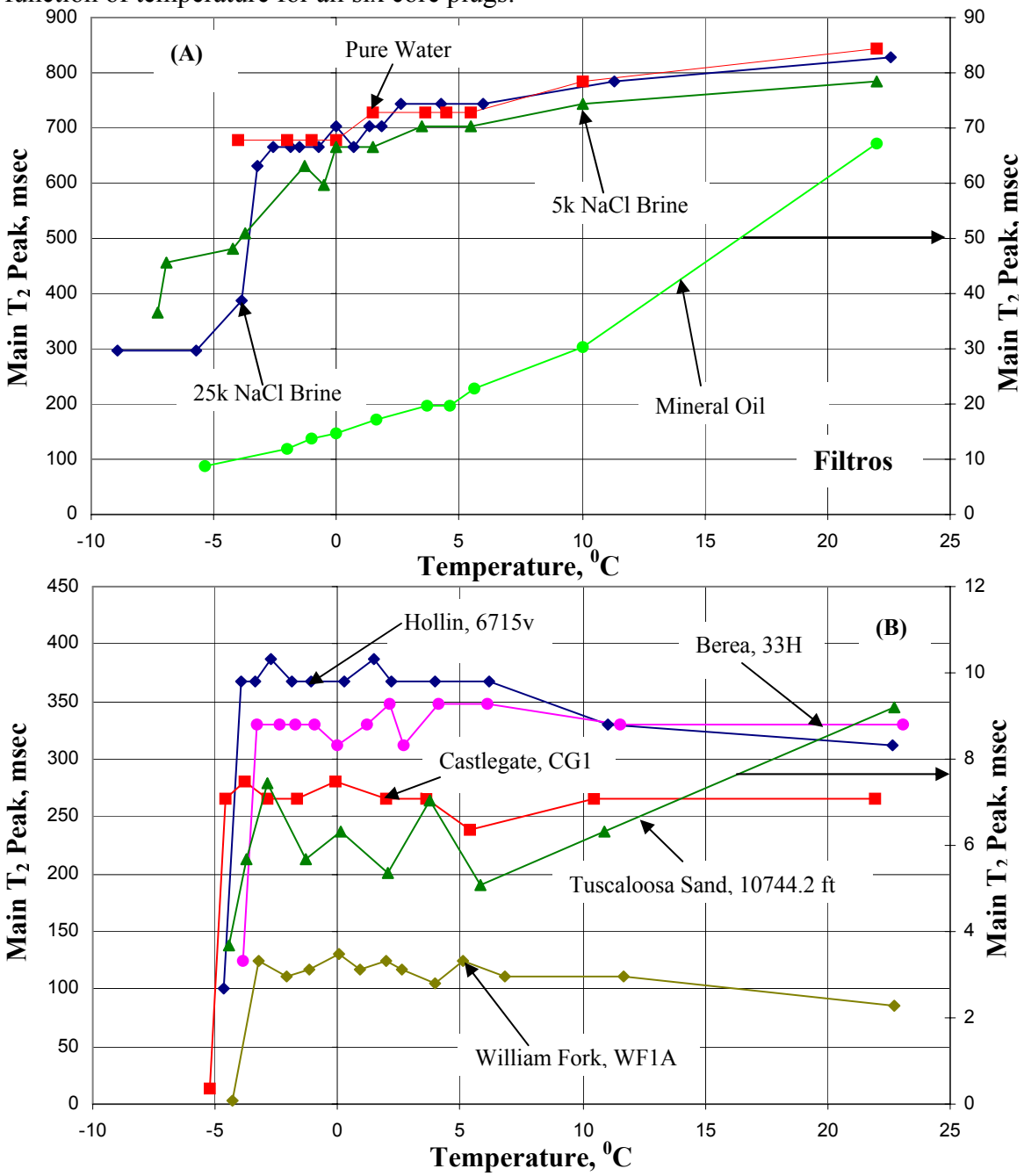

Figure 4.6.2: Shift in relaxation times of the main T_2 peak as a function of temperature. (A) Filtros saturated with 5k (triangles), 25k ppm (diamonds) NaCl brine, HPLC water (squares) and mineral oil (circles). (B) Five sandstone core plugs saturated with 25k ppm NaCl brine. Note that the T_2 times for the Filtros consistently decrease with decrease in temperature while the actual reservoir rocks display mixed behaviors. The shift in mineral oil response is due to bulk effect only.

There is no systematic dependency of transverse relaxation time (T_2) on temperature. **Fig. 4.6.2(A)** indicates peak relaxation times in Filtros consistently decrease with temperature, i.e., the T_2 times shift toward a lower value irrespective of the type of fluid in the system. **Fig. 4.6.2(B)** shows a mixed response. The Tuscaloosa sandstone displays the greatest variation in T_2 peak shifting, and it also has a substantial chlorite component. The sharpest decrease in the peak T_2 times corresponds to the freezing process. Surface relaxation is directly related to surface to volume ratio, S/V, and inversely related to surface relaxivity, ρ. The thermal effects on pore geometry can be estimated through a knowledge of the thermal expansion coefficients of the host matrix. The majority of the minerals present in the cores have positive thermal expansion coefficients. A decrease in temperature would lead to grain contraction which would cause the pore dimension to decrease. As T_2 is directly proportional to pore size, a decrease in pore dimension will result in shift of the T_2 time towards smaller time. Consider the simplistic case, four spheres of equal radii arranged in a cubic packing

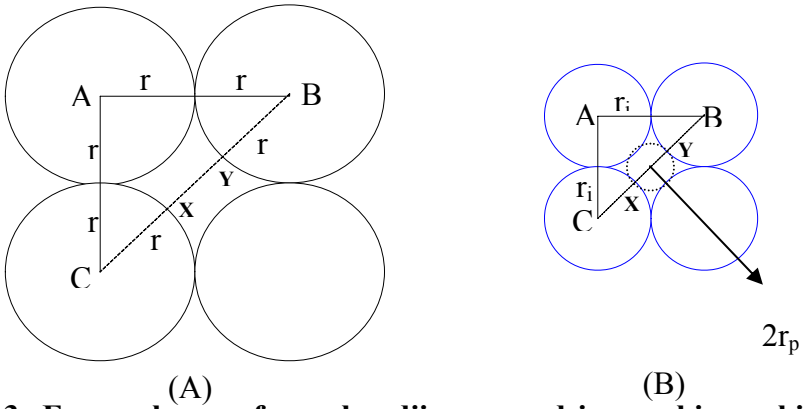

Figure 4.6.3: Four spheres of equal radii arranged in a cubic packing. (A) Before cooling the radius of the grain is r (B) After cooling the radius of the grain is r_i. The positive thermal expansion coefficient results in contraction of the grain particles i.e., $r > r_i$. r_p is the radius of the largest pore body.

The radius of the biggest pore body in a cubic packing can calculated as follows:

$$AC = AB = 2r \quad \{4.4\}$$

$$CB = \sqrt{4r^2 + 4r^2}$$

$$= 2r\sqrt{2}$$

$$CB = 2r + XY$$

$$XY = 2r_p = -2r + 2r\sqrt{2}$$

$$r_p = r(\sqrt{2} - 1)$$

$$r_p = 0.414r \quad \text{.....\{4.5\}}$$

Thus the radius of the biggest pore space in cubic packing is equal to 0.414r. Assuming a grain radius (r) = 100 μm, a volumetric thermal expansion coefficient of quartz (α) = 24.3 x 10^{-6} / ^{0}K (Ahrens, 1995) and surface relaxivity (ρ) = 25μm/sec, we calculate an expected shift in T_2 relaxation peak due to temperature (see **Table 5**).

Temperature ^{0}C	Temperature ^{0}K	Grain Volume μm^3	Grain Radius μm	Pore Radius μm	T_2 msec
22.0	295.15	4190476.19	100.00	41.40	552.00
10.0	283.15	4189254.25	99.99	41.40	551.94
5.0	278.15	4187523.67	99.98	41.39	551.87
3.0	276.15	4185590.29	99.96	41.38	551.79
1.0	274.15	4183454.38	99.94	41.38	551.69
0.0	273.15	4181217.91	99.93	41.37	550.59

Table 5: Summary of the estimated grain radii, pore radii and T_2 time for a single pore as a function of decreasing temperature. Note the T_2 shift is insignificant.

The grain volume at each temperature is calculated with respect to the reference temperature through the following formula:

$$V(T) = V_{T_r}[1 + \alpha(T - T_r)] \quad \text{.....\{4.6\}}$$

where, V(T) volume of the grain at temperature T, V_{Tr} is the volume at reference

temperature, α is volumetric thermal expansion coefficient, and T_r is the reference temperature = 22 ^{0}C. Thus it is observed that for the temperature range of 22 ^{0}C to -12 ^{0}C the effect of the thermal expansion is almost negligible. The estimated shift in peak T_2 time is only 1 msec, i.e., smaller than the noise in measurement.

Alternatively, if surface relaxivity of minerals within the rock exhibits a temperature dependence which could be positive or negative then a mixed shifting would be expected. All six core plugs are mineralogically different as determined by FTIR (**Fig. 4.6.4**). Based on the inversion[4] of the FTIR spectral data the mineralogical composition of the samples can be quantified in terms of weight percentage.

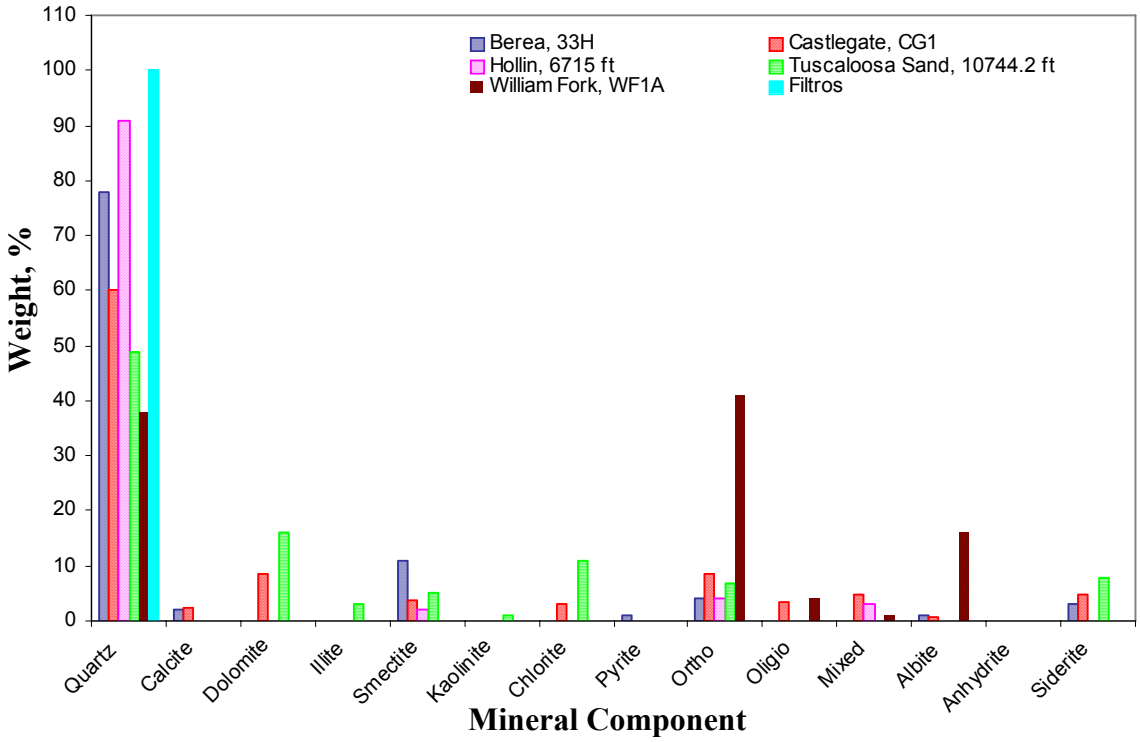

Figure 4.6.4: Histogram of the mineralogy present in the six core plugs. Note that the samples are all quartz rich. The Tuscaloosa is significantly chlorite and dolomite rich.

Variations in mineralogy will influence the surface chemistry which in turn affects the surface relaxivity. The variation in the surface relaxivity with temperature can shift the T_2

distribution in either direction. The cumulative response will be reflected in the apparent shifting of T_2 relaxation spectral peaks. The observed shifts in peak T_2 relaxation times for reservoir rocks are interpreted to reflect a temperature dependence of surface relaxivity. While the influence of temperature on surface relaxivity is not fully understood, attempts have been made to explain it on the basis of activation energy (e.g. Godefroy et al., 2001).

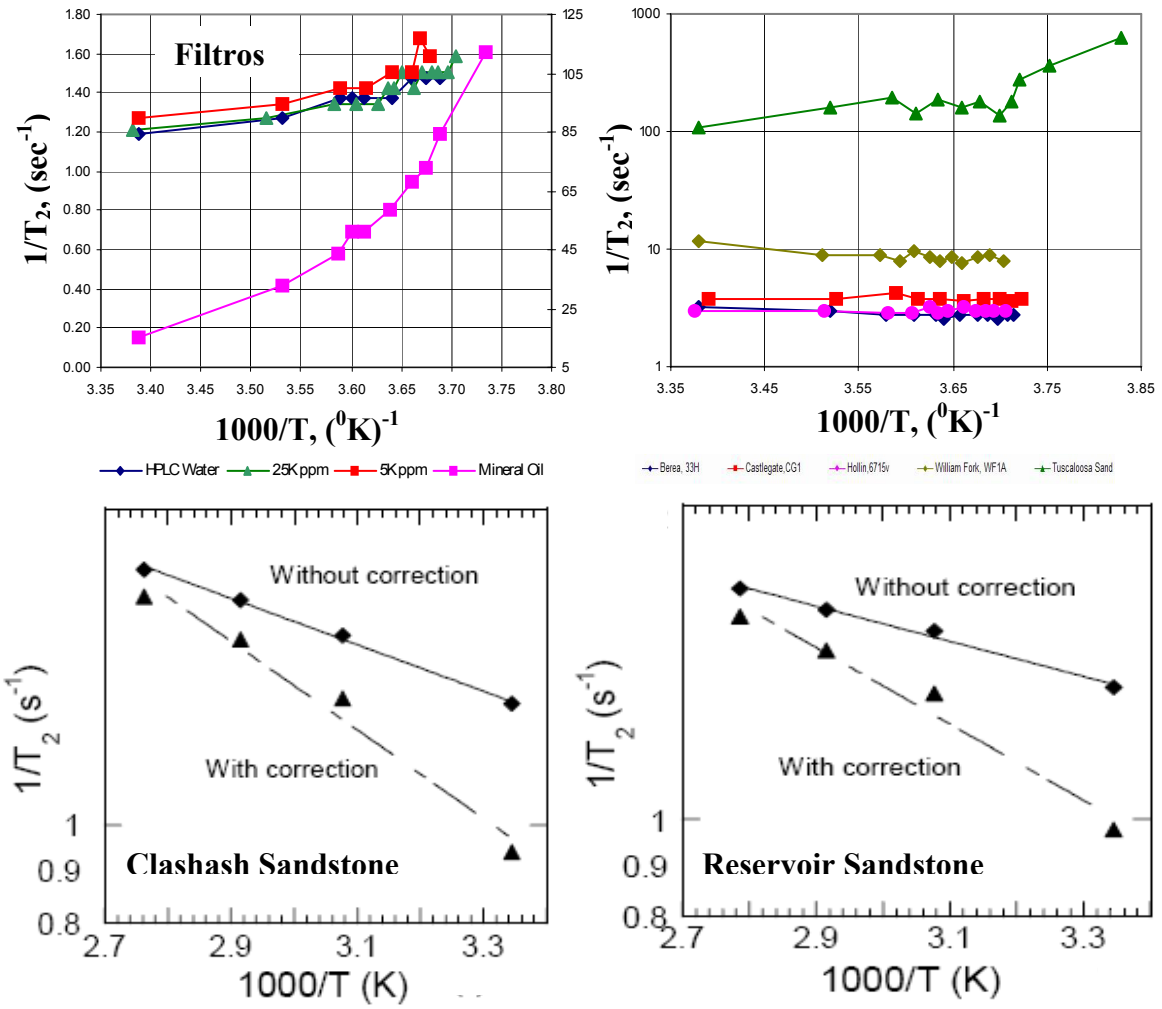

Figure 4.6.5: Arrhenius plot of $1/T_2$ as a function of inverse of temperature for different water saturated reservoir and artificial rocks. Clashash and Reservoir sandstone data corresponds to the study done by Godefroy et al., 2001. With correction indicate the removal of bulk relaxation effect. Filtros and Tuscaloosa Sand (in the present study) is characterized by positive activation energy while rest of the core plugs are characterized by negative activation energy.

Fig. 4.6.5 is a comparison of $1/T_2$ as a function of inverse temperature (1/T) for different types of sandstone. $1/T_2$ is directly proportional to surface relaxivity (**Eqn. 2.7**). Temperature has a minimum effect on pore dimension (**Table 5**). Thus surface relaxivity possesses the same dependence to the inverse of temperature (1/T) as observed in **Fig. 4.6.5** between $1/T_2$ and 1/T. Surface relaxivity is directly proportional to the difference in the activation energy (ΔE) describing surface translation or diffusion (E_m) and energy associated with the surface chemical bonding (E_s) which depends on the temperature of the system, **Eqn. 2.10** (Godefroy et al., 2001). The effective activation energy (ΔE) can be positive or negative depending on whether the diffusion barrier energy (E_m) is greater than or smaller than surface bonding energy (E_s). In case of Filtros and Tuscaloosa sand the surface relaxivity increases with decrease in temperature i.e., negative temperature dependence. For the remainder of the samples (this study and Godefroy et al., 2001), the surface relaxivity decreases or stays almost constant with decrease in temperature i.e., positive or weak temperature dependence. In short, the dependence is controlled by how easy it is for the water molecule to stay attached to the matrix mineral or to diffuse to the bulk water (**Fig. 4.6.6**).

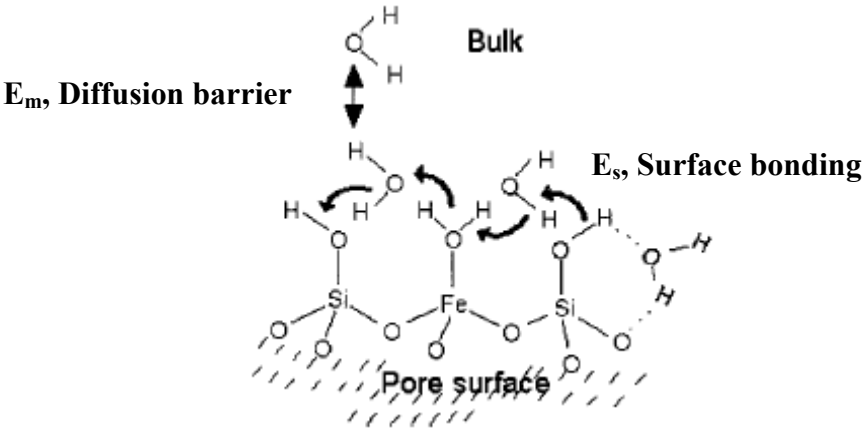

Figure 4.6.6: Transition of water molecule between SiO_2, paramagnetic impurities (Fe^{2+} or Fe^{3+}) and bulk phase. The duration of the stay is dominated by the energy barrier between the surface and bulk phase (Modified from Godefroy et al., 2001).

4.7 Unfrozen Brine Content & Correlation

Experimental data (**Fig. 4.7.1**) indicate that there will be always a fraction of unfrozen brine present in the system. When a salt solution freezes, the pure solvent (water) freezes first leaving behind the solute (salt) which further increases the concentration of the remaining solution. The increased salt concentration further depresses the freezing point.

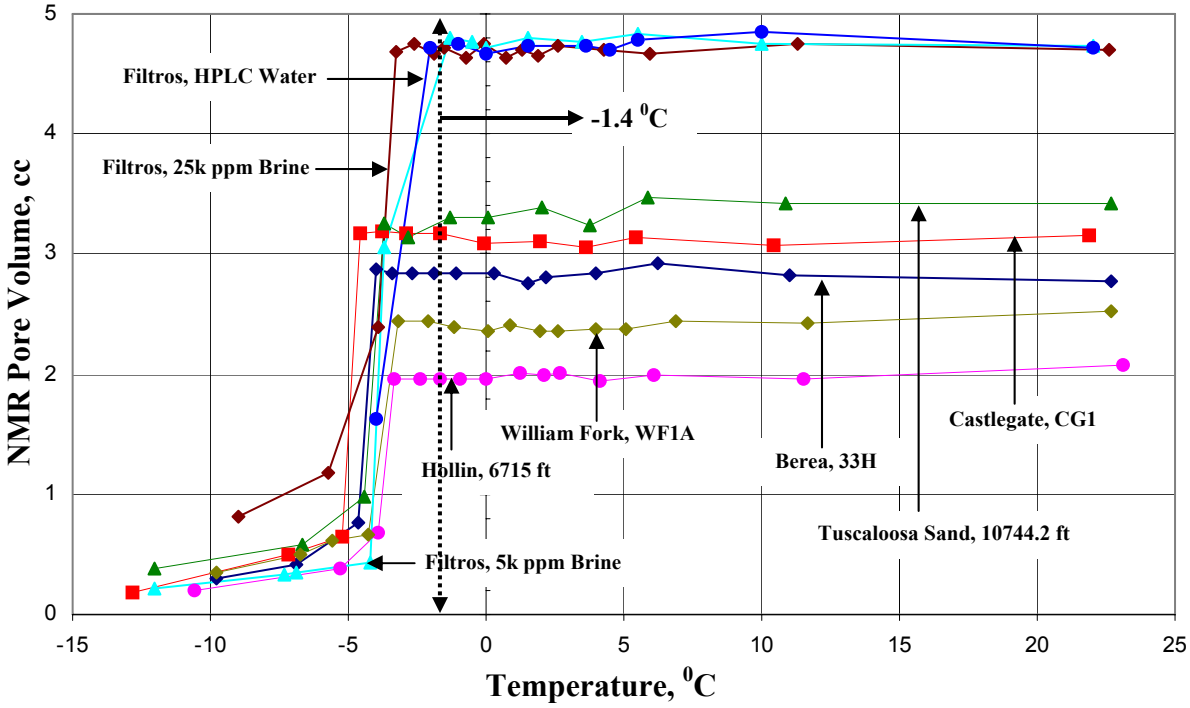

Figure 4.7.1: Amount of solution present in the core plugs as a function of decrease in temperature. The Filtros sample was saturated with 25k ppm (circle), 5k ppm (triangle) NaCl brine and HPLC water (diamond). For all other core samples the saturating fluid is 25k ppm NaCl brine. The freezing point of 25k ppm NaCl brine is -1.4 ^{0}C.

For Filtros saturated with HPLC water and 5k ppm NaCl brine the freezing initiates between -1.0 ^{0}C and – 3.0 ^{0}C while for the remaining core samples saturated with 25k ppm NaCl brine the process initiates between -4.0 ^{0}C and – 4.6 ^{0}C. Except for the pure water case, there is always a fraction of fluid which remain unfrozen at -12 ^{0}C. Given an initial brine salinity of 25,000 ppm NaCl and a pore volume of 2.079 cc. The amount of

NaCl presents is 0.052 gm. At -4.4 ^{0}C, the new pore volume is 0.551cc. Thus the remaining fluid has a salinity of 94,400 ppm NaCl and a freezing point of -5.79 ^{0}C. If this logic is true, where brine begins to freeze has consequences for the overall behavior of the porous medium. Freezing of large pores, increases salinity and lowers the freezing point of the fluid in the cracks while freezing the crack fluid first reduces the freezing point of fluid in big pores. The knowledge of amount of unfrozen brine present in the system is essential for water saturation estimation which relates to the economics of the reservoir. The amount of unfrozen water (**Fig. 4.7.1**) is correlated to ΔT (difference in temperature of the core and freezing of pure water) using power law (Anderson and Tice, 1973) and exponential model (Civan, 200). The power law model implies that all the water present in the system will freeze. The exponential model fits the current data set better than the power law model (**Fig. 4.7.2**).

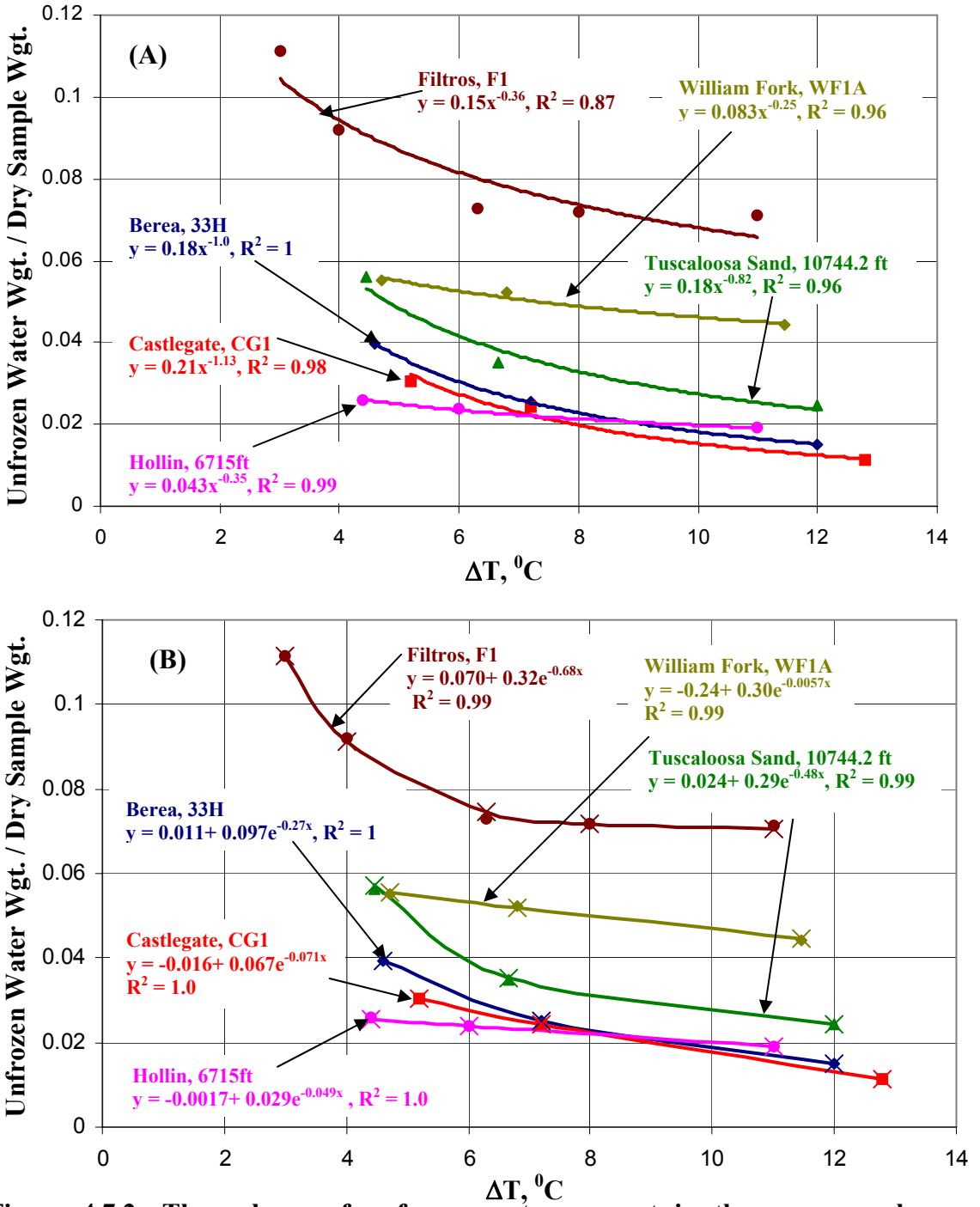

Figure 4.7.2: The volume of unfrozen water present in the core sample was correlated to ΔT (difference in temperature of the core and freezing of pure water) based on power law (Anderson and Tice, 1973) (A) and exponential model (Civan, 2000) (B). The symbol "X" in (B) indicates the calculated value using the exponential model while the circles are experimental values.

4.8 Estimation of Surface Relaxivity of Ice

Ice surface relaxivity is required to interpret NMR data of frozen and freezing materials. Experiments were designed and carried out to measure the surface relaxivity of ice. Few attempts to measure the surface relaxivity of ice have been reported in the literature. Attempts have been made to define the end members (Kleinberg and Griffin, 2005). The motivation behind this study is to quantify the surface relaxivity of ice. Two approaches were taken.

4.8.1 First Approach

Background

The operating temperature of 2MHz MARAN Ultra[5] spectrometer (**Fig. 3.7.1)** is maintained at 30 ^{0}C. When measuring ice at 0 ^{0}C, the difference in the temperature will cause condensation along the wall of the glass holder. To estimate the effect of the condensation, NMR spectra were acquired on an empty cold glass vial. Signal acquisition parameters were optimize to capture short relaxation times. The empty glass vial (**Fig. 4.8.1**) was kept in the freezer at -20 ^{0}C for 5 hours, prior to measurements.

Figure 4.8.1: Empty Glass Vial (Internal Diameter = 1.0" and Height = 1.2")

Surface relaxivity is a property dependent on the paramagnetic properties of the surface materials. To capture the very early times, NMR spectra were acquired on the cold glass

vial at an inter echo spacing (TE) of 0.30 msec. To improve the signal to noise (S/N) ratio for the low pore volume anticipated the number of scans was set at 10000. The raw decay (**A**) and the T_2 distribution (**B**) of the cold glass vial is shown in **Fig. 4.8.2**. The noisy raw data and very small amplitude (note the vertical scale) indicates the effect of condensation is negligible, even the shale scale levels were in 1000's.

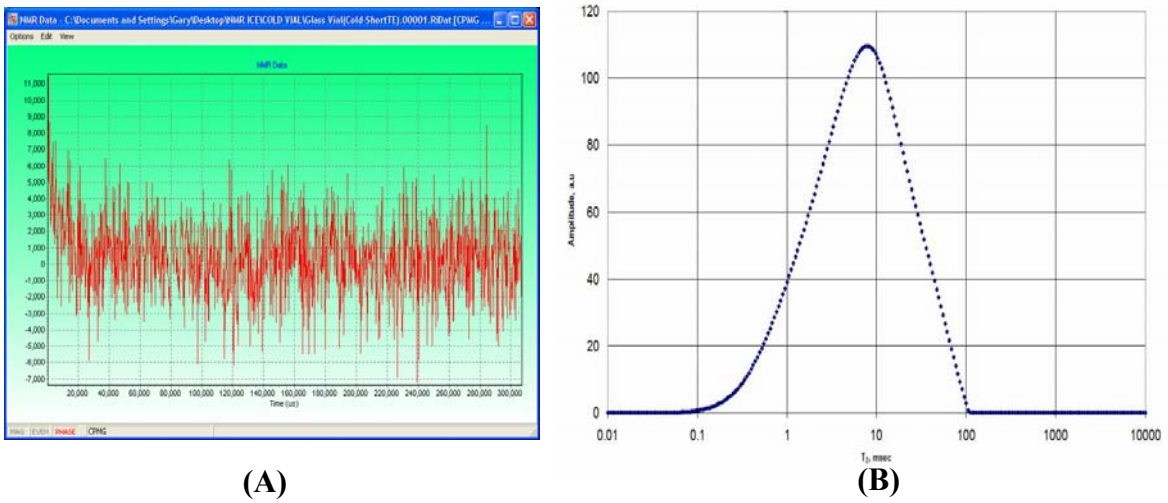

(A) **(B)**

Figure 4.8.2: (A) Raw NMR signal of cold glass vial and glass holder. (B) T_2 distribution of the raw signal. The amount of noise present in the raw signal indicates that the condensation is small. The calculated volume of fluid is 0.006 cc which is almost negligible. No. of scans = 10000.

The glass vial was filled with 3 cc of pure water and an aluminum rod (Diameter = 7.89 mm) was placed in the water filled glass vial. The complete assembly was placed in a freezer at -20 ^{0}C for 6 hours. The purpose of the aluminum rod was to create a hollow ice cylinder of known diameter. Three aluminum rods of different diameter namely 7.89 mm, 6.34 mm and 3.14 mm were used for this study. Once ice is formed, the aluminum rod is slowly removed from the system. This creates a hollow cylinder with a corresponding internal diameter (**Fig. 4.8.3**). Cold water (2 ^{0}C) is then injected into the empty space very carefully using a syringe.

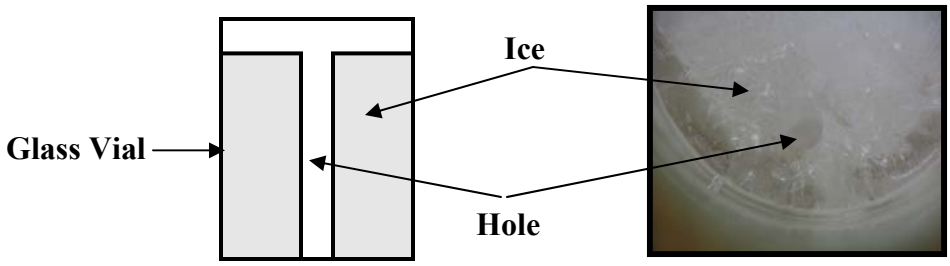

Figure 4.8.3: Sketch of a hollow ice cylinder. Holes are created using, three different aluminum rods of diameter 3.14mm, 6.34 and 7.89 mm, respectively.

NMR spectra were acquired with TE = 3.0 msec for all the three cases. Below TE = 3.0 msec, the decay was not stabilized. The T_2 distributions for all three hole sizes are shown in **Fig. 4.8.4**. For an ID less than 3.14 mm it became difficult to keep the fluid inside the empty space in the liquid state.

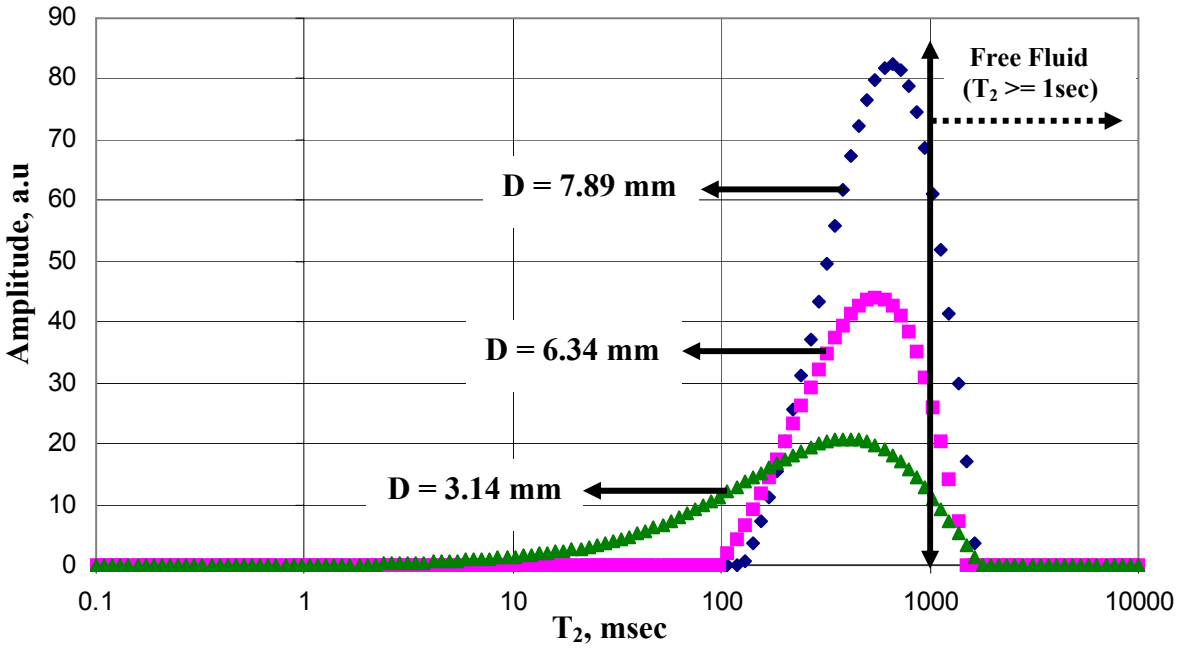

Figure 4.8.4: T_2 distribution of three hollow ice cylinders of diameter 3.14mm, 6.34 mm and 7.89 mm, respectively. With decreasing hole diameter there is a slight shift in the main T_2 peak and broadening at the lower T_2 time. No. of scans = 10.

It is interesting to observe that with pore dimension on the order of millimeters, the T_2 distribution is dominated by surface and not bulk relaxation (T_{2Bulk} >= 1 sec). **Table 6**

present the different T_2 values used for estimating the surface relaxivity.

S.No	Diameter mm	Smallest T_2 msec	Upper T_2 msec	Main Peak T_2 msec	Mean T_2 msec
1	3.14	1.99	1631.54	418.84	174.30
2	6.34	98.2	1361.00	549.74	488.97
3	7.89	128.9	1631.54	659.02	602.32

Table 6: Summary of the different T_2 used to estimate the surface relaxivity.

Fig. 4.8.5 is a crossplot between pore radius and different T_2 time (**Table 6**). Surface relaxivity is slope (**Fig. 4.8.5**) of the **Eqn. 2.7**. Surface to volume ratio for a cylinder is 2/R. In all the cases the estimated surface relaxivity (ρ) is a hundred times that of what is reported for a sandstone (Dunn et al., 2002). The average surface relaxivity for sandstone is around 25 μm/sec which is much lower than the estimated surface relaxivity of ice interface. The very high surface relaxivity indicates that the influence of pore dimension on T_2 time is minimum.

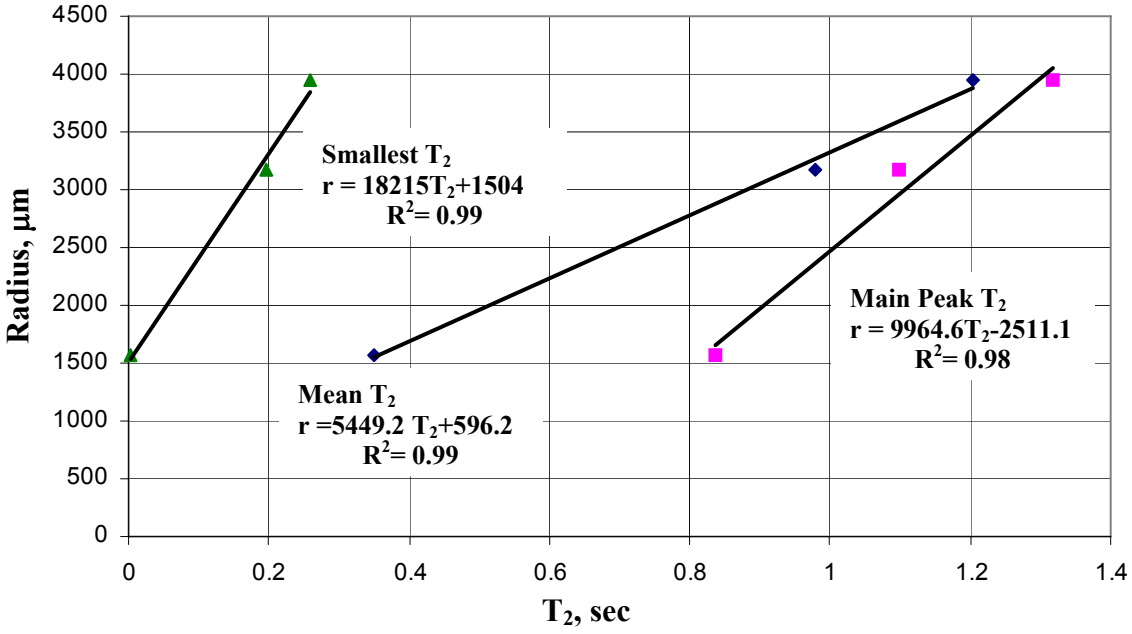

Figure 4.8.5: Plot of radius as a function of T_2. Surface relaxivity is twice the slope reported in each linear equation, i.e., 9117, 4982 and 2750 μm/sec.

The calculated T_2 time (using **Eqn. 2.7**) for each of the pore radii (1.57, 3.17 and 3.95 mm) assuming an average surface relaxivity (ρ, μm/sec) of 25 μm/sec, is 32 sec, 66.04 sec and 82.19 sec respectively. The calculated T_2 times indicate that fluid will behave as free fluid (T_2 >= 1 sec). However, the T_2 distribution (**Fig. 4.8.4**) for the fluid inside the hollow ice cylinder with pore radii of 1.57, 3.17 and 3.95 mm is not simply behaving as free fluid. Below pore diameter of 3.14 mm it was difficult to keep the water in liquid state; it freezes. An attempt has been made to use acetone in the hole. As surface relaxivity depends on mineralogy i.e., an intrinsic property of the matrix, the type of fluid has no influence. To verify the above fact two different material (**Fig. 4.8.6**) were considered; Filtros[9] and Kellundite[9]. Filtros is a glass bonded silica (SiO_2) and Kellundite is a ceramically bonded alumina (Al_2O_3).

(A) **(B)**

Figure 4.8.6: (A) Filtros, porosity and permeability are 35% and 5D. (B) Kellundite, porosity and permeability are in the same ranges.

The samples were saturated with water and acetone to examine the relaxivity dependencies. The T_2 distributions (**Fig. 4.8.7**) overlay on each other indicating that infact surface relaxivity is an intrinsic property of the matrix. The experiment was unsuccessful as acetone melted the ice immediately. Other fluids such as silicone oil etc., should be used to verify and extend these observation to smaller dimensions.

[9] http://www.filtrosltd.com/Materials.htm

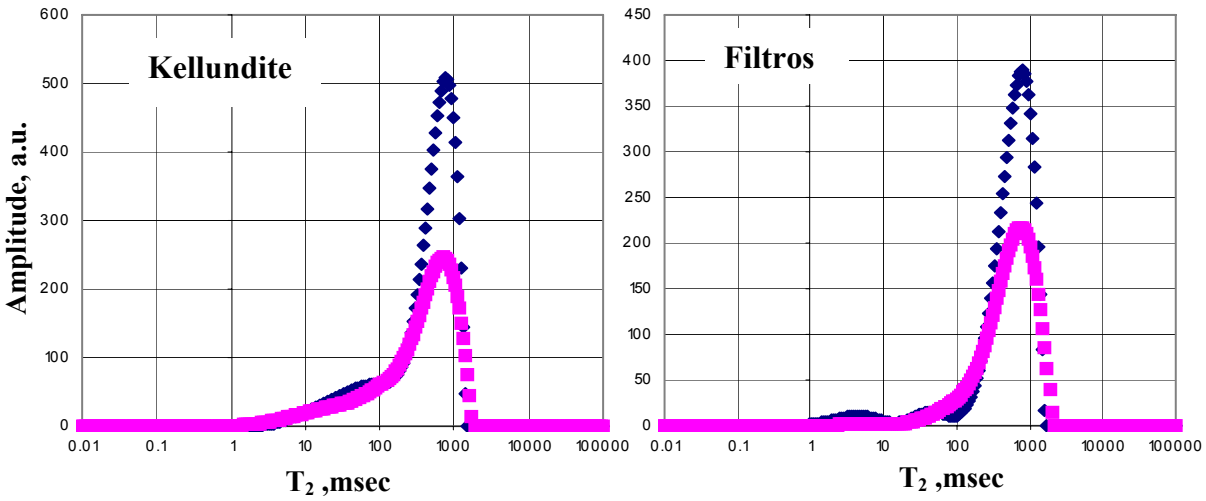

Figure 4.8.7: T_2 distribution of Filtros and Kellundite filled with water (Diamond) and acetone (square). No shift in T_2 distribution, indicate the surface relaxivity is an intrinsic property of the matrix while the difference in amplitude is due to difference in hydrogen index.

4.8.2 Second Approach

In this approach, crushed ice is placed in the vial and NMR spectra were acquired at different inter-echo spacing. As noted earlier the effect of condensation is negligible. The heat from the 2 MHz MARAN Ultra[5] spectrometer (T = 30 ^{0}C) will melt the crushed ice. Melting will start at the outer boundary of each of the pieces of ice. As ice starts to melt, water will appear first at the outermost boundary of the crushed ice surface. Depending on the inter echo spacing the surface layer of the water can be detected. At smaller inter-echo spacing, the T_2 decay is dominated by the surface relaxation (Coates et al., 1999). With time, the crushed ice will melt and the response will become that of bulk relaxation of water. The different inter-echo spacing used for this approach are 0.30, 0.6, 1.5, 2.0, 2.4 and 3.0 msec, respectively. NMR measurements were taken for each inter echo spacing at 3 minute interval. The cartoon (**Fig. 4.8.8**) is based on **Eqn. 2.7**; it shows the effect of pore size and relaxivity on T_2 decay.

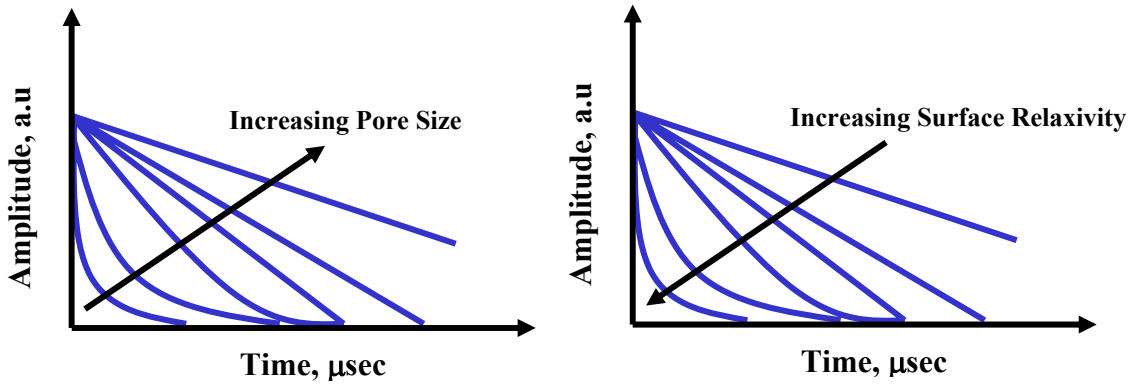

Figure 4.8.8: Raw T_2 decay as a function of increasing pore radius or surface relaxivity based on Eqn. 2.4. However in reality the raw decay curve is a combination.

In porous media, actually both dimensions and surface relaxivity change. It becomes difficult to separate the influence of each. The inter-echo spacing of 0.30 msec and 0.6 msec are being used conventionally for shale and sandstone, respectively. At an inter-echo spacing 0.30 msec the raw decay curve of the crushed ice could not be fitted to a T_2 distribution (**Fig. 4.8.9**).

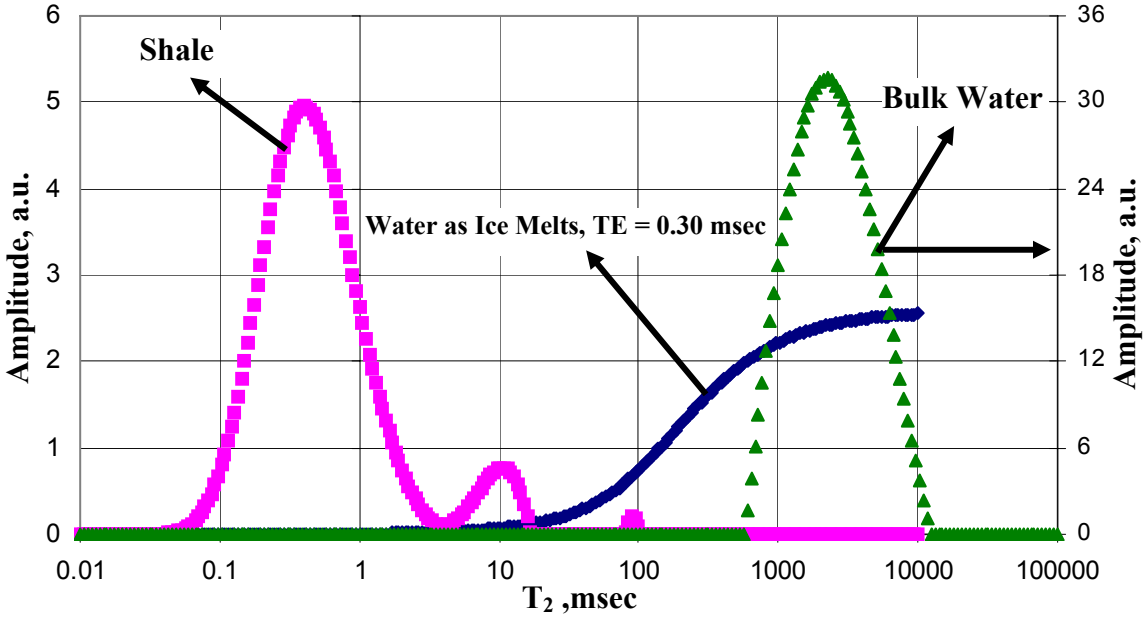

Figure 4.8.9: T_2 distribution of a shale sample, bulk water and water at the boundary of the crushed ice due to melting with TE = 0.30 msec. Number of scans for the crushed ice measurement is 10. The shale data is acquired using 10000 scans and then renormalized to 10 scans.

The incomplete distribution may be due to insufficient wait time for the ^{1}H atoms to reach an equilibrium state. The shale and ice melting is observed at an echo spacing of 0.30 msec while the bulk water signature is obtained at 1.5 msec. **Fig. 4.8.9** can be interpreted in two ways, first the relaxivity of ice (ρ_i) is at least greater than shale ($\rho_s \sim 1$ μm/s, Dunn et al., 2002) or second there is no surface relaxivity of ice. Combining the first approach and the first interpretation of the second approach suggests that the relaxivity of ice is at least greater than surface relaxivity of shale. The second interpretation could be based on the fact that the incomplete distribution is more towards the bulk water, indicating very small surface relaxivity. The comparison of the first of the 14 NMR spectra acquired for each echo spacing is shown in **Fig. 4.8.10**.

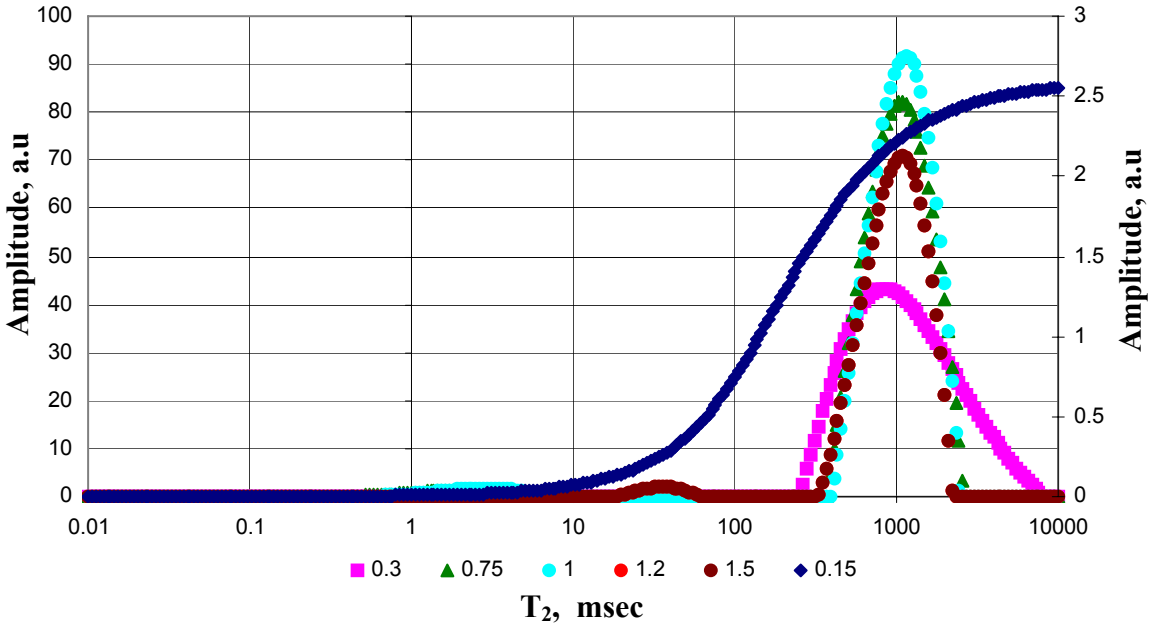

Figure 4.8.10:T_2 distribution of crushed ice at different τ (TE = 2τ) indicated by different colors. Each distribution is the first of the 14 NMR spectra acquired at an interval of 3 min. It is obvious that ice has surface relaxivity. No. of scans = 10. The amplitude are not temperature corrected.

The T_2 distributions for all the inter echo spacings are narrowly spaced on the time axis except for TE = 0.30 msec. Further, the main peak is near to 1 sec. Except at TE = 0.30

msec and TE = 0.6 msec, the remainder of the distribution is spread equally about T_2 = 1 sec. Melting of ice is faster when it is crushed. This most likely causes a layer of water on the surface of the ice as a result of a melt layer thick enough to behave as bulk water. At each inter echo spacing, as time progresses the heat melts the ice and the T_2 distribution shifts towards right (longer time) and when it is completely melted the response is that of bulk water relaxation time. The incomplete T_2 distribution is near the bulk relaxation of free water even at an inter echo spacing of 0.30 msec. This suggests that probably ice has very small relaxivity.

4.8.3 Heat Conduction Profile – Stefan Problem

The melting of ice due to the heat inside the MARAN Ultra[5] spectrometer (internal temperature = 30 ^{0}C) can be modeled as classical Stefan's problem (Carslaw and Jaeger, 1959). The important point is the existence of a moving phase boundary. In this model the ice is cylindrical in shape and the heat is applied in all directions. A simplified 1D problem (**Fig. 4.8.11**) is considered to estimate the thickness of the water layer with time.

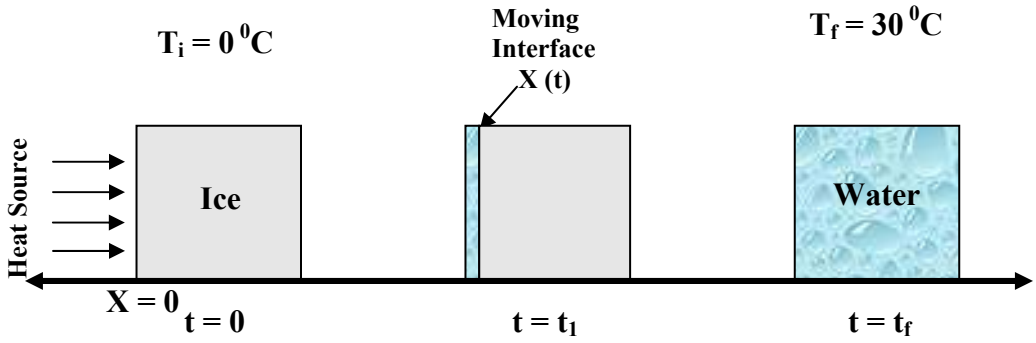

Figure 4.8.11: Heat conduction with melting

It is a free boundary problem and the only solution available is for infinite and semi infinite case. Assuming a semi infinite case at time t = 0, an ice cylinder (T = 0 ^{0}C) is kept inside the spectrometer. The spectrometer is maintained at 30 ^{0}C. The heat will start

to melt the ice. X (t) is the free boundary or the phase-change boundary/interface. Also, the effect of the glass cylinder is neglected. The melting problem can be formulated (Carslaw and Jaeger, 1959) as follows:

In the liquid region

$$C_L\rho_L \frac{\partial T_L}{\partial t} + C_L\rho_L u_x \frac{\partial T_L}{\partial t} = K_L \frac{\partial^2 T_L}{\partial x^2} \quad \text{.....\{4.7\}}$$

$$\text{Boundary Conditions}: 0 < X < X(t),\ t > 0$$
$$T_L(x,t)\big|_{t=0} = 0\ ^0C,\ T_L(x,t)\big|_{x\to\infty} = 30\ ^0C \quad \text{.....\{4.8\}}$$

In the Solid Region

$$C_S\rho_S \frac{\partial T_S}{\partial t} = K_S \frac{\partial^2 T_S}{\partial x^2} \quad \text{.....\{4.9\}}$$

$$\text{Boundary Conditions}: X(t) < X < \infty,\ t > 0$$
$$T_S(x,t)\big|_{x=0} = 30\ ^0C > 0\ ^0C,\ t > 0 \quad \text{.....\{4.10\}}$$

At the Interface

$$K_S \frac{\partial T_S}{\partial x} - K_L \frac{\partial T_L}{\partial x} = L\rho \frac{\partial X}{\partial t} \quad \text{.....\{4.11\}}$$

$$x = x(t)$$
$$T_L = T_S = 0\ ^0C \quad \text{.....\{4.12\}}$$

where C, ρ, K, T and L are specific heat, density, thermal conductivity, temperature and latent heat of fusion respectively. Subscripts L and S stand for liquid and solid phase. u_x is the velocity of the liquid phase if the densities of solid and liquid phases are not equal. In this case it is neglected. Applying the boundary condition, the position of the melting plane is given by (Carslaw and Jaeger, 1959)

$$x = 2\lambda\sqrt{\kappa_L t} \quad \text{.....\{4.13\}}$$

where λ is the root of

$$\frac{e^{-\lambda^2}}{erf\lambda} - \frac{K_S\sqrt{\kappa_L}\,T_1 e^{-\lambda^2\left(\kappa_L/\kappa_s\right)}}{K_L\sqrt{\kappa_S}\left(V - T_1\right)erfc\left[\lambda\sqrt{\kappa_L/\kappa_s}\right]} = \frac{\lambda l\sqrt{\pi}}{C_L\left(V - T_1\right)} \quad \text{.....\{4.14\}}$$

where κ, V and T_1 is the thermal diffusivity, outside temperature of 30 ^{0}C and ice temperature of 0 ^{0}C, respectively. λ is determined iteratively using the function **Goal Seek** in Excel. The numerical values of each of the constants used for solving **Eqn. 4.14** are given in **Table 7**. They are in c.g.s system. λ is dimensionless and the estimated value is 0.409.

Thermal Properties	Unit (c.g.s)	Water	Ice
Thermal Conductivity(K)	calorie/cm sec ^{0}C	0.00144	0.0053
Specific Heat (C)	calorie/gram ^{0}C	1.0	0.502
Density (ρ)	gm/cc	1.0	0.92
Diffusivity (κ)	cm^2/sec	0.00144	0.0115

Table 7: Thermodynamic properties of water and ice used in Eqn. 4.14.

The plot of X (t) (free boundary or the phase-change boundary/interface) as a function of time is shown in **Fig. 4.8.12**. Even assuming the simplest case, the thickness of the water layer approaches the higher end of the pore radius system within the time frame of our observations. That is why the T_2 distribution in each of the cases appears to be dominated by the bulk relaxation time (T_2= 1 sec) of free water.

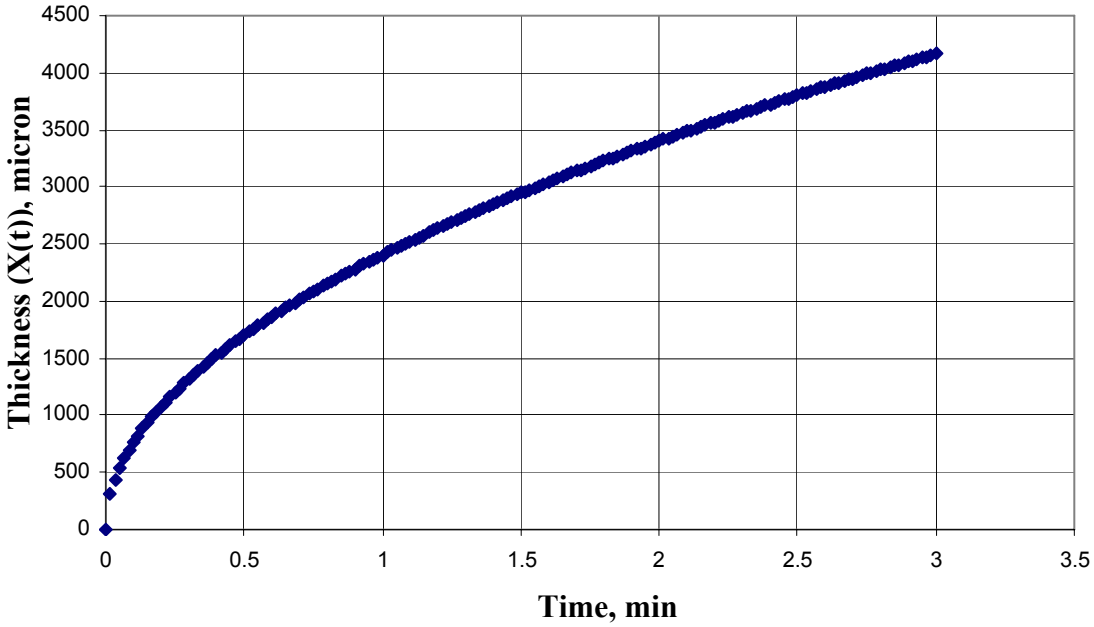

Figure 4.8.12: Position of the phase boundary from X = 0 w.r.t time

4.8.4 Shortcomings

In this study two different approaches were made to estimate the surface relaxivity of ice. The first approach suggests the relaxivity of ice (ρ_i) is very large as compared to that of relaxivity of common matrix minerals (ρ_p). While the second approach suggests that the relaxivity of ice (ρ_i) is very small as compared to that of relaxivity of matrix (ρ_p); two approaches, two contradictory results. Estimating surface relaxivity requires the knowledge of characteristics T_2 time and dimension of the pore. In both attempts, because of heat inside the MARAN Ultra[5] spectrometer (internal temperature = 30 ^{0}C), ice starts to melt. It is difficult to determine the actual water layer thickness. The estimated thickness of the water layer (Stefan's Solution) become rather larger very quickly. This causes the main peak of the T_2 distribution to move towards the bulk relaxation time of water even at the shortest inter echo spacing. The ideal case for estimating surface relaxivity of ice is to have ice particles of known shape and dimension

(such as sphere or cylinder, etc.) in contact with water. The sample holder has to be below 0 ^{0}C to prevent melting of the ice and at the same time the water has to be in liquid state.

4.8.5 Interpretation of Surface Relaxivity

This study is designed to answer one of the most critical questions related to the interpretation of NMR logs in permafrost region i.e., the surface relaxivity of ice. Porous media in a permafrost region comprises of matrix, hydrocarbon, brine, and ice. This is different from the conventional reservoir which constitute of only matrix, hydrocarbon and brine. The T_2 response of a water saturated porous media is defined by **Eqn. 2.7** which is modified to include the effect of ice as **Eqn. 2.18.** However **the** surface relaxivity of ice (ρ_i) is unknown. When a porous medium freezes, the brine in the system will freeze. The observed T_2 spectra will reflect where in the pore space the ice forms. The most simplistic cases are that of ice along the boundary or in the center, see **Fig. 4.8.13**. A number of scenarios were evaluated based on varying values of surface relaxivity of ice and pore dimension as a function of unfrozen water volume for ice along the pore wall (pore lining) and ice in the center of the pore (pore filling).

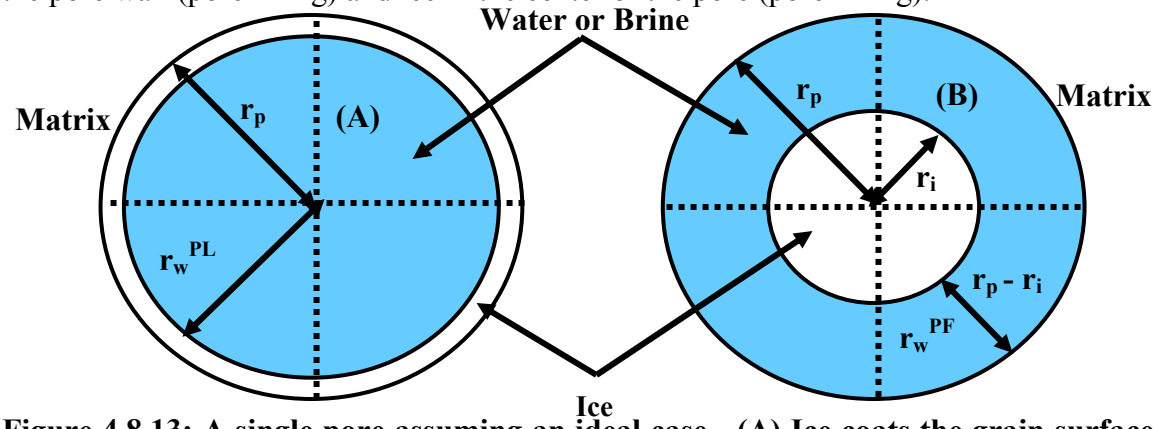

Figure 4.8.13: A single pore assuming an ideal case - (A) Ice coats the grain surface (pore lining) (B) Ice fills the center of the pore (pore filling). Drawing is not to the scale.

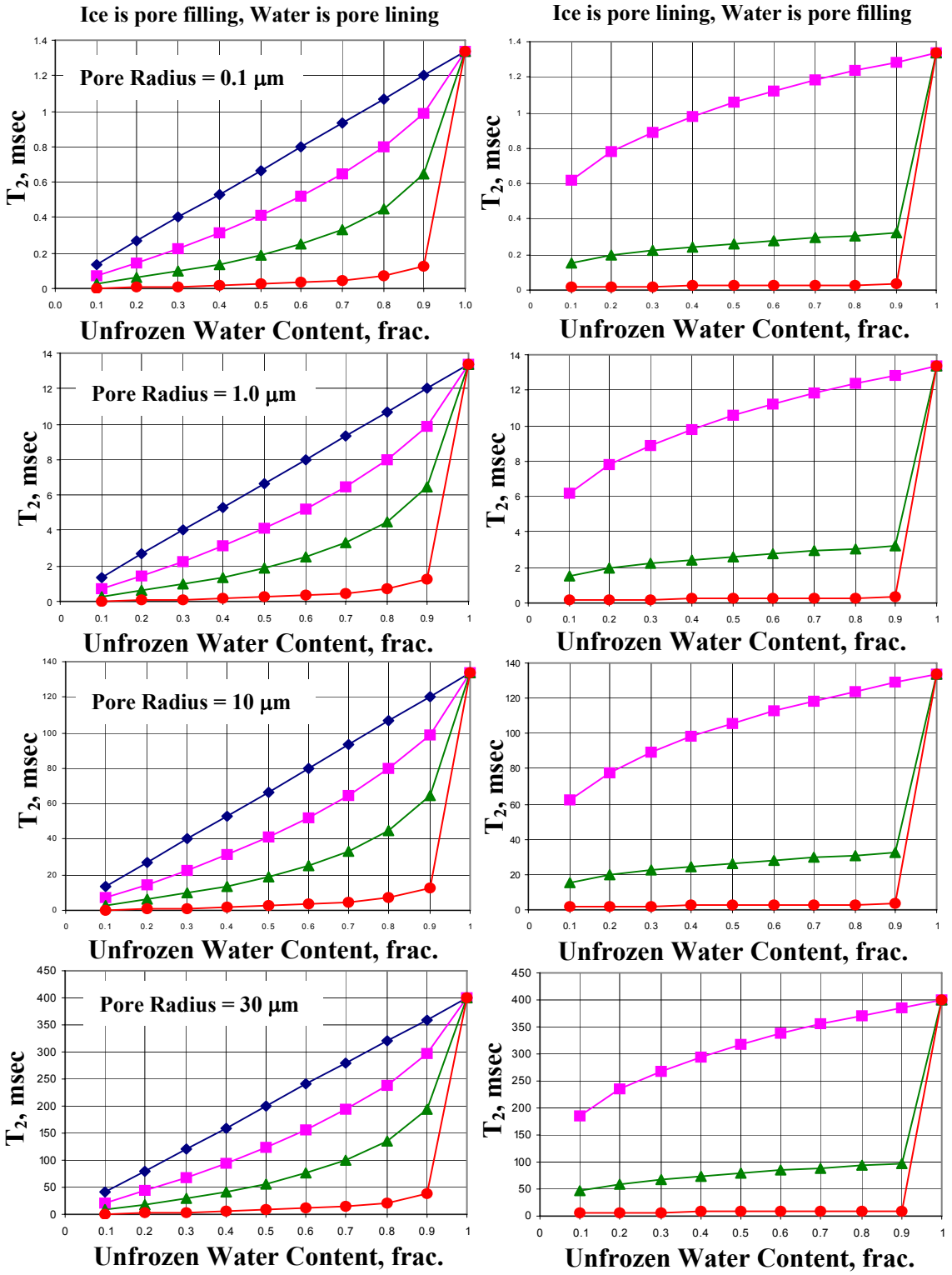

Figure 4.8.14: Estimated T_2 time as a function of unfrozen water for pore filling and pore lining ice for a single pore assuming different surface relaxivities of ice, i.e., blue diamond (0), pink square (25), green triangle (100) and red circle (1000). The trend in the shift in T_2 time remains same for pore bodies with different dimensions.

Pore lining and pore filling models are conceptual. Pore lining ice is defined as a continuous layer of ice along the grain surface. Pore filling ice is defined as ice present within the pore with water layer always in contact with the grain boundary.

The calculated T_2 time for a single pore as a function of unfrozen water (fraction of the water that is in liquid state) for pore lining and pore filling ice is plotted in **Fig. 4.8.14**. Calculation details are described in **Appendix G** .The T_2 time is estimated for various combination of surface relaxivity of ice (ρ_i = 0, 25, 100 and 1000 μm/sec) and pore bodies of different radii (r_p = 0.1, 1, 10 and 30 μm). The surface relaxivity of the pore matrix (ρ_p) is assumed to be 25 μm/sec. The trend in the shift of T_2 peak time with decrease in unfrozen water content is different for pore filling and pore lining ice. However the trends remain the same irrespective of the pore dimension. If surface relaxivity of ice is zero and a continuous layer of ice is present along the pore wall i.e., pore lining ice then there will be no surface relaxation. The ^1H atom will have a bulk relaxation with relaxation time (T_{2Bulk}) greater than 1.0 sec. The absence of any pattern for ρ_i = 0 μm/sec for pore lining ice in **Fig. 4.8.14** is due to the fact noted earlier. There is no T_2 time corresponding to complete ice in the system, as ice is invisible to a 2 MHz NMR spectrometer. The relaxivity of ice-water system is unknown but attempts have been made to define the end members (Kleinberg et al., 2003a, Kleinberg et al., 2003b and Kleinberg and Griffin, 2005). Kleinberg and Griffin (2005) suggested that the relaxivity of ice is lower than that of the rock or matrix.

Case 1: $\rho_i >> \rho_{ma}$

For the same fractional change of water into ice in both the cases (**Fig. 4.8.13**), r_w^{PF} is smaller (**Fig. 4.8.13 (B)**) as compared to r_w^{PL} (**Fig. 4.8.13 (A**)). The mobile hydrogen

atom in the water is going to relax faster due to the decrease in the distance between the relaxing surfaces. As soon as ice forms along the pore wall, the decrease in T_2 time is very rapid as compared to pore filling ice (**Fig. 4.8.14**). Afterward the frequency shift in the case of pore lining is very gradual. However, in the case of pore filling ice, the T_2 time continues to decrease and even go to a value lower than what is observed in case of pore lining ice at the same unfrozen water content. The shape of the T_2 distribution will remain unchanged for the case of pore filling ice as compared to that of pore lining ice due to presence of water layer surrounding the grain matrix.

Case 2: $\rho_i << \rho_{ma}$

Similar to previous case, r_w^{PF} is smaller (**Fig. 4.8.13 (B)**) as compared to r_w^{PL} (**Fig. 4.8.13 (A)**). However for the same fractional change of water into ice, the decrease in T_2 time is greater for pore filling ice as compared to that of pore lining ice. The reason being in case of pore filling ice, the mobile hydrogen atom will at least have one surface whose relaxivity is higher resulting in faster relaxation as compared to that of pore lining ice, where the relaxivity of the ice surface is lower causing the relaxation to happen at a longer time. When the surface relaxivity of ice is equal to zero i.e., $\rho_i \approx 0$, for pore lining ice, the relaxation mechanism of ^1H atom will be bulk relaxation with a corresponding time (T_{2Bulk}). For the pore filling ice, the presence of water layer next to the grain matrix will result in surface relaxation and its thickness will govern the T_2 time (**Fig. 4.8.14)**. The shape of the T_2 distribution will be preserved for pore filling.

Case 3: $\rho_i \approx \rho_{ma}$

This scenario is similar to that of the previous two cases where r_w^{PF} is smaller (**Fig. 4.8.13 (B)**) as compared to r_w^{PL} (**Fig. 4.8.13 (A)**). The rate of decrease of the

characteristic T_2, i.e., shift to lower T_2 time is greater when ice preferentially fills the center of the pore as compared to ice coating the grain boundary (**Fig. 4.8.14**). To understand this complex process, the peak T_2 times for six different core plugs which were temperature cycled from 22 ^{0}C to -12 ^{0}C are analyzed. The T_2 distributions during the cooling cycling for all the six core plugs at different temperature are presented in **Fig. 4.5.2 - 4.5.7**. As soon as freezing initiates, there is a decrease in the amplitude due to formation of ice and a shift in the peak T_2 time. **Fig. 4.8.15** is a plot of the peak T_2 time as a function of unfrozen water content for the six core plugs. Unfrozen water content in this case is defined as the ratio of the amplitude corresponding to the peak T_2 time after freezing and before freezing.

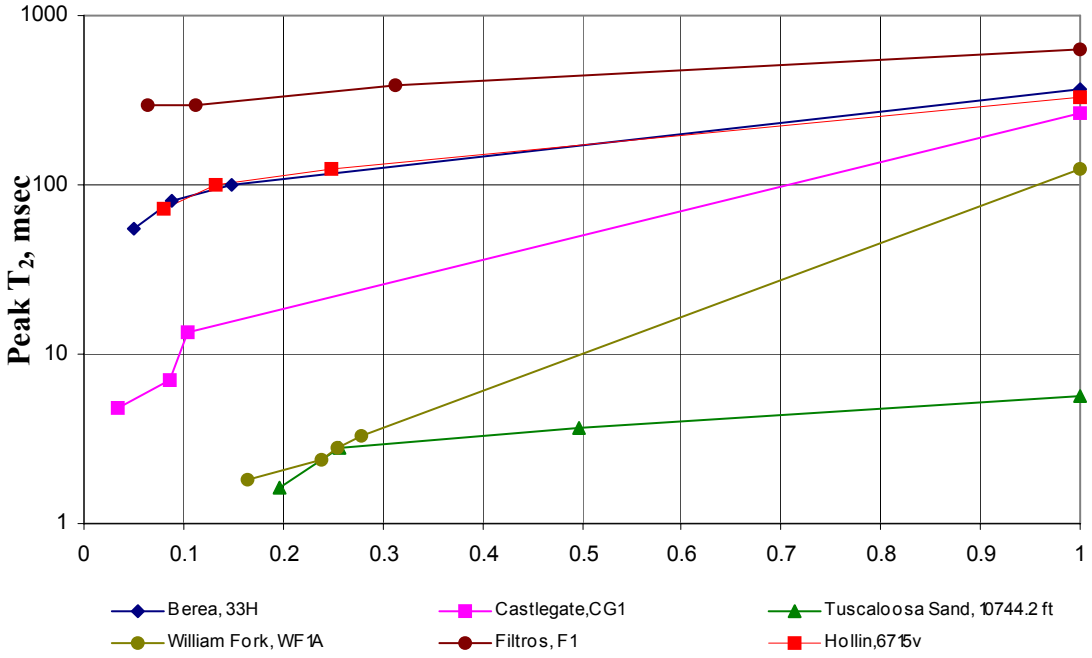

Figure 4.8.15: Position of the peak T_2 time as a function of unfrozen water for six core plugs. Unfrozen water content in this case is defined as the ratio of the amplitude corresponding to the peak T_2 time after freezing and before freezing.

The observed shift in the T_2 time during freezing of the brines shows a mixed behavior. One important issue in comparing actual (**Fig. 4.8.15)** with in theory (**Fig. 4.8.14)** is the

sparseness of observation. The amount of unfrozen water reduces by half as soon as freezing initiates (**Fig. 4.7.1)**. This in part is due to our limited ability to make rapid measurement. This results in fewer data points or sampling issues. Further the T_2 values are absolute in nature. **Fig. 4.8.16** is a crossplot between the ratio of peak T_2 (partially frozen) to peak T_2 (unfrozen) as a function of peak unfrozen water content (ratio of the peak NMR amplitude after freezing and before freezing). Points are plotted for both theoretical and observed values.

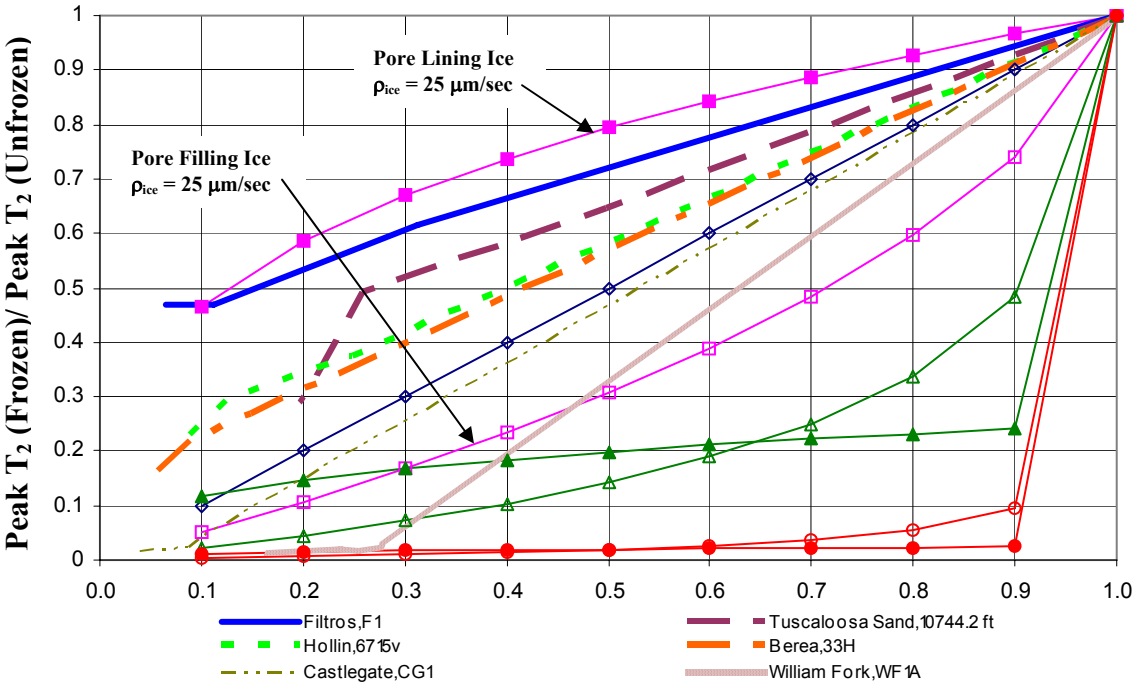

Figure 4.8.16: Ratio of the peak T_2 time between partially frozen and unfrozen is plotted across fraction of peak unfrozen water. The ratio of the theoretically estimated T_2 time is represented as blue diamond (ρ_i = 0, hollow), pink squares (ρ_i = 25, solid & hollow), green triangle (ρ_i = 100, solid & hollow) and red circle (ρ_i = 1000, solid & hollow). Solid represented pore lining ice while hollow represented pore filling ice. The ratio of the observed T_2 time shows a mixed behavior.

With exception of the William Fork, WF1A, the profile of the ratio of T_2 time and fraction of unfrozen water content lies between the two end members defining completely pore lining and pore filling with a surface relaxivity of ice similar to that of the matrix

i.e., $\rho_i \approx \rho_{ma}$. This suggests that the ice cannot have a very large surface relaxivity nor can it be completely pore filling or pore lining. The T_2 distribution retains the shape even after freezing has initiated in all of the six core plugs (see **Fig. 4.5.2 - 4.5.7**). As noted earlier (**Fig. 4.5.8**), all the pores are not completely filled with ice. The presence of unfrozen brine throughout the porous network and similarity in the shape of the T_2 distribution suggested that the brine is present along the pore wall. However, for heterogeneous ice nucleation a surface is required; the mineral matrix provides these nucleation sites (refer to section 2.3.1).

Thus based on the nucleation process, shape of the T_2 distribution after freezing and relaxivity of ice, it can be concluded that residence of ice inside a pore space is somewhere in between pore lining (required for nucleation of ice) and pore filling (similarity in the shape of the T_2 distribution) with a relaxivity of ice similar to that of the pore space. Importantly a class of models; 1) either pore filling or pore lining 2) very high or very low relaxivity are eliminated.

4.9 Thawing Process

The partially frozen core plugs were temperature cycled from -12 ^{0}C to 22 ^{0}C. The NMR spectra were acquired at temperature points along the thawing cycle. As the temperature of the circulating fluid increased the liquid filled porosity of the partially frozen core plug increased as expected. However, there exists a hysteresis between the freezing and thawing curves due to the latent heat of fusion. Thawing started immediately as soon as the temperature of the circulating fluid went up by 1 ^{0}C. Remember the freezing process produced “pure ice” by excluding salt. After the partially frozen core plug was completely thawed the NMR porosity (temperature corrected) is within ± 0.5 % of the

starting porosity (**Fig. 4.9.1**). This indicates that there is no loss of fluid during the freezing and thawing process.

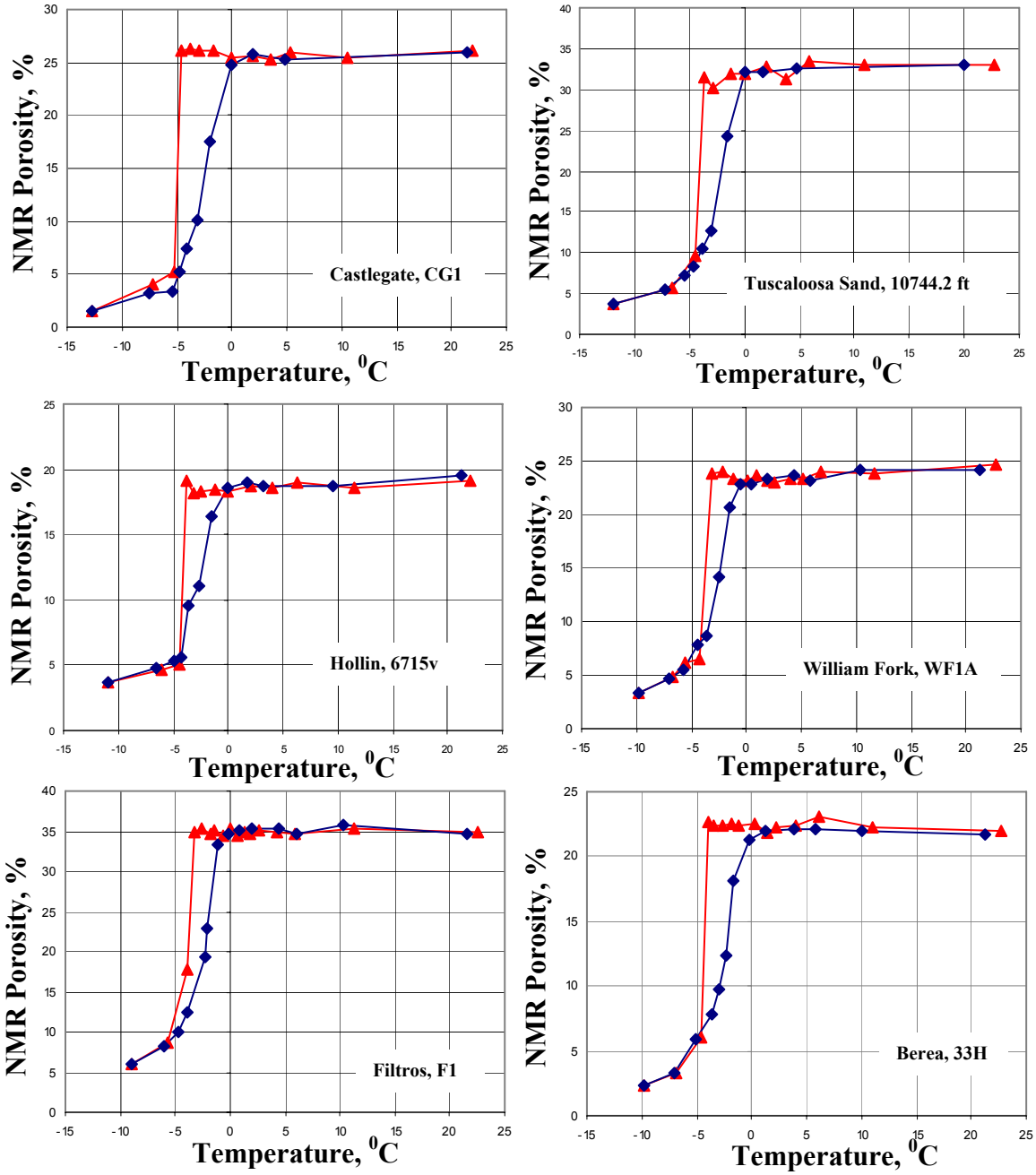

Figure 4.9.1: Estimated NMR porosity during freezing (triangle) and thawing (diamond). Presence of hysteresis between freezing and thawing is due to the latent heat of fusion or melting. Both freezing and thawing NMR porosity are temperature corrected. The error in temperature is ± 2.0 ^{0}C and in NMR porosity is ± 0.5 %.

Consistently, the NMR porosity estimated during thawing is lower than that during the freezing process before the core plug is completely thawed. Also, the gradual increase in NMR porosity during the thawing cycle is in accordance with the fact that melting is a gradual process and not instantaneous. **Fig. 4.9.2** shows the progressive change in the T_2 distribution during the thawing process of a partially frozen core plug (Castlegate, CG1). The T_2 distribution for rest of the core plugs as a function of increasing temperature from -12 ^{0}C to 22 ^{0}C are presented in **Fig. 4.9.3 - 4.9.7**. With increase in temperature, the ice in the porous medium starts to melt producing water; this is observed as an increase in the amplitude of the T_2 distribution. The increase in the amplitude is a gradual process. Along with the increase in amplitude, there is a relative change in position of the T_2 distribution along the time axis. But there exists a sudden jump in the T_2 distribution towards longer relaxation time when the temperature changes from -7.2 ^{0}C to -5.6 ^{0}C, -4.2 ^{0}C to -3.0 ^{0}C, -3.0 ^{0}C to -2.0 ^{0}C and -2.0 ^{0}C to 0 ^{0}C when all the pores are completely unfrozen. The T_2 distributions shift from smaller time to larger time as melting proceeds. This observation is true for all of the core plugs. The increase in amplitude in early time suggest one kind of model in which the small pores are unfreezing first as compared to the big pores. This implies they contain pure ice.

This raises an important question, what happened during the freezing process. As soon as a stable nuclei of ice forms, more than 50% of the pore water freezes immediately (experimental limitation). The T_2 distributions of all six core plugs during freezing suggest (**Fig. 4.5.2 - 4.5.7**) that the contribution the smaller pores did not change even after 50% of the pore water froze.

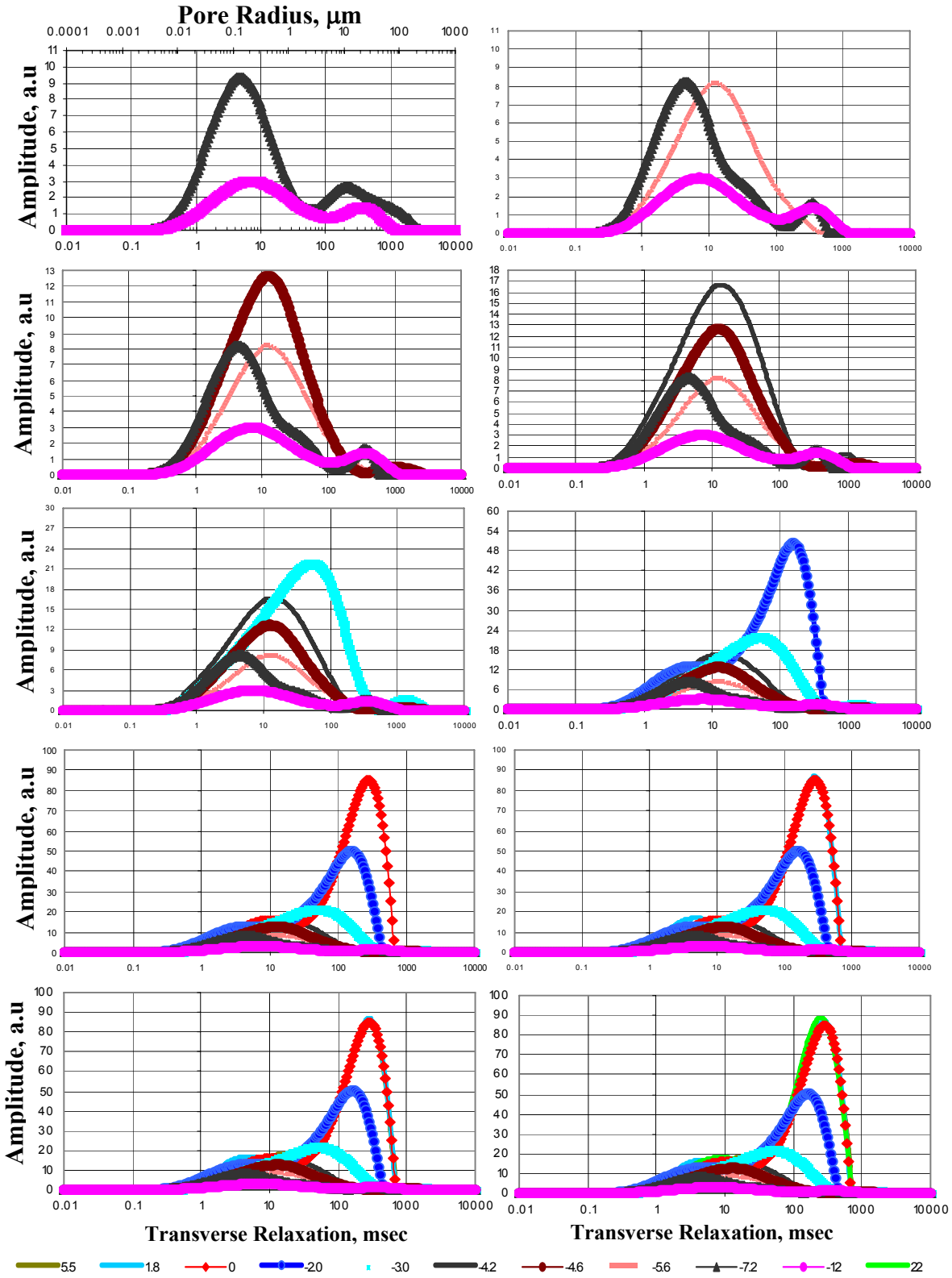

Figure 4.9.2: NMR T_2 distribution during the thawing process of partially frozen core plug (Castlegate, CG1). With increase in temperature there is an increase in the amplitude due to melting of the ice as well as a frequency shift in the T_2 distribution. The secondary X axis is same for all the distributions.

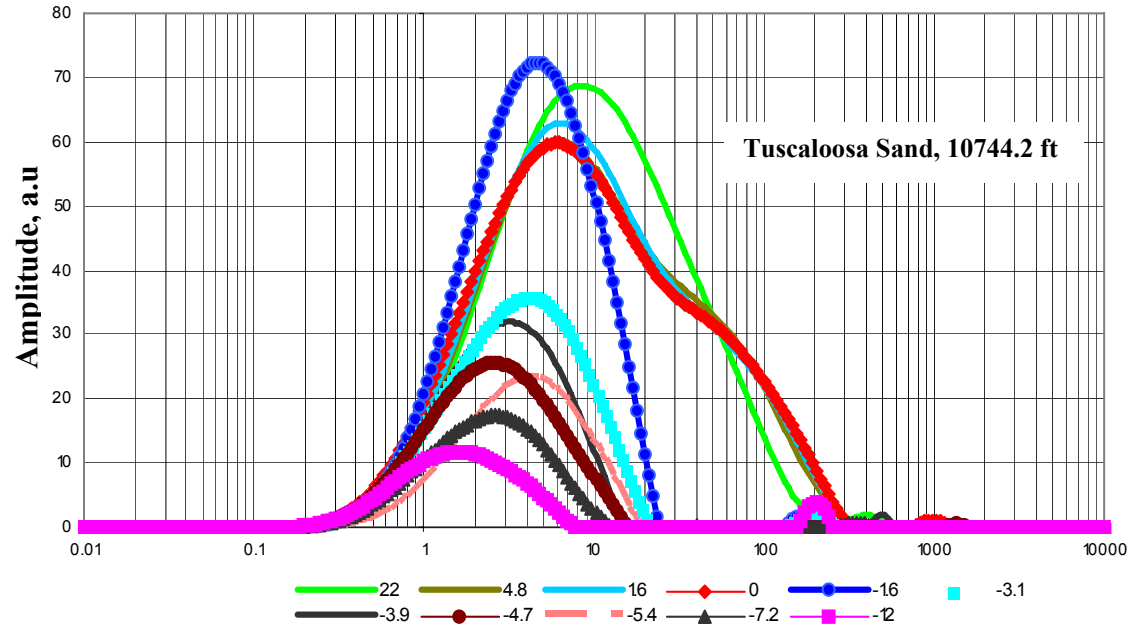

Figure 4.9.3: NMR T_2 distribution during the thawing process of partially frozen core plug (Tuscaloosa Sand, 10744.2 ft). With increase in temperature there is an increase in the amplitude due to melting of the ice as well as a frequency shift in the T_2 distribution. The equilibration time at each temperature is 2 hours.

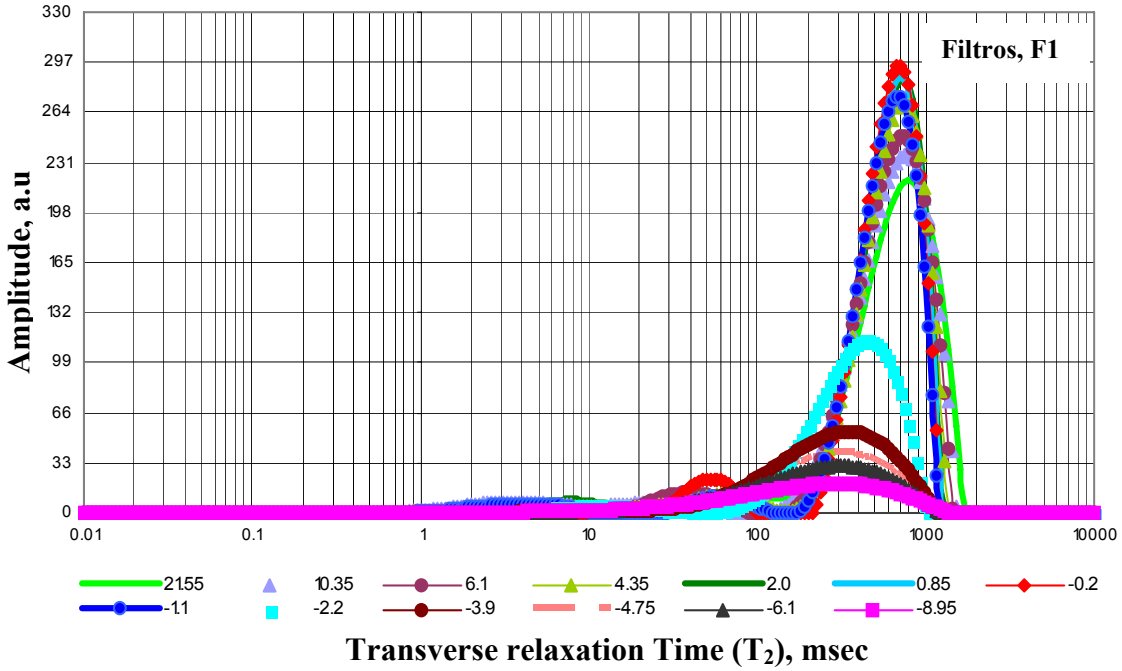

Figure 4.9.4: NMR T_2 distribution during the thawing process of partially frozen core plug (Filtros, F1). With increase in temperature there is an increase in the amplitude due to melting of the ice as well as a frequency shift in the T_2 distribution. The equilibration time at each temperature is 2 hours.

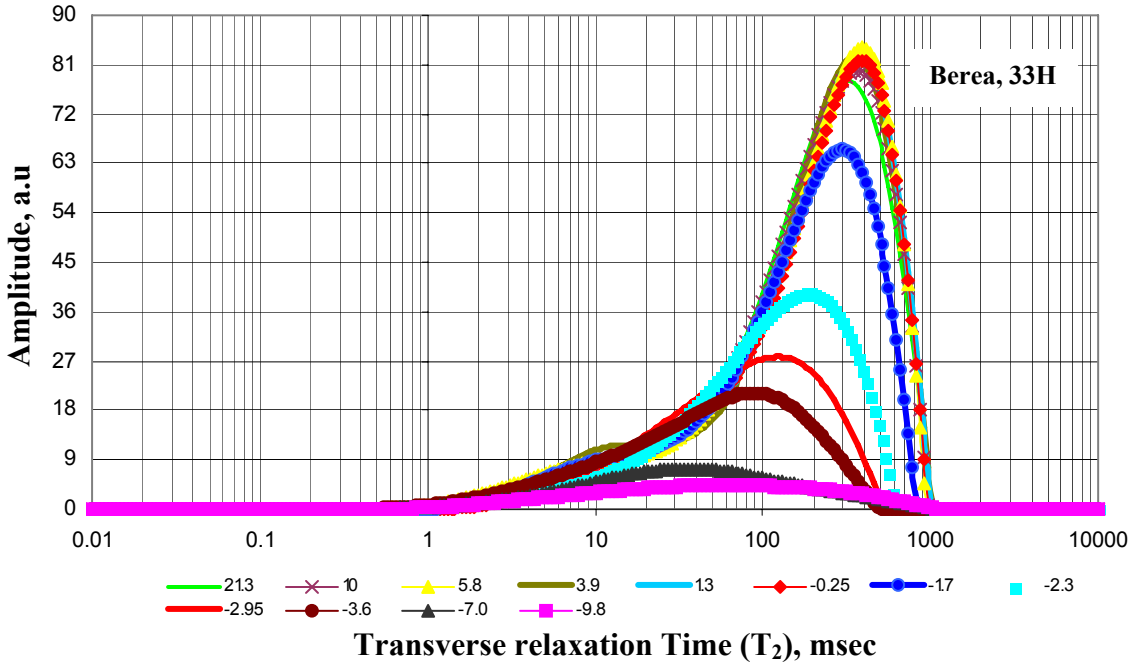

Figure 4.9.5: NMR T_2 distribution during the thawing process of partially frozen core plug (Berea, 33H). With increase in temperature there is an increase in the amplitude due to melting of the ice as well as a frequency shift in the T_2 distribution. The equilibration time at each temperature is 2 hours.

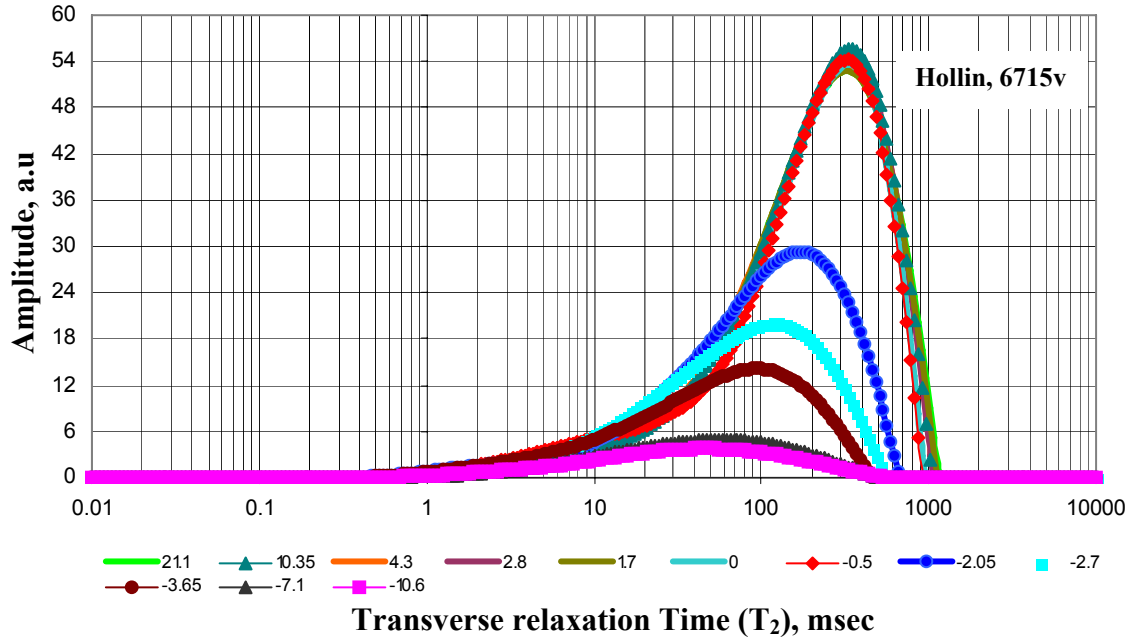

Figure 4.9.6: NMR T_2 distribution during the thawing process of partially frozen core plug (Hollin, 6715v). With increase in temperature there is an increase in the amplitude due to melting of the ice as well as a frequency shift in the T_2 distribution. The equilibration time at each temperature is 2 hours.

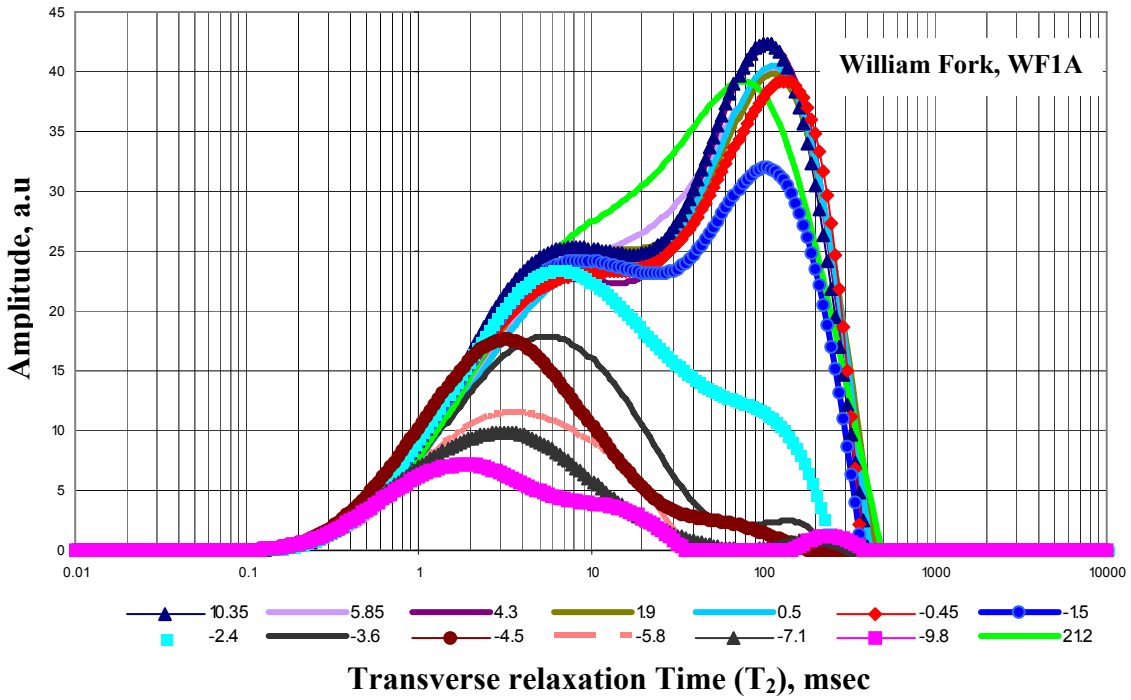

Figure 4.9.7: NMR T_2 distribution during the thawing process of partially frozen core plug (William Fork, WF1A). With increase in temperature there is an increase in the amplitude due to melting of the ice as well as a frequency shift in the T_2 distribution. The equilibration time at each temperature is 2 hours.

The resolution of the freeze-thaw experimental setup is not capable of capturing the intermediate steps, i.e., between the formation of stable nuclei and formation of 50% ice in the pore system. This suggested that the small pores are not freezing, infact they are super saturated with a very high salinity brine. However, the increase in amplitude during the thawing process (**Fig. 4.9.2 - 4.9.7**) would suggest otherwise. It appears that it is the failure to capture the intermediate steps during the freezing process which results in belief that the small pores are not frozen first. A similar observation is verified optically by Colbeck (1981). This interpretation is similar to what was concluded by Sondergeld and Rai (2007). The progressive shift in the T_2 time towards longer time suggest that the ice in small pores is melting before the ice in the big pores. This behavior is consistent in

all core plugs. **Fig. 4.9.8** shows the temperature dependence of the peak T_2 time during thawing cycle and follows the freezing curve.

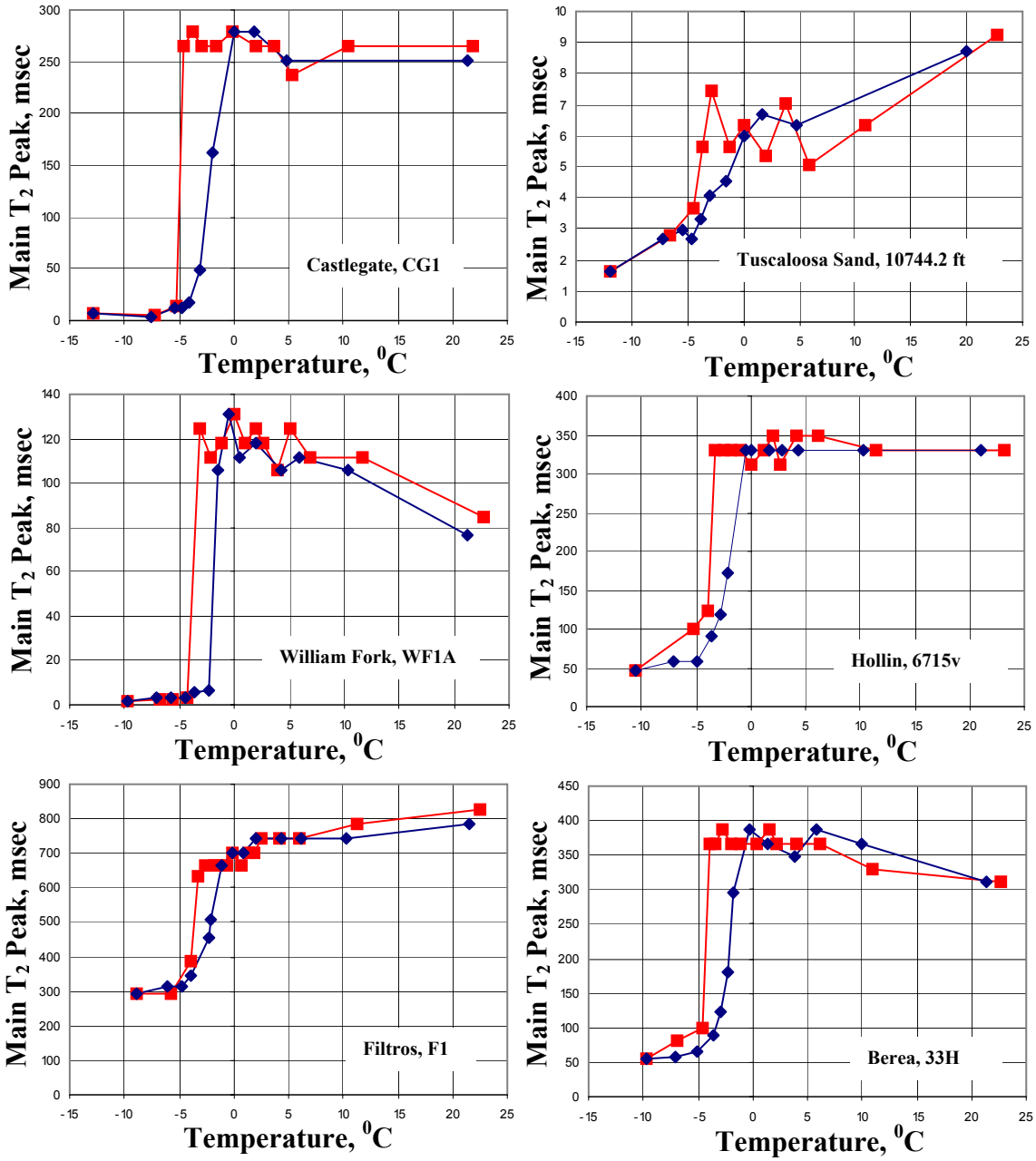

Figure 4.9.8: The presence of hysteresis in the peak T_2 time during freezing (square) and thawing (diamond) cycle is similar to what is observed in the NMR porosity plot. The wait time between each NMR measurement at a particular temperature is 2 hours.

4.10 Data Integration

In recent years considerable interest has been centered on energy issues. It was Hubbert who first predicted that the peak US oil production would occur around 1970's (Deffeyes, 2001). It was true in some way that most of the big reservoirs were discovered during that era. Using the Hubbert's analysis, energy experts such as Campbell and Laherrere (1998) Hatfield (1997) and Kerr (1998) predicted that the peak oil production will be seen during 2004-2008. Whether it was Hubbert or Campbell and Laherrere, 1998 or Hatfield, 1997 or Kerr, 1998, there is a growing concern related to supply of fossil fuels primarily raised as a consequence of the increasing gap between supply and demand and geo-politics. In view of the mounting energy requirements, oil companies are focusing more on unconventional resources such as heavy oil, tar sand, tight gas, coal bed methane, oil shale, shale gas, and oil and gas fields in Artic region and gas hydrates.

For the past few decades NMR has been extensively used in the oil and gas industry to answer key questions related to exploration and production. The advantage of NMR over other logging tools is its negligible sensitivity to matrix properties and its fluid dominated sensitivity. However reservoirs in the Artic and certainly gas hydrate differ from conventional reservoirs in that they contain ice in the pores. The addition of ice in the system complicates the interpretation of the result obtained from the commonly used exploration tools such as acoustics (Sondergeld and Rai, 2007), electrical and nuclear. This is not only important for porous media in the permafrost region but also important for the analyzing unconsolidated cores (Torsaeter and Beldring, 1987) which are preserved by means of freezing. Crystallization of liquid water into ice initiates with the formation of a stable nuclei. The nucleation can be either homogeneous or heterogeneous.

The formation of ice in a porous network is a heterogeneous process due to the presence of a nucleating agent such as pore walls, impurities, surface roughness, etc. Bulk water freezes at 0 ^{0}C at 1 atm. The same water present inside a capillary will be super cooled before it starts to freeze. Further if the water is saline in nature i.e., brine the freezing point is further depressed and the depression is governed by the concentration of the salt present in the water. The shape of the ice is according to the shape of the confining surface (Colbeck, 1981).

The presence of ice in the system raises two important question; 1) Are the big pores or the small pores freezing first, and 2) where does the ice resides in a pore i.e. pore filling or pore lining/grain boundary? From an exploration and production standpoint answers to these questions can have a significant economic impact. The total pore volume of hydrocarbon present in a porous media is determined by:

$$HCPV = (1 - S_w)\phi AH \quad \{4.15\}$$

where HCPV is the hydrocarbon pore volume, ϕ is the porosity, A is the area and H is the height. If ice forms preferentially in big pores, the amount of HCPV will reduce more than if ice forms preferentially in small pores. Therefore the economic evaluation of an oil or gas field depends upon where the ice or hydrate occur. Also, the presence of ice will affect the compressibility of the rock and hence the seismic velocities. Ice coating the grain boundaries will act as a cement and support the matrix while if ice resides in the center of the pore it will not influence the stiffness. These considerations are important in evaluating prospects and stability of the facilities in cold regions. A number of researchers (King, 1977, King et al., 1988, Pandit and King, 1979, Sondergeld and Rai, 2007 and Timur, 1968) have investigated the effect of ice in naturally occurring reservoir

rocks undergoing freeze-thaw cycles using acoustics or a resistivity techniques. Very few studies (Kleinberg et al., 2003a, Kleinberg et al., 2003b and Kleinberg and Griffin, 2005) have been carried out using NMR as a tool to verify these processes. These NMR based studies were carried out during the thawing process of the core (sandstone and mudstone) recovered from North Slope of Alaska using a logging tool.

The characteristic T_2 time for the ^1H atom present in ice is approximately 17 μsec (Okada et al., 2002). At 2 MHz resonant frequency, ice is invisible to the low frequency NMR spectrometer resulting in reduction of the net integrated amplitude. Both laboratory and logging tools operate at this frequency. When the system is completely filled with ice, the raw NMR data is just noise (**Fig. 4.10.1**).

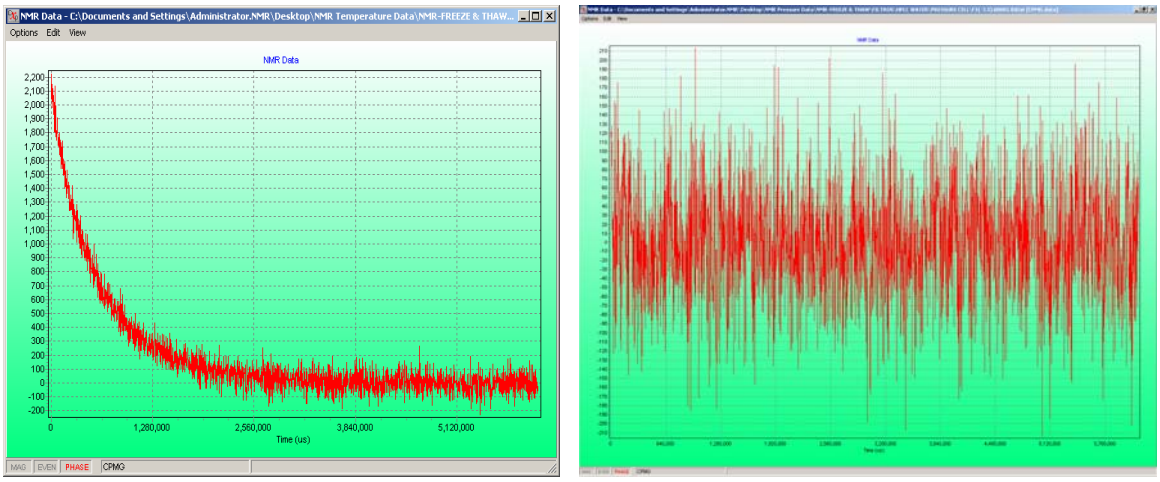

T = -4 ^{0}C **T = -7.5 ^{0}C**

Figure 4.10.1: Raw NMR signal for partially frozen (T = -4.0 ^{0}C) and completely frozen (T = -7.5 ^{0}C) Filtros core sample. At 2MHz resonating frequency, the spectrometer is unable to resolve the very short relaxation time of proton in ice crystals (T_2 ~ 17 μsec). Number of scans = 50.

The T_2 distribution obtained in a NMR log can be mapped to pore size distribution if surface relaxivity is known and the relaxation is in fast diffusion limit. This provides an advantage over velocity and resistivity methods as it provide more information about pore size distributions. Thus the fluid can be classified by location in the pore space, i.e.,

small pore or big pores. A cartoon (**Fig. 4.10.2**) shows how the ideal T_2 distribution will look if small pores freeze first (**A**) or freezing initiates in big pore (**B**). **Eqn. 2.18** describes mathematically the T_2 distribution for an ice bearing rock after subtracting the bulk relaxation effect.

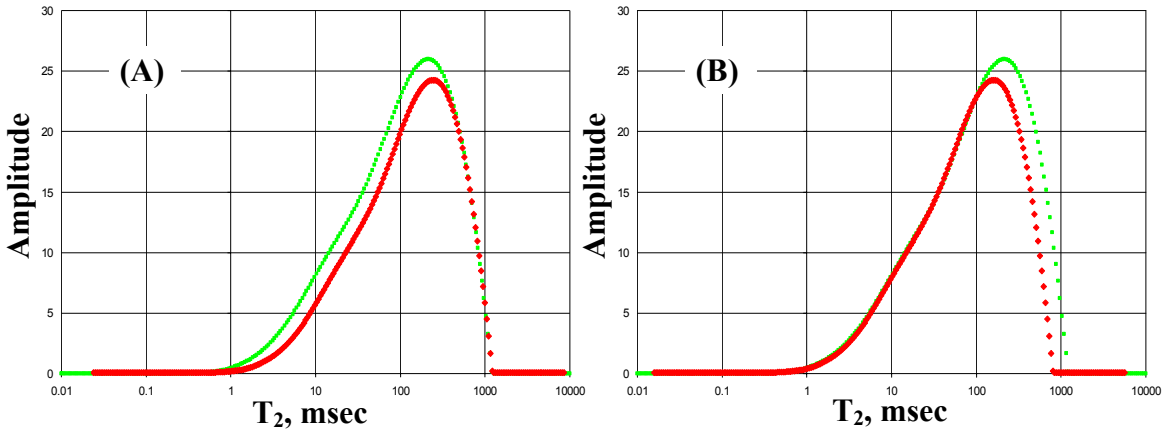

Figure 4.10.2: Ideal Case - NMR T_2 distribution of a 100% saturated porous media before (square) and after freezing (diamond) initiates. (A) Indicates freezing initiate first in small pores (B) indicate freezing initiates first in big pores.

Sondergeld and Rai (2007) suggested from their velocity and resistivity measurements that water in small pore freezes first which is contradictory to popular belief (King, 1977; King et al., 1988; Pandit and King, 1979; and Timur, 1968). The presence of higher water content in clay and silt under subzero conditions made the above researchers believe that the big pore freezes before the smaller ones. King (1977), King et al., (1988), Pandit and King (1979) and Timur (1968) observed that there is an increase in compressional wave velocity when the brine present in the pore system is transformed into ice. They also observed an increase in resistivity due to the decrease in conductive fluid. Sondergeld and Rai (2007) also observed a similar behavior in the compressional wave velocity and resistivity. Sondergeld and Rai (2007) also measured the shear wave velocity. The shear wave velocity also increases with transformation of pore fluid into ice. However the change is greater than that of compressional wave velocity. Shear wave is more

dependent on crack and small pores as compared to compressional wave velocity. One possible explanation is that the small pore or the cracks freeze before the big pores.

In this freeze-thaw study the change in amplitude of the NMR T_2 distribution at the early times is very small even after more than 50% of the pore water freezes (**Fig. 4.5.2 - 4.5.7**). In all of the core plugs the contribution from the early time either remains same or changed (increase/decrease) slightly even at lowest possible temperature (~-10 ^{0}C). As noted earlier (**Fig. 4.5.13**), all the pores are not completely frozen i.e., brine with salinity greater than 25,000 ppm is present in the entire porous network. Further the shape of the T_2 distribution remains similar even after pore water has partially frozen. This is probably due to the presence of water lying next to the grain boundaries. The presence of water next to the grain boundaries will result in an increase of the amplitude of the T_2 distribution at the early time. But in all the spectra there is no relative amplitude increase at smaller T_2 time. This could only happen when the smaller pores are freezing first. Also during the thawing process, it was consistently observed that the small pores are unfreezing first before the big ones (**Fig. 4.9.2 - 4.9.7**). The gradual shift in the peak T_2 time from smaller value to larger value is direct evidence that the small pores are thawing before the big ones. To better understand the correlation between T_2 distribution and pore dimension, an independent pore dimension measurement can be considered. The instantaneous freezing of the brine results in our instability to adequately monitor the intermediate steps during the freezing process. The thawing experimental equivocally verifies the indirect observation from the freezing experiment.

The formation of ice in a porous network is a heterogeneous nucleation process. The mineral matrix provides the surface for heterogeneous nucleation. The presence of

high salinity brine next to the grain surface suggests that the ice is not continuous along the pore wall. Thus the two assumed models pore lining or pore filling (**Fig. 4.8.13**) regarding the residence of ice represent the ideal case. As soon a stable embryo of ice forms on the mineral matrix, the pore water starts to freeze. The freezing continues until the salinity of the brine increases enough to depress the freezing point of the remaining brine. The presence of the unfrozen brine next to the grain surface results in the retention of the similarity in the T_2 distribution before and after freezing (**Fig. 4.5.2 - 4.5.7**).

In summary the freeze-thaw behavior of naturally occurring reservoir rocks using a 2 MHz NMR spectrometer and a CPMG pulse sequence technique is performed for the first time. The effect of temperature on NMR amplitude and transverse relaxation time is not negligible. The observed amplitudes need to be corrected using Curie's law. The observed shift in the transverse relaxation time corresponds to the temperature dependency of the surface relaxivity. Similarity in surface relaxivity between ice and pore suggest that for ^1H atom partially frozen rock is same as unfrozen except in terms of pore dimension. The progressive shift in the T_2 time towards longer time clearly indicate that the ice in small pores is melting before ice in the big pores. There is always a fraction of the pore fluid which remains unfrozen down to -12 ^0C. The residence of ice inside a pore space is in between pore lining and pore filling.

4.11 Conclusions

The major conclusions of this study are:

1. Temperature has a substantial effect on the ^1H NMR response in a saturated porous media. Uncorrected temperature dependent net magnetization over the

range of 22 ^{0}C to -12 ^{0}C results in an over estimation of porosity by as much as 4%.

2. The observed frequency shifts in peak T_2 times during thermal cycling are attributed to the temperature dependency of surface relaxivity.
3. All pores are not completely frozen even down to -12 ^{0}C. Unfrozen brine is present throughout the porous network. Amount of unfrozen water depends on the initial salinity of the brine and final temperature of the experiment. The volume of unfrozen water can be best describe with an exponential function (Civan, 2000)
4. Hysteresis exists between the freezing and thawing curve due to the latent heat of fusion. The progressive shift in the peak T_2 time towards longer time clearly indicate that melting is a gradual process, and suggest ice in small pores are thawing first relative to the big pores. Freeze on the other hand, is a nucleation process having a very rapid onset once initiated.
5. Exact definition of which part of the pore system freezes first illusive. Thawing clearly indicates that small pores thaw first. When they froze is not clearly determined.
6. Indirect evidence suggested that the surface relaxivity of ice (ρ_i) is similar to that of the matrix.
7. Ice preferentially fills the center of the pore space with unfrozen brine of higher salinity present along the pore wall.

CHAPTER 5 – NMR MEASUREMENTS ON SHALE PLUGS AND CUTTINGS

5.1 Abstract

Nuclear magnetic Resonance (NMR) has being widely used in petrophysical evaluation of conventional reservoirs. This experimental study is designed to evaluate the possibility of extracting petrophysical information such as porosity and bound water from shale and shale cuttings

Shales not only act as a source and seal but also act as reservoirs e.g. Barnett, Caney, Fayetteville, etc. Without direct measurement of R_w standard resistivity analysis in shale is impossible. NMR techniques, however are appealing because the response is affected by the pore fluid, and the fluid need not be sampled. In this study NMR measurements were performed on six different shale plugs. The six unpreserved shale plugs were then crushed into small pieces to represent drill cuttings. The estimated NMR porosity from the cuttings was consistently lower than plug porosity but with in +/- 1.0 p.u. The estimated water saturation from cuttings is about 60% lower than that of corresponding plug. This difference may also depend on cutting size. This result in lower clay bound and capillary bound water saturation. Ninety percent of the water present in the six shale plugs/cuttings is bound to the surface either as structural or capillary water. A drawback of the study is the use of unpreserved core plugs which leaves uncertainty in the absolute values of NMR porosity and bound water estimated. Out of six cuttings, five were then immersed in water to mimic actual drill cuttings from well site and NMR spectra were acquired. There is an increase in the apparent bound water saturation. It is observed that the T_2 distribution is a combination of pore structure inside the shale

samples and the water trapped between the cuttings. It is very difficult to separate the two responses. The oil immersed cutting show a visible difference between pore water and bulk oil, but the effect is dominated by bulk oil. However because of the large separation in water and oil T_2 response, porosity and S_w estimates could be obtained from oil immersed cutting.

5.2 Introduction

In an exploration situations operators try to answer two important questions as quickly as possible: first, reserve (porosity, saturation, aereal and vertical extent); and second deliverability (permeability, etc.) (Egermann et al., 2005). Well logs provide some of the vital information such as porosity, saturation and thickness along the well which can then be mapped or extrapolated to the whole field. However the wellbore is an anomaly. The borehole suffers from invasion, formation damage, temperature perturbation, and stress concentrations. For effective reservoir delineation it is necessary to have the wireline log data calibrated with the core data. Core characterization is an important intermediate step towards better understanding the reservoir. Apart from many advantages core characterization involves fundamental issues such as coring which is time consuming and expensive. To reduces expense operators try to avoid taking core or sidewall plugs and deal with cuttings. This leads to large uncertainty in the reservoir evaluation and future production forecasts. As an alternative, drill cuttings which are abundant and cheap and can potentially provide information regarding the formation being drilled. But the problems with the cuttings include small size, uncorrected depth registration, and contamination by drilling fluids. In spite of all the limitations, drill cuttings can be

calibrated against the core measurement. Once calibrated, response from the cuttings can be used for calibrating logs. Log calibration will result in reduction of uncertainty in reservoir evaluation as well as economic benefit. This study evaluates the estimation of NMR porosity and bound water on shale plugs and cuttings. The cuttings obtained in the field are always coated with either water based or oil based mud. We therefore immersed our cuttings in water and oil and performed NMR measurements.

5.3 NMR Signature of the Background

Shale has characteristically very low permeability on the order of nanodarcies, and very low porosity compared to normal sedimentary reservoir rocks. The low porosity results in a very small volume of pore fluid present in the porous network. The small amount of pore fluid is sometimes comparable to that present in the background, i.e., room humidity. This raises an important question; whether the response of NMR is from the core sample/cuttings or background. To improve the signal to noise (S/N) ratio for the low pore volume measurement, the number of scans used for this study is 10000. The time required to perform each measurement is approximately 2.5 hrs due to the large number of scans. To see the effect of the room humidity, an NMR measurement was performed with only glass core holder inside the 2 MHz MARAN Ultra[5] spectrometer. The raw decay and the T_2 distribution of the background with the glass core holder inside the spectrometer is shown in **Fig. 5.3.1**. The noisy raw data and very small amplitude indicates the negligible effect of background.

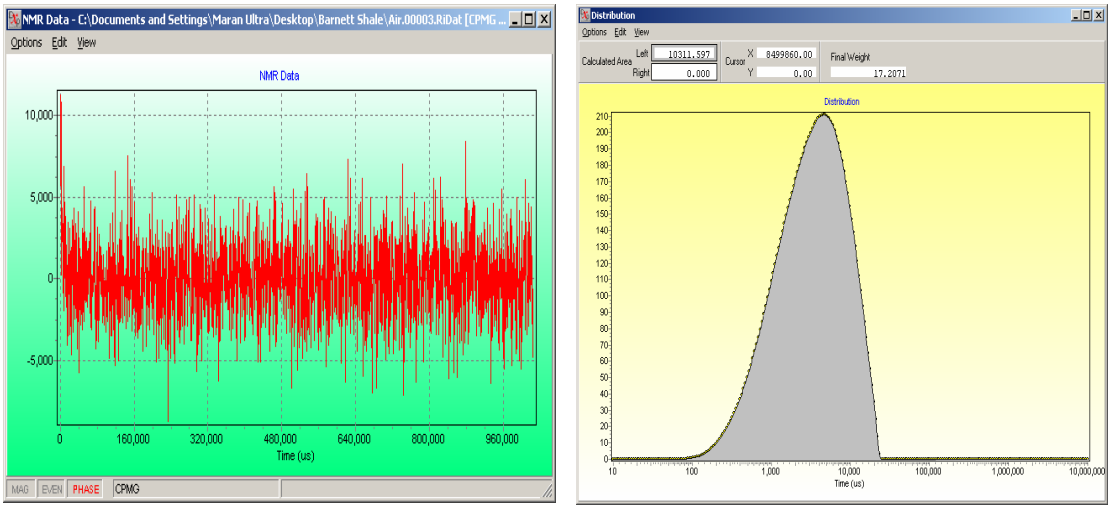

A **B**

Figure 5.3.1: (A) Raw NMR background signal without any shale sample. (B) T_2 distribution of the raw signal. The noise present in the raw signal indicates the effect of background is small. The calculated volume of fluid is 0.005 cc which is almost negligible. No. of scans is 10000.

5.4 NMR Estimated Porosity

Based on the average grain size, sediments and clastic sedimentary rocks are classified as conglomerate, sandstone, siltstone and shale. Of these four types, shale has the smallest grain size (< 2μm) causing it to have the highest surface to volume (S/V) ratio. NMR T_2 relaxation in shale is predominantly surface relaxation ($T_{2Surface}$). Surface relaxation is inversely proportional to surface to volume ratio (**Eqn. 2.7**) i.e., higher the S/V ratio, smaller is the corresponding T_2 time. This implies that all the water associated with the shale relaxes at a much earlier time then say in a sandstone. The acquisition parameters need to be adjusted to capture this very fast decay water response. The inter echo spacing (TE) is set at 0.30 ms to capture the water signature. To improve the signal to noise (S/N) ratio the number of scans required will be greater as compared to that of sandstone. To optimize the number the scans required, NMR spectra were acquired for different number

of scans. **Fig. 5.4.1** shows the plot of NMR porosity as a function of number of scans. Between 8000 to 12000 scans the porosity is constant.

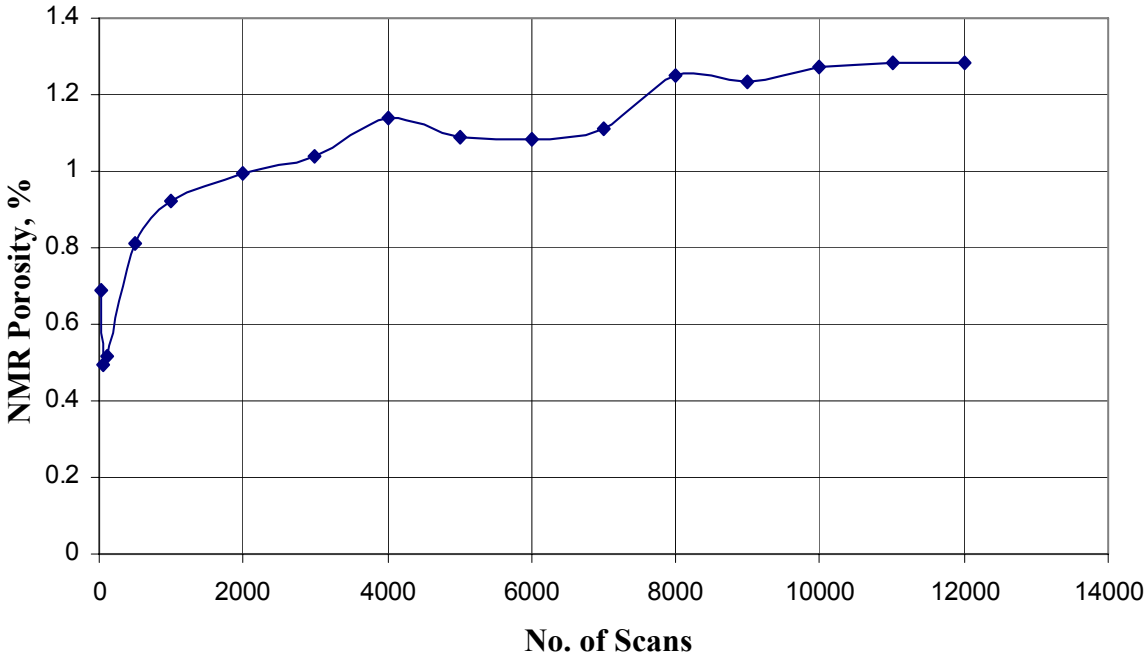

Figure 5.4.1: Estimated NMR porosity as function of number of scans. After 8000 scans the porosity is almost constant.

Further, the plugs will be crushed to form cuttings which will be variable in size. To improve the signal averaging the number of scans used for this study is 10000. **Fig. 5.4.2** shows the raw decay and the T_2 distribution of a shale sample (X546.2 ft). Martinez and Davis (2000) performed measurement on shale samples which act as seals. The shale samples were rich in clays and quartz. The interecho spacing (TE) was 0.10 msec. The T_2 distribution observed by Martinez and Davis (2000) on their shale samples have similar three characteristics peaks as seen in **Fig. 5.4.2 (B)**.

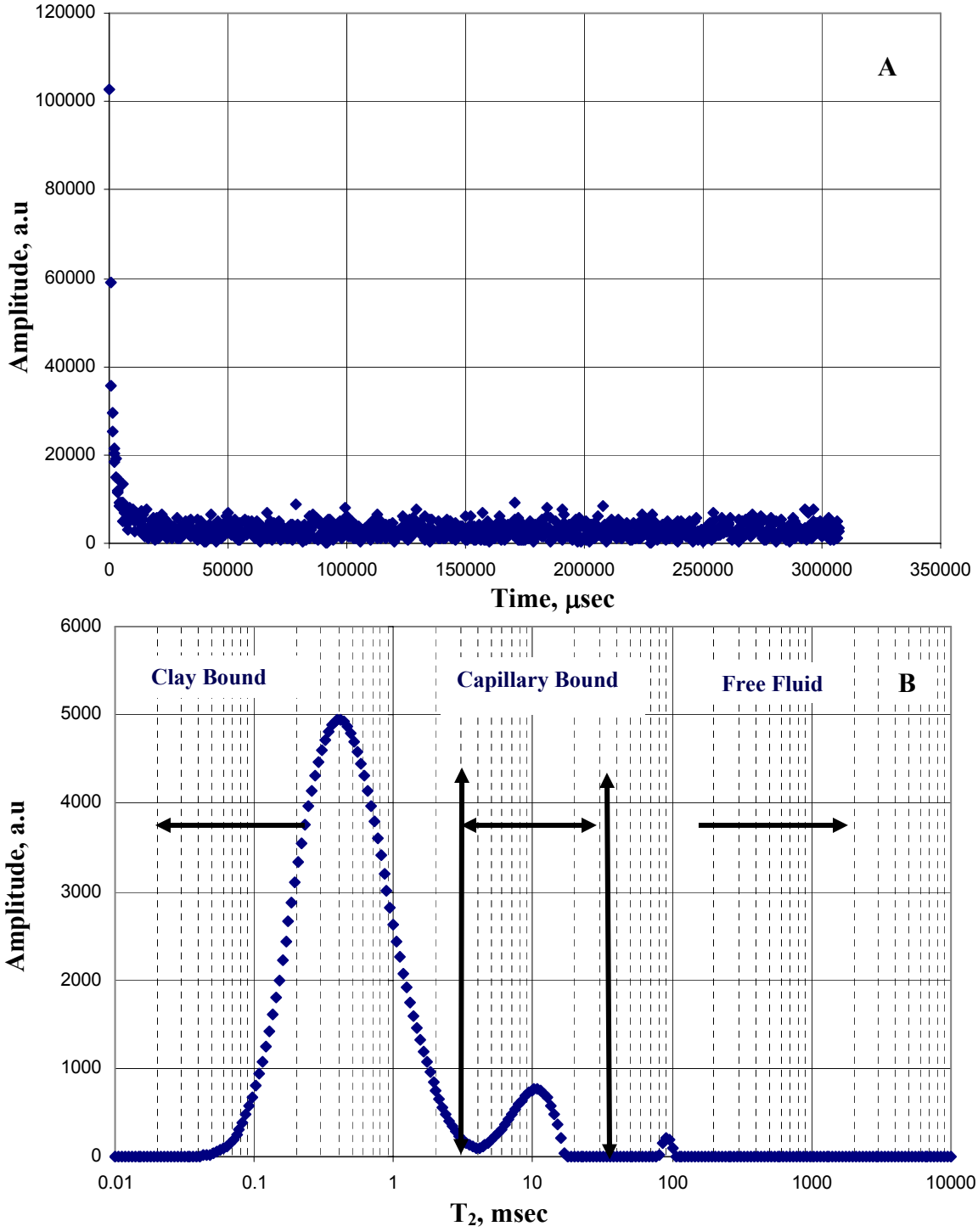

Figure 5.4.2: (A) Raw NMR signal of a shale plug sample (X546.2 ft). (B) T_2 distribution of the raw signal. The calculated volume of water present is 0.19 cc. The total amplitude of the T_2 distribution of the plug is almost 35 times that of the background (see Fig. 5.3.1). This gave us a confidence that NMR is seeing the pore fluid and is not affected by background moisture. The fluids are bound either capillary or structurally in the clays.

The T_2 distribution is based on a fit to 256 exponentials. The NMR estimated porosity (ϕ_{NMR}) for the six shale plugs are range from 1.12 % to 2.11 % (± 0.06 %) which is very small as compared to traditional sandstones. Three different relaxation regions are characterized as free fluid, capillary bound and clay bound water based on T_2 cutoff of 33 msec and 3 msec respectively. The core plugs were crushed in a special crucible (**Fig. H.1**) to form cuttings. The weights before and after crushing were carefully monitored. The loss due to crushing and transportation for each of the six samples is less than 0.1 %. **Fig. 5.4.3** shows image of one of the shale sample (X749.2 ft) before (A) and after it has been crushed (B).

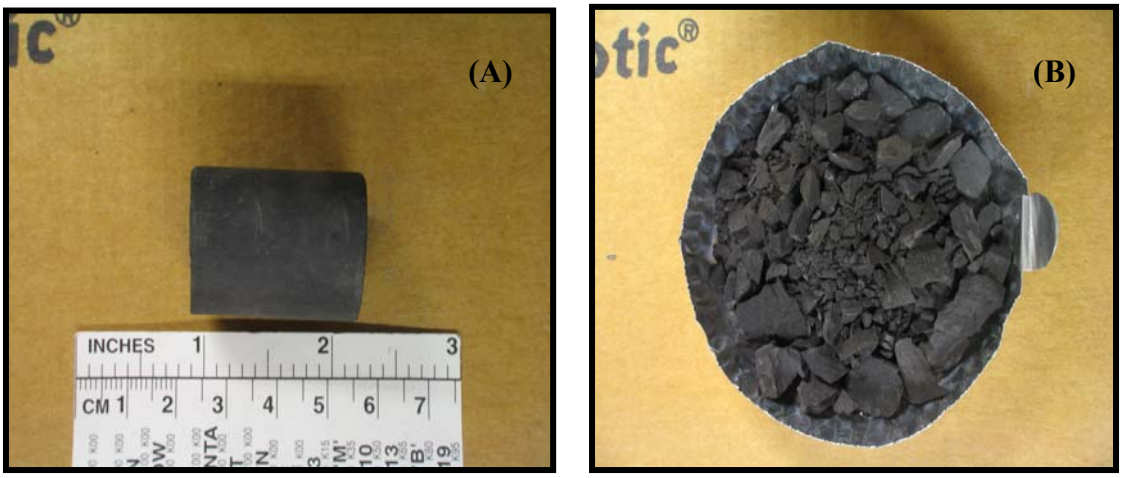

Figure 5.4.3: (A) Plug (X749.2 ft). (B) Crushed sample in the form of cuttings.

Using the same acquisition and processing parameters an NMR measurement was performed on shale cuttings. The plot of incremental porosity and cumulative porosity between the plug and cuttings is shown in **Fig. 5.4.4**. In all the six shale samples the T_2 distribution of cuttings is similar to that of the plug but with decrease in amplitude. All of the three peaks remain distinct. The decrease in amplitude reflect some mass loss and water loss. **Fig. 5.4.5** is the crossplot of NMR estimated porosity from the plugs and from the cuttings after crushing the same sample.

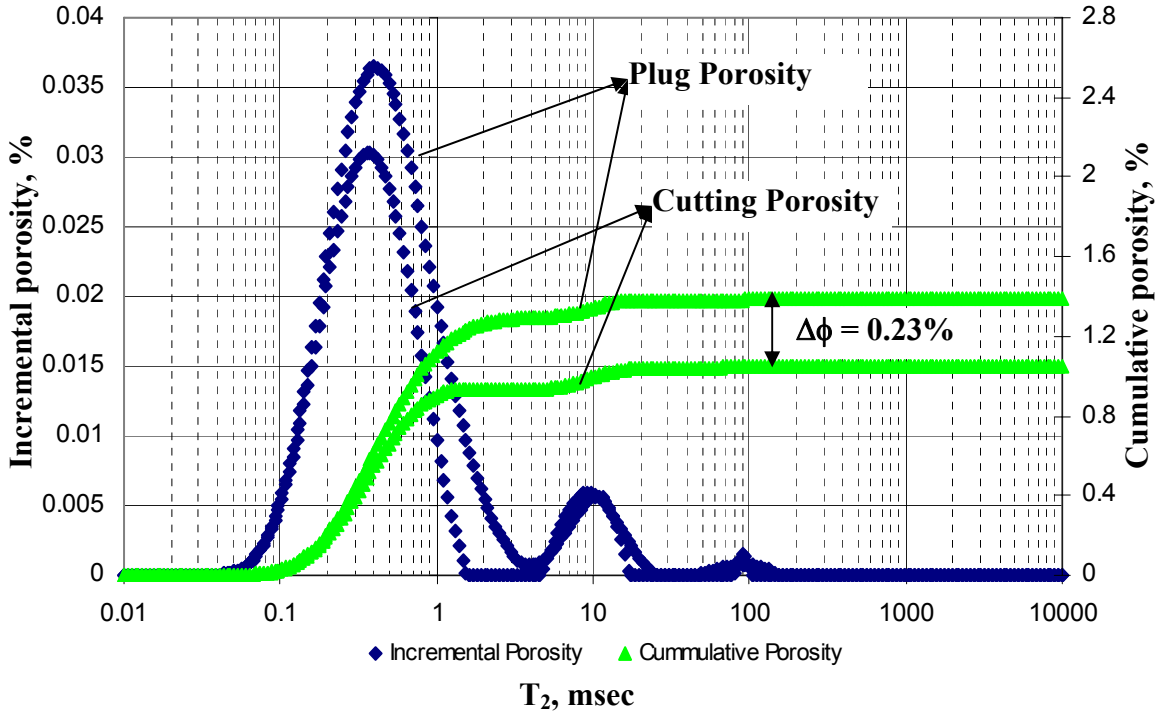

Figure 5.4.4: Comparison of incremental and cumulative porosity for a shale plug and cutting from the same depth X546.2 ft. The difference in the total porosity between plug and cuttings is within +/- 0.5 p.u.

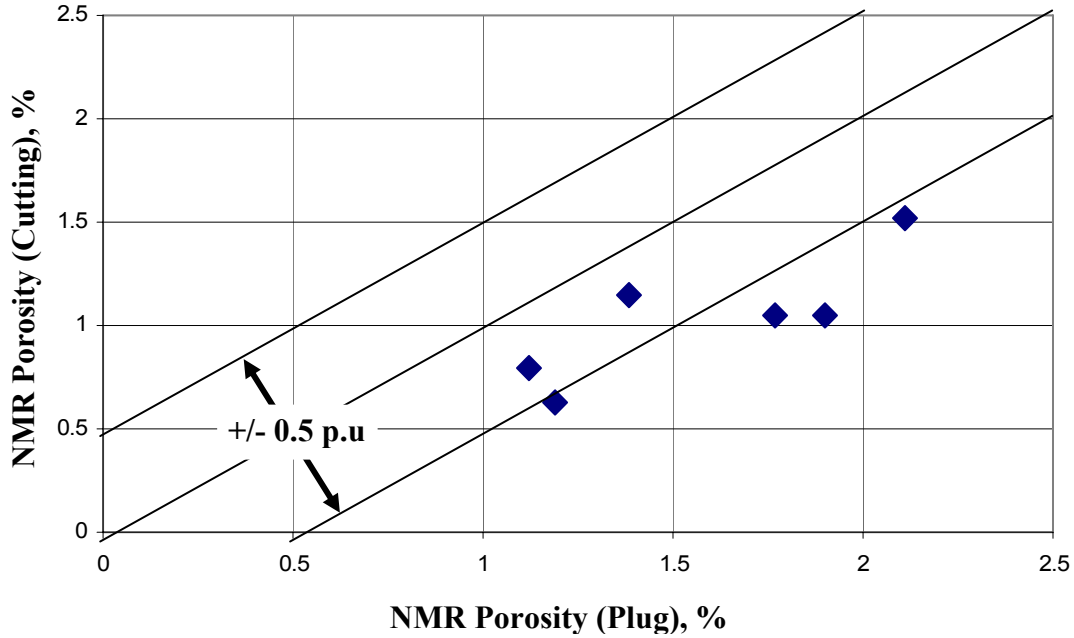

Figure 5.4.5: Crossplot of NMR estimated porosity from plug and crushed shale sample (cutting). The porosity derived from cuttings is always less than that measured on the whole plug; however the difference while systematic is still within the experimental uncertainty.

Consistently, the NMR porosity estimated from the cuttings is lower than that of the plug but within +/- 1.0 p.u. Probably the very small decrease in the porosity is due to loss of mass during crushing/transportation and/or loss of water. So, using a table top NMR at the rig site can provide similar (within the acceptable experimental error) porosity estimates from the drill cuttings. From the economic standpoint this is a huge advantage as it will save both time and expense of recovering core.

5.5 Bound Water Estimation

Estimation of bound water is a crucial step in reservoir evaluation. It is especially important when evaluating shale or shaly formation where resistivity logs give erroneous water saturation estimates. T_2 distribution is broadly classified into two region one free fluid region and bound fluid. Bound fluid comprises of capillary bound and clay bound region. Capillary bound water is due to the capillary forces while the clay bound water is the water electrostatically associated with the clay mineral, i.e. the hydration water. It is observed that water associated with relaxation time less than 3 msec is clay bound while that between 3 msec and 33 msec is considered capillary bound (Matteson et al., 2000). The plugs were crushed in a crucible (**Fig. H.1**) and then dried in a vacuum oven at 100 ^{0}C for 16 hrs to remove the free water associated with the sample (**Appendix H**). Using Low pressure pycnometer (**Fig. H.2**) the grain volume ($\sigma_{vol.} = \pm 0.002$ cc) is determined and total pore volume is calculated. Water saturation is estimated by taking the ratio of NMR pore volume to dry pore volume. Water saturation (S_w) is estimated for both plug and cuttings. **Table 8** summarizes the total porosity, NMR porosity from plug and

cutting, and the estimated S_w for all six shale samples. The error propagation for the LPP porosity estimation is also noted in **Table 8**.

S.No	Depth ft	LPP Porosity (Total), %	NMR Porosity (Plugs), %	NMR Porosity (Cuttings), %	Estimated S_w,%		
					Plug	Cuttings	Ratio Plug/Cuttings
1	X489.2	2.60 ± 0.10	2.11	1.52	81.2	58.4	1.39
2	X542.6	5.62 ± 0.04	1.77	1.05	31.4	18.7	1.68
3	X546.2	5.73 ± 0.08	1.38	1.15	24.2	20.1	1.20
4	X616.4	5.07 ± 0.08	1.38	0.79	22.1	15.6	1.42
5	X691.9	7.30 ± 0.09	1.19	0.63	16.3	8.6	1.89
6	X749.5	3.80 ± 0.03	1.90	1.05	50.0	27.6	1.81

Table 8: Summary of the porosity determined using LPP and NMR. Estimated water saturation (S_w) for both plug and cuttings.

S.No	Depth, ft	Estimated Water Saturation (S_w) ,%					
		T_2 < 3ms (Clay Bound)		3ms < T_2 < 33 ms (Capillary Bound)		T_2 > 33ms (Free Fluid)	
		Plug	Cuttings	Plug	Cuttings	Plug	Cuttings
1	X489.2	75.0	53.1	6.1	4.4	0.1	1.0
2	X542.6	28.7	16.7	2.7	2.0	0.1	0.0
3	X546.2	22.5	17.9	1.6	2.0	0.1	0.2
4	X616.4	19.9	13.2	1.9	2.2	0.4	0.2
5	X691.9	14.6	7.2	1.6	1.3	0.1	0.1
6	X749.5	45.3	24.6	4.4	2.8	0.4	0.3

Table 9: Summary of the water saturation estimated for different regimes in a T_2 distribution i.e., clay bound, capillary bound and free fluid on six different shale plugs and their respective cuttings. Note most of the water is found at less than 3msec, suggesting it is likely clay bound.

The estimated S_w is then further subdivided (**Table 9**) into clay bound, capillary bound and free fluid based on different cutoffs (Matteson et al., 2000). The estimated water saturation from the cuttings is lower than that of plugs. The decrease is because of the decrease in porosity estimation from the cuttings. The saturation is estimated by taking the ratio of the corresponding water filled pore volume to total pore volume. The estimated water saturation from cuttings is 60% lower than from the plugs. The variation in water saturation is going to overestimate the in place gas approximately by a factor of 2. This deviation is due to the slight variation in the estimated porosity from cuttings. The variability in the porosity and water saturation of the six samples from 300 ft of core suggests the core is spatially heterogeneous. NMR measurements on cuttings underestimates the water saturation. This will result in overestimation of the gas in place.

5.6 NMR of Immersed Sample

Drill cuttings from the well site are always coated with drilling fluid which is either a water or oil based mud. Out of six shale samples, five (X489.2 ft, X542.6 ft, X546.2 ft, X691.9 ft and X749.5 ft) were immersed (**Fig. 5.6.1**) in water while the sixth (X616.4 ft) one was immersed in mineral oil.

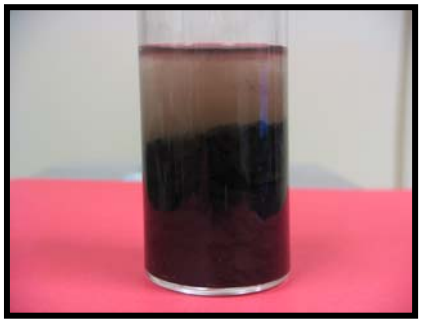

Figure 5.6.1: Crushed shale sample (X749.2 ft) in the form of cuttings immersed in water.

NMR T_2 spectra were acquired with all the shale cuttings immersed in water and mineral

oil at two different sets of acquisition parameters i.e., short TE (Inter-Echo = 0.30 msec) and long TE (2.0 msec). Short TE is needed to provide information regarding clay bound and capillary bound while the long TE provides mostly the free fluid index. **Fig. 5.6.2** shows T_2 distribution of the shale cutting (X546.2 ft) immersed in water with short TE (0.30 msec) acquired with 10000 scans.

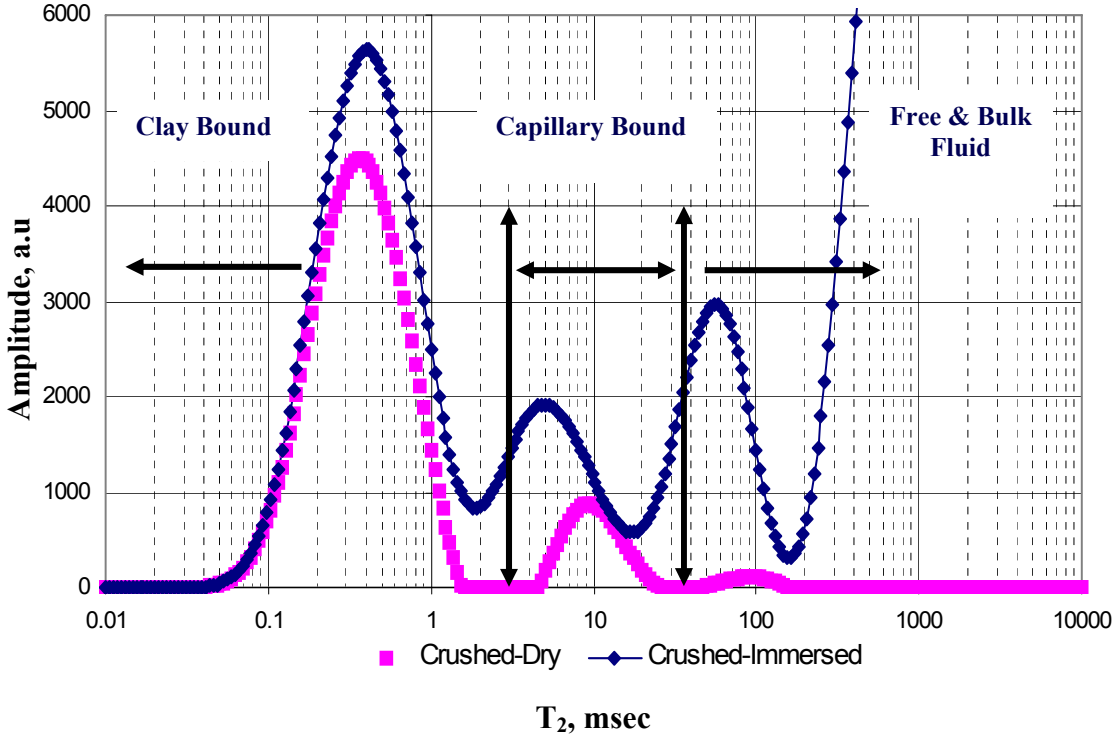

Figure 5.6.2: Comparison of T_2 distribution of immersed (water) and non-immersed shale cuttings, X542.6 ft. The NMR spectra was acquired at TE = 0.30 msec. Number of scans is 10000.

There is an increase in amplitude in all the three regions. Because the cuttings are randomly arranged and immersed in the water filled glass vial, a secondary porous structure will be generated. The NMR T_2 distribution of the immersed cuttings will encompass both the porous structure inside the shale sample and the structure generated by the stacking of the particles. It is difficult to separate these two effects. Clay bound water is an intrinsic property of the clay mineral. The increase in clay bound saturation is

due to the effect of hydration water and not related to any other porous structure generated by the arrangement of cutting within the glass vial. For the capillary bound, the water present between the cutting fragments may act as a capillary bound. The superposition of the two porous structures is due to the water wet nature of the shale sample. Bulk response of the water is mainly observed in long TE experiment. Shale sample (X616.4 ft) is immersed in oil. **Fig. 5.6.3** shows T_2 distributions of the shale cuttings (X616.4 ft) immersed in oil with short TE (0.30 msec) and long TE (2.0 msec).

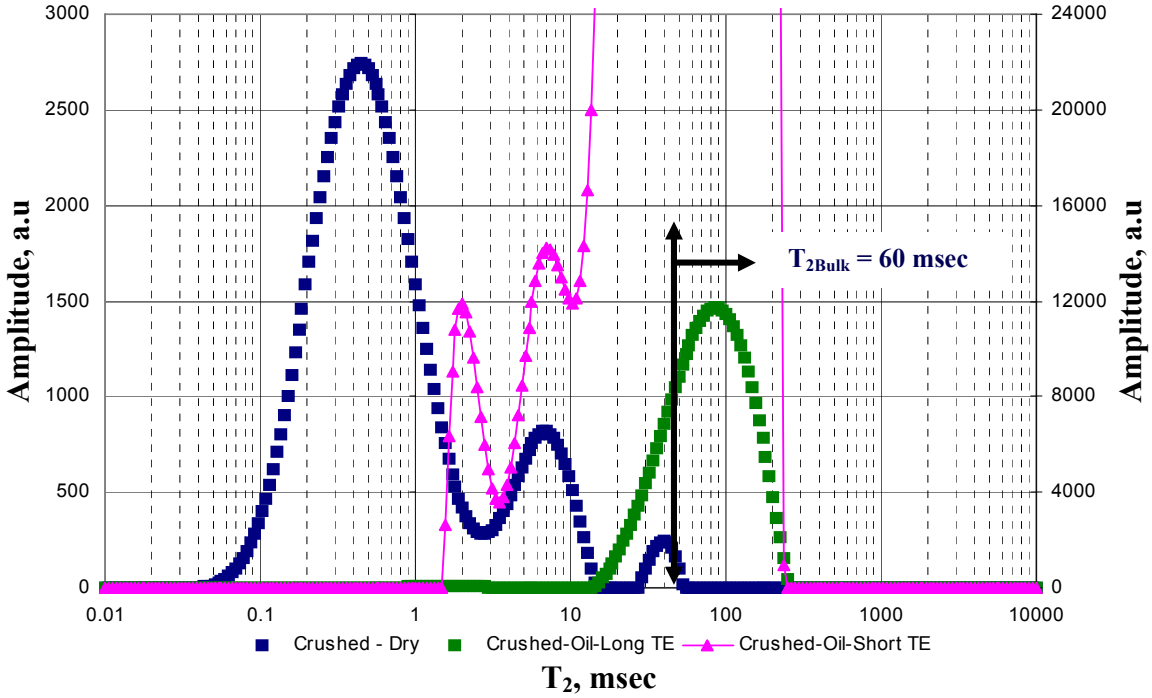

Figure 5.6.3: Comparison of T_2 distribution of non-immersed and immersed (mineral oil) shale cuttings, X616.4 ft. The NMR spectra was acquired at short TE = 0.20 msec and long TE = 2.0 msec.

The bulk relaxation (T_{2Bulk}) of mineral oil is approximately 60 msec. The T_2 distributions for short TE and long TE are dominated by the bulk effect of the mineral oil. For long TE (2.0 msec) measurement the T_2 distribution for immersed shale sample (X616.4 ft) separates out completely from the non-immersed sample. However, there exists a very

small region of overlap between immersed and non-immersed responses for the short TE (0.30 msec) measurements. The shape of the distribution in the overlap region is similar to that of non-immersed shale sample shifted to right on T_2 time scale. To better distinguish both curves, an oil whose bulk relaxation is on the order of hundreds of millisecond is required. If the shale samples are water wet, the oil present between the cuttings behaves as free fluid. This shows that if shale samples are drilled with oil, there is a good possibility of estimating of NMR porosity and bound water from the cuttings. There exists two sources of hydrogen atoms (^{1}H), one present in the water associated with shale sample and the other present in the mineral oil. The relaxation rate of both the ^{1}H is different and a subtraction of a long TE spectrum from a short TE spectrum can separate out the two fluids. The S_w estimates for each of the three regions before and after the immersion are in presented in **Table 10**.

S.No	Depth, ft	Estimated Water Saturation (S_w) ,%					
		T_2 < 3ms (Clay Bound)		3ms < T_2 < 33 ms (Capillary Bound)		T_2 > 33ms (Free Fluid)	
		Cuttings	Cuttings Immersed	Cuttings	Cuttings Immersed	Cuttings	Cuttings Immersed
1	X489.2	53.1	100.0	4.4	*	1.0	*
2	X542.6	16.7	37.4	2.0	21.7	0.0	*
3	X546.2	17.9	25.0	2.0	7.5	0.2	*
4	X616.4	13.2	13.4	2.2	*	0.2	*
5	X691.9	7.2	30.2	1.3	18.6	0.1	*
6	X749.5	24.6	55.3	2.8	51.5	0.3	*

Table 10: Summary of the clay bound, capillary bound and free fluid saturation for all the six shale samples immersed in water. * means the response is that of bulk fluid.

With the exception of shale cutting from X616.4 ft (immersed in mineral oil), there is an increase in clay bound saturation, and it is almost twice that of non-immersed sample. If the shale formation is drilled using water, it will be difficult to separate the NMR signature between porous media and the structure generated by the water are cutting fragments; however, it might be possible if the cuttings are immersed in oil based mud.

5.7 Field Application of the Study

This study is designed to answer three critical questions related to shale gas; first, the use of NMR on cuttings, second is to estimate porosity and third is to estimate bound water from cuttings. With increasing gas prices the gas shales are currently one of the hottest plays in the United States. Shales are not only considered as seals and sources but also as a reservoirs. But, there are some critical issues associated with gas shales which control economics such as low porosity, extremely low permeabilities, on the order of nanodarcies, and gas in place (GIP) estimation. Due to low (nanodarcy) matrix permeability the commercial gas production relies heavily on natural or simulated fracture systems.

Core characterization is an expensive and time consuming process. The cost of extracting a core from the subsurface can be about $10,000/ foot plus additional associated rig time. To avoid this extra cost, oil companies try to avoid coring if possible, this creates an uncertainty in the log interpretation caused by the lack of calibration. As an alternative, companies look for drill cuttings to provide reliable information with defined uncertainties. This study shows that the estimation of NMR porosity from cuttings is within +/- 1.0 p.u of the corresponding plug measurement. This definitely

defines the magnitude of the uncertainty. Operating a table top NMR machine at the wellsite can provide porosity estimation from the drill cuttings. This looks very attractive in the sense that the result from the cuttings can be calibrated with plugs retrieved from fewer wells. One of the main factors going into estimation of gas in place is the water saturation. Common logging tools such as resistivity, density, porosity, etc., are adversely affected by the presence of shale. The presence of high clay content is going to lower the resistivity which will overestimate the water saturation and underestimate the gas in place value. But in reality the formation has lower water content. Nuclear Magnetic Resonance (NMR) which is being used extensively in the conventional reservoirs for estimation of water saturation can yield a bound volume estimate in shale. The estimated water saturation from cuttings can be used to calculate the gas in place but the variations in porosity and water saturation need to be taken into consideration.

The other important question to answer is what fraction of the water present in the pore space is going to produce, i.e., estimation of the bound water index. As observed here ninety percent of the total water present in the pore space is bound water. The remaining 10% is mobile and will flow during the gas production. This is information which will be very helpful during completion design. All of the above studies are performed using samples which are at room condition and unfortunately not preserved.

In reality, the drill cuttings at the well site are always coated with water or oil based mud. It is observed that the presence of surface water on the cuttings will tremendously influence the resultant NMR signature. Clay bound water is intrinsic and will not be affected by additional water. The main effect of immersion will be on the capillary bound water. The capillary bound water will be overestimated due to the presence of water

between the cuttings fragments. In short there will be less water production than estimated. If the cuttings are immersed in pure oil, it is possible to differentiate the external oil and fluid present inside the porous medium. This is done by making measurements at two different inter echo spacings. Finally whether it is core or cuttings, they need to be preserved upon recovery.

5.8 Conclusions and Future Work

The major conclusions of this work on shale and shale cuttings are:

1. Porosity estimated from cuttings is within +/-1.0 p.u of the plug porosity, but typically less than plug porosity.
2. NMR can be used to determine shale porosity and bound water from cuttings especially if the drilling muds are oil based.
3. Ninety percent of the water present in the sample is bound water as expected.
4. Estimation of porosity and bound water from a water immersed sample is not a straight forward problem if the rock is water wet.
5. Shale samples appear to be water wet.

The following recommendations are being made for future research:

1. NMR measurement should be made on preserved core plugs and cuttings for accurate comparison of porosity and bound water estimation.
2. Use cuttings of larger dimension. Study the effect of cutting dimensions on the measurement.

CHAPTER 6 –PORE VOLUME COMPRESSIBILITY USING NMR

6.1 Motivation

In the subsurface there are two different types of stress; overburden, which is related to the weight of the overlying rock, and pore or fluid pressure. During the production phase of the reservoir, overburden stays constant while the pore pressure is reduced. This results in an increase in effective pressure. Effective pressure is the difference between overburden and pore pressure. Effective stress controls the mechanical behavior of porous materials. The increase in effective pressure results in increase in compaction of the porous reservoir rock, which could eventually lead to collapse of the pore space or subsidence. This is especially important in unconsolidated formations. Compaction is controlled by the bulk compressibility of the porous media. Bulk compressibility is a function of matrix compressibility, pore compressibility, and porosity of the rock (Collins, 1990). Matrix compressibility is very nearly a constant and depends on the mineral matrix. However the pore compressibility depends on pore pressure, pore shape, crack density and orientation which will change during the production phase. Further, the knowledge of pore volume compressibility is required to accurately estimate oil in place (Hall, 1953).

Many pore volume compressibility measurements are performed with non-polar fluids such as kerosene, mineral oil, air and N_2. The main objective of this research is to evaluate using NMR to measure pore volume compressibility in the presence of polar fluid such as brine. The advantage of NMR is its ability to sense the pore fluid directly which if fully saturated reflect pore volume.

6.2 Introduction

Pore volume compressibility controls the reservoir production and reservoir stability. Compressibility in general is defined as the change in volume of a substance due to change in pressure at constant temperature (Craft and Hawkins, 1959). Mathematically it is represented as:

$$C = \frac{1}{V}\left(\frac{dV}{dP}\right) \quad \{6.1\}$$

where C is the compressibility of the substance (1/psi), V is the initial volume before the application of the pressure, dV is change in volume and dP is the change in pressure. If the compression is carried out at constant temperature the compressibility is called as the isothermal compressibility. For a porous medium bulk compressibility is defined as (Collins, 1990):

$$C_B = (1-\phi)C_S + \phi C_P \quad \{6.2\}$$

where C_B is the bulk compressibility (1/psi), Φ is the porosity, C_S is the matrix compressibility (1/psi) and C_P is the pore volume compressibility(1/psi). Overburden stress and C_s remain constant over the life of the field. However the pore fluid pressure changes due to production causing an increase in effective pressure. The increase in effective pressure results in compression of the pore space which results in subsidence or collapse of the reservoir. Pore volume compressibility is defined as the change in pore volume per unit of pore volume per unit change in confining pressure, with pore pressure kept constant (Craft and Hawkins, 1959, Zimmerman, 1984). It is represented as:

$$C_p = \frac{1}{V_p}\left(\frac{dV_p}{dP_c}\right)_{P_P} \quad \{6.3\}$$

where C_P is the pore volume compressibility(1/psi), V_p is the initial pore volume, dV_p is the change in pore volume, dP_c is the change in confining pressure. Generally pore volume compressibility (C_p) for a reservoir rocks lies in the range of 2×10^{-6} to 25×10^{-6}, psi^{-1} (Craft and Hawkins, 1959). Many researchers have measured compressibility on core samples in laboratory for typical reservoir rocks (Dobrynin, 1962; Fatt, 1957; Gonten and Choudhary, 1969; Hall, 1953; Knapp, 1958; Newman, 1972; Zimmerman, 1984). Geertsma (1956) provide theoretical insight into the effect of change in fluid pressure on elastic deformation of porous rocks. Dobrynin (1962) noted that physical properties such as porosity, permeability, resistivity, and acoustic properties of a porous media depend on pore volume compressibility.

Pore volume compressibility is not constant but depends on effective pressure. The pore volume compressibility decreases with increase in confining pressure. Knapp (1958) described a linear relation between fractional pore volume and effective pressure. The empirically derived linear relation was used to model the dependence of pore volume compressibility as a function of porosity. Dobrynin (1962) and Gonten and Choudhary (1969) estimated the pore volume compressibility using polar fluids water and brine. Fatt (1957) and Newman (1972) performed a similar study using non-polar fluid, kerosene and refined oil. Gonten and Choudhary (1969) experimental data suggested that the pore volume compressibility increases with increase in temperature. Zimmerman (1984) observed that compressibility depends on effective pressure and experimentally verified this fact using polar fluid water in three different sandstones (Boise, Bandera and Berea). Chen et al., 1994 studied the effect of hydrostatic pressure on magnetic relaxation behavior of proton in saturated artificial and natural porous media. It was observed that

pressure has a minimum effect on longitudinal relaxation times (T_1) of proton in artificial and natural porous media. Surface relaxation has little to no dependence on pressure. This is important as the saturated core plugs in this study underwent a hydrostatic compression but pore pressure was kept at atmospheric pressure. Eliminating the pressure dependence of relaxation means that variations in T_2 spectra due to compression are related to changes in rock microstructure. Chen et al., 2002 investigated the variations in pore size distribution in siltstone under pressure using a 200 MHz nuclear magnetic resonance imaging instrument. The core plugs were saturated with kerosene and NMR measurements were performed at various confining pressures. There is little or no change in the T_2 distribution in short relaxation time, i.e., the variability in T_2 distribution is restricted to big pores only.

6.3 Experimental Procedure

All the core plugs were first cleaned in a Soxhlet extractor. Once cleaned, the samples were then dried in a gravity convection oven at a constant temperature. Boyle's law porosimetry technique was used to estimate the effective porosity of the sample (**Fig. 3.3.1**) at 100 psi. The CMS 300^3 (**Fig. 3.4.1**) was used to estimate the porosity and permeability of dry core plugs at various confining pressures. The dry core plugs were then saturated with 25,000 ppm NaCl brine at 1000 psi for 24 hrs. Saturation was checked by comparing the dry pore volume with saturated pore volume. The six saturated core samples were hydrostatically pressurized from 0 psi to 5000 psi in a specially designed fiberglass pressure vessel (**Fig. 3.8.2**). The experimental setup for acquiring NMR spectra on saturated core plugs under confining pressure is same as that used

during the freeze-thaw cycle (**Fig. 3.8.1**) except a hand pump is used to apply the confining pressure. A fiberglass pressure vessel was used to hold the jacketed saturated core plugs and to allow pressurizing the sample (see **Fig. 3.8.2**). The position and configuration of the sample relative to the fiberglass pressure vessel and the pole of the spectrometer is similar to that used during the thermal cycling experiment. The confining fluid is FLUORINERT[6] (FC-40) which is devoid of any hydrogen atom. NMR measurements were performed at room temperature and various confining pressures from 800 to 5000 psi. Initial NMR measurements were performed at atmospheric pressure. A hand pump was used to increase the confining pressure on the saturated core plugs. At each pressure point the wait time before each NMR measurement was performed is approximately 15 minutes. This is to allow the pressure equilibration.

6.4 Sample Information

In this study NMR spectra were acquired for six different brine saturated core plugs as a function of confining pressure from 0 to 5000 psi. All the core plugs are reservoir sandstones. **Table 11** summarizes the average properties of the core plugs.

S.No	Sample	Predominant Mineral	Core Image	Porosity,%	Permeability, md
1	Berea, B1	Quartz		18.8	69.7
2	Berea, B2	Quartz		18.8	89.7
3	Berea, B5	Quartz		19.2	111.0
4	Castlegate, CG1	Quartz		26.1	1000
5	Berea, 33V	Quartz		22.9	611.7
6	Berea, 37V	Quartz		23.2	788.7

Table 11: Summary of core information used for pore volume compressibility study. Note the wide range in permeabilities but narrow range in porosity.

6.5 CMS Porosity and Permeability

This study is concerned with understanding the effect of pressure on sandstone. **Fig. 6.5.1** represents the measured CMS porosities as function of confining pressure. Increase in

confining pressure results in a decrease in porosity due to closing of cracks and pores. At any confining pressure the decrease in porosity for all the six samples is less than 10%. Porosity at any particular confining pressure can be described by the following form:

$$\phi = -a \times \mathrm{Ln}(P_c) + b \quad \{6.4\}$$

where ϕ is porosity (%), P_c is the confining pressure (psi), a and b are empirically derived constants.

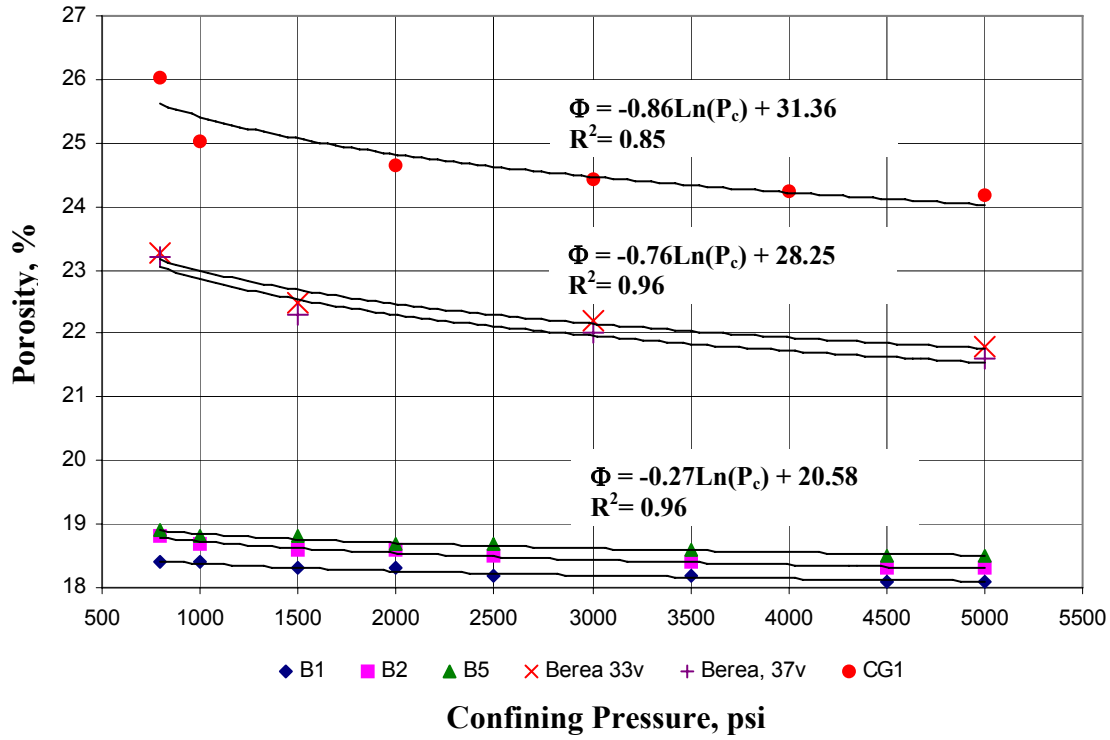

Figure 6.5.1: Porosity as a function of confining pressure. With increase in confining pressure, the porosity decreases. However the decrease is less than 10% for the entire pressure range.

Klinkenberg corrected permeability follows a trend similar to porosity. The permeability ranges from 70 md to 1000 md over a small porosity range 19% to 26%. The large variation in permeability is due to differences in the sorting, shape and size of the grain, cementation, and digenesis. **Fig. 6.5.2** resents the Klinkenberg corrected permeability as

function of confining pressure. Permeability at any particular confining pressure can be described in the following form:

$$k = -a \times Ln(P_c) + b \quad \{6.5\}$$

where k is permeability (md), P_c is the confining pressure (psi), a and b are empirically derived constants.

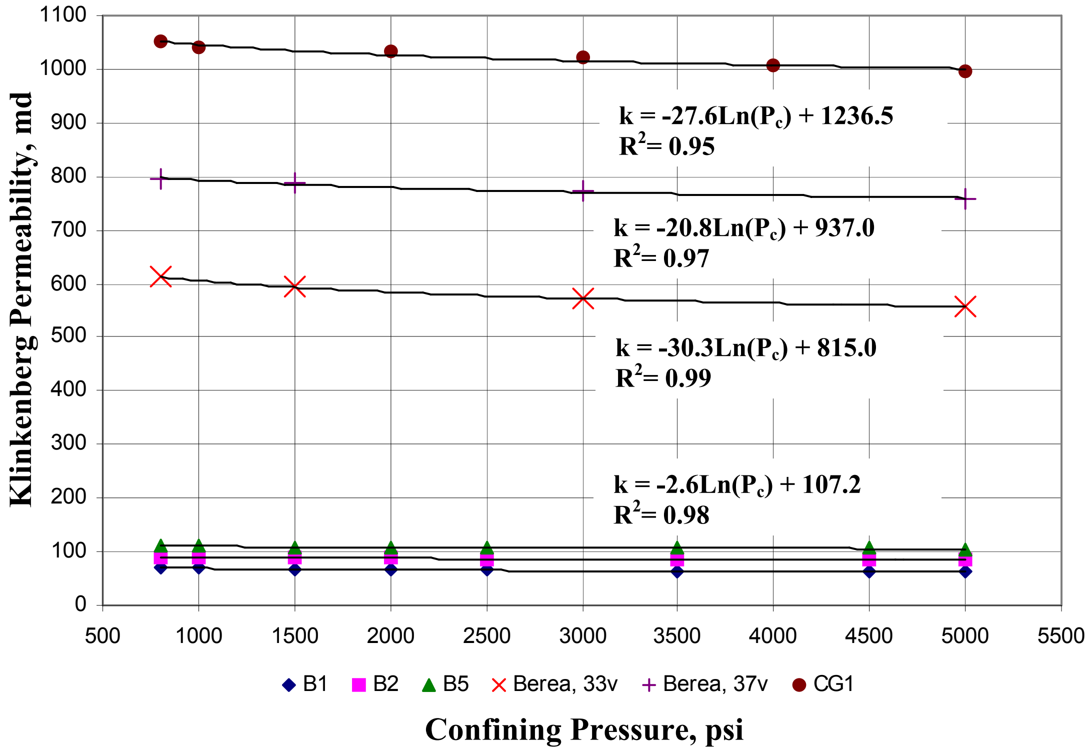

Figure 6.5.2: Klinkenberg corrected permeability as a function of confining pressure. As with porosity, decrease in permeability is less than 10% for the entire pressure range.

6.6 NMR Porosity Estimation and Pressure Effect

Fig. 6.6.1 shows the cross plot of NMR porosity (@ room condition) and saturated porosity obtained using gravimetric technique. The estimated porosity is within ± 0.5% of the gravimetric porosity. The saturated samples were placed in the pressure vessel and NMR spectra were acquired as a function of confining pressure from 0 to 5000 psi.

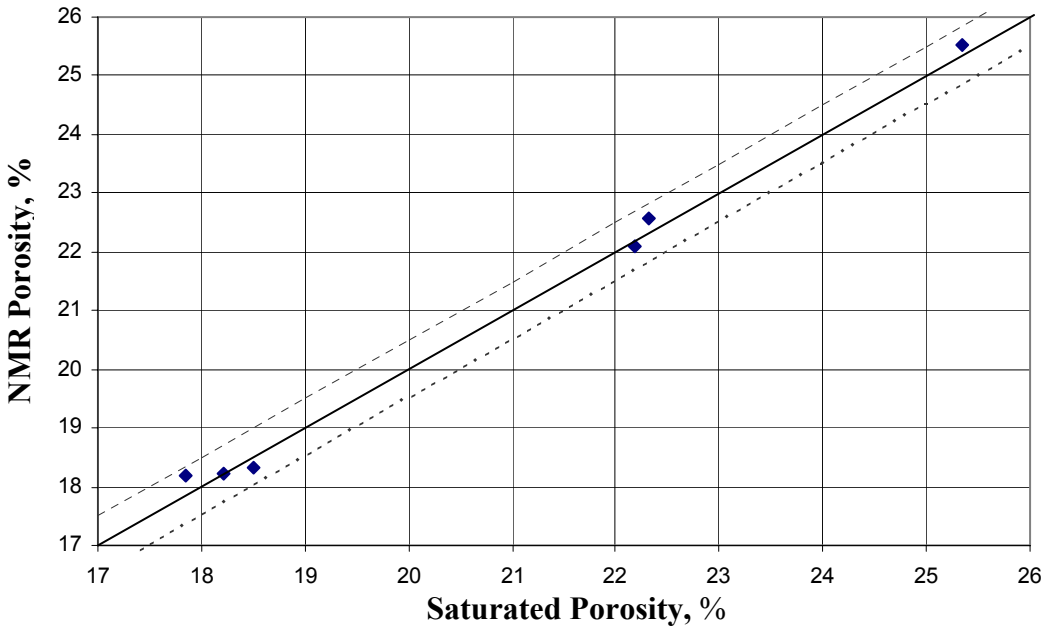

Figure 6.6.1: Crossplot of saturated porosity versus NMR estimated porosity. The saturated porosity was determined gravimetrically. The NMR estimated porosity (@ room condition) lies within ± 0.5 % of the standard measure of porosity. The solid line is a 1:1 line.

The T_2 distribution for all the six core plugs during the pressure cycle is shown in **Fig. 6.6.2 - 6.6.7**. There are three distinct characteristics present in all of the T_2 distributions for each of the samples after confining pressure was applied. The three characteristics are: 1) decrease in peak amplitude; 2) peak T_2 time shift towards smaller value; and 3) broadening of T_2 distribution towards longer T_2 time due to release of pore fluid. Application of confining pressure to a saturated core plugs results in release of the pore fluid. The majority of the released fluid comes from the most dominant pore bodies. The pore radii for the five Berea core plugs and for Castlegate CG1 are estimated assuming a cylindrical pore geometry and an average surface relaxivity (ρ, μm/sec) of 25 μm/sec for Berea and 21.5 μm/sec for Castlegate, CG1. Majority of the pore fluid is released upon the initial application of confining pressure (800 psi).

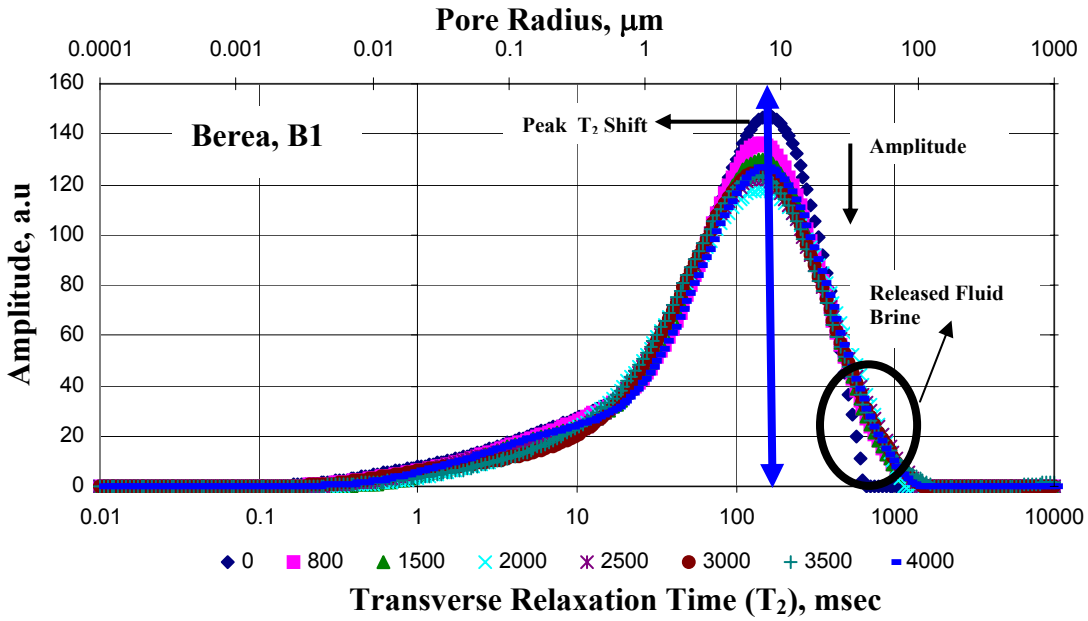

Figure 6.6.2: T_2 distributions of Berea, B1 saturated with 25K ppm NaCl brine as a function of confining pressure from 0 psi to 4000 psi. The different colors indicate different confining pressures. Compression of the pore space is accompanied by an amplitude decrease and shift in peak T_2 time. The released pore fluid is observed by the presence of amplitude at longer T_2 time.

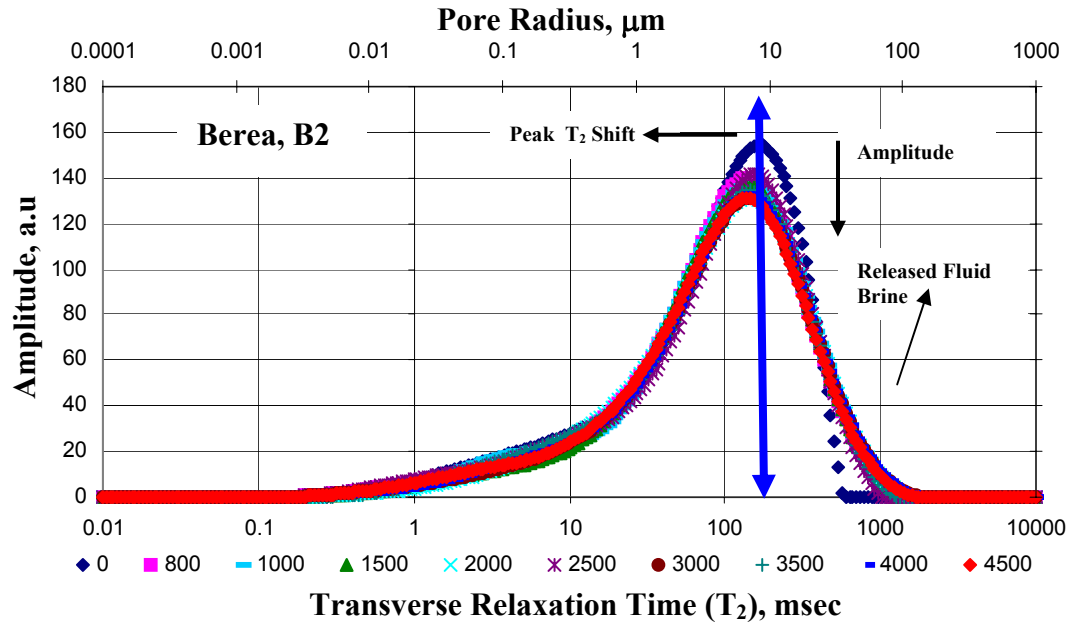

Figure 6.6.3: T_2 distributions of Berea, B2 saturated with 25K ppm NaCl brine as a function of confining pressure from 0 psi to 4500 psi. The different colors indicate different confining pressures. Compression of the pore space is accompanied by an amplitude decrease and shift in peak T_2 time. The released pore fluid is observed by the presence of amplitude at longer T_2 time.

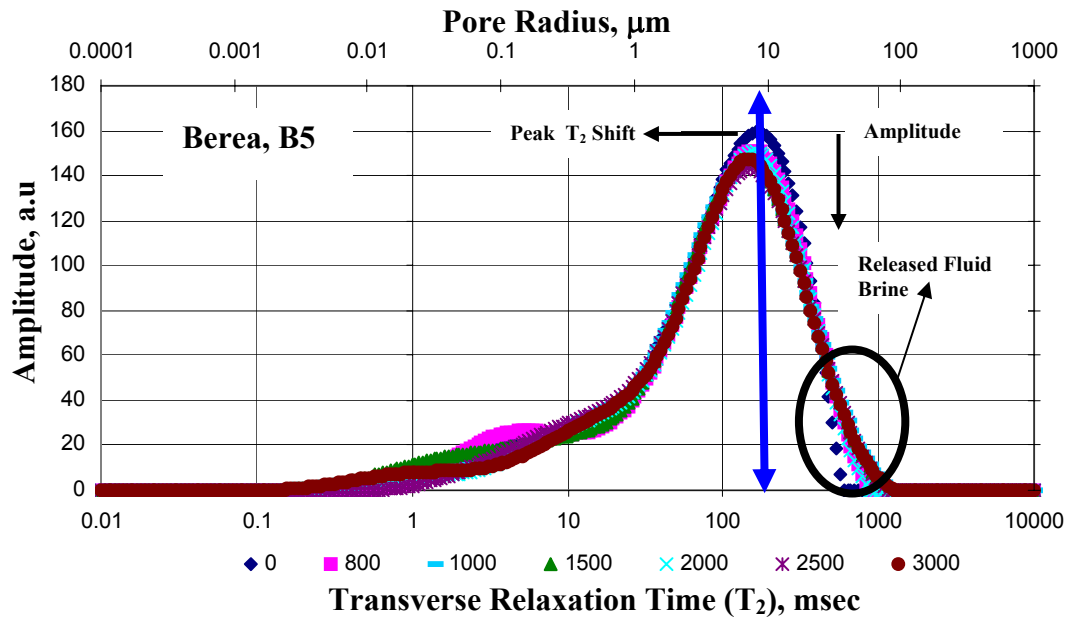

Figure 6.6.4: T_2 distributions of Berea, B5 saturated with 25K ppm NaCl brine as a function of confining pressure from 0 psi to 3000 psi. The different colors indicate different confining pressures. Compression of the pore space is accompanied by an amplitude decrease and shift in peak T_2 time. The released pore fluid is observed by the presence of amplitude at longer T_2 time.

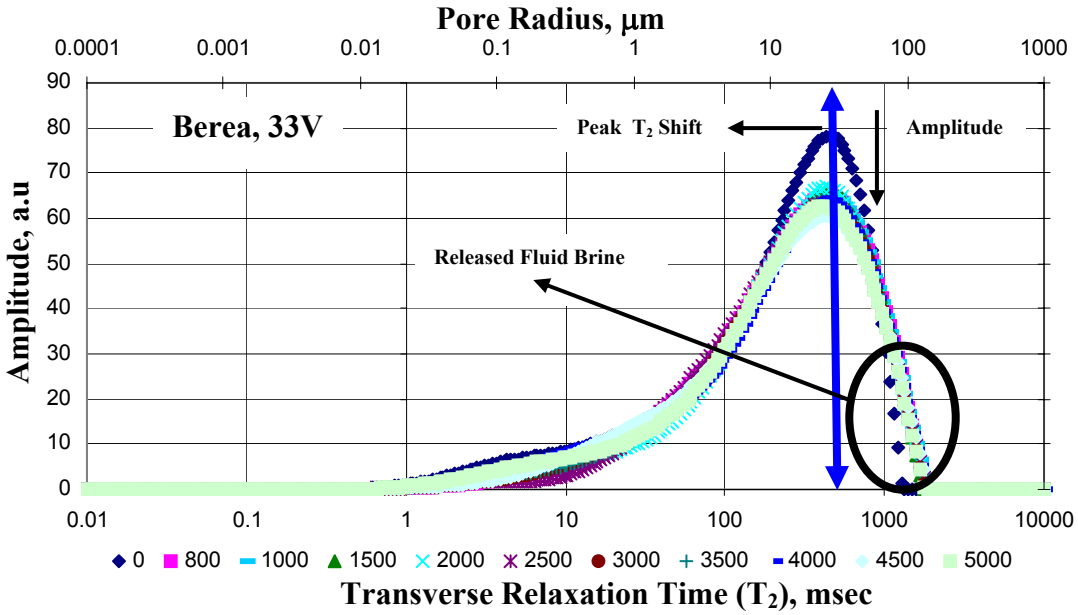

Figure 6.6.5: T_2 distributions of Berea, 33V saturated with 25K ppm NaCl brine as a function of confining pressure from 0 psi to 5000 psi. The different colors indicate different confining pressures. Compression of the pore space is accompanied by an amplitude decrease and shift in peak T_2 time. The released pore fluid is observed by the presence of amplitude at longer T_2 time.

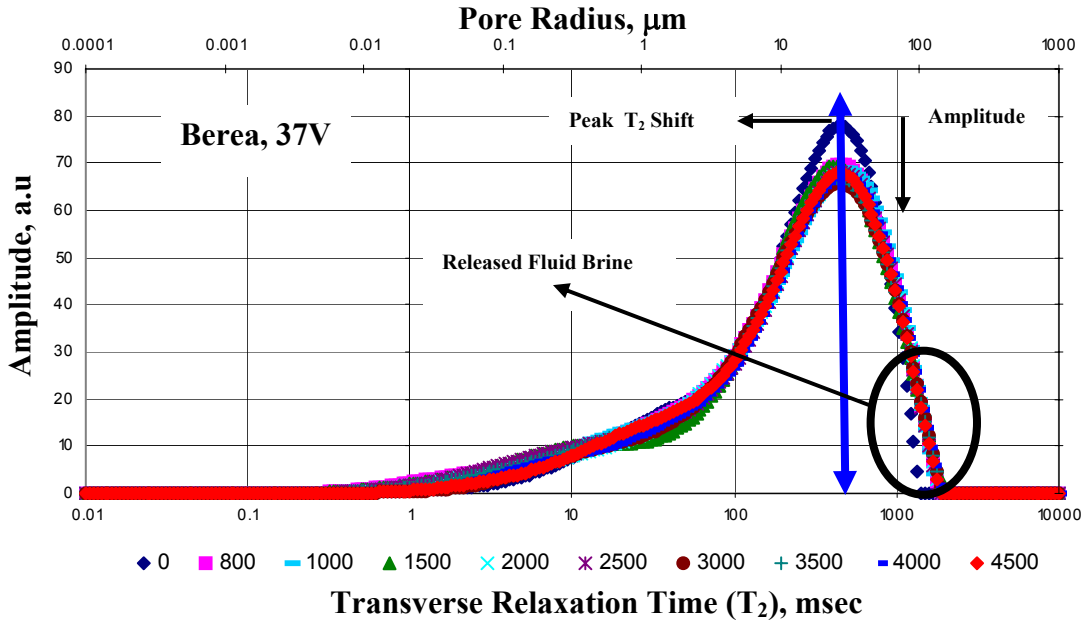

Figure 6.6.6: T_2 distributions of Berea, 37V saturated with 25K ppm NaCl brine as a function of confining pressure from 0 psi to 4500 psi. The different colors indicate different confining pressures. Compression of the pore space is accompanied by an amplitude decrease and shift in peak T_2 time. The released pore fluid is observed by the presence of amplitude at longer T_2 time.

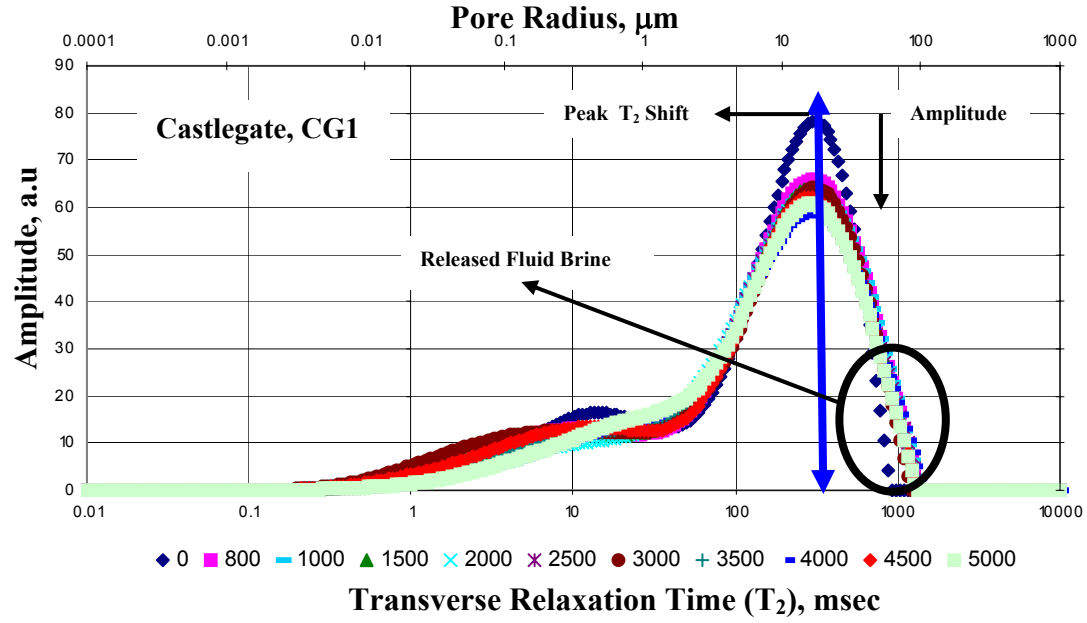

Figure 6.6.7: T_2 distributions of Castlegate, CG1 saturated with 25K ppm NaCl brine as a function of confining pressure from 0 psi to 5000 psi. The different colors indicate different confining pressures. Compression of the pore space is accompanied by an amplitude decrease and shift in peak T_2 time. The released pore fluid is observed by the presence of amplitude at longer T_2 time.

The released pore fluid is observed by the presence of amplitudes at longer T_2 time. In acoustic measurements, the observance is that application of confining pressure results in closing of cracks or small pores. NMR cannot resolve the details of crack closure, but does seem to record the reduction of porosity taking place in the larger pores. The NMR response to the closure of small pores or cracks (early T_2 time) is minimal. This observation is similar to Chen et al., 2002 experimental observation, where the variation in T_2 distribution due to application of confining pressure is dominated in big pores. NMR porosity as a function of confining pressure for all the six core plugs is shown in **Fig. 6.6.8**.

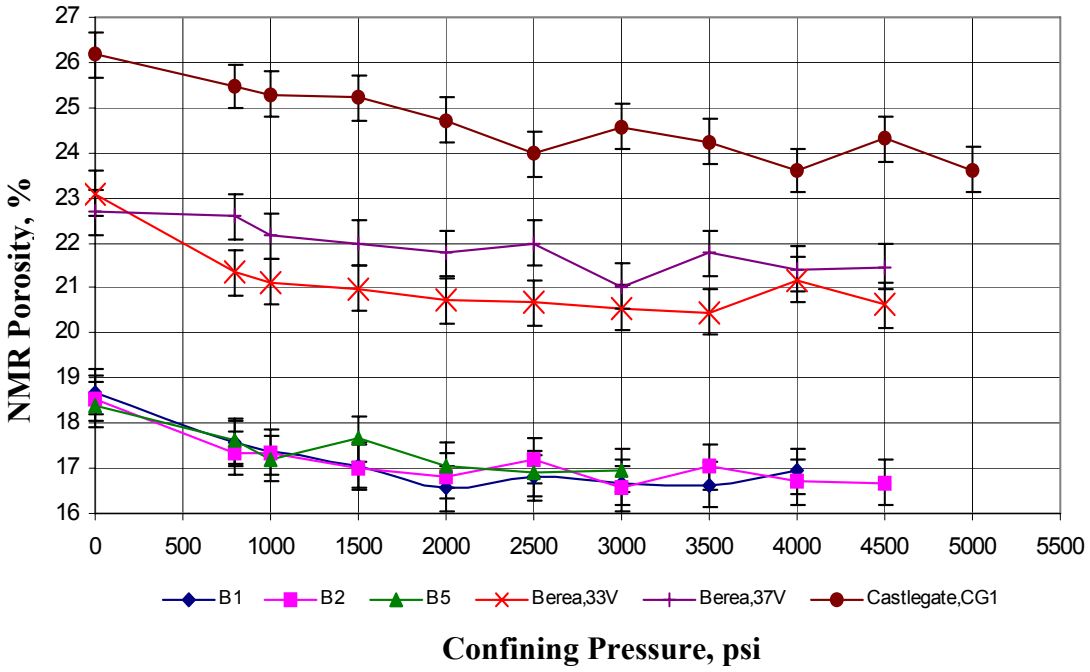

Figure 6.6.8: NMR Porosity as a function of confining pressure. With increase in confining pressure, the porosity decreases. The error bar in the porosity estimation is ± 0.5 %.

The fluctuation in porosity measurement reflects the uncertainty in NMR measurement. Time shift in peak T_2 time as a function of confining pressure for all the six core plugs is shown in **Fig. 6.6.9**. The shift in the T_2 time towards smaller value is due to release of

pore fluid from the larger pores.

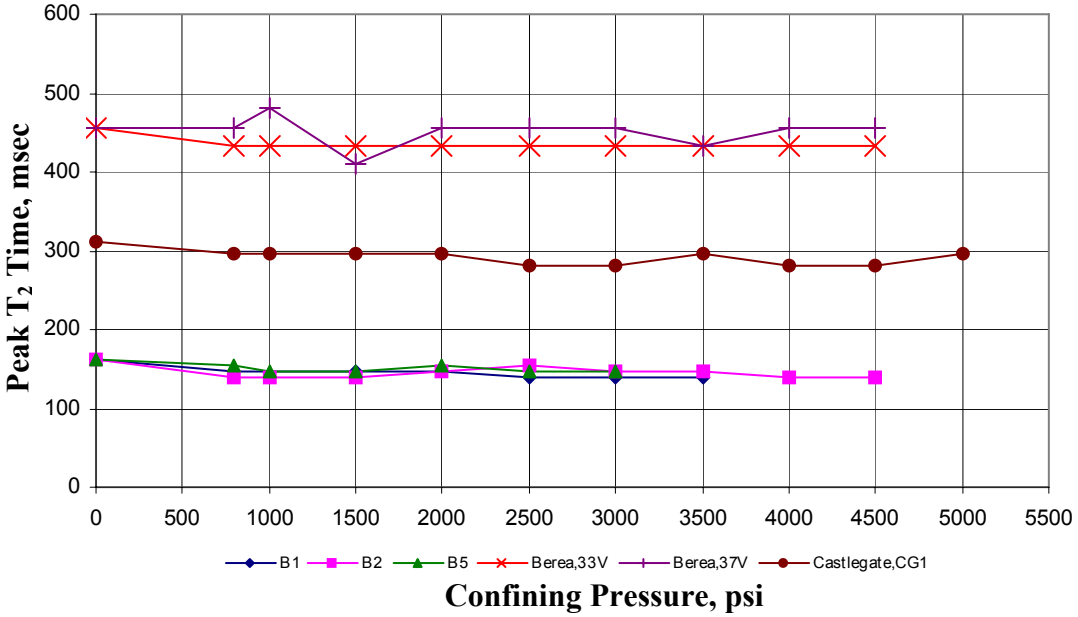

Figure 6.6.9: Position of the peak T_2 time as a function of confining pressure. Generally T_2 time decreases with increase in confining pressure. This is due to the release of the pore fluid from the most dominant pore body due to application of confining pressure.

6.7 Pore Volume Compressibility

The amount of fluid expelled from a saturated core at a particular pressure, P is the difference between the pore volume at 0 psi and pore volume at that particular pressure, P. The ratio of the released fluid to the initial pore volume is known as pore volume strain. The slope of the pore volume strain-effective pressure plot will provide the compressibility of the pore. In this study the pore pressure is zero. Thus the effective pressure is the applied confining pressure. **Fig. 6.7.1** is the pore volume strain-effective pressure plot for all the six saturated core plugs. Each plot has pore volume strain estimated using helium and brine (25,000 ppm NaCl) on the same core plug.

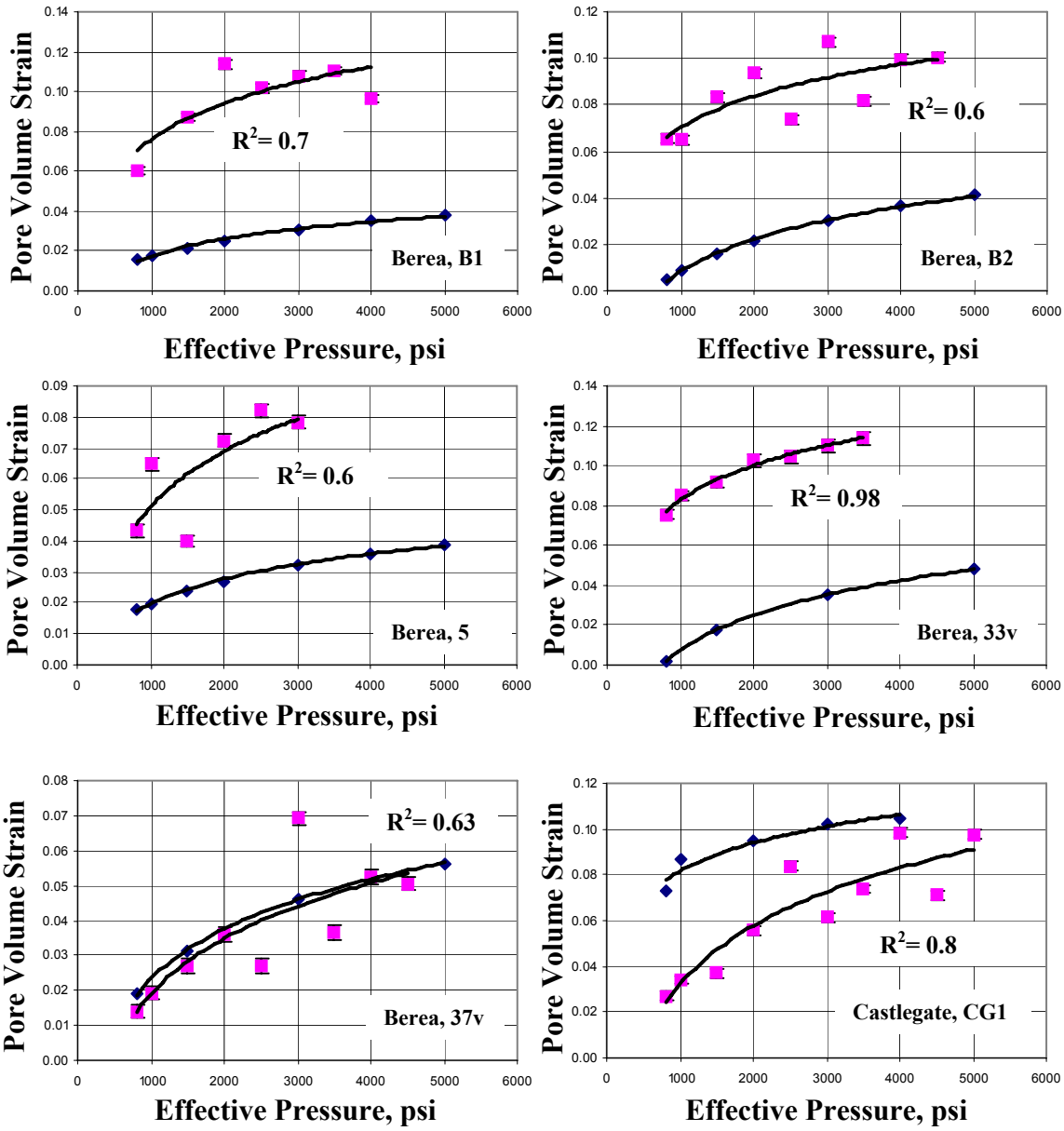

Figure 6.7.1: Pore volume strain plotted versus effective pressure for all the six core plugs. Pore strain is calculated from Helium (diamond) injection and brine (square) expulsion. Except for Berea, 37v and Castlegate, CG1 the pore strain estimated using NMR is same or more than Helium injection. The error bar in the pore strain estimation from NMR is ± 3.0 %. The R^2 for pore strain estimated using Helium is 1.0.

Helium is injected at each confining pressure and pore volume is estimated. The difference in the pore volume at 0 psi and pore volume at that particular pressure, P is the

differential pore volume. The ratio of the differential pore volume to the pore volume at 0 psi is known as the pore strain estimated using helium. In case of NMR measurement, the differential pore volume is the difference in area under the T_2 distribution at 0 psi and at a particular confining pressure, P. The ratio of the differential pore volume to the NMR pore volume at 0 psi is known as the pore strain derived from NMR measurement. At each effective pressure, the pore strain estimated using NMR is larger as compared to that derived from Helium injection measurement (**Fig. 6.7.1**) except Berea, (37v) and Castlegate, (CG1). In case of Berea, (37v) both pore strains are similar while in case of Castlegate, (CG1), the pore strain derived from NMR measurement is smaller than that estimated from Helium injection. The 3% error bar in pore strain estimation is derived from ± 0.5% error in NMR porosity estimation. The non-linear relation between pore volume strain and confining pressure is correlated using a logarithmic function (y=a + b*lnx), a and b are empirically derived coefficient. Graphically differentiating the calculated pore strain versus confining pressure plot provides the pore volume compressibility at each pressure point.

Fig. 6.7.2 presents the pore volume compressibility as a function of confining pressure. On an average the estimated pore volume compressibility using brine as the pore fluid (NMR measurement technique) is greater than that derived using helium. Thus the effect of compression on a brine saturated sample is greater as compared to the same sample when filled with air or helium. Water affects the silicates in the matrix directly by forming bonds with SiO_2 making them weaker (Parks, 1984 and Paterson, 1989). This requires only a monolayer of water. Clark et al., 1980 and Wyllie et al., 1962 also observed a similar effect in the elastic properties due to presence of polar fluid.

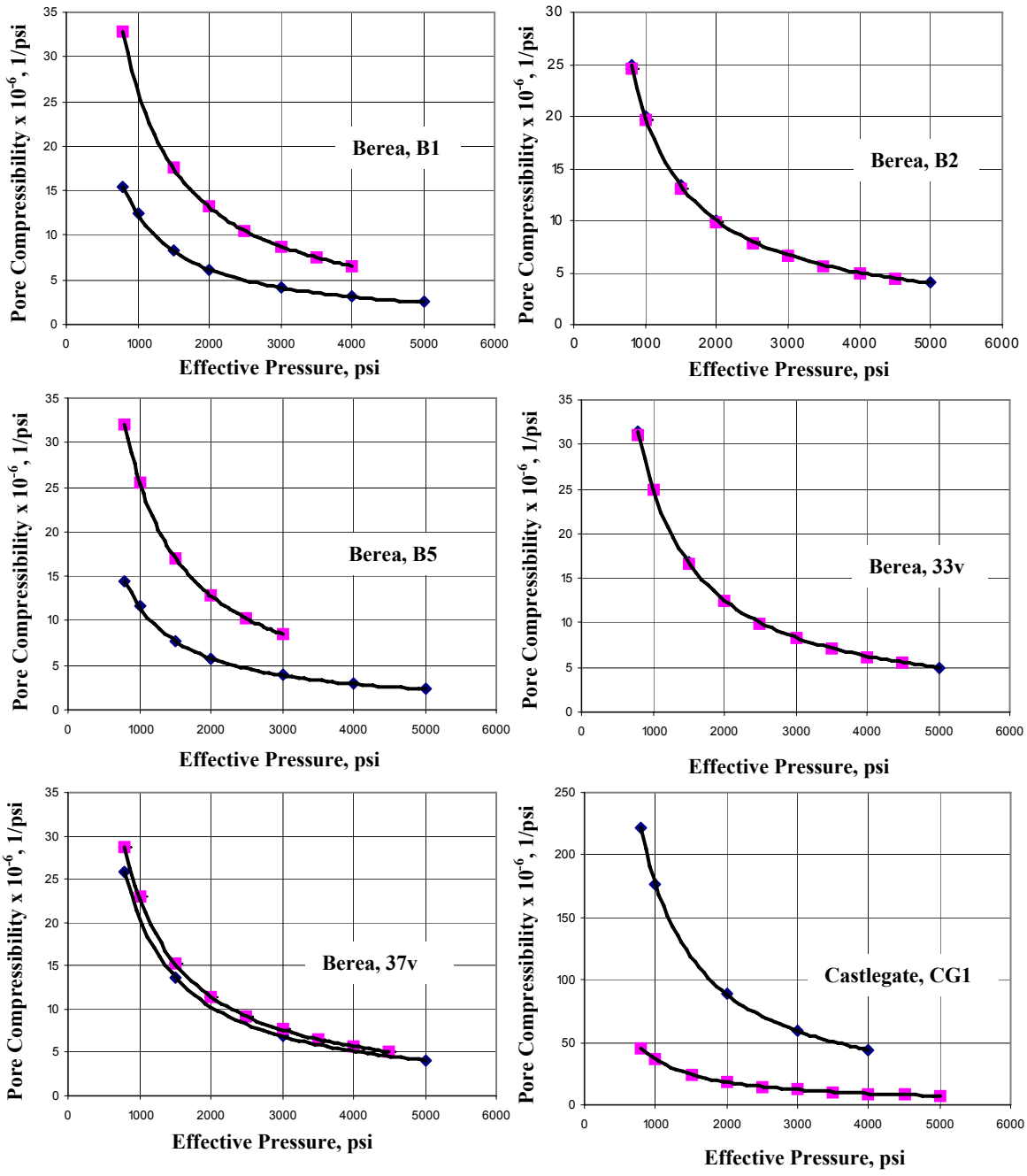

Figure 6.7.2: Pore volume compressibility as a function of confining pressure for the six different sandstones. The diamonds represent pore volume compressibility estimated using Helium injection while square represents pore volume compressibility estimated using NMR. The error in pore volume compressibility estimation from NMR is ± 3.0 %.

The second effect is dependent upon having free water. The exact state of saturation during CMS measurement is unknown but thought to be at most a monolayer. However,

during the NMR measurement we know we have free water. We would therefore expect the maximum softening effect to take place during the NMR experiment and we observe this. Exact resolution of this requires future study.

A comparison of Zimmerman's (1984) and this NMR based study is presented in **Fig. 6.7.3**. The anomalous behavior in pore compressibility between the two methods warrants further evaluation.

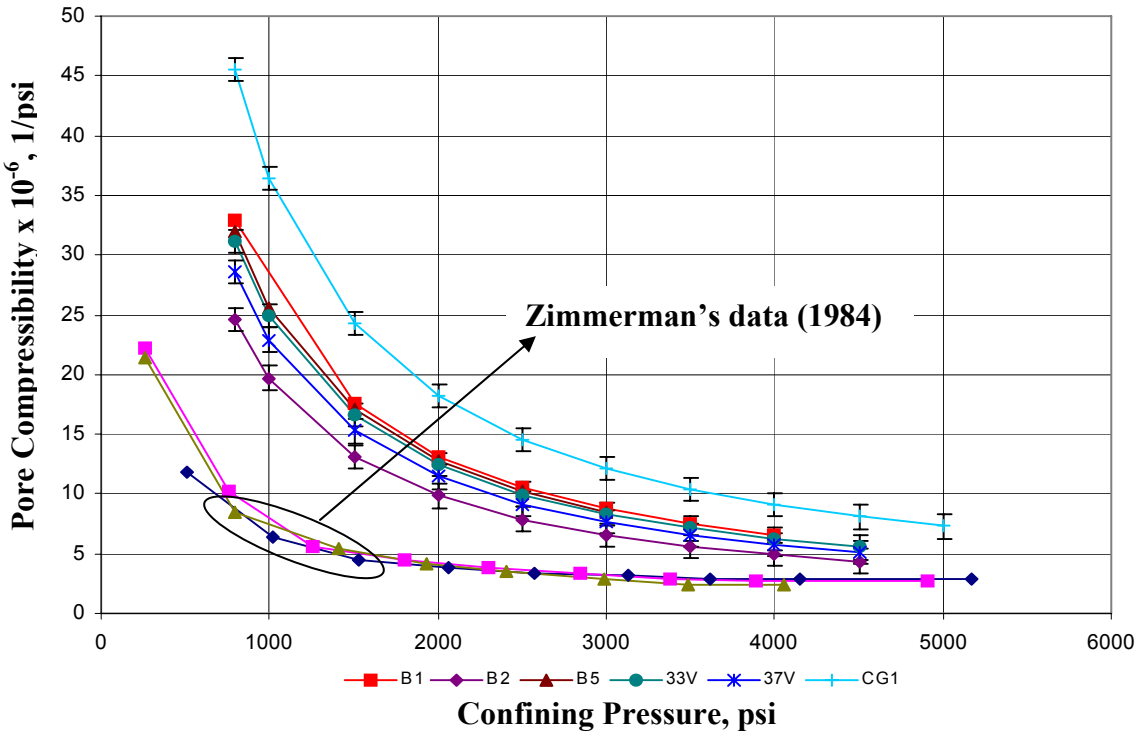

Figure 6.7.3: Comparison of pore volume compressibility estimated by Zimmerman (1984) and this NMR based study. The estimated pore volume compressibility based on NMR is three times (average) higher than Zimmerman's data (1984). The error in pore volume compressibility estimation from NMR is ± 3.0 %.

6.8 Conclusions and Future Work

As noted earlier the knowledge of pore volume compressibility is essential not only from reservoir engineering perspective but also mechanical stability perspective. The major conclusions of this work are:

1. NMR techniques can be used to measure pore compressibility in the presence of a natural polar fluid. We expect NMR to provide better resolution in higher porosity samples
2. The effect of pressure variation on T_2 distribution reflects changes in the rock microstructure.

The following recommendation is being made for future research:

1. The anomalous behavior of higher pore volume compressibility estimation with polar fluid needs further evaluation. To confirm the influence of polar fluid have a measure compressibility, a series of experiments are planned using non-polar fluid such as kerosene, mineral oil, etc.

CONCLUSIONS

The major conclusions of this NMR based experimental study on freezing and thawing of saturated porous media and application to shale and pore volume compressibility are:

1. NMR can be used to map the water saturation even in the presence of ice.
2. The exact value of the surface relaxivity of ice is still unknown, however it cannot be zero or very large and is most likely very similar to that of our rock samples.
3. The water saturation, porosity and bound water can be measured in shale plugs and cuttings.
4. Almost all the water in shale are bound water.
5. NMR can be used to measure pore volume compressibility directly. Measured values appear smaller than those measured with helium, which may reflect the weakening of H_2O.

REFERENCES

1. Allen, S. G., Stephenson, P. C. L., and Strange, J. H., 1997, Morphology of Porous Media Studied by Nuclear Magnetic Resonance, *Journal of Chemical Physics*, vol. 106, no. 18, p. 7802-7809.

2. Allen, S. G., Stephenson, P. C. L., and Strange, J. H., 1997, Internal Surfaces of Porous Media Studied by Nuclear Magnetic Resonance, *Journal of Chemical Physics*, vol. 108, no. 19, p. 8195-8198.

3. Ahrens, T. J., 1995, *Mineral Physics & Crystallography*, American Geophysical Union, USA, p. 38.

4. Anderson, D. M., and Tice, A. R.., 1973, The Unfrozen Interfacial Phase in Frozen Soil Water Systems, *Physical Aspects of Soil Water and Salts in Ecosystem*, Springer-Verlag, New York, p. 107-124.

5. Andersland, O. B., and Ladanyi, B., 2004, *Frozen Ground Engineering*, John Wiley and Sons, Inc., p. 8.

6. Bloch, F., Hansen, W. W., and Packed, M. E., 1946, Nuclear Induction," *Physical Review*, vol. 69, p. 127.

7. Bendel, P., 1990, Spin-Echo Attenuation by Diffusion in Non-Uniform Field Gradients, Journal of Magnetic Resonance, vol. 86, p. 509-515.

8. Brownstein, K. R., and Tarr, C. E., 1979, Importance of Classical Diffusion in NMR Studies of Water in Biological Cells, *Physical Review*, Series A, vol. 19, p. 2446-2453.

9. Campbell, C. A. and Laherrere, J. H., 1998, The End of Cheap Oil, *Scientific American*, vol. 278, no. 3, p. 78-83.

10. Carslaw, H. S., and Jaeger, J. C., 1959, *Conduction of Heat in Solids*, Oxford University Press, p. 282-296.

11. Chen, Q., Kinzelbach, W., Ye, C., and Yue, Y., 2002, Variations of Permeability and Pore Size Distributions of Porous Media with Pressure, *Journal of Environmental Quality*, vol. 31, p. 500-505.

12. Chen, R., Stallworth, P. E., Greenbaum, S. G., and Kleinberg, R. L., 1994, Effects of Hydrostatic Pressure on Proton and Deuteron Magnetic Resonance of Water in Natural Rocks and Artificial Porous Media, *Journal of Magnetic Resonance*, Series A, vol. 110, p. 77-81.

13. Churaev, N. V., Bardasov, S. A., and Sobolev, V. D., 1993, On the Non Freezing Water Interlayers between Ice and a Silica Surface, *Colloids and Surfaces A: Physicochemical and Engineering Aspects*, vol. 79, p. 11-24.

14. Civan, F., 2000, Unfrozen Water in Freezing and Thawing Soils: Kinetics and Correlation, *Journal of Cold Regions Engineering*, vol. 14, no. 3, p. 146-156.

15. Clark, V. A., Tittmann, B. R., and Spencer, T. W., 1980, Effect of Volatiles on Attenuation (Q-1) and Velocity in Sedimentary Rocks, *Journal of Geophysics Research*, vol. 85, no. B10, p. 5190-5198.

16. Clennell, M. B., Hovland, M., Booth, J. S., Henry, P., and Winters, W. J., 1999, Formation of Natural Gas Hydrates in Marine Sediments - Conceptual Model of Gas Hydrate Growth conditioned by Host Sediment Properties, *Journal of Geophysical Research*, vol. 104, no. B10, p. 22985-23003.

17. Coates, G., Marschall, D., Mardon, D., and Galford, J., 1997, A New Characterization of Bulk–Volume Irreducible Using Magnetic Resonance, paper QQ 38th Annual SPWLA Logging Symposium Transactions, 14p.

18. Coates, G. R., Xiao, R., and Prammer, M. G., 1999, *NMR Logging Principles and Applications*, Gulf Publishing Company, Houston, Texas, p. 41-66.

19. Colbeck, S. C., 1981, Configuration of Ice in Frozen Media, *Soil Science*, vol. 133, p. 116-122.

20. Collins, R. E., 1990, *Flow of Fluids Through Porous Media*, Research and Engineering Consultants Inc., Colorado, p. 21.

21. Cowan, B. P., 1997, *Nuclear Magnetic Resonance and Relaxation*, Cambridge University Press, Cambridge, p. 21-22.

22. Craft, B. C., and Hawkins, M. F, 1959, *Applied Petroleum Reservoir Engineering*, Prentice Hall Inc, New Jersey, p. 132, 259.

23. Dastidar, R., Rai, C. S., Sondergeld, C. H., and Shahreyar, R., 2006, NMR Response of Two Clastic Reservoirs: Influence of Depositional Environment, *Petrophysics*, vol. 47, no. 3, p. 214-222.

24. Deffeyes, K. S., 2001, *Hubbert's Peak: The Impending World Oil Shortage*, Princeton University Press, New Jersey, p. 4.

25. Dobrynin V. M., 1962, Effect of Overburden Pressure on Some Properties of Sandstones, *Society of Petroleum Engineers Journal*, p. 360-366.

26. Dvorkin, J., Helgerud, M. B., Waite, W. F., Kirby, S. H. and Nur, A., 2000, Introduction to Physical Properties and Elasticity Models, in *Natural Gas Hydrate in Oceanic and Permafrost Environments*, Kluwer Academy, Norwell, Mass., p. 245-260.

27. Dunn, K. J., Bergman, D. J., and Latorraca, G. A., 2002, *Nuclear Magnetic Resonance Petrophysical and Logging Application*, Elsevier Science Ltd., UK, p. 85, 91.

28. Egermann, P., Lenormand, R., and Longeron, D., 2005, A Fast and Direct Method of Permeability Measurements on Drill Cuttings, *SPE Reservoir Evaluation and Engineering*, vol. 4, no. 3, p. 269-275.

29. Everett, D. H., 1961, Thermodynamics of Frost Damage to Porous Solids, Transactions Faraday Society, vol. 57, no. 465, p. 1541-1551.

30. Fatt, I., 1957, Pore Volume Compressibilities of Sandstone Reservoir Rocks, *Journal of Petroleum Technology*, p. 64-66.

31. Fofonoff, N. P. and Millard, R. C., 1984, Algorithms for Computation of Fundamental Properties of Seawater, *UNSECO Technical Paper Marine Science*, no. 44, p. 1-53.

32. Geertsma, J., 1956, The Effect of Fluid Pressure Decline on Volumetric Changes of Porous Rocks, SPE paper 728-G, *in* Proceedings of the 1956 SPE Petroleum Branch Fall Meeting: Society of Petroleum Engineers.

33. Godefroy, S., Fleury, M., Deflandre, F., and Korb, J. P., 2001, Temperature Effect on NMR Surface Relaxation, SPE paper 71700, *in* Proceedings of the 2001 SPE Annual Technical Conference: Society of Petroleum Engineers.

34. Godefroy, S., Korb, J. P., Fleury, M., and Bryant, R. G., 2001, Surface Nuclear Magnetic Relaxation and Dynamics of Water and Oil in Macroporous Media, *Physical Review E*, vol. 64, p.1-13.

35. Gonten, W. D. V., and Choudhary, B. K., 1969, The Effect of Pressure and Temperature on Pore Volume Compressibility, SPE paper 2526, *in* Proceedings of the 1969 SPE Annual Fall Meeting: Society of Petroleum Engineers.

36. Gultekin, D. H., and Gore, J. C., 2005, Temperature Dependence of Nuclear Magnetization and Relaxation, *Journal of Magnetic Resonance*, vol. 172, p. 133-141.

37. Hall, H. N., 1953, Compressibility of Reservoir Rocks, Transactions AIME, vol. 198, p. 309-311.

38. Hansen, E. W., Simon, C., Haugsrud, R., Raeder, H., and Bredesen, R., 2002, Probing Pore Size Distribution by Cryogenic and Relaxation ^{2}H – NMR, *Journal of Physical Chemistry B,* vol. 106, p. 12396-12406.

39. Hansen, E. W., Stöcker, M., and Schmidt, R., 1996, Low-Temperature Phase Transition of Water Confined in Mesopores Probed by NMR. Influence on Pore Size Distribution, *Journal of Physical Chemistry*, vol. 100, p. 2195-2200.

40. Hansen, E. W., Schmidt, R., and Stöcker, M., 1996, Pore Structure Characterization of Porous Silica by ^{1}H NMR Using Water, Benzene, and Cyclohexane as Probe Molecules , *Journal of Physical Chemistry*, vol. 100, p. 11396-11401.

41. Hatfield, C. B., 1997, Oil Back on the Global Agenda, *Nature*, vol. 387, p. 121.

42. Jones, S. C., 1972, A Rapid Accurate Unsteady-State Klinkenberg Permeameter, *SPE Journal*, vol. 12, no. 5, p. 383-397.

43. Keller, P. J., 1991, *Basic Principles of MR Imaging*, Chapter 4, GE Medical Systems.

44. Kenyon, W. E., 1992, Nuclear Magnetic Resonance as a Petrophysical Measurement, *Nuclear Geophysics*, vol. 6, no. 2, p. 153-171.

45. Kerr, R. A., 1998, The Next Oil Crisis Looms Large-And Perhaps Close, *Science*, vol. 281, no. 5380, p. 1128-1131.

46. King, M. S., 1977, Acoustic Velocities and Electrical Properties of Frozen Sandstones and Shales, *Canadian Journal of Earth Science*, vol. 14, p. 1004-1013.

47. King, M. S., Zimmerman, R. W., and Corwin, R. F., 1988, Seismic and Electrical Properties of Unconsolidated Permafrost, *Geophysical Prospecting*, vol. 36, p. 349-364.

48. Kleinberg, R. L., Flaum, C., Straley, C., Brewer, P. G., Malby, G. E., Peltzer, E. T., Friederich, G., and Yesinowski, J. P., 2003a, Seafloor Nuclear Magnetic Resonance Assay of Methane Hydrate in Sediment and Rock, *Journal of Geophysical Research*, vol. 108, no. B3, p. 2137-2150.

49. Kleinberg, R. L., Flaum, C., Griffin, D. D., Brewer, P. G., Malby, G. E., Peltzer, E. T., and Yesinowski, J. P., 2003b, Deep Sea NMR: Methane Hydrate Growth Habit in Porous Media and its Relationship to Hydraulic Permeability, Deposit accumulation, and Submarine Slope Stability, *Journal of Geophysical Research*, vol. 108, no. B10, p. 2508-2525.

50. Kleinberg, R. L., and Griffin, D. D., 2005, NMR Measurement of Permafrost: Unfrozen Water Assay, Pore Scale distribution of Ice, and Hydraulic Permeability of Sediments, *Cold Regions Science and Technology*, vol. 42, p. 63-77.

51. Knapp, W. W. D., 1958, Nonlinear Behavior of Elastic Porous Media, SPE paper 1124-G, *in* Proceedings of the 1958 SPE Annual Fall Meeting: Society of Petroleum Engineers.

52. Latour, L. L., Kleinberg, R. L., and Sezginer, A., 1992, Nuclear Magnetic Resonance Properties of Rocks at elevated Temperatures, *Journal of Colloid and Interface Science,* vol. 150, no. 2, p. 535-548.

53. Liu, Z., Muldrew, K., Wan, R. G., and Elliott, J. A. W., 2003, Measurement of Freezing Point Depression of Water in Glass Capillaries and the Associated Ice Front Shape, *Physical Review E*, vol. 67, p. 1-9.

54. Martinez, G. A., and Davis, L. A., 2000, Petrophysical Measurements on Shales Using NMR, SPE paper 62851, *in* Proceedings of the 2000 SPE/AAPG Western Regional Meeting: Society of Petroleum Engineers.

55. Matteson, A., Tomanic, J. P., Herron, M. M., Allen, D. F., and Kenyon, W. E., 2000, NMR Relaxation of Clay/Brine Mixtures, *SPE Reservoir Evaluation and Engineering*, vol. 3, no. 5, p. 408-413.

56. Morishige, K., and Kawano, K., 1999, Freezing and Melting of Water in a Single Cylindrical Pore: The Pore-Size Dependence of Freezing and Melting Behavior, *Journal of Chemical Physics*, vol. 110, no. 10, p. 4867-4872.

57. Mullin, J. W., 2001, *Crystallization*, Butterworth-Heinemann, Oxford, p. 55, 181-215.

58. Nakano, Y., and Brown, J., 1971, Effect of a Freezing Zone of Finite Width on the Thermal Regime of Soils, *Water Resources Research*, vol. 7, no. 5, p. 1226-1233.

59. Newman, G., H., 1971, Pore Volume Compressibility of Consolidated, Friable, and Unconsolidated Reservoir Rocks Under Hydrostatic Loading, SPE paper 3835, *in* Proceedings of the 1971 SPE Rocky Mountain Regional Meeting: Society of Petroleum Engineers.

60. Okada, R., Matsukawa, S., and Watanabe, T., 2002, Hydration Structure and Dynamics in Pullulan Aqueous Solution Based on ^{1}H NMR Relaxation Time, *Journal of Molecular Structure*, vol. 602-603, p. 473-483.

61. Overloop, K., and Gerven, L. V., 1992, Freezing Phenomena in Adsorbed Water as Studied by NMR, *Journal of Magnetic Resonance,* Series A, vol. 101, p. 179-1993.

62. Pandit, B. I., and King, M. S., 1979, A Study of the Effects of Pore Water Salinity on some Physical Properties of Sedimentary Rocks at Permafrost Temperatures, *Canadian Journal of Earth Science*, vol. 16, no. 8, p. 1566-158

63. Parks, G. A., 1984, Surface and Interfacial Free Energies of Quartz, *Journal of Geophysics Research*, vol. 89, no. B6, p. 3997-4008.

64. Paterson, M. S., 1989, The Interaction of Water with Quartz and its Influence in Dislocation Flow - An Overview, *in Rheology of Solids and of the Earth*, Oxford University Press, Oxford, p. 107-142.

65. Patrick, B. B., and Tice, A. R., 1989, Comparison of Soil Freezing Curve and Soil Water Curve Data for Windsor Sandy Loam, *Water Resources Research*, vol. 25, no. 10, p. 2205-2210.

66. Sloan, E. D., 1990, *Clathrate Hydrates of Natural Gases*, Mercel Dekker, New York, p. 58-59.

67. Sondergeld. C. H., and Rai, C. S., 1993, A New concept in Quantitative Core Characterization, *The Leading Edge*, vol. 12, no. 7, 774-779.

68. Sondergeld, C. H., and Rai C. S., 2007, Observation of Velocity and Resistivity Changes During Freeze-Thaw Cycles in Berea Sandstone, *Geophysics*, vol. 72, no. 2, p. 99-105.

69. Stapf, S., and Kimmich, R., 1995, Molecular Dynamics in Confined Monomolecular Layers. A Field-Cycling Nuclear Magnetic Resonance Relaxometry Study of Liquids in Porous Glass, *Journal of Chemical Physics*, vol. 103, no. 6, p. 2247-2250.

70. Straley, C., Rossini, D., Vinegar, H., Tutunjian, P., and Morriss, C., 1997, Core Analysis by Low field NMR, *The Log Analyst*, vol. 36, no. 1, p. 40-56.

71. Strange, J. H., and Webber, J. B. W., 1997, Spatially Resolved Pore Size Distributions by NMR, *Measurement Science and Technology*, vol. 8, p. 555-561.

72. Timur, A., 1968, Velocity of Compressional Waves in Porous Media at Permafrost Temperatures, *Geophysics*, vol. 33, no. 4, p. 584-595.

73. Torsaeter, O., and Beldring, B., 1987, The Effect of Freezing of Slightly Consolidated Cores, *SPE Formation Evaluation*, p. 357-360.

74. Valiullin, R., and Furo, I., 2002, The Morphology of Coexisting Liquid and Frozen Phases in Porous Materials as revealed by Exchange of Nuclear Spin Magnetization followed by ^{1}H Nuclear Magnetic Resonance, *Journal of Chemical Physics*, vol. 117, no. 5, 2307-2315.

75. Vinegar, H., 1995, *Relaxation Mechanisms*, Chapter 3 in Georgi, D.T., ed., 36th Annual SPWLA Logging Symposium: Nuclear Magnetic Resonance Logging short course notes.

76. Washburn, E. W., 1921, Note on a Method of Determining the Distribution of Pore Sizes in a Porous Material, Proceedings: National Academy of Science, vol. 7, p. 115-116.

77. Wyllie, M. R. T., Gregory, A. R., and Gardner, G. H. F., 1962, Studies of Elastic Wave Attenuation in Porous Media, *Geophysics*, vol. 27, no. 5, p. 569-589.

78. Zimmerman, R. W., 1984, The Effect of Pore Structure on the Pore and Bulk Compressibilities of Consolidated Sandstones, Ph.D thesis, University of California Berkeley, 126pp.

NOMENCLATURE

B_o	: Static magnetic field, tesla
f	: Larmor frequency, MHz
γ	: Gyromagnetic ratio, dimensionless
B_1	: Amplitude of the oscillating field
T_2^*	: Free induction decay (FID) time constant, μsec
M(t)	: Magnitude of the magnetization at a time t, a.u
M_o	: Magnitude of the magnetization at a time t = 0, a.u
t	: Time, μsec
T_2	: Transverse relaxation time, msec
τ	: Time over which the oscillating field is applied, msec
N	: Number of nuclei per unit volume
h	: Planck's constant, 6.626×10^{-34} J/s
I	: Spin quantum number of the nucleus, dimensionless
k	: Boltzman's constant, 1.3807×10^{-23} J/K
T	: Temperature, ^{0}C
C	: Constant
M_{oi}	: Magnitude of the magnetization of the i^{th} pore at a time t = 0, a.u
T_{2i}	: Transverse relaxation time of the i^{th} pore, msec
T_{2Bulk}	: Bulk relaxation time, sec
η	: Viscosity, cp
$T_{2Surface}$	: Surface relaxation time, msec
ρ_2	: Surface relaxivity, μm/sec
$\left(\frac{S}{V}\right)_{pore}$	: Ratio of the pore surface to the pore volume
$T_{2Diffusion}$	: Diffusion relaxation time, msec
D	: Molecular diffusion coefficient, cm^2/sec
G	: Gradient of the magnetic field, G/cm
r	: Radius of the pore, μm

τ_m : Translation correlation time, μsec

ΔE : Effective activation energy, kcal/mol

R : Universal gas constant, J/ K mol

α : Constant

ΔH : Latent heat of fusion, calorie/gm

$\Delta G_{Het.}$: Gibbs free energy associated with heterogeneous nucleation

$\Delta G_{Hom.}$: Gibbs free energy associated with homogeneous nucleation

f : Correlating factor

θ : Contact angle, degree

γ_{sl} : Interfacial tension between solid-liquid interface, J/m^2

γ_{cs} : Interfacial tension between crystal-solid interface, J/m^2

γ_{cl} : Interfacial tension between crystal-liquid interface, J/m^2

t_f : Freezing point of the saline solution, ^0C

S : Salinity of the brine, ppm

a_0 : Constant, -0.0575

a_1 : Constant, 1.710523×10^{-3}

a_2 : Constant, -2.154996×10^{-4}

b : Constant, -7.53×10^{-4}

p : Pressure, psi

ΔT_f : Depression in freezing point, ^0K

T_f : Freezing point in a capillary tube, ^0K

T_{fb} : Bulk freezing temperature, ^0K

ρ_i : Density of ice, kg/m^3

L_{fb} : Latent heat of melting in the bulk, J/kg

K : Constant, 494 ± 19.6 K $Å^{-1}$

$\frac{S_i}{V}$: Ratio of the ice surface to the remaining pore fluid volume

W : Ratio of the mass of the unfrozen water to the dry mass of soil, dimensionless

β : Constant

ΔT	: Difference in temperature of the soil and freezing of pure water, ^0C
W_a	: Ratio of adsorbed mass of the water to the dry mass of the soil, dimensionless
k	: Empirical Constant
Φ	: Porosity, %
V_P	: Pore volume, cm^3
V_B	: Bulk volume, cm^3
V_G	: Grain volume, cm^3
A	: Absorbance of a mineral mixture, dimensionless
ε_i	: Absorptivity of the i^{th} mineral
l	: Absorption path length
c_i	: Concentration of the i^{th} mineral, wt%
P_c	: Capillary Pressure, psi

APPENDICES

Appendix A: NMR Calibration[1]

Steps for MARAN Ultra[5] Resonance Instrument calibration

The following is a stepwise calibration procedure for the NMR machine i.e., Resonance Instrument MARAN Ultra[5]:

1. Click on RINMR, the acquisition and processing software for MARAN Ultra.
2. Put the calibration standard, i.e., a glass vial filled with mineral oil in the NMR sample holder.
3. Adjust the length of the sample holder to 23.5 cm (position in uniform portion of the field) and put sample holder inside the NMR machine
4. From the **"TOOL"** menu on the menu bar click on **"LOAD"** and select the **"Wobble"** option.
5. Click on **"GS1"** option from Command menu on menu bar to execute the Wobble command.
6. There will be a display of two parabolas one normal and one inverted in the Data Window.
7. From the **"VIEW"** menu select the **"MAGNITUDE"** option. It will toggle the display of inverted parabola.
8. Adjust the **"RED KNOB"** on the machine to make the parabola centered at origin.
9. Click on **"STOP"** option in Command menu.
10. Execute the **"AUTO01"** command in the Command menu. After the command is executed you will see a window pop up that will show the value of **"OFFSET"**.

Click "OK" and rerun the **"AUTO01"** command. You will see two bars (green/yellow) one for real and other for the imaginary data that will be parallel to each other. Once again a window will pop up that will show a value of **"OFFSET"**.

11. Click on the **"Acquisition Parameter"**. If the offset is negative or positive, subtract it or add it from the Spectrometer Frequency (MHz). Make sure you take the unit conversion into consideration. Repeat Steps 10 & 11 until the offset lies between -1 to +1. Note the offset and the Spectrometer Frequency (MHz).
12. From the **"TOOL"** menu on the menu bar click on **"LOAD"** and select the **"Train 90"** option.
13. Click on **"GS1"** option from Command menu on menu bar to execute the Train 90 command. You will see small bars in yellow and green parallel to each other.
14. The two should overlay on each other near the x-axis and should be lying on x-axis. If not then type in **"P90"** command and hit enter in the command line which is just below the command history window.
15. You will see a value next to P90 written in the command line. Use **"PgUp or PgDn"** key so that the bars should lie as close as possible to the x-axis. Repeat this step till you get a good match. Note the value that appears next to P90.
16. Click on **"STOP"** option in Command menu and from the **"TOOL"** menu on the menu bar click on **"LOAD"** and select the **"Train 180"** option.
17. Click on **"GS1"** option from Command menu on menu bar to execute the Train 180 command. You will again see small bars in yellow and green parallel to each other lying near to x-axis.

18. Follow Step 14 & 15 again except instead of ***"P90"*** command use **"P180"** command. Note the value that appears next to P180.
19. Click on **"STOP"** option in Command menu.
20. Open the **"Acquisition Parameter"**. Make sure that Spectrometer Frequency (MHz), Offset from SF (Hz), 90 Degree Pulse (μs) and 180 Degree Pulse (μs) are same as above.
21. The machine is calibrated now and ready for use.

Appendix B: Effect of Number of Exponential on T_2 Distribution

For a multiple pore body system such as a porous network, the exponential raw decay is a summation of the individual decays. Using an inversion processing technique the raw decay curve is fitted to a T_2 spectrum or distribution. The inversion process is based on finding a least square solution to a set of linear equation (Coates et al, 1999). The number of unknowns is predefined by number of exponentials e.g. 16, 32, 64, 128 or 256.

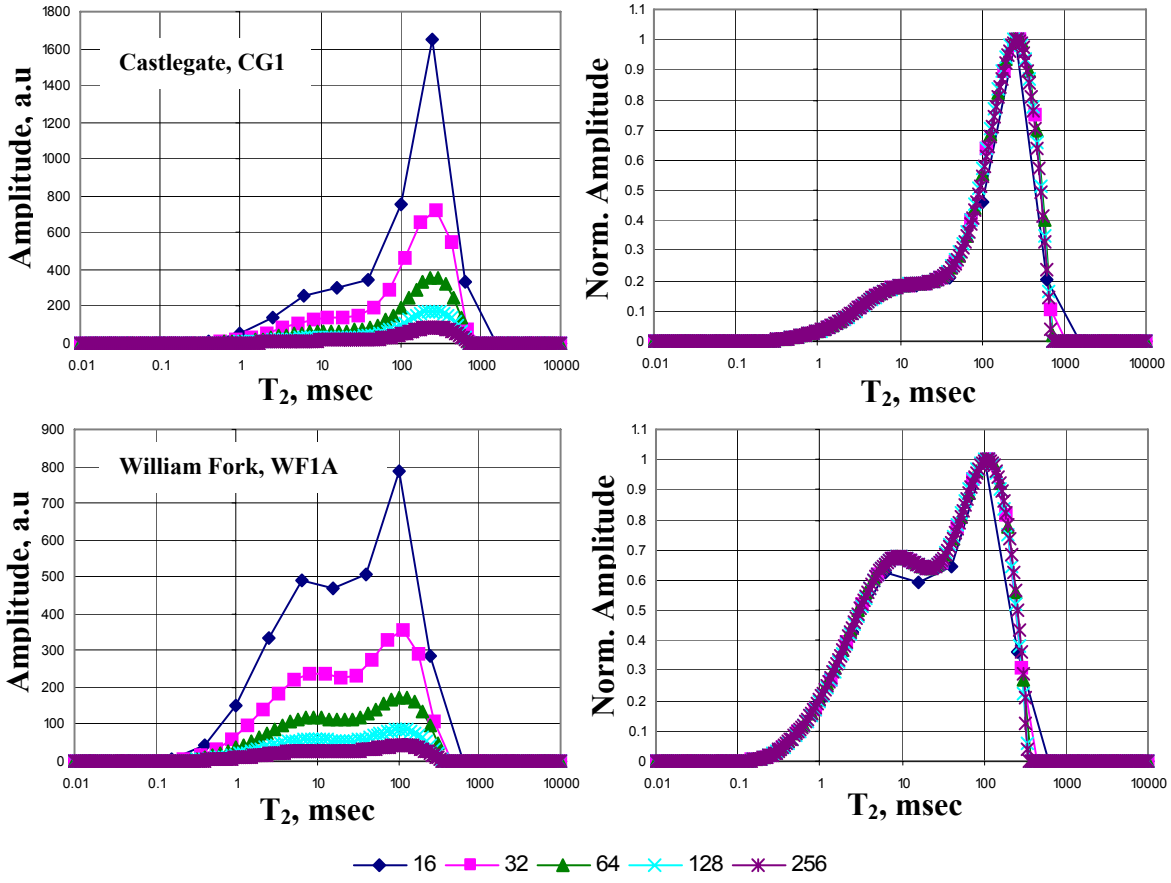

Figure B.1 T_2 distribution of Castlegate, CG1 and William Fork, WF1A as a function of number of exponentials i.e., 16, 32, 64, 128 and 256. For both the sample the shape and the peak of the T_2 distribution is retained irrespective of the number of exponents. The effect of number of exponential on shape and the area under the T_2 distribution is minimum.

Appendix C: Parameters used in the MARAN Ultra[5] System

Description	***ID***	***Value***
---SYSTEM---		
90 Degree Pulse (us)	P90	20.1
180 Degree Pulse (us)	P180	38.7
Probe Dead Time (us)	DEAD1	80.0
Receiver Dead Time (us)	DEAD2	20.0
Spectrometer Frequency (MHz)	SF	2.202286
Offset from SF (Hz)	O1	0.82
---APPLICATION---		
Filter Width (Hz)	FW	4000.0
Dwell Time (us)	DW	1.0
Points per Echo (points)	SI	1
Number of Echoes	NECH	2048
Number of Scans	NS	50
Receiver Gain (%)	RG	100.00
Relaxation Delay (us)	RD	8000000.0
90-180 Degree Pulse Gap (us)	TAU	300.00
90 Degree Pulse Phase List (rec: 0213)	PH1	0213
Receiver Phase List (rec: 0213)	PH2	0213
180 Degree Pulse Phase List (rec: 1122)	PH3	1122
Dummy Scans	DS	0
RF Amplitude (%)	RFA0	100.0

Table C: System and acquisition parameter for the MARAN Ultra Resonance instrument.

Appendix D: Optimization of Inter Echo time (TE) and Wait Time (TW)

Selection of proper inter echo spacing (TE) and wait time (TW) is crucial for NMR experiments otherwise information will be lost during signal acquisition. NMR experiments were performed on a Hollin core sample (6715v) saturated with 25,000 ppm NaCl brine at 28 ^{0}C to optimize values of TE and TW.

Wait Time (TW): The wait time (TW) is defined as the time during which repolarization of the hydrogen atoms takes place before the start of the next CPMG pulse sequence. On average TW should be set to a value greater than equal to $3T_2$ but less than $5T_2$, where T_2 is the transverse relaxation time of the bulk fluid (Coates et al., 1999).

Inter Echo Spacing (TE): The inter-echo spacing (TE) is defined as the gap between the two rephasing pulses i.e., between 180^0 and 180^0 pulse in a CPMG pulse sequence. Short TE values cause spin echoes to be generated faster, producing a better signal to noise ratio. Short values of TE will capture the early time information in the raw decay, i.e., the short times in the T_2 distribution. These are associated with the smallest pore bodies.

Case 1: Affect of Inter Echo Spacing (TE) - Hollin, 6715 v

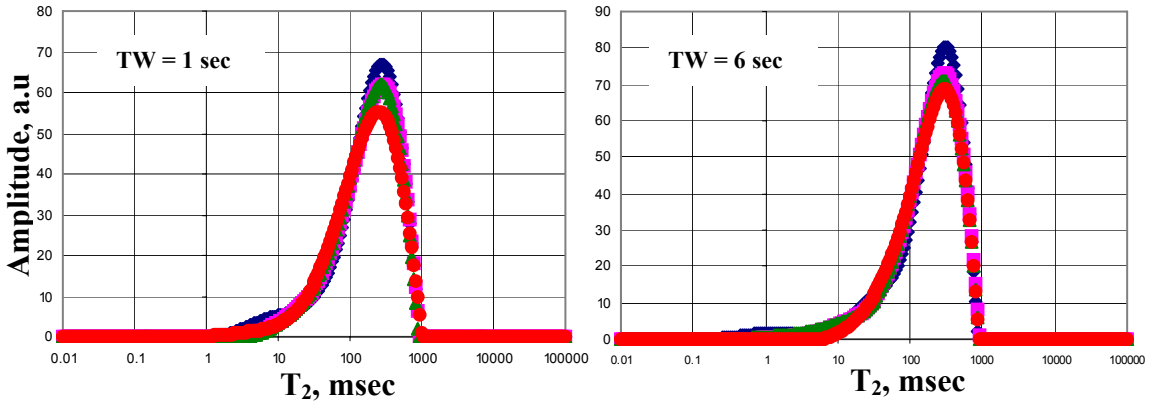

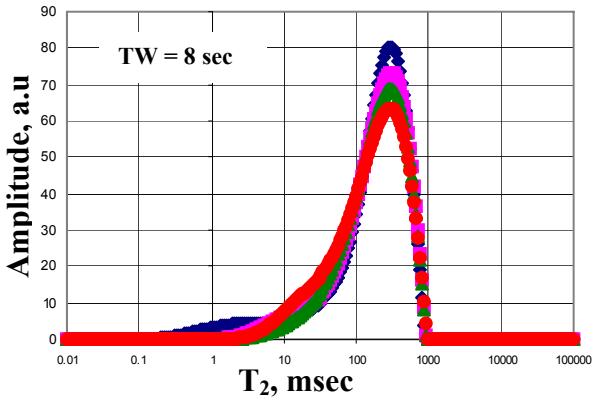

Figure D.1 T_2 distribution of a Hollin core plug (6715v) as a function of inter-echo spacing (TE) for different wait times (TW). The different inter-echo spacing considered for this study are 0.6 msec (blue diamond), 1.0 msec (magenta square), 1.5 msec (green triangle) and 3.0 msec (red circle). All of the T_2 distributions have many common features, e.g., the presence of side lobes and the peak amplitude positions. The only difference is in the total amplitude which results in differences in the estimated porosity.

Case 2: Affect of Wait Time (TW) - Hollin, 6715 v

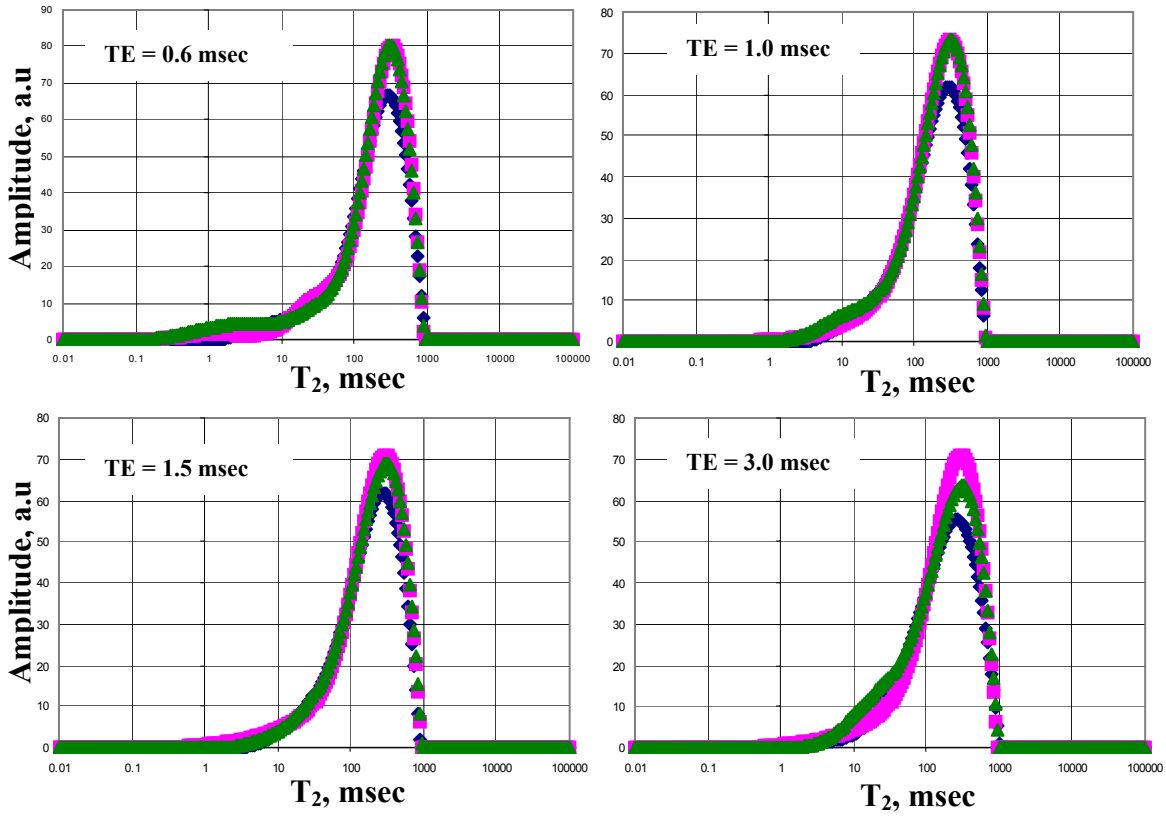

Figure D.2 T_2 distribution of Hollin core plug (6715v) as a function of wait time (TW) for different inter-echo spacings (TE). The different wait time considered for this study are 1.0 sec (blue diamond), 6.0 sec (magenta square) and 8.0 sec (green triangle) All of the T_2 distributions have many common features. The difference in the total amplitude which results in the differences in the estimated porosity.

S.No.	Sample ID	Saturated Porosity (%)	TE msec	TW sec	Bulk Vol. (cc)	No. Scans	S.F	NMR Area	NMR Porosity (%)	$\Delta\phi$, %
1	6715v	18.58	0.6	1	10.86	50	24	2269.747	17.42	-1.16
2	6715v	18.58	1.0	1	10.86	50	24	2197.468	16.86	-1.72
3	6715v	18.58	1.5	1	10.86	50	24	2198.067	16.87	-1.71
4	6715v	18.58	3.0	1	10.86	50	24	2139.369	16.42	-2.16
5	6715v	18.58	0.6	6	10.86	50	24	2439.369	18.72	0.14
6	6715v	18.58	1.0	6	10.86	50	24	2457.902	18.86	0.28
7	6715v	18.58	1.5	6	10.86	50	24	2455.435	18.84	0.26
8	6715v	18.58	2.0	6	10.86	50	24	2341.906	17.97	-0.61
9	6715v	18.58	0.6	8	10.86	50	24	2619.761	20.10	1.52
10	6715v	18.58	1.0	8	10.86	50	24	2531.024	19.42	0.84
11	6715v	18.58	1.5	8	10.86	50	24	2435.014	18.68	0.10
12	6715v	18.58	3.0	8	10.86	50	24	2501.265	19.19	0.61

Table D.1: Summary of the NMR estimated porosity for different TE's and TW's for Hollin, 6715v. Note that two combinations of TE and TW produce the best agreement with the known value of the porosity e.g., TE = 0.6 msec and TW = 6 sec and TE = 1.5 msec and TW = 8.0 sec.

Summary of the area under the T_2 distribution, the estimated porosity and the difference between saturated and NMR porosity is presented in **Table D.1**. The T_{2Bulk} relaxation time of the brine used for the study is 2.1 sec at 22 ^{0}C. Thus the optimum TW is 6.0 sec while for TE it can be 0.6, 1.0, 1.5 or 2.0 msec. It is better to use TE of 0.6 msec to capture the small pore bodies as observed in prominent side lobes in **Fig. D.1** and **Fig. D.2**. Further, the NMR estimated porosity lies within ± 0.5 % of the saturated porosity. Optimization of acquisition parameter was performed on all samples before conducting the freeze-thaw experiments.

S.No.	Sample ID	Saturated Porosity (%)	TE msec	TW sec	Bulk Vol. (cc)	No. Scans	S.F	NMR Area	NMR Porosity (%)	Δϕ, %
1	33H	22.37	0.6	1	12.68	50	24	2963.869	19.48	-2.89
2	33H	22.37	1.0	1	12.68	50	24	2860.824	18.80	-3.57
3	33H	22.37	1.5	1	12.68	50	24	2831.237	18.61	-3.76
4	33H	22.37	2.0	1	12.68	50	24	2826.837	17.49	-5.88
5	33H	22.37	3.0	1	12.68	50	24	2759.302	18.13	-4.24
5	33H	22.37	0.6	6	12.68	50	24	3361.083	22.09	-0.28
6	33H	22.37	1.0	6	12.68	50	24	3254.180	21.39	-0.98
7	33H	22.37	1.5	6	12.68	50	24	3225.003	21.19	-1.18
8	33H	22.37	2.0	6	12.68	50	24	3244.665	21.32	-1.05
9	33H	22.37	3.0	6	12.68	50	24	3163.678	19.57	-3.80
10	33H	22.37	0.6	8	12.68	50	24	3321.017	21.83	-0.54
11	33H	22.37	1.0	8	12.68	50	24	3355.215	22.05	-0.32
12	33H	22.37	1.5	8	12.68	50	24	3383.964	22.24	-0.13
12	33H	22.37	2.0	8	12.68	50	24	3256.115	21.40	-0.97
12	33H	22.37	3.0	8	12.68	50	24	3230.742	19.98	-3.39

Table D.2: Summary of the NMR estimated porosity for different TE's and TW's for Berea, 33H.

S.No.	Sample ID	Saturated Porosity (%)	TE msec	TW sec	Bulk Vol. (cc)	No. Scans	S.F	NMR Area	NMR Porosity (%)	Δϕ, %
1	CG1	25.88	0.6	1	12.10	50	24	3557.000	24.50	-1.38
2	CG1	25.88	1.0	1	12.10	50	24	3524.097	24.27	-1.61
3	CG1	25.88	1.5	1	12.10	50	24	3368.772	23.20	-2.68
4	CG1	25.88	2.0	1	12.10	50	24	3455.728	22.40	-3.48
5	CG1	25.88	3.0	1	12.10	50	24	3534.715	24.34	-1.54
5	CG1	25.88	0.6	6	12.10	50	24	3847.324	26.50	0.62
6	CG1	25.88	1.0	6	12.10	50	24	3871.218	26.66	0.78
7	CG1	25.88	1.5	6	12.10	50	24	3667.845	25.26	-0.62
8	CG1	25.88	2.0	6	12.10	50	24	3625.628	24.97	-0.91
9	CG1	25.88	3.0	6	12.10	50	24	3597.524	23.32	-2.56
10	CG1	25.88	0.6	8	12.10	50	24	3976.661	27.39	1.51
11	CG1	25.88	1.0	8	12.10	50	24	3711.650	25.56	-0.32
12	CG1	25.88	1.5	8	12.10	50	24	3733.374	25.71	-0.17
12	CG1	25.88	2.0	8	12.10	50	24	3611.134	24.87	-1.01
12	CG1	25.88	3.0	8	12.10	50	24	3509.549	22.75	-3.13

Table D.3: Summary of the NMR estimated porosity for different TE's and TW's for Castlegate, CG1

S.No.	Sample ID	Saturated Porosity (%)	TE msec	TW sec	Bulk Vol. (cc)	No. Scans	S.F	NMR Area	NMR Porosity (%)	$\Delta\phi$, %
1	10744.2 ft	32.15	0.6	1	10.36	50	24	4157.511	33.44	1.29
2	10744.2 ft	32.15	1.0	1	10.36	50	24	3990.687	32.10	-0.05
3	10744.2 ft	32.15	1.5	1	10.36	50	24	3768.833	30.32	-1.83
4	10744.2 ft	32.15	2.0	1	10.36	50	24	3885.678	29.42	-2.73
5	10744.2 ft	32.15	3.0	1	10.36	50	24	3181.893	25.59	-6.56
5	10744.2 ft	32.15	0.6	6	10.36	50	24	4031.326	32.43	0.28
6	10744.2 ft	32.15	1.0	6	10.36	50	24	3997.584	32.16	0.01
7	10744.2 ft	32.15	1.5	6	10.36	50	24	3576.382	28.77	-3.38
8	10744.2 ft	32.15	2.0	6	10.36	50	24	3215.974	25.87	-6.28
9	10744.2 ft	32.15	3.0	6	10.36	50	24	3418.280	25.88	-6.27
10	10744.2 ft	32.15	0.6	8	10.36	50	24	4068.037	32.72	0.57
11	10744.2 ft	32.15	1.0	8	10.36	50	24	4042.931	32.52	0.37
12	10744.2 ft	32.15	1.5	8	10.36	50	24	3777.851	30.39	-1.76
12	10744.2 ft	32.15	2.0	8	10.36	50	24	3288.913	26.46	-5.69
12	10744.2 ft	32.15	3.0	8	10.36	50	24	3246.770	24.58	-7.57

Table D.4: Summary of the NMR estimated porosity for different TE's and TW's for Tuscaloosa Sand, 10744.2 ft. Note that two combinations of TE and TW produce the best agreement with the known value of the porosity e.g., TE = 1.0 msec and TW = 1 sec and TE = 1.0 msec and TW = 6.0 sec.

Appendix E: Incremental Mercury Injection

High pressure mercury injection was performed from 0 to 60,000 psia on end pieces of all the six core plugs. Effective surface relaxivity is estimated by comparing the normalized incremental mercury injection curve with the normalized T_2 distribution.

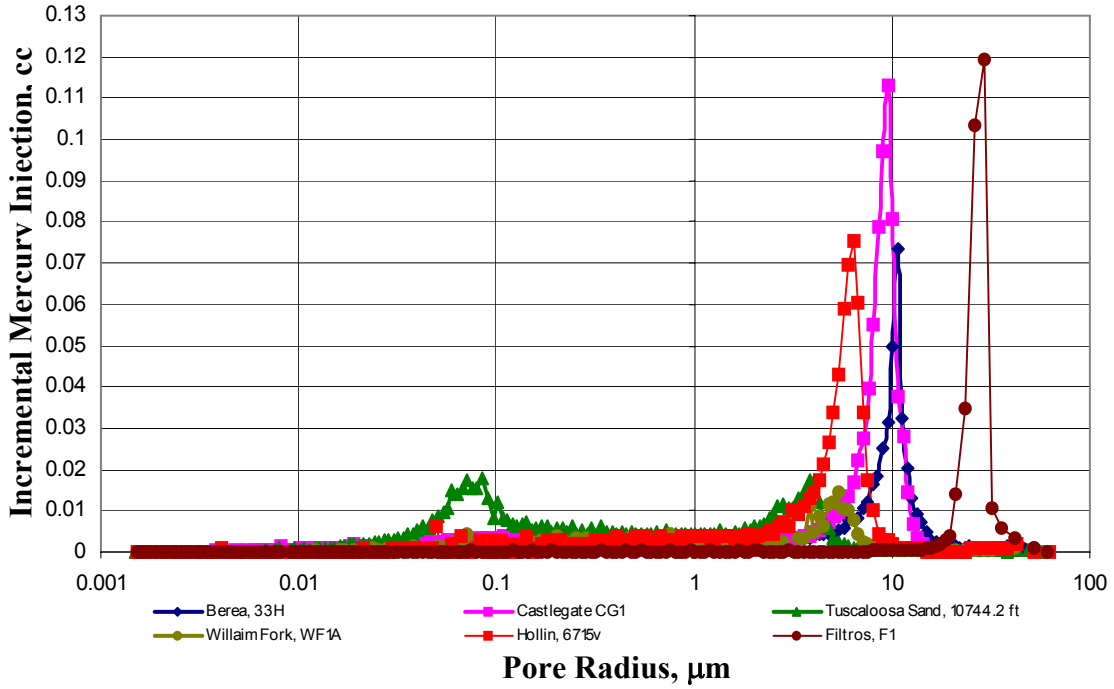

Figure E.1: Except Tuscaloosa sand, 10744.2 ft and William Fork, WF1A, rest of the core plugs are dominated by a narrow range of bigger pore throat. Further Tuscaloosa sand, 10744.2 ft and William Fork, WF1A shows a bimodal pore throat size distribution as seen in NMR T_2 distribution.

Appendix F: Estimation of Surface Relaxivity

NMR T_2 Relaxation :

$$\frac{1}{T_2} = \rho \frac{S}{V}$$

Assuming cylindrical pores : $\frac{S}{V} = \frac{2}{r_b}$

$$\frac{1}{T_2} = \rho \frac{2}{r_b}$$

$$= \rho \left(\frac{2}{r_b} \right) \left(\frac{r_{th}}{r_{th}} \right); \text{where } r_{th} \text{ is radius of the throat}$$

$$= \rho \left(\frac{r_{th}}{r_b} \right) \left(\frac{2}{r_{th}} \right)$$

$$\frac{1}{T_2} = \rho_e \left(\frac{2}{r_{th}} \right)$$

where, $\rho_e \left(\text{Effective Surface Relaxivity} \right) = \rho \left(\frac{r_{th}}{r_b} \right)$ .....(1)

Washburn equation :

$$P_c = \frac{2\gamma \cos\theta}{r_{th}} \text{.....(2)}$$

Comparing Eqn.(1) and (2)

$$\rho_e = \frac{\gamma \cos\theta}{P_c T_2}$$

γ = 485dynes/cm = 7.01 x 10^{-5} psi.m, $\theta = 140^0$, $P_c \bullet T_2$ = 2.5psi.sec

$$\rho_e = \frac{5.37 * 10^{-5}}{2.5} \mu m/sec$$

ρ_e = 21.5μm/sec

Appendix G: Simple Model Calculation

Assuming a spherical pore with pore radius (r_p) = 10 μm

$$\text{Total Pore Volume (Vp)} = \frac{4}{3}\pi r_p = 4190.48\ \mu m^3$$

Assume surface relaxivity of pore (ρ_p) = 25 μm/sec
Assume different surface relaxivity of the ice (ρ_i) = 0, 25, 100, and 1000 μm/sec

NMR T_2 time for 100% liquid filled water

$$\frac{1}{T_2} = \rho\frac{S}{V} = 25\ (\mu m/sec)\frac{3}{10(\mu m)}$$

$$T_2 = 133.3\ msec$$

Assuming water and ice have the same density, volume of unfrozen water, volume of ice, the radius of water and radius of ice are calculated during the water-ice transformation for a single pore (r_p = 10 μm).

S.No.	Unfrozen Water fraction	Volume of Water cc	Volume of Ice cc	Radius of Ice μm	Radius of Water μm
1	1.0	4190.5	0.0	0.00	10.00
2	0.9	3771.4	419.0	4.64	9.65
3	0.8	3352.4	838.1	5.85	9.28
4	0.7	2933.3	1257.1	6.69	8.88
5	0.6	2514.3	1676.2	7.37	8.43
5	0.5	2095.2	2095.2	7.94	7.94
6	0.4	1676.2	2514.3	8.43	7.37
7	0.3	1257.1	2933.3	8.88	6.69
8	0.2	838.1	3352.4	9.28	5.85
9	0.1	419.0	3771.4	9.65	4.64
10	0	0.0	4190.5	10.00	0.00

Table G.1: Calculated volume of unfrozen water, volume of ice, the radius of water and radius of ice for different fractions of unfrozen water content. Radius of ice is used for pore filling ice case while radius of water is considered for pore lining ice.

Two idealistic models (**Fig. 4.8.13**) are considered when water and ice coexist in a pore. The T_2 time is calculated using **Eqn. 2.18**.

As an example, T_2 time is calculated for pore filling and pore lining ice when 30% of the water is frozen, i.e., unfrozen water content is 0.7.

Case 1: Pore Lining Ice; Pore Filling Water (**Fig. 4.8.13 (A)**), **Eqn. 2.18**. is modified as

$$\frac{1}{T_2} = \rho_i\left(\frac{S_i}{V_L}\right) \quad \ldots\ldots\ldots\ldots\ldots\ldots\ldots\ldots\ldots\ldots\ldots\ldots \{G.1\}$$

In this case, there will always a layer of ice next to the grain surface whose thickness increases as freezing progresses from 0 % to 100%.

$$\text{Pore radius } (r_p) = 10\ \mu m$$

$$\text{Total pore volume (Vp)} = \frac{4}{3}\pi r_p = 4190.48\ \mu m^3$$

$$\text{Volume of water unfrozen} = 0.7 \times 4190.48 = 2933.3\ \mu m^3$$

$$\text{Radius of the water } (r_w) = \sqrt[3]{\frac{2933.3}{(4/3)\times(22/7)}} = 8.88\ \mu m$$

$$\frac{1}{T_2} = \rho_i \left(\frac{4\pi r_w^{\ 2}}{(4/3)\pi r_w^{\ 3}} \right)$$

$$T_2 = \frac{1000}{\rho_i} \times \frac{r_w}{3}$$

For surface relaxivity of ice (ρ_i) = 0 μm/sec, there is no surface relaxation only bulk relaxation. This is independent of the amount of the ice present in the system.

For surface relaxivity of ice (ρ_i) = 25 μm/sec

$$T_2 = \frac{1000}{25} \times \frac{8.88}{3} = 118.39\ \text{msec}$$

For surface relaxivity of ice (ρ_i) = 100 μm/sec

$$T_2 = \frac{1000}{100} \times \frac{8.88}{3} = 29.6\ \text{msec}$$

For surface relaxivity of ice (ρ_i) = 100 μm/sec

$$T_2 = \frac{1000}{1000} \times \frac{8.88}{3} = 2.96\ \text{msec}$$

Case 2: Pore Filling Ice; Pore Lining Water (**Fig. 4.8.13 (B)**), **Eqn. 2.18**. is modified as

$$\frac{1}{T_2} = \rho_p \left(\frac{S_p}{V_L} \right) + \rho_i \left(\frac{S_i}{V_L} \right) \quad \text{..... \{G.2\}}$$

where V_L is the volume of the liquid present in the system, S_p is the surface area of the pore and S_i is the surface area of the spherical ice. Volume of the liquid (V_L) is product of the unfrozen water fraction and total pore volume. Surface area of the pore (S_p) remains constant while the surface area of the ice (S_i) changes with freezing.

$$\frac{1}{T_2} = \rho_p \left(\frac{4\pi r_p^{\,2}}{0.7 \times 4190.48} \right) + \rho_i \left(\frac{4\pi r_i^{\,2}}{0.7 \times 4190.48} \right)$$

$$\frac{1}{T_2} = \rho_p \left(\frac{4\pi r_p^{\,2}}{2933.3} \right) + \rho_i \left(\frac{4\pi r_i^{\,2}}{2933.3} \right)$$

For surface relaxivity of ice (ρ_i) = 0 μm/sec

$$\frac{1}{T_2} = 25 \left(\frac{4 \times \left(22/7 \right) \times (10)^2}{2933.3} \right) + 0 \times \left(\frac{4 \times \left(22/7 \right) \times (6.69)^2}{2933.3} \right)$$

$$T_2 = 93.33 \text{ msec}$$

For surface relaxivity of ice (ρ_i) = 25 μm/sec

$$\frac{1}{T_2} = 25 \left(\frac{4 \times \left(22/7 \right) \times (10)^2}{2933.3} \right) + 25 \times \left(\frac{4 \times \left(22/7 \right) \times (6.69)^2}{2933.3} \right)$$

$$T_2 = 64.48 \text{ msec}$$

For surface relaxivity of ice (ρ_i) = 100 μm/sec

$$\frac{1}{T_2} = 25 \left(\frac{4 \times \left(22/7 \right) \times (10)^2}{2933.3} \right) + 100 \times \left(\frac{4 \times \left(22/7 \right) \times (6.69)^2}{2933.3} \right)$$

$$T_2 = 33.42 \text{ msec}$$

For surface relaxivity of ice (ρ_i) = 1000 μm/sec

$$\frac{1}{T_2} = 25 \left(\frac{4 \times \left(22/7 \right) \times (10)^2}{2933.3} \right) + 1000 \times \left(\frac{4 \times \left(22/7 \right) \times (6.69)^2}{2933.3} \right)$$

$$T_2 = 4.93 \text{ msec}$$

The procedure mentioned above is employed for calculating T_2 time from 100 % unfrozen to completely frozen for four different pore radii 0.1, 1, 10 and 30 μm. The result is tabulated in **Table G.2, Table G.3, Table G.4** and **Table G.5**. The tabulated result is graphically presented in **Fig. 4.8.14**.

S.No.	Unfrozen Water fraction	Estimated T_2 time for a Single Pore of Radius 0.1 μm during Freezing Process							
		T_2 , msec (Pore Filling Ice; Pore Lining Water)				T_2 , msec (Pore Lining Ice; Pore Filling Water)			
		ρ = 0	ρ = 25	ρ = 100	ρ =1000	ρ = 0	ρ = 25	ρ = 100	ρ = 100
1	1.0	1.33	1.33	1.33	1.33	1.33	1.33	1.33	1.33
2	0.9	1.20	0.99	0.64	0.12	No Relaxivity	1.29	0.32	0.03
3	0.8	1.07	0.79	0.45	0.07	No Relaxivity	1.24	0.31	0.03
4	0.7	0.93	0.64	0.33	0.05	No Relaxivity	1.18	0.30	0.03
5	0.6	0.80	0.52	0.25	0.04	No Relaxivity	1.12	0.28	0.03
6	0.5	0.67	0.41	0.19	0.03	No Relaxivity	1.06	0.26	0.03
7	0.4	0.53	0.31	0.14	0.02	No Relaxivity	0.98	0.25	0.02
8	0.3	0.40	0.22	0.10	0.01	No Relaxivity	0.89	0.22	0.02
9	0.2	0.27	0.14	0.06	0.01	No Relaxivity	0.78	0.19	0.02
10	0.1	0.13	0.07	0.03	0	No Relaxivity	0.62	0.15	0.02
11	0.0	No Relaxivity	No Relaxivity	No Relaxivity	No Relaxivity	No Relaxivity	No Relaxivity	No Relaxivity	No Relaxivity

Figure G.2 Estimated T_2 time as a function of unfrozen water for pore filling and pore lining ice for a single pore of radius 0.1 μm assuming different surface relaxivities of ice 0, 25, 100 and 1000 μm/sec. The completely frozen pore has no relaxivity.

S.No.	Unfrozen Water fraction	Estimated T_2 time for a Single Pore of Radius 1.0 μm during Freezing Process							
		T_2 , msec (Pore Filling Ice; Pore Lining Water)				T_2 , msec (Pore Lining Ice; Pore Filling Water)			
		ρ = 0	ρ = 25	ρ = 100	ρ =1000	ρ = 0	ρ = 25	ρ = 100	ρ = 100
1	1.0	13.33	13.33	13.33	13.33	13.33	13.33	13.33	13.33
2	0.9	12.00	9.87	6.45	1.25	No Relaxivity	12.87	3.22	0.32
3	0.8	10.67	7.95	4.50	0.73	No Relaxivity	12.38	3.09	0.31
4	0.7	9.33	6.45	3.34	0.49	No Relaxivity	11.84	2.96	0.30
5	0.6	8.00	5.19	2.52	0.35	No Relaxivity	11.25	2.81	0.28
6	0.5	6.67	4.09	1.89	0.25	No Relaxivity	10.58	2.65	0.26
7	0.4	5.33	3.12	1.39	0.18	No Relaxivity	9.82	2.46	0.25
8	0.3	4.00	2.24	0.96	0.12	No Relaxivity	8.93	2.23	0.22
9	0.2	2.67	1.43	0.60	0.08	No Relaxivity	7.80	1.95	0.19
10	0.1	1.33	0.69	0.28	0.03	No Relaxivity	6.19	1.55	0.15
11	0.0	No Relaxivity	No Relaxivity	No Relaxivity	No Relaxivity	No Relaxivity	No Relaxivity	No Relaxivity	No Relaxivity

Figure G.3 Estimated T_2 time as a function of unfrozen water for pore filling and pore lining ice for a single pore of radius 1.0 μm assuming different surface relaxivities of ice 0, 25, 100 and 1000 μm/sec. The completely frozen pore has no relaxivity.

S.No.	Unfrozen Water fraction	Estimated T_2 time for a Single Pore of Radius 10.0 μm during Freezing Process							
		T_2 , msec (Pore Filling Ice; Pore Lining Water)				T_2 , msec (Pore Lining Ice; Pore Filling Water)			
		ρ = 0	ρ = 25	ρ = 100	ρ =1000	ρ = 0	ρ = 25	ρ = 100	ρ = 100
1	1.0	133.33	133.33	133.33	133.33	133.33	133.33	32.18	133.33
2	0.9	120.00	98.73	64.45	12.48	No Relaxivity	128.73	32.18	3.22
3	0.8	106.67	79.48	45.05	7.27	No Relaxivity	123.78	30.94	3.09
4	0.7	93.33	64.45	33.42	4.93	No Relaxivity	118.78	29.60	2.96
5	0.6	80.00	51.85	25.22	3.52	No Relaxivity	112.46	28.11	2.81
6	0.5	66.67	40.90	18.94	2.54	No Relaxivity	105.83	26.46	2.65
7	0.4	53.33	31.16	12.87	1.81	No Relaxivity	98.24	24.56	2.46
8	0.3	40.00	22.37	9.63	1.23	No Relaxivity	89.26	22.31	2.23
9	0.2	26.67	14.32	6.00	0.75	No Relaxivity	77.97	19.49	1.95
10	0.1	13.33	6.90	2.8	0.35	No Relaxivity	61.89	15.47	1.55
11	0.0	No Relaxivity	No Relaxivity	No Relaxivity	No Relaxivity	No Relaxivity	No Relaxivity	No Relaxivity	No Relaxivity

Figure G.4 Estimated T_2 time as a function of unfrozen water for pore filling and pore lining ice for a single pore of radius 10.0 μm assuming different surface relaxivities of ice 0, 25, 100 and 1000 μm/sec. The completely frozen pore has no relaxivity.

S.No.	Unfrozen Water fraction	Estimated T_2 time for a Single Pore of Radius 30.0 μm during Freezing Process							
		T_2 , msec (Pore Filling Ice; Pore Lining Water)				T_2 , msec (Pore Lining Ice; Pore Filling Water)			
		ρ = 0	ρ = 25	ρ = 100	ρ =1000	ρ = 0	ρ = 25	ρ = 100	ρ = 100
1	1.0	400.00	400.00	400.00	400.00	400.00	400.00	400.00	400.00
2	0.9	360.00	296.19	193.36	37.43	No Relaxivity	386.20	96.55	9.65
3	0.8	320.00	238.45	135.14	21.80	No Relaxivity	371.33	92.83	9.28
4	0.7	280.00	193.35	100.27	14.79	No Relaxivity	355.16	88.79	8.88
5	0.6	240.00	155.55	75.67	10.57	No Relaxivity	337.37	84.34	8.43
6	0.5	200.00	122.70	56.82	7.63	No Relaxivity	317.48	79.37	7.94
7	0.4	160.00	93.49	41.61	5.43	No Relaxivity	294.72	73.68	7.37
8	0.3	120.00	67.10	28.89	3.69	No Relaxivity	267.77	66.94	6.69
9	0.2	80.00	42.97	17.99	2.26	No Relaxivity	233.92	58.48	5.85
10	0.1	40.00	20.70	8.46	1.04	No Relaxivity	185.66	46.42	4.64
11	0.0	No Relaxivity	No Relaxivity	No Relaxivity	No Relaxivity	No Relaxivity	No Relaxivity	No Relaxivity	No Relaxivity

Figure G.5 Estimated T_2 time as a function of unfrozen water for pore filling and pore lining ice for a single pore of radius 30.0 μm assuming different surface relaxivities of ice 0, 25, 100 and 1000 μm/sec. The completely frozen pore has no relaxivity.

Appendix H: Grain Volume Determination[10]

The following is a stepwise procedure to estimate the grain volume and porosity from shale samples.

1. A shale sample weighing approximately (~ 8 gm) is obtained.
2. Using mercury immersion technique determines the bulk volume (V_b) of the sample.
3. Clean with acetone crucible and all the aluminum sheets to avoid any contamination.
4. The sample is then crushed in the crucible (**Fig. H.1**) with the cover secured.

Figure H.1: Covered crucible to crush shale samples. Allows crushing the sample without loss of material.

5. Very carefully transfer the powdered sample into the aluminum cell of Low Pressure Porosimeter (LPP) (**Fig. H.2**).

[10] Protocol Developed by Mr. Argyrios Karastathis & presented at Experimental Rock Physics Consortium Annual Meeting, University of Oklahoma, Norman (2006).

Figure H.2: Low pressure pycnometer (LPP) and aluminum measuring vial.

6. Determine the weight of the powdered sample and calculate the weight loss with respect to the original weight.
7. The weight loss needs to be less than 0.1% otherwise repeat Step 1 to 6.
8. The LPP aluminum cell containing the powdered sample is kept in a vacuum oven at 100^{o}C for 16 hours.
9. Remove the aluminum cell from the vacuum oven and store it in a desiccator to bring it to room temperature.
10. Measure the weight of the aluminum cell containing the powdered sample and calculate the weight of the powdered sample (m_3) and weight loss (Δm) due to heating.
11. The LPP aluminum cell containing the powdered sample is placed in the LPP pycnometer to determine the grain volume V_g.

12. Repeat Step 11 three to four times to get a consistent number for the grain volume and calculate an average grain volume.

13. The grain density can be calculated by using the following formula:

$$\rho_g = \frac{m_3}{V_g} \quad \text{..... \{H.1\}}$$

14. Calculate the corrected grain volume due to weight loss as a result of crushing and transportation of the sample.

$$V^*_g = V_g + \frac{\Delta m}{\rho_g} \quad \text{..... \{H.2\}}$$

15. Calculate the water free porosity

$$\phi = \frac{V_b - V^*_g}{V_b} \quad \text{..... \{H.3\}}$$